In situ Studies of Photo-Induced Dynamics at Liquid Interfaces and in Solution Utilising X-ray and Neutron Scattering Techniques

Dissertation

zur Erlangung des Doktorgrades
der Mathematisch-Naturwissenschaftlichen Fakultät
der Christian-Albrechts-Universität zu Kiel
vorgelegt von

Svenja C. Hövelmann

Kiel, 2025

Erste Gutachterin:	PD Dr. Bridget M. Murphy
Zweite Gutachterin:	Prof. Dr. Thisbe K. Lindhorst
Tag der mündlichen Prüfung:	04.08.2025

URN: urn:nbn:de:gbv:8:3-2025-01241-7

Kurzfassung

In dieser Arbeit wurde lichtinduzierte Struktur- und Formveränderungen an flüssigen Grenzflächen, im Speziellen von Salzlösungen, Langmuir-Monolagen und Flüssigkristallen, mit Röntgen- und Neutronenstreumethoden unter anderem Röntgenreflektometrie (XRR), Beugung unter streifendem Einfall (GID), Röntgenfluoreszenz unter Totalreflektion (XRFNTR), Laser Pump - Röntgen Probe, Kleinwinkelröntgenstreuung (SAXS) und Neutronenreflektometrie (NR).

Die Form und Mesophase von Flüssigkristallen, bestehend aus Phospholipiden und künstlichen Azobenzol Amphiphile, wurde mittels *in situ* Kleinwinkelstreuung untersucht. Dabei wurden lichtinduzierte Mesophasenübergänge von einer lamellaren zu einer kubischen Mesophase für Kombinationen mit dem zuckerlosen Azobenzol Amphiphil entdeckt. Das Ausbilden und die Übergänge zwischen kubischen Mesophasen ist wichtig zum Entwerfen von Transportsystemen für Medikamente und zum Verstehen von Membraneigenschaften während strukturellen Übergängen wie zum Beispiel bei Membranverschmelzungen.

Modellmembrane, in die photoschaltbare künstliche Glycolipide eingebaut sind, zeigten Änderungen der Monolagenstruktur und die Möglichkeit die Ausrichtung der Kopfgruppe der Glycolipide zu kontrollieren. Die Änderungen in der Membrandicke und das Verschwinden der geordneten Ausrichtung der Kopfgruppen wurde mit *in situ* XRR, GID und NR Messungen beobachtet. Damit zeigen die Ergebnisse potenzielle Anwendungen von photoschaltbaren Glycolipiden um das Anhaften von Proteinen und Bakterien an Lipidmembranen zu kontrollieren.

Untersuchungen der oberflächennahen Ionen in Jodsalzlösungen mit XRR und XRFNTR zeigten Abweichungen an der Oberfläche von der erwarteten Ionenkonzentration im Volumen auf. Dies deutet auf eine Anreicherung von Jod-Ionen an der Grenzfläche bei Raumtemperatur hin. Zudem deuten die Daten eine Änderung der Ionenkonzentration unter Beleuchtung mit UV Licht an. Das Verständnis von Ionen An- und -abreicherungsprozessen an der Grenzfläche ist wichtig für das Verstehen von chemischen Reaktionen an Flüssiggrenzflächen.

Des Weiteren können Ionen durch Laserpulse im UV Bereich angeregt werden und die Fotoreaktionen geschehen auf Zeitskalen von wenigen fs bis µs. In Vorbereitung auf Messungen solcher Fotoreaktionen wurde der Laser Pump - Röntgen Probe Aufbau am

Flüssigkeitsdiffraktometer (englisch: Liquid Interface Scattering Apparatus (LISA)) an dem Messplatz P08, PETRA III im Rahmen dieser Arbeit erweitert. Damit wurden der Bereich der Zeitabstände zwischen Laser- und Röntgenpuls vergrößert, eine gleichmäßige Leistungsverteilung des Laserstrahls auf hitzeempfindliche Proben ermöglicht und die Bedienbarkeit der Instrumente verbessert.

Abstract

In this thesis light-induced structure and morphology changes at liquid interfaces, specifically of aqueous salt solutions, Langmuir monolayers and lyotropic liquid crystals, were investigated by utilising X-ray and neutron scattering techniques, i.e. X-ray reflectivity (XRR), grazing incidence diffraction (GID), X-ray fluorescence near total reflection (XRFNTR), laser pump - X-ray probe, small angle X-ray scattering (SAXS) and neutron reflectivity (NR).

Studying the morphology of lyotropic liquid crystals formed by compositions of phospholipids and artificial azobenzene amphiphiles with *in situ* SAXS identified their shapes and mesophases. Light-induced mesophase transitions from a lamellar to a cubic mesophase for combinations with the azobenzene amphiphiles without a sugar group attached to the head group were revealed. The formation and transition between cubic mesophases are of high interest for designing drug delivery systems and to study membrane properties during membrane fusions.

Embedding photoswitchable glycolipids containing an azobenzene switch into model membranes revealed changes of the monolayer structure and the possibility to control the head group orientation of the glycolipid. The changes in the layer thickness and disappearance of the head group ordering were observed with complementary *in situ* XRR, GID and NR studies. These findings show high potential for photoswitchable glycolipids to control protein and bacteria adhesion at lipid membranes.

XRR and XRFNTR studies on surface near ions in aqueous sodium iodide (NaI) salt solutions showed a deviation from the expected ion concentration in the bulk suggesting an enrichment of iodide ions at the interface at room temperature. Under UV laser irradiation, the data indicated a change of the iodide concentration at the interface. Studying ion enrichment and depletion at liquid interfaces contributes to understanding and explaining chemical reactions at liquid surfaces.

Moreover, ions can be excited by UV laser pulses and the photoreactions occur on time scales of few fs to µs. In preparation to study such photoexcitation, the laser pump - X-ray probe setup at the LISA endstation at P08, PETRA III was upgraded within this thesis to extend the range of delays between the laser and X-ray pulses, to create a uniform laser intensity distribution for heat sensitive samples and to enhance operability.

Contents

1
Introduction

71% of our planet is covered with water which makes the water-air interface the largest connected surface area on our planet. [1]

In nature, a plurality of important and fundamental processes occur at liquid interfaces, which influence our health, climate and environment. Investigating and characterising solid-liquid, liquid-liquid and liquid-vapour interfaces helps to better understand atmospheric, biological, chemical and physical processes. This work discusses three aspects of light interactions at liquid interfaces: light-induced kinetics in Langmuir monolayers at the water-air interface, light-induced mesophase transitions in lyotropic crystals and laser-induced interaction and excitation of salt ions at the water-air interface. In the following, I will present these fields of research and the importance of my results.

Lipid membranes present one of the most fundamental interfaces in nature by acting as a physical barrier separating the cell inner part from the outer environment. Additionally, at the membrane biological, chemical and physical processes take place such as ion transportation through the membrane [2, 3], protein (de-)activation and attachment to glycolipids [4–6], membrane fusion or separation into two cells [7–9]. Physical properties of the membrane such as fluidity, rigidity and functionality are defined by the specific composition of lipids, sugars, nucleic acids and proteins [10–12]. The main component in most biological membranes are phospholipids from which over 1000 different kinds have been identified in mammalian cells so far [13, 14]. While the phospholipids and cholesterol define the general structure and flexibility of the membrane [15–17], the sugar group at the head group of glycolipids is responsible for cell signalling and attachment of proteins and other cells [18, 19]. Proteins display selective behaviour and only attach to specific carbohydrate groups [4, 20] that has also been shown in multiple studies on bacteria attaching to glycolipids [21, 5]. Further, by changing the angle of the glycan head a detachment of the bacteria [22–25] and proteins [26, 27] from the glycolipid could be observed. Therefore, controlling

the orientation of the glycan heads allows designing bespoke membranes to de- and activate protein and bacteria attachment to cells. To determine the orientation of the glycolipid orientation many studies employ nuclear magnetic resonance (NMR) spectroscopy [28].

Utilising light as trigger to induce structural changes in the membrane has received great attention [29–32]. Commonly, azobenzene switches are used which can be switched between their *trans* and *cis* isomers with light in the visible and UV range. Upon switching to the *cis* isomer, the double N=N bond of the azobenzene group bends from 0° to a 90° angle [33, 29, 34]. Studies on Langmuir monolayers with lipids containing azobenzene switches in their acyl chains of the tail groups found a strong change in the layer thickness [35, 31, 36, 37] and change in the bilayer fluidity [38] upon switching. However, only few studies investigate lipids containing a photoswitch in their head group because of the often observed hydrophobic character of the photoswitches and thus reduced water-solubility [23].

In this work, photoswitchable artificial glycolipids with an azobenzene switch placed between the carbohydrate head group and the acyl chains of the tail group are investigated in model membranes. Previous Langmuir isotherm and XRR measurements on Langmuir monolayers containing two azobenzene mimetics and the phospholipid 1,2-Dipalmitoyl-*sn*-glycero-3-phosphocholine (DPPC) [37] revealed an additional phase transition in the liquid condensed phase for which bidirectional switching behaviour above and below this phase transition point with an increase and decrease, respectively, of layer thickness and surface pressure was observed. Though the vertical structure was characterised, no conclusion could be drawn on the in-plane structure and subsequently on the glycan head group orientation. Following the open question on the in-plane structure of the monolayer, my studies focus on identifying the position and orientation of the azobenzene switch in the layer and determining whether and how the carbohydrate head group changes its orientation upon switching between the isomers of the azobenzene switch. To identify the position of the azobenzene switch and the head group orientation, complementary XRR and NR measurements in combination with GID were conducted, which are presented in Chap. 5.

Investigating the formation of and transition between mesophases in lyotropic liquid crystals is fundamental to understand cell fusion processes and to design drug delivery systems. Amphiphilic lipids self-assemble to lyotropic liquid crystals upon dispersion in aqueous solutions and their mesophase describes the morphology of their partially ordered structure [39, 40]. The initial lipid mesophase depends on the water content [41] and lipid composition [42]. In nature, biological cells form

mostly spherical lipid vesicles with one flexible lipid bilayer being in the lamellar mesophase [43–45]. However, non-bilayer and non-lamellar mesophases, such as hexagonal or cubic phases, can form from almost every type of cytomembrane [46, 47, 45]. Furthermore, the existence of non-lamellar intermediate structures at the contact point of the two vesicle membranes during cell fusion processes has been demonstrated by membrane simulations [48] and experimental studies [8, 49]. This makes the transition between mesophases highly interesting to understand cell fusion processes. Moreover, non-lamellar lipid mesophases are of great interest for drug delivery systems [50]. Changing between mesophases opens pores through which the enclosed drugs can be released [51–53]. Furthermore, the release rate of enclosed drugs depends on the lipid mesophase [54]. This allows the design of bespoke drug delivery systems. Mesophase transitions can be induced by changes of the lipid hydration or temperature [54, 41], also known as lyotropic polymorphism [55, 46], in given lipid compositions. In addition, changes in the salinity [56, 57] and pH [58] have been employed to induce mesophase transitions. Meanwhile, Wang et al. [59] have used light as an activator to induce irreversible transition from multilamellar vesicles to work-lime micelles.

In this work, light is introduced to induce reversible, repeatable and reproducible mesophase transitions from lamellar to bicontinuous cubic phases in lyotropic liquid crystals. Data from *in situ* SAXS and differential scanning calorimetry (DSC) measurements are presented in Chap. 6 which characterise and identify the lipid mesophases and phase transition temperatures of model lipid crystals consisting of either phospholipid DPPC or 1,2-Dilauroyl-*sn*-glycero-3-phosphocholine (DLPC) and photoswitchable artificial glycolipids. Furthermore, the results from time-resolved SAXS investigations are shown in Sec. 6.6 to follow the temporal evolution of the mesophase transitions.

Not only lipids or surfactants in general affect the liquid interface, ions dissolved in aqueous solutions influence the properties of the water interface and bulk. These in water dissolved ions alter physical properties such as the surface tension [60], the boiling point [61] and electrical conductivity [62]. Further, experimental X-ray scattering [63] and second-harmonic generation (SHG) [64] studies in addition to molecular dynamics (MD) calculations [65–68] have shown that ions, especially large halides, can be attracted to the interface and enhance chemical reactions. The experimental studies employed surface sensitive methods such as SHG, sum frequency generation (SFG) spectroscopy and XRR or performed surface tension and potential measurements. The phenomena of ions at the interface is of great importance to understand chemical processes at liquid interfaces, such as water droplets, in the

field of atmospherical chemistry. In addition to chemical reactions, the ions at the interface absorb light and can be electronically excited. Such electronic excitation can provoke charge-transfer-to-solvent (CTTS) processes and the formation of solvated electrons. This CTTS process occurs on the fs time scale and the solvated electrons recombine within hundreds of ps [69–73]. Most studies use a laser pump - laser probe spectrometer setup, mass spectrometry or vibrational sum frequency generation (VSFG) to study the short time scales of the CTTS photoreaction and solvated electron dynamic. To investigate the influence of the solvated electrons on the electronic properties and ion distribution at aqueous interfaces, laser pump - X-ray probe experiments can be performed. A number of beamlines at synchrotron radiation facilities all over the world offer laser pump - X-ray probe setups on the tens of ps time scale, such as the pump - probe setup at the Liquid Interface Scattering Apparatus (LISA) endstation [74] at Beamline P08 [75], PETRA III, Deutsches Elektronen-Synchrotron (DESY), Germany. During this thesis, I worked at the ErUM-Pro funded LISA instrument and femtosecond laser and performed numerous beamtimes myself in addition to supporting other research groups during their measurements. A detailed description of the laser pump - X-ray probe setup available at LISA, P08, PETRA III is presented in Sec. 7.1 together with the technical developments designed and implemented within the scope of this work.

Using the laser pump - X-ray probe setup at LISA, P08 to study the water-air interface of aqueous salt solutions, experiments on aqueous NaI solutions with varying concentration were performed. The ion distribution at the interface was studied with XRR and complementary XRFNTR measurements. Both, XRR and XRFNTR are surface sensitive methods that give information on the electron profile of the interface and bulk. While an accumulated electron density profile is measured with XRR, the XRFNTR spectra provide information on the ion species. Thus, combining these two techniques holds high potential to identify the kind and concentration of the ions present at the surface. Being interested in the effect UV light has on the ion distribution at the interface, the laser was used to illuminate the salt solution with a wavelength of 258 nm during the measurements. The results of these *in situ* studies are presented and discussed in Sec. 7.2.1.

The general structure of this thesis is as follows: in Chap. 2, first the fundamentals of liquid interfaces, lipid membranes and the theoretical backgrounds for X-ray and neutron scattering techniques are presented together with the principles of laser radiation. This is followed by the description of the materials and sample preparation in Chap. 3. These introductory chapters are concluded with the details on the experimental setup and methods given in Chap. 4. The main results and discussion

part of this work is divided into the three research topics: bidirectional photoswitching in Langmuir monolayers (Chap. 5), photo-induced mesophase transition in lyotropic liquid crystals (Chap. 6) and laser-induced dynamics at liquid interfaces (Chap. 7). In the result chapters, at first an overview of the measured data and if applicable, results from unpublished results are presented together with first conclusions on the sample preparation and necessary measurement setup. This is followed by the publications and manuscripts with a short summary each of the main findings. The whole work is then summarised in the conclusion in Chap. 8. Two accepted and published publications [PSH 1] and [PSH 2] are included in this dissertation. Further, two manuscripts, [MSH 1] and [MSH 2], have been submitted and are under peer-review at the moment of submission of this dissertation. The third manuscript [MSH 3] is prepared for submission.

2
Fundamentals

2.1 Liquid interfaces

Liquid surfaces are found in a variety of liquid-solid, liquid-foam and liquid-liquid systems on which chemical, biological and physical processes take place. Per definition, the surface of a liquid is the boundary between two bulk phases with different density [76] at which self-assembling structures can form as schematically shown in Fig. 2.1

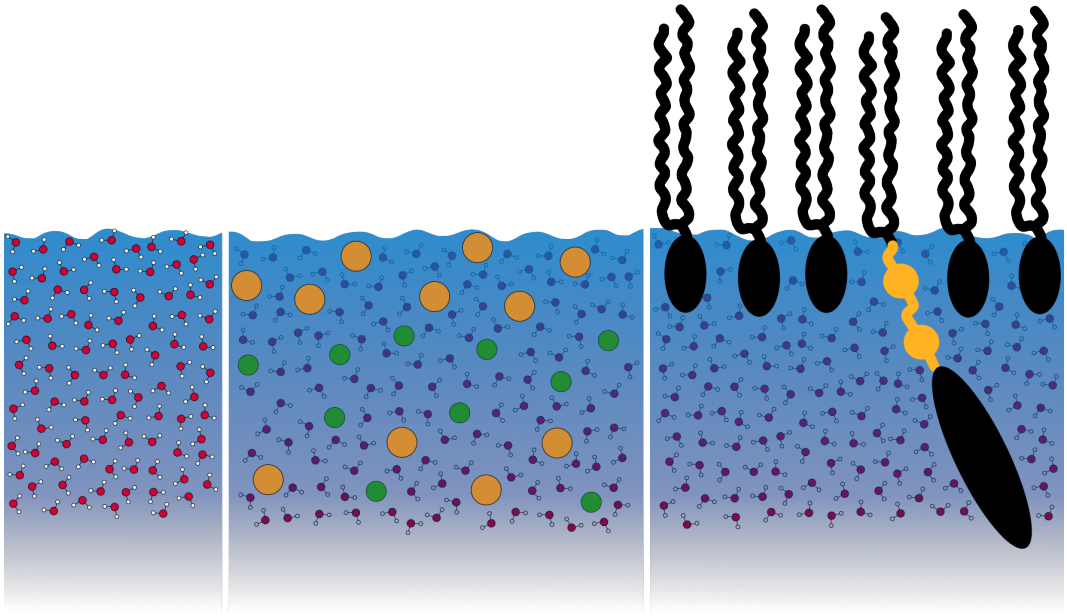

Figure 2.1: Drawing of the water-air interfaces studied in this thesis highlighting the corresponding focus. Left, the pure water surface with the water molecules and in the middle a salt solution with ions showing schematically the enhanced presence of cations (orange) and the depletion of anions (green) at the interface is illustrated. Right, a surface containing lipids represents the phospholipids and photoswitchable glycolipids studied in this thesis.

for the water-air interface. The interfacial region has a typical thickness of few nm and roughness due to capillary waves. Furthermore, the chemical and physical properties of the interfacial region differ from the bulk phases. This provides a unique environment for chemical and physical processes such as energy conversion processes in living organisms, transport through lipid membranes, electrochemical processes, drug delivery in pharmacology and emulsions. [77]

In the following sections, the main concepts of surface tension and the capillary waves are introduced based on the textbooks [76, 78, 79]. Further, the existence of ions in this interfacial region is discussed in Sec. 2.1.3 and the properties of lipid membranes at the water interface are presented in Sec. 2.2.

2.1.1 Surface tension

At the liquid-vapour and liquid-liquid interfaces, cohesive and adhesive forces act on the particles of the liquid. While adhesive forces only act on particles at the interface of two phases, the cohesive force acts on all particles of the same phase within the bulk and at the interface [78]. For particles in the bulk, the cohesive forces arise from all directions of the neighbouring molecules equally, thus revoke themselves because of the symmetry. Meanwhile, particles at the interface experience an effective force due to the symmetry breach at the interface. If the adhesive force is stronger than the cohesive force, the particles evaporate or mix with the other liquid phase. Otherwise, if the cohesive force dominates, the particles are drawn towards the bulk of the liquid and the area of the surface is minimised. To quantify this back driving force, the surface tension Γ describes the necessary energy W for an increase of surface area A with $\Gamma = \mathrm{d}W/\mathrm{d}A$. [76, 78].

2.1.2 Capillary waves

Waves arise at liquid interfaces and their dynamics and phase velocities depend mainly on the gravitational force and the surface tension. Depending on which force dominates, the waves are referred to as gravitation or capillary waves. While gravitational waves can possess large wavelengths on the length scale of metres, the typical wavelength of capillary waves is up to few cm [79]. At liquid surfaces in equilibrium state and without any external perturbation such as wind, vibrations or objects floating or falling on the surface, the capillary waves have a wavelength of few Å. These capillary waves are formed by the local surface profile and thermal motion. The local surface profile is described by the intrinsic roughness σ_i and is of the dimension of the atomic radius of the atoms at the interface. [80, 81] Meanwhile, the thermally induced height fluctuations depend on the surface tension

Γ and temperature T. This capillary roughness σ_c depends on the wavevector q_z and can be calculated according to [82, 83] by

$$\sigma_c^2(q_z) = \frac{k_B T}{2\pi\Gamma} \ln\left(\frac{q_{max}}{\delta q_{xy}}\right) \tag{2.1}$$

with the Boltzmann constant k_B, maximum wavevector q_{max} and the instrument resolution δq_{xy}. The maximum wavevector and instrument resolution are discussed in more detail in Sec. 2.3.1.

Utilising X-ray scattering methods, in particular XRR, the capillary roughness can be determined experimentally. XRR measurements are sensitive to changes of few tens of Å, which enables the study of temperature [84–87] and surface tension [88, 89] induced changes of the capillary roughness [81, 90]. For a pure water surface, the capillary roughness increases by approximately 0.5 Å upon a temperature rise from 20 °C to 30 °C or a reduction of the surface tension by 2.5 mN m^{-1} from 72.8 mN m^{-1}. Ions at the water surface increase the surface tension and therefore decrease the capillary roughness. Meanwhile, lipid surfactants at the interface reduce the surface tension, which can be seen in an increase of capillary roughness.

2.1.3 Ion distribution

Traditional theoretical models of ions at the water surface predict a repulsion of the ions from the interface by the image charge repulsion [91]. This theory was experimentally supported by the rise of the surface tension with increasing salt concentration in water solutions [92] because the increase in surface tension is associated with a negative surface excess in the Gibbs adsorption equation [76, 78]. However, this simple model of an ion-free region at the surface had to be reworked as experimental findings in atmospheric chemistry suggest a presence of ions at the interface to rationalise chemical reactions [93, 94]. MD simulations modelling polarisable ions [95, 96] indicate a possible presence of polarisable anions at the outermost liquid layers. The anisotropy of the interface leads to a deformation of the electron shells of these surface near ions, that results in the formation of a dipole. Which ion is repelled or attracted to the surface depends on the polarisability of the halide. Small halides, such as F^-, are repelled from the surface while the larger halides I^- and Br^- are likely to be found at the interface. Cl^- has a neutral prediction of position. [66, 97] This enhanced presence of anions at the interface is reversed a few Å towards the liquid bulk. There, the anions are depleted while the cation presence is enhanced. This results in a double layer with reversed presence of the anions and cations as shown schematically in Fig. 2.1. Integrating over the interfacial region shows a reduced ion concentration in this surface near region compared to

the bulk value. The relative depletion of ions at the interface is in accordance with the Gibbs adsorption equation and the experimentally observed increase of surface tension. [67, 98]

The description of a double layer of anions and cations at the surface is valid for monovalent ions which form solvent-separated ion pairs. However, MD simulations of the divalent salt $SrCl_2$ in water show an enhancement of both Cl^- and Sr^{2+} ions at the interface considering polarisation of the ions [99]. This study suggests, that both anions and cations are present at the interface due to the higher positive charge of the Sr^{2+} ions and subsequently larger interaction with the Cl^- ions. A presence of surface layering in $SrCl_2$ has been experimentally shown in XRR studies [100] and is in good agreement with the theoretical prediction.

2.2 Lipid membranes and their characterisation

Lipid membranes consist of a variety of lipids, proteins and sugars as illustrated in Fig. 2.2, which define the physical properties of the membrane [7, 10, 2] and are responsible for physical and chemical processes at the membrane and across the membrane [6, 18, 19]. Phospholipids are the main component and possess a hydrophilic head group and hydrophobic tail group. This amphiphilic characteristic leads to a self-assembly upon contact with water and so called Langmuir monolayers form at water-air or water-oil interfaces and lyotropic lipid crystals in bulk water. In the following sections, the lipid properties and the methods to characterise Langmuir

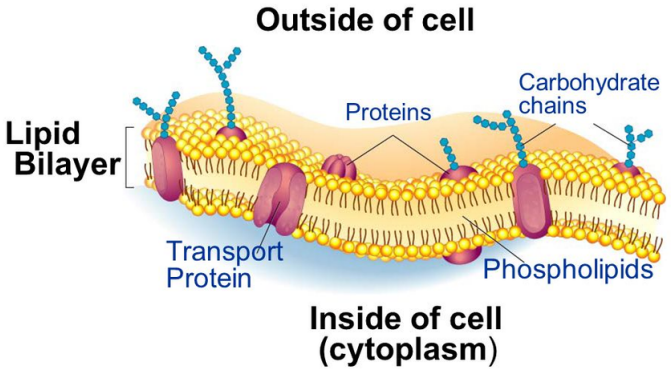

Figure 2.2: Illustration of a cell membrane showing a bilayer composed of phospholipids, proteins and carbohydrates attached to proteins and lipids taken from [101] ©2018 IEEE.

monolayers and lyotropic liquid crystals are introduced based on the textbooks [102, 10, 2, 103, 104], lecture text [105] and review articles [106, 6].

2.2.1 Amphiphilic lipids

The term lipid is commonly used to describe a large group of organic compounds. A more concrete definition has been introduced with the LIPID MAPS classification system [107] that defines lipids as hydrophobic or amphiphilic molecules with either ketoacyl groups or isoprene groups. The lipids are divided into eight categories: fatty acyls, glycerolipids, glycerophospholipids, sphingolipids, saccharolipids, polyketides, sterol lipids and prenol lipids. The phospholipids DPPC and DLPC (see Sec. 3.1) and the artificial amphiphilic glycolipids described in Sec. 3.2, which are examined in this work, belong to the group of glycerophospholipids. These lipids possess a hydrophilic head group and hydrophobic tail group, which makes them amphiphilic. Each lipid possesses its individual phase transition temperature at which it melts from the gel to the liquid phase. Lipids with long alkyl chains in the tail group melt at higher temperatures than short tailed lipids due to the stronger Van der Waals interaction within the tail group. [108] Thus, in membranes consisting of multiple lipids, two phases can coexist in separate domains when some lipids are in the gel while others are in the liquid phase at a given temperature.

2.2.2 Langmuir isotherms

Amphiphilic molecules self-assemble at water-air interfaces due to their hydrophilic head group and hydrophobic tail group and form Langmuir monolayers. Characterisation of these monolayers is done with Langmuir isotherms, which relate the mean area per molecule with the surface pressure of the film. [109] These Langmuir isotherms are collected with Langmuir troughs, which consist of a trough filled with water, one or two movable barriers and a surface tension balance. To measure the surface tension, a so called Wilhelmy plate is used, which consists of a spring balance and a plate made of typically either metal or filter paper. The plate is drawn down by the gravitation force and lifted upwards by the buoyancy forces acting on the plate upon touching the water surface as shown in Fig. 2.3. The effective force related to the surface tension is measured with a spring balance. Using the Wilhelmy equation [110]

$$\Gamma = \frac{F}{L \cdot \cos\theta} \tag{2.2}$$

the surface tension Γ is calculated by the capillary force F acting on the wetted plate with the perimeter $L = 2l_1 + 2l_2$ and under the contact angle θ as shown in Fig. 2.3.

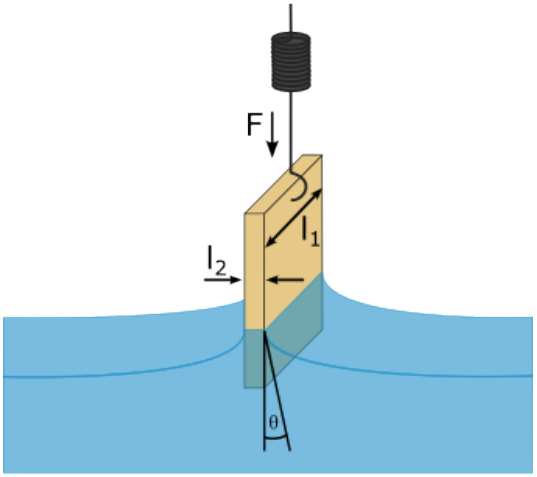

Figure 2.3: Schematic of the design and function of the Wilhelmy plate to measure the surface tension with the capillary force F acting on the wetted plate with the perimeter $L = 2l_1 + 2l_2$ and under the contact angle θ.

The Langmuir monolayers are formed by spreading molecules onto the water surface on one side of the barrier and the barriers are used to reduce or expand the area the molecules are located on. To keep the water level at constant height, the barrier is only reaching partially into the water to allow a flow of water from one side of the barrier to the other side. Though the water can flow below the barrier, the molecules stay at the interface because of their hydrophobic tail groups. Therefore, the effective area of the molecules can be altered which affects the ordering and interaction between the molecules. Measuring the surface tension while compressing the area as shown in Fig. 2.4a allows quantifying the degree of ordering within the monolayer.

Often, the surface pressure π

$$\pi = \Gamma_0 - \Gamma \tag{2.3}$$

is used as relative change to the surface tension Γ_0 of pure water. At high area per molecule A_{mol} and low surface pressure π the molecules can be described as being in a gaseous analogue phase. Compressing the area leads to a phase transition into the liquid-expanded (LE), liquid-condensed (LC) and solid (S) phases as illustrated in Fig. 2.4b. Further compressing results in a collapse of the monolayer at the collapse pressure [111]. Based on the isotherm, molecules can be characterised and identified because the existence of phase transitions is lipid specific [112, 106]. Further factors are experimental conditions such as temperature and compression rate. For example, a DPPC Langmuir monolayer shows a plateau at the LE to LC phase transition, where a coexistence of both phases can be found (see Fig. 2.4). Langmuir isotherm

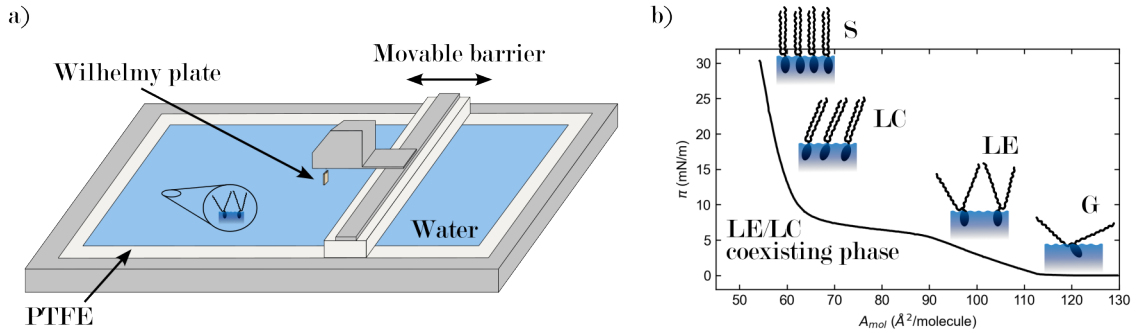

Figure 2.4: a) Schematics of the Langmuir trough used for the experiments at Kiel University and DESY (see Sec. 4.5.1) with the movable barrier and Wilhelmy plate and b) a recorded Langmuir isotherm of DPPC and the corresponding phases: solid (S), liquid-condensed (LC), liquid-expanded (LE) and gaseous (G). The phases are presented similar to [105].

measurements on mixed monolayers further allow conclusions on the miscibility of molecules and formation of domains. The dis- and appearance of phase transitions as well as the shift of the collapse pressure to higher or smaller values indicate how homogeneously the molecules are distributed in the monolayer [113]. To characterise the size and physical form of domains Brewster-angle microscopy [114] measurements can be performed simultaneously to the isotherm measurements. During this study, Brewster-angle microscope test measurements were performed on mixed DPPC and azobenzene amphiphiles monolayers to identify possible inhomogeneities and formations of domains. Within the resolution of 12 µm of the Brewster-angle microscope from KSV NIMA MicroBAM, no domain formation for either the *trans* and *cis* state could be observed.

2.2.3 Lyotropic liquid crystals

In solvents, lipids aggregate and form lyotropic liquid crystals with a variety of shaped structures, also called mesophases. This ability to form different structures is called polymorphism. Which mesophases the lyotropic liquid crystals exhibit, depend on the individual lipid curvature, water content, temperature and pH to name a few [115, 46, 104]. These structures show short- and long-range molecular ordering and geometric shapes of micelles, cylinders, hexagonal aligned cylinders, vesicles and flexible bilayers with their lamellar and bicontinuous structures as shown in Fig. 2.5b. The water channels within the bicontinuous cubic structure are subdivided into separate water reservoirs by the lipid bilayers.

To predict the curvature and resulting lipid geometry, the critical packing parameter

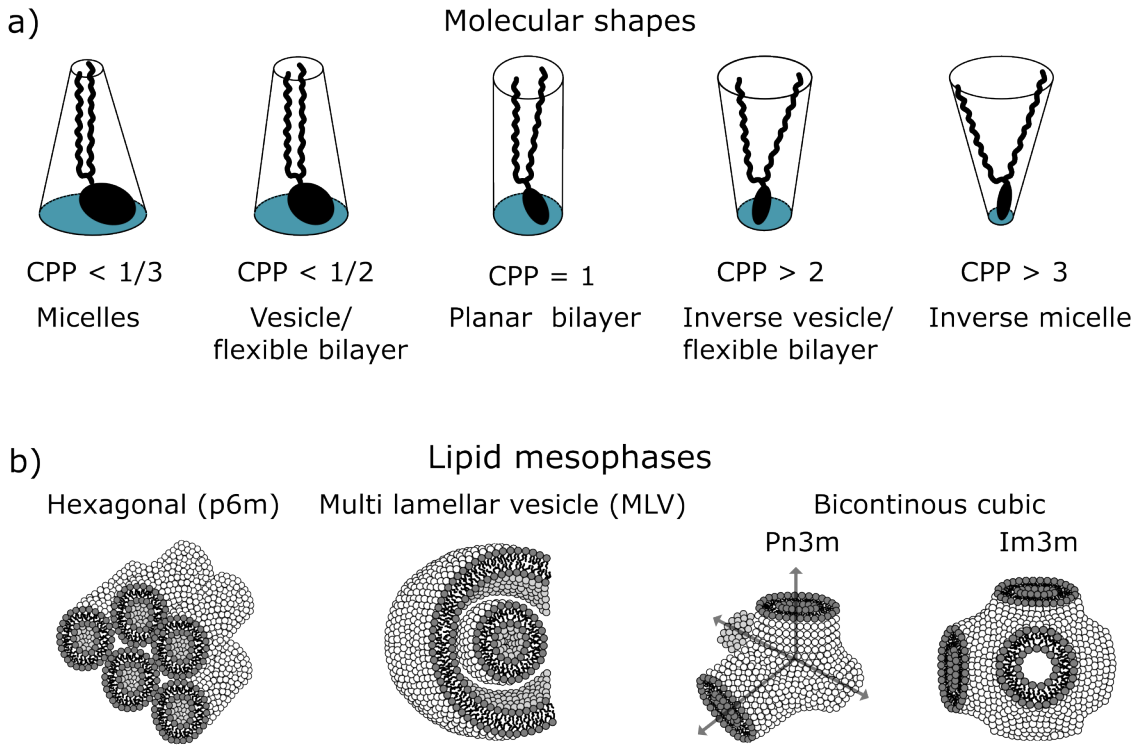

Figure 2.5: a) Schematic presentation of the molecular shape of the lipids and the corresponding critical packing parameter (*CPP*) values and formed structures. b) Illustration of lipid mesophases that form from flexible bilayers based on [41].

(*CPP*) introduced by [116] and [117] is utilised and calculated with

$$CPP = \frac{V_{\text{chain}}}{a_{\text{head}} l_{\text{chain}}} \tag{2.4}$$

where V_{chain} and l_{chain} are the volume and length of the hydrophobic chain, respectively, and a_{head} is the effective area of the hydrophilic head group. Molecules with a $CPP \simeq 1$ show a cylindrical shape, while molecules with a *CPP* different from 1 exhibit a cone-shape with positive or negative curvature causing a reformation into micellar, hexagonal or cubic or their reversed correspondent as shown in Fig. 2.5a. Micellar and inverse micellar structures are found for $CPP < 0.3$ and $CPP > 3$, respectively. When $0.3 < CPP < 0.5$ and $2 < CPP < 3$, hexagonal and inverse hexagonal shapes, respectively, are identified and for $0.5 < CPP < 2$ flexible bilayers and inverse flexible bilayer, respectively, are observed. Planar lipid bilayers are determined for $CPP = 1.0$.

2.2.4 Phase transition temperature and differential scanning calorimetry

Similar to other substances, lipids can melt upon reaching their phase transition temperature which results in an increase in membrane fluidity. At low temperatures the mobility of the lipids is reduced and the membrane exhibits a crystalline-like state which is referred to as gel phase. Upon reaching the phase transition temperature, the lipids melt to the liquid crystalline phase, also called liquid disordered phase [106] (see Fig. 2.6a). For some lipid bilayers an intermediate ripple phase can be observed such as for DPPC lipids [118, 119]. Each lipid has its own characteristic phase transition temperature which is influenced by the length and degree of unsaturation of the alkyl chains in the tail group and the head group type and hydration [115, 108, 120, 121]. Lipids with long alkyl chains have a higher phase transition temperature than lipids with shorter tail group due to higher van der Waals forces between the longer alkyl

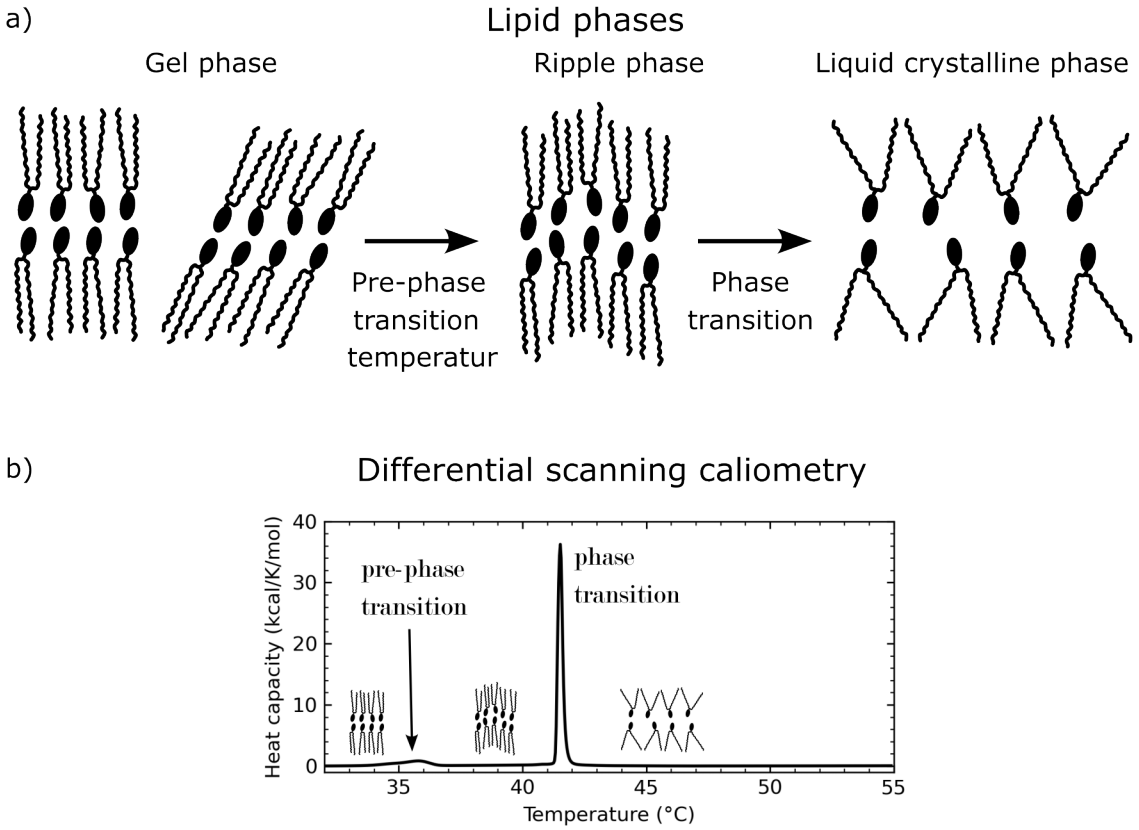

Figure 2.6: a) Illustration of the phase transitions between lipid phases based on [122] and b) a DSC curve of DPPC multilamellar vesiclemultilamellar vesicles (MLVs) measured during this thesis at P08, PETRA III.

chains. Similarly, lipids with unsaturated alkyl chains have a lower phase transition temperature as the state of order is disrupted by the bend of the C=C double bond.

To determine the phase transition temperature, differential scanning calorimetry (DSC) [123–126] can be performed. While heating up the sample and the pure solvent as reference in separate capillaries, the energy needed to increase the temperature is measured for both solutions simultaneously. Upon reaching the phase transition temperature, the energy needed to increase the sample temperature further in- or decreases depending on whether the phase transition is an exothermic or endothermic process. Meanwhile, the heat capacity of the reference solution does not change. In Fig. 2.6b the data from a DSC measurement of DPPC vesicles shows two peaks in the heat capacity at the temperatures belonging to the pre-phase and phase transition. In summary, DSC is used to characterise sample properties such as the phase transition temperatures for crystallisation and glass transition as well as to observe fusion events and to study chemical reactions.

2.3 X-ray and neutron scattering techniques

With the discovery of X-ray radiation by Wilhelm C. Röntgen in 1895 and the formulation of diffraction laws by William L. and William H. Bragg and by Max von Laue both in 1912 X-ray scattering techniques became known and are nowadays widely used to investigate soft and hard matter. Meanwhile, neutron reflectometry is a relatively new technique that became popular in the 1970s and 1980s [127]. Though, X-ray and neutron scattering methods are similar and both allow characterisation of the sample structure and properties, both have their dis- and advantages. The measurement time with X-rays, especially synchrotron radiation, is short and dynamics can be probed down to the fs time scale. Whereas, with neutrons dynamics can only be measured down to µs because of the low flux and long measurement times. However, the sensitivity of the neutrons to the nucleus of the atoms enables the identification of the isotope specific compositions of the sample and the magnetic properties. Combining XRR and NR as complementary techniques allows precise characterisation of a variety of samples.

In the following, the theoretical background for the X-ray and neutron scattering techniques utilised to study light-induced phase transitions in lipid monolayer (Chap. 5) and in lyotropic liquid crystals in bulk water (Sec. 6.5 and 6.6) as well as laser induced redistribution of the ions close to the water-air interface (Sec. 7.2.1) is shortly presented. Detailed descriptions can be found in lecture notes [128], textbooks on the general principles [129–131], textbooks with a focus on liquid surfaces [79]

and synchrotron radiation based measurements [132] and overview articles [133–136]. The following descriptions are mainly based on [130], [131] and [128].

2.3.1 X-ray reflectivity

An incoming X-ray wave with its reciprocal wavevector $\mathbf{k}_\mathrm{i}$ and angle α is partially reflected at an interface under the same angle α with the reflected wavevector $\mathbf{k}_\mathrm{r}$ while the remaining part penetrates into the material with the transmitted wavevector $\mathbf{k}_\mathrm{t}$ under an angle α' as shown in Fig. 2.7. Considering continuity as boundary conditions for the waves and their derivatives at the interface and small angle approximation, Snell's law

$$n_0 \cos\alpha = n_1 \cos\alpha' \tag{2.5}$$

and the Fresnel equations

$$\begin{aligned} r &= \frac{\alpha - \alpha'}{\alpha + \alpha'} \quad \text{and} \\ t &= \frac{2\alpha}{\alpha + \alpha'} \end{aligned} \tag{2.6}$$

are derived, where n_0 and n_1 are the refractive index of the materials and r and t are the amplitude reflectivity and transmittivity, respectively [128, 130]. Based on Snell's law describing the change of propagation direction of electromagnetic waves entering transparent materials, the transmitted wave is bend towards the surface when coming from optical dense and entering optical less dense material. To describe the optical density of the material, the complex refractive index n with its material

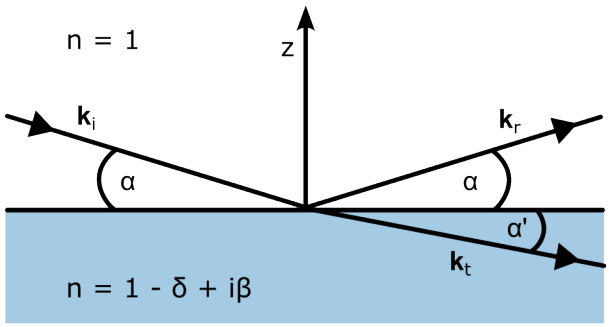

Figure 2.7: Reflection geometry on a surface with the refractive index n, the wavevectors $\mathbf{k}_\mathrm{i}$, $\mathbf{k}_\mathrm{r}$ and $\mathbf{k}_\mathrm{t}$ and corresponding angles α and α' after [130].

specific dispersion δ and absorption β is used

$$\begin{aligned} n &= 1 - \delta + i\beta \\ \delta &= \frac{\lambda^2}{2\pi}\rho(z)r_\mathrm{e} \\ \beta &= \frac{\lambda}{4\pi}\mu \end{aligned} \tag{2.7}$$

where λ is the X-ray wavelength, $\rho(z)$ is the average electron density at position z along the surface normal, $r_\mathrm{e} = 2.82\,\mathrm{fm}$ is the classic electron radius and μ is the absorption coefficient. [128, 130] For X-ray radiation, materials possess $n < 1$ which makes them less dense materials than air and leads to total scattering of the incoming beam at angles smaller than the critical angle

$$\alpha_\mathrm{c} \approx \sqrt{2\delta}. \tag{2.8}$$

During X-ray reflectivity measurements the intensity of the specular reflected wave is determined for various incident angles α and thus reflected angles α. The difference between incoming and reflected wavevector is the so called wavevector transfer or scattering wavevector $\mathbf{Q} = \mathbf{k}_\mathrm{r} - \mathbf{k}_\mathrm{i}$. An incoming wavevector $\mathbf{k}_\mathrm{i}$ and reflected wavevector $\mathbf{k}_\mathrm{r}$ in the yz-plane can be described as:

$$\mathbf{k}_\mathrm{i} = \frac{2\pi}{\lambda}\begin{pmatrix} 0 \\ \cos\alpha \\ -\sin\alpha \end{pmatrix} \quad \text{and} \quad \mathbf{k}_\mathrm{r} = \frac{2\pi}{\lambda}\begin{pmatrix} 0 \\ \cos\alpha' \\ \sin\alpha' \end{pmatrix}. \tag{2.9}$$

Under the condition that the entrance and exit angle are identically, the scattering wavevector $\mathbf{Q} = (q_x,q_y,q_z)$ is derived to:

$$\mathbf{Q} = \mathbf{k}_\mathrm{r} - \mathbf{k}_\mathrm{i} = \frac{4\pi}{\lambda}\begin{pmatrix} 0 \\ 0 \\ \sin\alpha \end{pmatrix} \tag{2.10}$$

$$q_z = \frac{4\pi}{\lambda}\sin\alpha. \tag{2.11}$$

The critical wavevector q_c can be written analogue to α_c (see Eq. 2.8) as $q_\mathrm{c} = 4\pi/\lambda \cdot \sqrt{2\delta}$ and will be denoted as the critical angle in the following as well. [128, 130] For an ideal surface without any roughness, the Fresnel reflectivity formulated by Augustin-Jean Fresnel describes the q_z dependent intensity distribution as

$$R_\mathrm{F}(q_z) = |r(q_z)|^2 = \frac{q_z^4}{\left(q_z + \sqrt{q_z^2 - q_\mathrm{c}^2}\right)^4}. \tag{2.12}$$

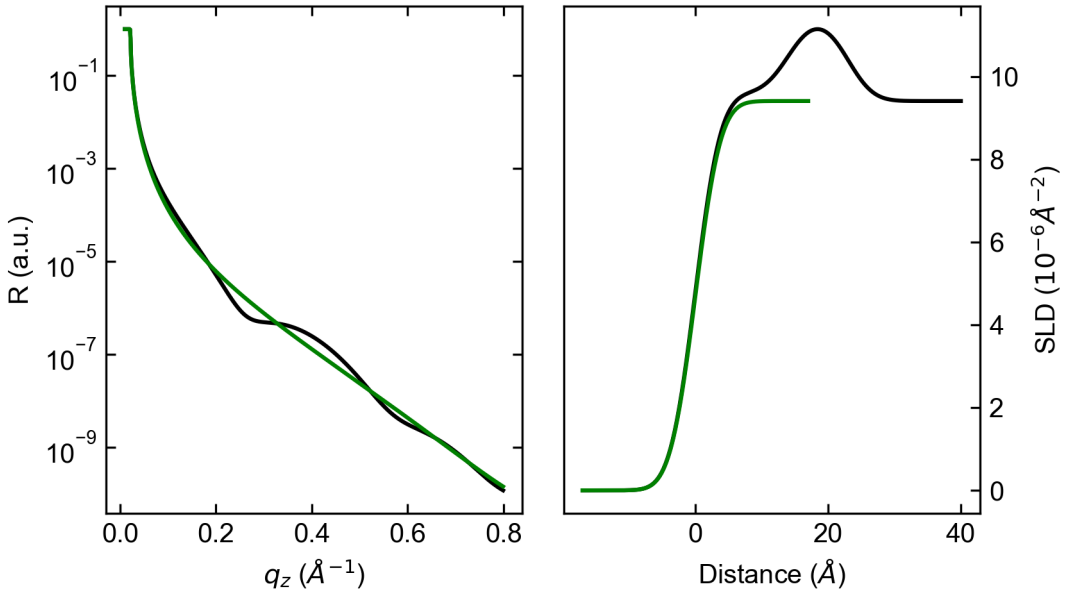

Figure 2.8: Model XRR curves (left) and the corresponding scattering length density (SLD) profiles (right) from a pure water-air interface (green) and a Langmuir monolayer at the water-air interface (black) showing the typical Kiessig fringes.

For larger angles than the critical angle $q_z \gg q_c$, the Fresnel reflectivity can be approximated to $R_F \approx (q_c/2q_z)^4$ and the intensity decreases with $I \propto q_z^{-4}$ as shown exemplarily in Fig. 2.8a for a reflectivity from a water-air surface measured at the LISA endstation (see Sec. 4.5.1).

Studying real, rough interfaces such as liquid surfaces, the sharp step in the electron density profile considered in the Fresnel reflectivity is not utilisable. Local surface profile and thermally induced capillary height fluctuations shape the liquid surface topology and electron profile. Small variations of the electron density on the atomic length scale along the surface normal (z-direction) create a dependency of z on the refraction index $n(z)$. A numeric approach to take these variations into account and to describe the measured reflectivity $R(q_z)$ is done with the so-called master formula [137, 138]

$$R(q_z) = R_F(q_z) \cdot |\Phi(q_z)|^2 = R_F(q_z) \cdot \left| \frac{1}{\rho_\infty} \int_{-\infty}^{+\infty} \frac{\delta\langle\rho(z)\rangle}{\delta z} \, e^{-iq_z z} \, dz \right|^2 \tag{2.13}$$

with the averaged electron density $\langle\rho(z)\rangle$, the electron density ρ_∞ in the bulk and the phase information of the wavevector $e^{-iq_z z}$. The structure factor $\Phi(q_z)$ of the interface describes a modulation of the idealised Fresnel reflectivity with a Fourier transformation of the normalised gradient of the averaged electron density $\delta\langle\rho(z)\rangle/\delta z$. In practice, a model for the electron density profile is fitted to the measured reflectivity

curve because the phase information of the wavevector is lost due to the dependency of $R(q_z)$ on the square of the absolute value of the electron density and wavevector. A common way to describe the electron density profile at the interface includes an error function $\langle\rho(z)\rangle = \mathrm{erf}(z/\sqrt{2}\sigma)$ with σ as standard deviation to specify the electron density declination at the interface [139, 136]. Thus, the reflected intensity $R(q_z)$ may be written as

$$R(q_z) = R_\mathrm{F}(q_z)\ e^{-q_z^2\sigma^2}. \tag{2.14}$$

Yet, this reflectivity description in Eq. 2.14 violates time reversal and was extended by the *Nevot-Croce* factor [140] for a correct solution

$$R(q_z) = R_\mathrm{F}(q_z)\ e^{-q_z q_z'\sigma^2} \tag{2.15}$$

with $q_z = k \cdot \sin\theta$ and $q_z' = k' \cdot \sin\alpha'$ [141].

One of the surface properties investigated and discussed in this work is the roughness of the surface. To describe the roughness of the surface, σ can be written as

$$\sigma^2 = \sigma_\mathrm{i}^2 + \sigma_\mathrm{c}^2 \tag{2.16}$$

with the intrinsic roughness σ_i and capillary wave roughness σ_c. The intrinsic roughness is of the dimension of the atomic radius of the atoms at the interface. Meanwhile, the capillary roughness describes the height fluctuations induced by the capillary waves at the interface (see Sec. 2.1.2) and takes the temperature T, surface tension Γ and the instrument resolution δq_{xy} into account:

$$\sigma_\mathrm{c}^2(q_z) = \frac{k_\mathrm{B}T}{2\pi\gamma}\ln\left(\frac{q_\mathrm{max}}{\delta q_{xy}}\right) \tag{2.17}$$

where k_B is the Boltzmann constant.

The instrument resolution depends on the detector distance, detector pixel size and the size of the chosen region for intensity integration on the 2D detector image. Choosing a region of interest (ROI) of 30×30 pixels, as used for the data analysis in Sec. 5.1, and the detector settings described in Sec. 4.5, a capillary roughness of $\sigma_\mathrm{c} = 2.1\,\text{Å}$ is calculated. Together with the intrinsic roughness, a total roughness of $\sigma = 2.8\,\text{Å}$ is determined. This corresponds well with the roughness of $(2.8 \pm 0.3)\,\text{Å}$ found with fitting the experimental XRR curves and other experimental measurements [142, 143]. The fit routine is described in detail in Sec. 4.6.1.

To calculate the X-ray intensity from a multilayer systems, the Parratt formalism [144] is applied, which considers the reflectivity and transmittivity at every interface between the layers in a recursive way. The reflected waves at the top and bottom of each layer interfere and this creates an oscillation of the intensity reflectivity

known as Kiessig fringes as shown in Fig. 2.8 for the modelled data from a Langmuir monolayer sample. Based on the distance Δq_z between the minima of the Kiessig fringes the thickness d of the slabs can be calculated with $d = 2\pi/\Delta q_z$.

Conventionally, in order to characterise a material the scattering length density (SLD) is used instead of the electron density which depends on the intrinsic scattering length b of all N atoms inside the viewed volume V according to

$$\mathtt{SLD} = \frac{\sum_{i=1}^{N} b_i}{V} = \frac{\rho_\infty N_\mathrm{a} r_\mathrm{e} \sum_{i=1}^{N} f_i}{\sum_{i=1}^{N} M_i} \tag{2.18}$$

with the bulk electron density ρ_∞, Avogadro constant N_a, atomic factor f_i and atomic molar mass M_i for each element i [132, 131]. For X-rays, the SLD is approximately proportional to the atomic number Z of the elements.

2.3.2 Neutron reflectivity

While X-ray radiation interacts with the electron shell of the atoms and gives information about the electron density of the material, neutrons scatter at the nucleus and their cross section is isotope specific. Therefore, the scattering length b of the atoms is isotope dependent as shown for a selection of atoms in Tab. 2.1.

Thus, for example, H_2O holds an SLD of $-0.56 \times 10^{-6}\,\text{Å}^{-2}$ while D_2O scatters more strongly with an SLD of $6.39 \times 10^{-6}\,\text{Å}^{-2}$ [131]. This makes NR very powerful for determining the isotopic properties of a material. Further, this isotope specific scattering behaviour enables contrast matching, to highlight specific parts of the sample while making other parts indiscernible. To match a contrast, a mixture of H_2O and D_2O at a given proportion is prepared to achieve the same SLD as parts of the sample. If specific parts, for example the tail group of a lipid sample shall be

Table 2.1: X-ray and neutron scattering lengths in 10^{-5}Å for selected atoms taken from [145–147]. For the neutrons, the coherent nuclear scattering length is given.

	X-ray	neutron
^{1}H	0.999974	-3.7406
D	0.999974	6.671
^{16}O	8.01075	5.803
^{12}C	6.00313	6.6460
^{14}N	7.006	9.36
^{31}P	14.8	16.13794
^{32}S	5.13	2.847

highlighted, the lipid can be deuterated [148]. By interchanging the hydrogen atoms with deuterium atoms, the scattering length is changed and thus the SLD. Taking NR of multiple contrasts with hydrogenated lipids and their deuterated counterpart on different proportions of H_2O and D_2O allows determining accurately the arrangement of the lipids within the membrane. Within this work, NR was performed on Langmuir monolayer at the water-air interface (see Chap. 5) to identify the vertical position of the azobenzene amphiphiles within in the monolayer. Apart from the calculation of the SLD, the NR follows the scattering laws as described above for the XRR and can be calculated identically. The power and complementarity of NR to XRR lies in the ability of contrast matching and thus differentiating between parts of the monolayers and lipids.

2.3.3 Grazing incidence X-ray diffraction

As introduced in Sec. 2.3.1 and Sec. 2.3.2, the vertical component of the wavevector q_z is measurements with XRR and NR. To obtain information of the in-plane sample structure, in the q_x and q_y direction, grazing incidence diffraction (GID) measurements are performed. In contrast to XRR measurements, the incident angle α of the X-ray beam is kept constant and lower than the critical angle for GID studies. At this small angle, total reflection of the primary beam occurs. However, a small portion of the incoming beam is refracted and penetrates the medium [141, 131]. The intensity of this evanescent wave decreases exponentially as it transmits deeper into the medium and the penetration depth Λ is defined as the depth at which the intensity is reduced to 1/e with [130]

$$\begin{aligned}\Lambda &= \frac{\lambda}{4\pi \cdot Im(\alpha')} \\ &= \frac{\lambda}{2\sqrt{2}\pi \cdot \sqrt{\sqrt{(\alpha^2-\alpha_c^2)^2+4\beta^2}-(\alpha^2-\alpha_c^2)}}.\end{aligned} \tag{2.19}$$

The imaginary part of the angle α' of the transmitted wave is derived from Snell's law. Approximating small angles, the cosines in Snell's law (see Eq. 2.5) can be written as

$$\alpha^2 = \alpha'^2 + \alpha_c^2 - 2i\beta \tag{2.20}$$

with the incident angle α, the critical angle α_c and the refractive index β (see Eq. 2.7) [136, 149]. With this equation, the incident angle dependent penetration depth of X-ray radiation with an energy of 18 keV in pure water can be calculated as shown in Fig. 2.9a. By changing the incident angles, the probed volume can be changed from few nm to multiple tens of µm.

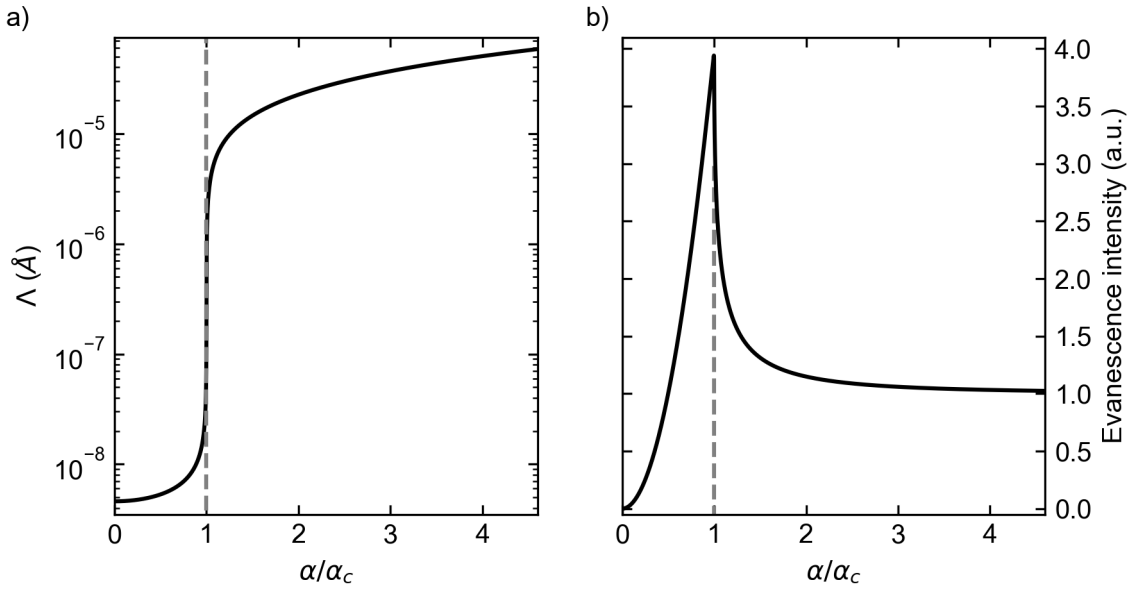

Figure 2.9: a) Simulated penetration depth of 18 keV X-ray radiation into water and b) the intensity of the evanescent wave at the water interface calculated with Eq. 2.6 in dependence to the incident angle normalised to the critical angle. The critical angle is marked as dashed line.

While the intensity of the evanescent wave decreases exponentially into the depth of the material, the intensity just below the interface can be derived from the square of the amplitude transmittivity t in Eq. 2.6 [130] and is shown in Fig. 2.9b. The amplitude of the evanescent wave is defined by the interference of the incident and reflected wave. For angles below the critical angle, total reflection occurs and the amplitudes of the two waves are of equal strength. At the critical angle, both waves are in phase and the amplitude (intensity) of the evanescent wave is double (four times) the incident wave amplitude (intensity). For smaller angles, the waves get out of phase, which results in an attenuation of the evanescent wave amplitude. Meanwhile, at angles larger than the critical angle, the amplitude of the reflected wave decreases with $I \propto q_z^{-4}$ (see Eq. 2.12) while the amplitude of the evanescent wave approaches the incident wave amplitude. [133, 141]

For interfaces with a lateral two-dimensional order such as often observed in Langmuir monolayers, the evanescent wave is diffracted by this two-dimensional lattice [150, 133, 151] as schematically shown in Fig. 2.10. Due to the grazing incident angle, the incident wave is scattered from the atomic planes perpendicularly to the surface and thus is sensitive to the surface near in-plane structure. The

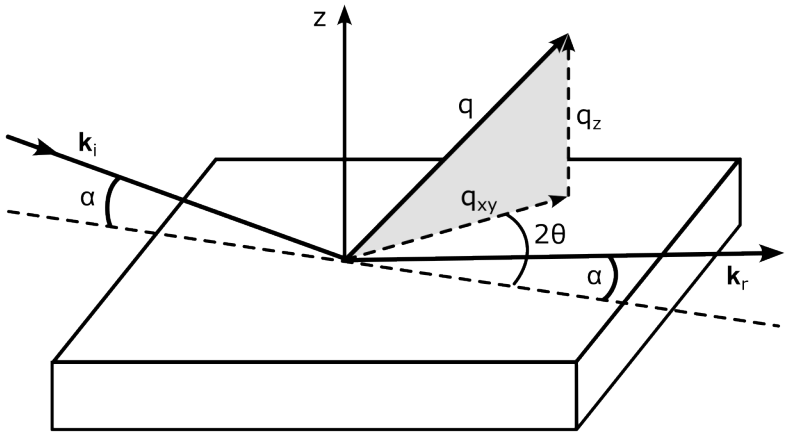

Figure 2.10: Schematic of grazing incidence X-ray diffraction from a lipid monolayer at the water-air interface after [151].

scattering signal is recorded with an area detector placed at a distance d. Each detector pixel corresponds to a unique pair of scattering vectors q_z and q_{xy}, allowing a transformation of the detector image into the q-space. Analysing the position and width of the diffraction pattern allows conclusions on the lattice parameters [150, 133, 131]. Assuming, the lipid monolayer possesses a two-dimensional long range order the lipids are ordered on a two-dimensional lattice with the primitive cell vectors $\boldsymbol{a}$ and $\boldsymbol{b}$ with an angle γ between them. In most monolayers, the tail groups are ordered in a hexagonal lattice. For hexagonal lattices, the conditions $a = b$ and $\gamma = 120°$ are valid while for a distorted hexagonal lattice $\gamma \neq 120°$ applies. An oblique lattice is found for sheared lattices with lattice lengths $a \neq b$ and $\gamma \neq 120°$.

In addition, the chains of the tail group can be approximated as a cylinder standing at the interface with a tilt angle τ between the cylinder direction and the z-axis [152, 153].

From the q_{xy} position of the Bragg peaks in the scattering pattern, the lattice repeat distances can be calculated with

$$d_{hk} = \frac{2\pi}{q_{xy}^{hk}} \tag{2.21}$$

where h and k are Miller indices [154, 155]. Different to the Bragg peak in the q_{xy} direction, the scattering along the q_z direction corresponds to Bragg rods due to the two-dimension lattice extension and the missing third dimension. Analysing the positions and intensity profiles of the Bragg rods in q_z direction, the tilt angle of the

tail groups and the thickness of the ordered layer can be estimated with

$$D = 0.9 \cdot \frac{2\pi}{\text{FWHM}} \tag{2.22}$$

where FWHM is the full width half maximum of the Bragg peak in q_z direction [152, 106]. The analysis steps performed in this work are presented in Sec. 4.6.2 in detail.

To conclude, performing GID measurements on Langmuir monolayers at the water-air interface allows the study of the two-dimensional lattice structure of ordered lipid monolayers [150, 133, 153]. Together with complementary XRR measurements, GID studies are a powerful tool to describe the monolayer structure and changes in the molecule orientation and layer structure in the vertical and in-plane direction.

2.3.4 Small angle X-ray scattering

Studying lyotropic liquid crystals in water solutions, small angle X-ray scattering (SAXS) measurements were performed to determine their size and morphology [156]. Different to reflectometry studies, the sample is measured in transmission geometry and the scattered beam is detected on a 2D detector and for isotropic sample the intensity is azimuthally averaged giving a plot of scattered intensity versus scattering wavevector. Based on the Thomson scattering formula the intensity distribution can be described as

$$I(\mathbf{Q}) = f(\mathbf{Q})^2 \cdot S(\mathbf{Q}) \approx \left| \int_V f \rho_{\text{at}} e^{i\mathbf{Q}\mathbf{r}} dV \right|^2 \tag{2.23}$$

where $f(\mathbf{Q})$ and $S(\mathbf{Q})$ are the atomic or molecular form factor and structure factor, respectively, and ρ_{at} is the average density [130, 53, 157]. Typically, dilute solutions of particles or molecules are analysed by applying the Guinier analysis [158], Porod analysis [159] and determination of radius of gyration methods to investigate the radius of the particle, the shape of the particle and the mean distance from the particle's centre of gravity, respectively. However, the mentioned methods cannot be applied for polydispersed systems or high concentrated systems with interacting particles [130]. Therefore, the SAXS data in this work was analysed by investigating the peaks coming from repeating distances in the crystals allowing a conclusion about their overall morphology on the nm length scale as shown in Sec. 4.6.3.

2.3.5 X-ray fluorescence near total reflection

The X-ray fluorescence near total reflection (XRFNTR) analysis of an aqueous salt solution interface gives information on the chemical composition of the solution

in the surface near region. An incoming angle below the critical angle is chosen to obtain the total reflection of the X-ray beam. In aqueous salt solutions, the penetrating X-ray radiation interacts with the electrons of the ions and can excite the electrons from a core state to a bound state at higher energy. Upon returning to their ground states, the electrons emit photons with the energy corresponding to the energy difference between the two energy levels. These energy levels are unique for each element as they are defined by the composition of protons and neutrons in the nucleus [160, 161]. Measuring the emitted fluorescence signal allows the identification of the elements based on their specific emission lines. Performing this fluorescence measurement under total reflection of the X-ray beam, the chemical composition of the surface near region can be identified.

In addition to the chemical composition, the arrangement of the ions in the solution can be determined. The intensity of the fluorescence signal is proportional to the intensity of the incident beam. Classical fluorescence excitation experiments are performed with large incident angles. For these angles, the intensity of the wave field can be described as locally constant and exponentially decreasing inside the medium [162]. However, under shallow incident angles, especially in the region of total reflection, the incoming monochromatic wave interferes with the reflected wave above the surface where they cross each other. The electromagnetic field in this cross region is defined by the interference pattern and standing waves along the surface normal direction can be observed with an dependence on the incident angle [163, 161]. Therefore, the fluorescence signal of the atoms is proportional to the local intensity oscillations of the standing wave field describing the incident wave. By analysing the fluorescence signal for multiple incident angles, the depth profile of layered structures can be determined. In the following, the equations to calculate the fluorescence intensity of an infinite thick and flat substrate along with the intensity of a finite thick layer on top of a flat substrate are introduced based on [162]. For detailed derivations of the equations please refer to [163, 160, 164, 162].

In general and if self-absorption is neglected, the intensity of the X-ray beam within the thick substrate at a depth z can be described as

$$\begin{aligned} I(\alpha,z) &= I_0 \left(1 + R_\mathrm{F}(\alpha) + 2\sqrt{R_\mathrm{F}(\alpha)}\cos\Psi\right) e^{-z/\Lambda} \\ \text{with} \quad R_\mathrm{F}(\alpha) &= \left|\frac{\alpha - \alpha'}{\alpha + \alpha'}\right|^2 \\ \text{and} \quad \Psi(\alpha) &= \arccos\left(2\left(\frac{\alpha}{\alpha_\mathrm{c}}\right)^2 - 1\right) \end{aligned} \tag{2.24}$$

with the Fresnel reflectivity $R_\mathrm{F}(\alpha)$ (see also Eq. 2.12), phase shift $\Psi(\alpha)$, between

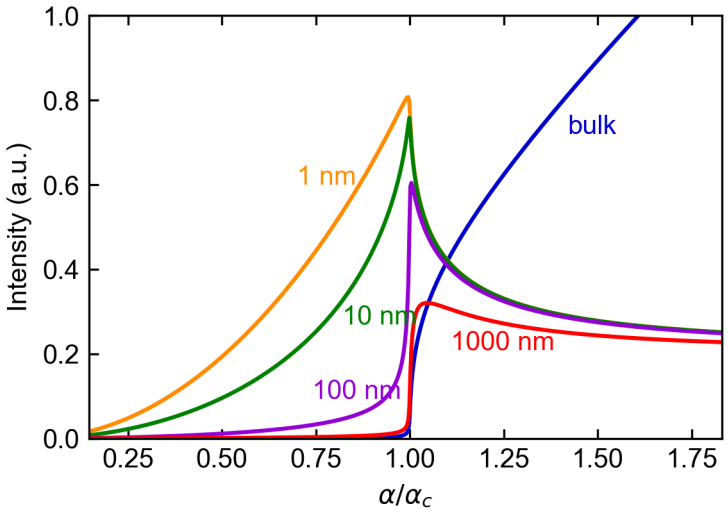

Figure 2.11: Simulated fluorescence signals from a bulk substrate (blue) and layers with multiple thicknesses (coloured) at different incident angles α.

the incoming and evanescence wave, and penetration depth Λ (Eq. 2.19). This X-ray beam with its intensity $I(\alpha,z)$ can induce a fluorescence signal from an atom in a depth z_i of the substrate. The intensity of the emitted fluorescence signal is proportional to the X-ray beam intensity $I(\alpha,z_i)$ at that depth. Thus, the total intensity from the substrate I_B is the sum of all signals and is derived by integrating Eq. 2.24 over a depth z from zero to infinity to

$$I_\mathrm{B}(\alpha) = I_\mathrm{n}\left(1 + R_\mathrm{F}(\alpha) + 2\sqrt{R_\mathrm{F}(\alpha)}\cos\phi\right)\Lambda(\alpha) \tag{2.25}$$

where I_n is a norm factor.

Considering a layer inside the substrate, the intensity of this buried layer I_L can be calculated by integrating Eq. 2.24 over the layer extent from depth z to $z+d$:

$$I_\mathrm{L}(\alpha, z) = I_\mathrm{n}\left(1 - R_\mathrm{F}(\alpha)\right) \cdot \frac{\alpha}{d} \cdot e^{-z/\Lambda(\alpha)} \cdot \left(1 - e^{-d/\Lambda(\alpha)}\right) \tag{2.26}$$

Simulated intensity profiles for fluorescence signals from a substrate and layers with multiple thicknesses at the interface of the substrate are shown in Fig. 2.11.

2.4 Laser studies

Pump - probe studies are performed to investigate excitation and relaxation dynamics in a wide range of samples. Here, laser radiation is utilised as a pump to excite

the sample thermally or electronically depending on the chosen wavelength. The structural changes are studied with X-ray scattering methods such as XRR, GID and XRFNTR as described in the previous sections. Synchronising the pump and probe pulses enables highly time-resolved measurements. The time resolution is then limited by the pulse lengths of the pump and probe. In the following, a short overview on the laser functionality and properties is given based on [165].

2.4.1 Principles of laser radiation

The acronym LASER stands for Light Amplification by Stimulated Emission of Radiation. Each laser consists of a laser medium, a pump and a resonator. Laser radiation is produced in the laser medium, which can be in solid, liquid or gas state. The main difference between lasers and other light sources such as lightbulbs, the sun or stars is that the emission of photons is stimulated in the laser. The stimulated emission of light is started by a spontaneous photon emission of the same energy by another atom. Afterwards this stimulated emitted photon triggers another stimulated photon emission. For the chain reaction to work, the number of atoms in the excited states must be higher than the number of atoms in the ground state and the atoms have to stay in the excited state for a relatively long time. The higher number of excited atoms is called population inversion and can only be achieved in a number of materials. The pump energy induced into the laser medium excites atoms into higher energy levels and is responsible to build up the population inversion. The emitted light is then reflected inside the resonator. This results in highly collimated and amplified radiation. Part of this radiation is passing the resonator mirror and exits the active medium. [166, 167, 165]

Generally, lasers are differentiated between continuous wave (CW) lasers and pulsed lasers. While CW lasers produce continuous laser radiation, pulsed lasers emit laser pulses with pulse length from as to µs. By reducing the pulse length, higher pulse energies can be achieved. Such fs laser pulses are used in a wide range of application fields ranging from engineering, manufacturing, pump - probe experiments, metrology, medical treatments to photochemistry.

2.4.2 Femtosecond laser pulses

Most femtosecond laser pulses are created by using mode-locked oscillators. An example for a passive mode-locking is the Kerr lens mode-locker, which is based on the optical Kerr effect. The generated laser pulses in the resonator pass through the saturable absorber, which is a nonlinear medium that leads to a deformation

of the wavefronts due to an induced phase difference between the axes parallel and perpendicular to the propagation direction resulting in a pulse focusing, the so-called self-focusing effect. This absorber absorbs energy from the laser pulses and can get saturated every time it is hit by a circulating pulse with high intensity. Upon saturation, the loss inside the medium is temporarily reduced and the pulse passes the absorber. Pulses hitting the absorber with lower intensities experience losses and are suppressed. By this, one circulating pulse is selected inside the resonator. [168–170]

At one of the resonator sides, this pulse is partially emitted at the output coupler mirror which leads to a regular emitted pulse train. The pulse repetition rate is defined by resonator length and is typically in the range of tens of MHz. In addition to the repetition rate, the resonator length determines the mode structure and generates standing waves inside the resonator. The resulting electric field distribution can be described by using the transversal electromagnetic modes (TEM-modes) nomenclature. The most fundamental and typical mode is the TEM_{00} mode, which corresponds to a Gaussian beam profile. [165]

Another component used to modify the laser pulses is the Pockels cell. The Pockels cell is placed inside the resonator and its refractive index depends on an external electric field (Pockels effect). Modifications of this external electric field result in a phase shift between the electric field components of the laser pulse along the fast and slow axis of the medium. This changes the polarisation state of the laser radiation from linear to elliptical or circular and leads to a reflection of the beam at the polariser placed between the Pockels cell and output mirror. The reflected pulse is therefore kept in the resonator and gets amplified further. Upon reaching the maximum pulse energy, the voltage applied to the Pockels cell is reduced and thus, the laser pulse passes trough the polariser and leaves the resonator. [165]

2.4.3 Excitation of ions with pulsed lasers

Ultra short laser pulses are known for their high pulse energies and possibility to heat up a sample locally by up to hundreds of °C [171]. However, laser radiation can also excite halide anions in solutions into their charge-transfer-to-solvent (CTTS) states. This photodetachment mechanism results in the release of a photoelectron into solution and the formation of a neutral halogen atom [172–175]. The free electron either recombines with the charged ion or diffuse away after hundreds of ps [69, 71, 176, 72]. To photoexcite the halide anion, light with the corresponding wavelength is necessary. For large halide anions, such as iodide, the CTTS bands

are in the deep UV range between 190 to 260 nm. Meanwhile, lighter halides exhibit CTTS bands at higher energies thus even smaller wavelengths [177].

3
Materials and sample preparation

3.1 Phospholipids

Phospholipids are the main component of lipid membranes and significantly define the membrane properties such as the rigidity and functionality. More than 1000 different phospholipids are found in mammalian cells [13, 178, 179, 14] and differences in their head and tail group lead to a variety of membrane functions. Within this study, two phospholipids, namely DPPC and DLPC, shown in Fig. 3.1, were used to create lipid model membranes. Both, DPPC and DLPC, were purchased from Avanti Polar (Inc.) and have an identical phosphatidylcholine head group and a tail group consisting of two saturated acyl chains. For the NR measurements, tail-deuterated DPPC (d_{62}-DPPC) was also purchased from Avanti Polar (Inc.). While DPPC has a pamitic acid tail group (16 carbon atoms in the acyl chain), DLPC possesses a lauric acid tail group (12 carbon atoms). The length of a straight palmitic acid chain with n CH_2 groups and a terminal CH_3 group can be estimated accordingly to [180, 181] by $l_{\text{chain}} = n \cdot 1.265\,\text{Å} + 1.54\,\text{Å}$. Subsequently, DPPC posses a total chain length of $l_{\text{chain}} = 19.21\,\text{Å}$ while the chain length of DLPC is shorter by 5.06 Å. The longer tail chained DPPC has its phase transition temperature at 41 °C (as shown in Fig. 2.6) while the DLPC acyl chains already melt at −2 °C [115, 123]. Thus, at room temperature, DLPC lipids are in the liquid crystalline phase and DPPC lipids are in the gel phase.

3.2 Synthetic photoswitchable lipid mimetics

In this study 14 different synthetic azobenzene amphiphiles and reference molecules, shown in Fig. 3.1 and provided by the group of Prof. Dr. Thisbe K. Lindhorst, Kiel University, were investigated. The lipid mimetics AZOL-C12, AZOL-C16, AZGL-C12, AZGL-C16, AZLL-C12, AZLL-C16, OL-C12, OL-C16, GL-C12, GL-C16, LL-C12 and LL-C16 (see Tab. 3.2) were synthesized by Dr. Franziska Reise, Kiel

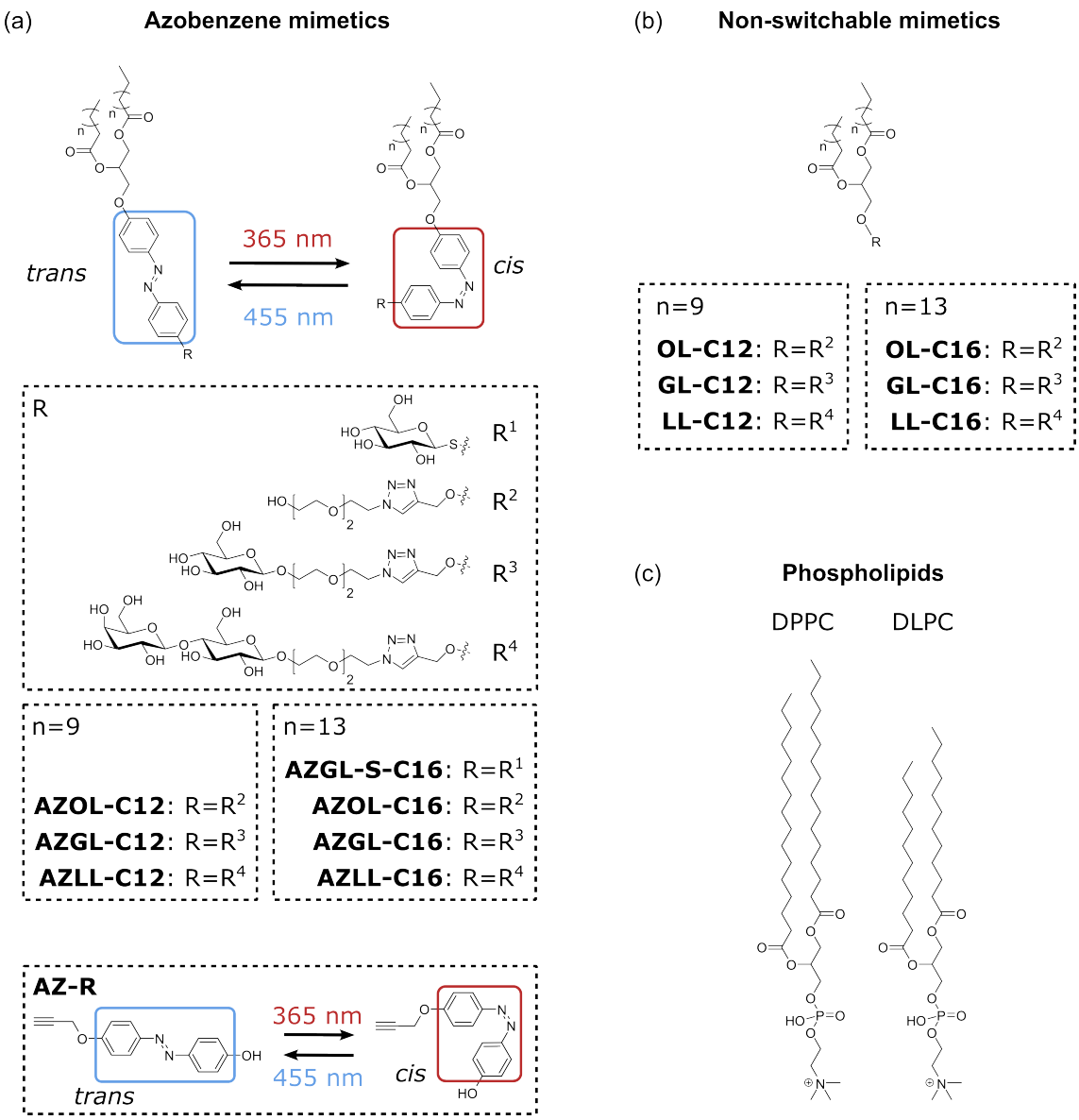

Figure 3.1: Overview of the photoswitchable and reference mimetics for their *trans* and *cis* isomer similar to [MSH 1].

University, within the scope of her work in the SFB 677 Function through switching following the synthesis routes published in [182]. The azobenzene mimetics differ in the length of the acyl chain groups and the type of carbohydrate attached to the head group. Comparing the observed switching behaviour and induced structural changes in the lipid membranes allows conclusions on the influence of the head and tail group composition.

All azobenzene amphiphiles possess a tail group consisting of two saturated acyl chains with either 12 or 16 carbon atoms which is identical to DLPC or DPPC,

respectively. Meanwhile, the head group of the amphiphiles differ in the number of attached glycan moieties. As head groups, aside from the non-glycosylated hydroxyl group, β-Dglucopyranosyl (glucose) and β-D-lactosyl (lactose) moieties were chosen (see Fig. 3.1 R^2, R^3 and R^4). The 4-Hydroxy-4'-propargyloxy azobenzene (AZ-R), a precursor in the synthesis of the azobenzene mimetics, was used for reference measurements.

The shorter azobenzene mimetic AZGL-S-C16 (see list of abbreviations) was designed and synthesized by Michael Röhrl, Kiel University. The glucose head group of the AZGL-S-C16 mimetic is linked via a sulphur atom directly to the azobenzene switch. This makes the mimetic AZGL-S-C16 (13.9 ± 0.6) Å shorter than the corresponding mimetic AZGL-C16. Comparing the length of the straight molecules, the AZGL-S-C16 mimetic is the shortest lipid while AZLL-C16 is the longest. The molecular lengths were determined with the program ChemSketch and the obtained lengths are listed in Tab. 3.1.

The azobenzene lipids possess two isomers, namely *trans* and *cis*, from which the *trans* state is the thermally stable form. By illumination with 365 nm the $\pi - \pi^*$ band of the N double bond is excited and the molecules switch into the *cis* isomer. Over time or by heating, the molecule relaxes back to its thermally stable *trans* isomer. In addition, the *trans* state can be induced by illumination with 455 nm light that is absorbed by the $\pi - n$ band. Switching the azobenzene switch between its *trans* and *cis* isomer, the N double bond of the azobenzene rotates and bends to an angle of about 90° [33, 31, 34].

Considering a molecule in its *trans* state at the water-air interface, the molecule self-assembles and is orientated perpendicular to the water surface. Switching to the *cis* isomer results in an increase of the molecules area and shortening of the molecule length $l_\perp$ as shown in Fig. 3.2 exemplarily for AZGL-C16. The vertical stretching for the *cis* isomer was estimated by the maximum extend of the head and tail group with the 90° azobenzene bond between them. Thus, the values listed in Tab. 3.1 only give a range for the vertical and horizontal stretching as the molecule can be tilted, the acyl chains are highly flexible and the head group can bend or rotate as well. The largest change in dimension by the azobenzene mimetics is expected for the AZLL-C12 and AZLL-C16 mimetics with the lactose head group.

Table 3.1: Molecular weight and length of phospholipids, reference mimetics and the azobenzene amphiphiles in their *trans* and *cis* state shown in Fig. 3.1. The lengths $l_\perp$ and $l_\parallel$ are defined as shown in Fig. 3.2 and were determined with the software ChemSketch. The errors are estimated to 0.3 Å by measuring multiple lengths from different reference points for comparison. The difference Δl corresponds to the length change upon switching from trans to cis.

Mimetic	M/ g mol^{-1}	$l_\perp$/ Å	$l_\parallel$/ Å
DPPC	734.053	31.6	5.0
DLPC	621.826	26.4	5.0
OL-C12	669.932	36.3	6.0
GL-C12	832.073	40,3	12.5
LL-C12	994.214	42.3	17.3
OL-C16	782.145	41.4	6.0
GL-C16	944.286	45.4	12.5
LL-C16	1106.426	47.4	17.3

Mimetic	M/ g mol^{-1}	$l_{\perp,t}$/ Å	$l_{\parallel,t}$/ Å	$l_{\perp,c}$/ Å	$l_{\parallel,c}$/ Å	$\Delta l_\perp$/Å	$\Delta l_\parallel$/Å
AZ-R	252.268	16.6	3.0	11.6	6.0	-5.0	3.0
AZOL-C12	866.137	48.2	14.5	37.3	20.4	-10.9	5.9
AZGL-C12	1028.278	50.7	14.5	40.9	25.0	-9.9	10.5
AZLL-C12	1190.418	54.3	14.5	43.5	31.6	-10.8	17.1
AZGL-S-C16	943.322	41.9	10.0	38.0	11.1	-3.8	1.1
AZOL-C16	978.350	53.4	14.5	42.5	20.4	-10.9	5.9
AZGL-C16	1140.490	55.8	14.5	46.0	25.0	-9.9	10.5
AZLL-C16	1302.631	59.4	14.5	48.6	31.6	-10.8	17.1

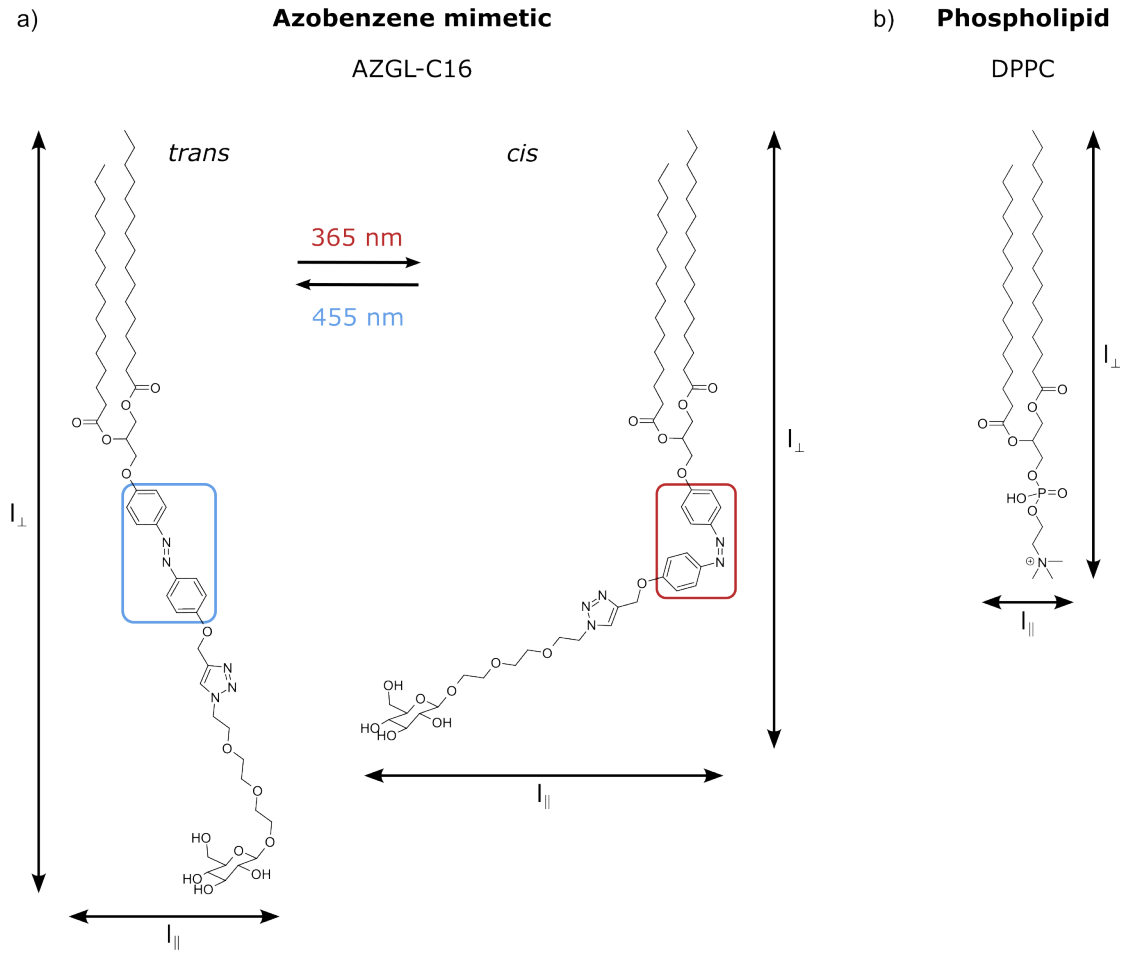

Figure 3.2: Schematic drawing of a) the AZGL-C16 mimetic's *trans* and *cis* isomer and b) the phospholipid DPPC with the lengths $l_{\perp}$ and $l_{\parallel}$.

Table 3.2: Abbreviations and full chemical names of the photoswitchable glycolipids shown in Fig. 3.1.

Abbreviation	full chemical name
AZOL-C12	(E)-[*p*-[(1,2-Didodecanoyloxycarbonyl)propyloxy]-*p′*-(2-{2-[2-(1-ethoxy-4-methoxy-1,2,3-triazolyl)]ethoxy}ethyl)]azobenzene
AZOL-C16	(E)-[*p*-[(1,2-Dihexadecanoyloxycarbonyl)propyloxy]-*p′*-(2-{2-[2-(1-ethoxy-4-methoxy-1,2,3-triazolyl)]ethoxy}ethyl)]azobenzene
AZGL-C12	(E)-[*p*-[(1,2-Didodecanoyloxycarbonyl)propyloxy]-*p′*-[(2-{2-[2-(1-ethoxy-4-methoxy-1,2,3-triazolyl)]ethoxy}ethyl)-β-D-glucopyranosyloxy]]azobenzene
AZGL-C16	(E)-[*p*-[(1,2-Dihexadecanoyloxycarbonyl)propyloxy]-*p′*-[(2-{2-[2-(1-ethoxy-4-methoxy-1,2,3-triazolyl)]ethoxy}ethyl)-β-D-glucopyranosyloxy]]azobenzene
AZGL-S-C16	1-*O*-(4-(4-(*S*-β-D-Glucopyranosyl)thiophenyldiazenyl)benzene)-2,3-di-*O*-hexadecanoyl-*rac*-glycero
AZLL-C12	(E)-[*p*-[(1,2-Didodecanoyloxycarbonyl)propyloxy]-*p′*-[(2-{2-[2-(1-ethoxy-4-methoxy-1,2,3-triazolyl)]ethoxy}ethyl)-β-D-galactopyranosyl-(1→4)β-D-glucopyranosyloxy]]azobenzene
AZLL-C16	(*E*)-[*p*-[(1,2-Dihexadecanoyloxycarbonyl)propyloxy]-*p′*-[(2-{2-[2-(1-ethoxy-4-methoxy-1,2,3-triazolyl)]ethoxy}ethyl)-β-D-galactopyranosyl-(1→4)β-D-glucopyranosyloxy]]azobenzene
OL-C12	1-{2-[2-(2-Hydroxyethoxy)ethoxy]ethyl]}-4-{[(1,2-didodecanoyloxy-carbonyl)propyloxy]methoxy}-1,2,3-triazole
OL-C16	1-{2-[2-(2-Hydroxyethoxy)ethoxy]ethyl]}-4-{[(1,2-dihexadecanoyloxy-carbonyl)propyloxy]methoxy}-1,2,3-triazole
GL-C12	1-{2-[2-(2-(β-D-Glucopyranosyloxy)ethoxy)ethoxy]ethyl]}-4-{[(1,2-didodecanoyloxycarbonyl)propyloxy]methoxy}-1,2,3-triazole
GL-C16	1-{2-[2-(2-(β-D-Glucopyranosyloxy)ethoxy)ethoxy]ethyl]}-4-{[(1,2-dihexadecanoyloxycarbonyl)propyloxy]methoxy}-1,2,3-triazole
LL-C12	1-{2-[2-(2-((β-D-Galactopyranosyl-(1→4)β-D-glucopyranosyloxy)ethoxy)ethoxy]ethyl]}-4-{[(1,2-didodecanoyloxycarbonyl) propyloxy]methoxy}-1,2,3-triazole
LL-C16	1-2-[2-(2-(β-D-Galactopyranosyl-(1→44)β-D-glucopyranosyloxy)ethoxy)ethoxy]ethyl]-4-[(1,2-dihexadecanoyloxycarbonyl) propyloxy]methoxy-1,2,3-triazole

3.3 Inorganic salts

In addition to the studies on lipid membranes and in the third project of this work, laser pump - X-ray probe measurements were performed on aqueous salt solutions containing sodium iodide (NaI), sodium chloride (NaCl) and rubidium bromide (RbBr). Salts were purchased from Sigma-Aldrich and Carl Roth GmbG & Co. KG with a purity of 99.99 % for NaI, 99.5 % for NaCl and 99.6 % for RbBr. To prepare the salt solutions, the salts were weighed and placed in an oven at 200 °C for over 8 h before adding ultra pure Milli-Q water® ($> 18\,\mathrm{M\Omega}$). Concentrations were chosen between 0.1 mol and 5 mol. The samples were stored in a fume hood to allow frequent sample exchange. For preservation of the solution, the NaI solutions were stored in brown glass bottles or bottles wrapped in aluminium foil because NaI can decompose to triiodide under absorbance of UV light. The presence of triiodide can be easily seen by a yellow colouring of the solution which intensifies over time under UV irradiation. Alteration of the pH was done by adding small amounts of sodium hydroxide (NaOH (aq)), hydrochloric acid (HCl (aq)), hydroiodic acid (HI (aq)), rubidium hydroxide (RbOH (aq)) and hydrobromic acid (HBr (aq)), respectively, to create acidic or alkaline solutions of NaI, NaCl and RbBr.

4
Experimental setup and methods

4.1 Langmuir monolayer sample cell

For measurements in the laboratory at Kiel University or PETRA III, the Langmuir monolayers were prepared in a Langmuir trough from Riegler & Koch. A detailed description of the trough setup and its integration into the beamline control at P08, PETRA III is presented in section 4.5.1. The Riegler & Koch Langmuir trough consists of a Teflon trough with a maximum area of 399.08 cm^2 and a single barrier is used to reduce the surface area to a minimum of 72.45 cm^2 as shown schematically in Fig. 2.4. With this trough, a compression ratio of 5.5 of the surface area is obtained. To measure the surface tension, a Wilhelmy plate, as described in section 2.1.1, is placed on the movable barrier holder. Calibration of the surface tension is done via tuning two potentiometers at the read out electronics. As reference points, the pure water surface is calibrated to 0 $mN\,m^{-1}$ and air to 72.8 $mN\,m^{-1}$ at room temperature. Area calibration is performed by moving the barrier to its minimum and maximum position and allocate this motor positions the corresponding minimum and maximum surface area. As Langmuir isotherm measurements are highly temperature dependent, the trough is water cooled. The Langmuir trough is enclosed by a metal housing serving multiple purposes such as reducing the amount of dust falling onto the water surface, preventing creation of turbulences or waves on the water surface by air flows (e.g. from air conditioning) and creating a gas tight atmosphere. Measurements in the laboratory were conducted in air atmosphere while all measurements at LISA at P08, PETRA III were performed under helium gas to reduce background scattering signal.

To form the Langmuir monolayer at the water - air interface, the lipids solved in chloroform were spread onto the water surface. Monolayers with more than one type of lipid were created by mixing the desired mol/mol percentage of lipids together in the chloroform solution and spreading the mixture. All spreading solutions were prepared with a molar concentration of 1 $mmol\,L^{-1}$. For a typical measurement, 50 to 60 mL lipid solution was spread onto the water surface. During experiments,

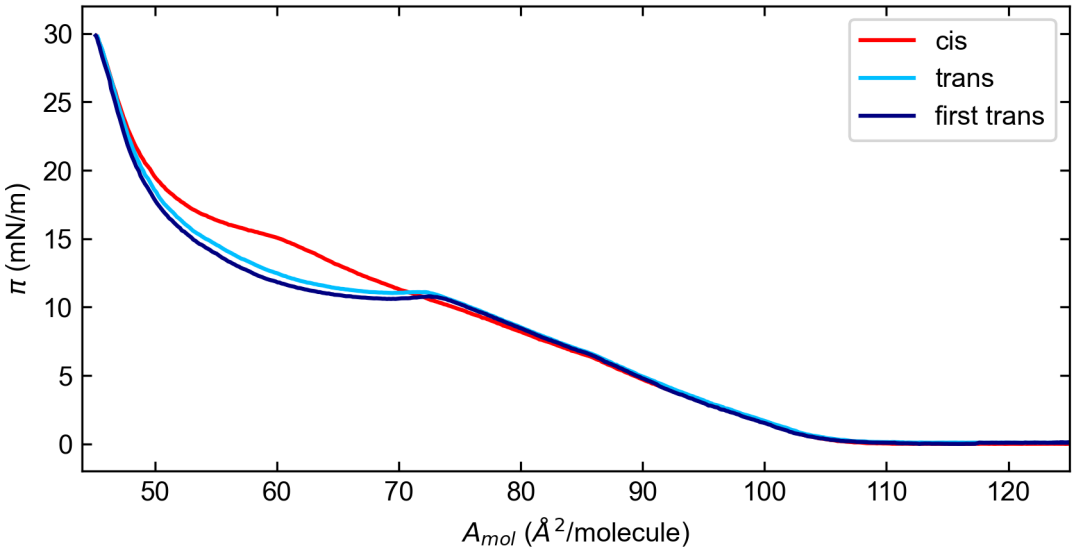

Figure 4.1: First *trans* (dark blue), *trans* (light blue) and *cis* (red) Langmuir isotherms of the mixed DPPC and AZLL-C16 monolayer with a ratio of 9:1.

the vials containing the lipid solutions were only taken out of the freezer (stored at −21 °C) and opened for spreading the solution. The time of the open vial was shortened to the minimum to reduce evaporation of chloroform and thus a change in concentration of the spreading solution.

Recording the Langmuir isotherms, the speed of the barrier was set to about 40 mm^2 min^{-1} for compression and expansion, respectively. For photoswitchable samples, a first isotherm without any illumination is taken by compressing up to a surface pressure of 35 mN m^{-1}. This isotherm is referred to as first *trans*. After expanding the area fully, the monolayer is illuminated with UV light (365 nm) for 5 min to switch to the *cis* state. Another isotherm up to a surface pressure of 35 mN m^{-1} is recorded, which is the *cis* isotherm. This is followed by expanding the area and illumination with blue light (455 nm) for 5 min to switch back to the *trans* state. Again, an isotherm is measured, which is referred to as *trans* isotherm. The difference between the first *trans* and *trans* isotherm is marginal compared to the *cis* isotherm and can be seen exemplarily in Fig. 4.1 for a mixed monolayer of 90 % DPPC and 10 % AZLL-C16. Both first *trans* and *trans* isotherms show the same trend and only differ slightly in the clarity of characteristics. This difference can be explained by the efficiency of the light-induced *trans* isomerisation of about 80 %. Thus, statistically up to 20 % of *cis* isomers are present in the *trans* state while thermal relaxation reaches 100 % *trans* isomers. As thermal relaxation takes

multiple hours for the studied azobenzene amphiphiles [182], all measurements were conducted on the light switched *trans* state. Recording consecutive isotherms with alternating illumination revealed, that the *trans* and *cis* isotherms are equal among each other. Though the first *trans* isotherms were collected, they were disregarded during the analysis process.

4.2 Lyotropic lipid crystal sample cell

All lyotropic lipid crystals studied within this work were prepared applying the thin-film hydration method. First, the desired mol/mol percentage of photoswitchable mimetics, DLPC and DPPC were mixed in chloroform with a concentration of $5\,\mathrm{mmol\,L^{-1}}$. These solutions were dried with a Rotavapor R-300 for over an hour at a bath temperature of 45 °C and pressure of 16 mbar. The Rotavapor is available at the P08 beamline at PETRA III. The dried films were stored in the fridge at 5 to 10 °C for up to four weeks. On the day of the measurement, the dried films were hydrated by adding warm (30 to 40 °C) Milli-Q® water to create a concentration of $1\,\mathrm{mmol\,L^{-1}}$ for the DSC measurements and $5\,\mathrm{mmol\,L^{-1}}$ and $10\,\mathrm{mmol\,L^{-1}}$, respectively, for the SAXS measurements at P12, EMBL and BL2, DELTA. The hydrated samples were shaken, vortexed and placed in a water bath between 45 °C and 60 °C until a homogenous solution was formed. If necessary, the solutions were held into the ultrasonic water bath to break larger lipid lumps. The hydrated samples were measured within 24 h and stored in the fridge between measurements. As the phase of the crystals is temperature dependent, the hydrated samples were taken out of the fridge at least 1 h before the SAXS or DSC measurements to allow the sample to reach room temperature.

4.3 Salt solution sample cell

The liquid cell consist of a 40 mm × 90 mm PCTFE trough in a gas-tight aluminium housing as shown in Fig. 4.2 and described in [183]. The cell is equipped with temperature, humidity, surface tension and pH sensors to monitor *in operando* the sample properties. Further, the cell can be flushed with wet nitrogen or helium to prevent evaporation of the liquid inside the cell. A copper cooling block underneath the PCTFE trough keeps the sample tempered and can be used to cool or heat the sample. The X-ray windows are made of Kapton foil and on one of the sides an adapter for the fluorescence detector is mounted, so that the fluorescence detector is positioned perpendicular to the X-ray beam. The laser beam passes through the

quartz glass window in the lid of the housing onto the sample under an angle of about 30° with respect to the axis normal to the sample surface.

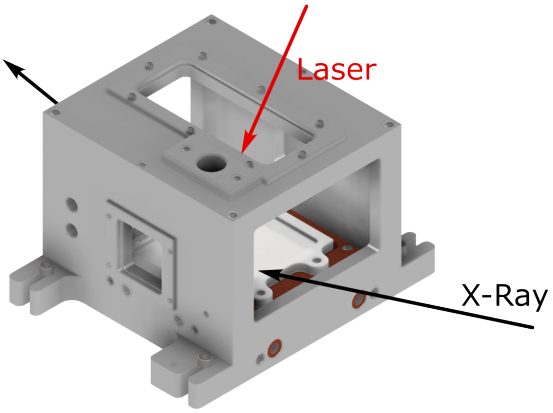

Figure 4.2: Sketch of the liquid cell used at the LISA endstation at the P08 beamline, PETRA III from [183] reproduced with permission of the International Union of Crystallography.

4.4 Differential scanning calorimetry measurements

Differential scanning calorimetry (DSC) measurements were performed at the MicroCal PEAQ-DSC instrument from Malvern Panalytical Ltd. available at P08, PETRA III. This microcalorimeter has two capillaries, one for the sample and one for the reference/buffer solution with a volume each of of 150 µL. For cleaning, the capillaries were flushed with ethanol at least three times at a temperature of 55 °C before flushing with ultra pure Milli-Q® water three times. This procedure was followed by a calibration measurement with pure water to verify the cleanliness of the capillaries.

The hydrated samples were prepared as described in section 4.2 with a concentration of 1 mmol L^{-1} and filled into the sample capillary. As reference, ultra pure Milli-Q® water was used. The calorimetry measurements were performed in the temperature range from 25 °C up to 60 °C. For every sample, one run with multiple heating and cooling cycles was recorded. Every run was started with a heating and cooling cycle with both a heating and cooling rate of 60 °C h^{-1} to ensure the sample to be in the equilibrium state. This first cycle was discarded during the analysis. For the second and third cycles, the heating rate was set to 12 °C h^{-1}. Another two cycles were

taken afterwards with a faster heating rate of $60\,^{\circ}\mathrm{C\,h^{-1}}$ to check sample stability. The cycles were always taken in pairs to verify reproducibility. Between the cycles, a waiting time of 10 minutes was added. At slower heating rates, the phase transition peaks are sharper and the phase transition temperature can be determined more accurately. Therefore, for the analysis in section 6.5 the second and third cycle with a heating rate of $12\,^{\circ}\mathrm{C\,h^{-1}}$ were used.

The data was exported as ASCII files from the instrument control software and analysed with self written python scripts. These scripts are available under [184] and were published together with the raw and processed data [185] of the publication [PSH 1] presented in section 6.5 following the FAIR principles [186] and the metadata schemata [187] proposed by the DAPHNE4NFDI project [188].

4.5 Beamline and instrumentation description

During the course of this work, measurements at multiple X-ray and neutron facilities have been conducted. Liquid-air interfaces were studied with X-rays at the LISA endstation at P08, PETRA III, Germany and at ID 10 ESRF, France. Complementary NR measurements were performed at BL16 Sofia at J-Parc, Japan. For the SAXS measurements, beamtime was requested and granted at the SAXS beamlines BL2 at DELTA, Germany and beamline P12 at PETRA III, Germany operated by the European Molecular Biology Laboratory (EMBL). In the following, the beamlines and the measurement configurations are described in more detail.

4.5.1 LISA, P08, PETRA III

PETRA III is a 3$^{\mathrm{rd}}$ generation storage ring operated by DESY and offers 25 beamlines for user operations. Classically, XRR measurements on solid samples are performed by tilting the sample to vary the incident angle of the X-ray beam. Yet, tilting liquid samples does not change the orientation of the liquid-air interface. Therefore, studying liquid interfaces with X-ray reflectometry requires a movable X-ray radiation source or a beam tilter in the X-ray beam path to vary the incident angle of the X-ray at the interface. At beamline P08 [75] the Liquid Interface Scattering Apparatus (LISA) [74] has been designed and optimised for XRR measurements on liquid-air and liquid-liquid interfaces. LISA is a double crystal beam tilter with two germanium (Ge) crystals as shown in Fig. 4.3. The incoming X-ray beam, here referred to as P08 beam, is reflected on the first Ge crystal over the Ge(111) reflection and on the

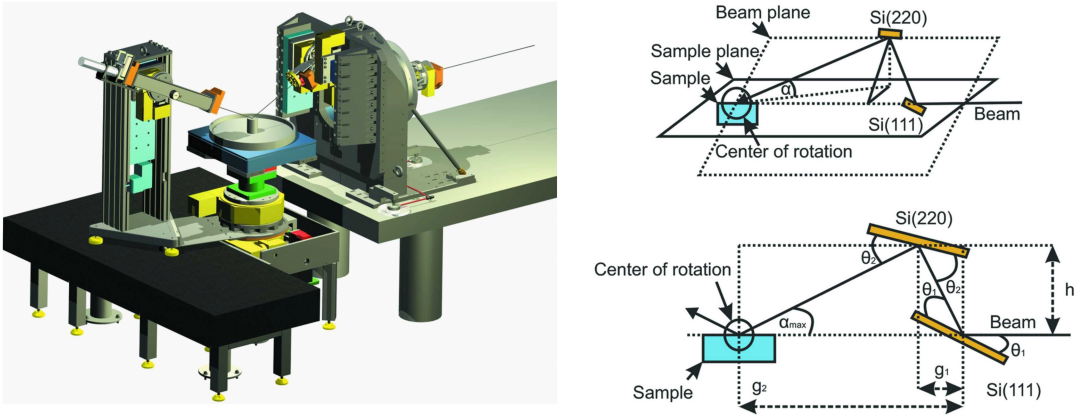

Figure 4.3: Sketches of the LISA instrument as a 3D model (left) and the principle of the double crystal Bragg deflection geometry (right) from two perspectives including important angles and distances from [74] reproduced with permission of the International Union of Crystallography.

second Ge crystal over the Ge(220) reflection to the sample as shown in Fig. 4.3.

During the alignment procedure, the rotation axes of the crystals, sample stage and detector stage are aligned to one pivot point on the sample. This particular alignment allows high precision positioning of the X-ray beam on the sample and ensures that the X-ray beam hits the sample on the same position during the XRR. Keeping the position of the X-ray beam on the sample constant is especially crucial for the laser pump - X-ray probe measurements during which the laser and X-ray footprint have to overlap for the whole q-range of the reflectivity.

At this beamline and instrument, Langmuir monolayer measurements and laser pump - X-ray probe experiments were performed. The respective setups are explained in the following paragraphs. All measurements were performed using a photon energy of 18 keV and a beam spot size of 100 µm × 400 µm. As detector, a Lambda 750k (X-Spectrum, Germany) detector with a pixel size of 55 µm × 55 µm was employed.

Langmuir monolayer setup

For studies of Langmuir monolayers at the water-air interface, the Langmuir trough described in section 4.1 is placed at the sample stage of LISA. The trough is placed on an anti-vibration table from The Table Stable Ltd. to counteract vibrations during movement of the sample stage, detector stage or the double crystal beam tilter. Furthermore, the trough is connected to a chiller to keep the temperature of the water constant at 21 °C. The housing of the trough is filled with Helium gas to

reduce background scattering and production of ozone. To monitor the gas flow, an oximeter detects the oxygen level. During measurements, the oxygen level was kept below 2 %.

To control the barrier movement and read out the surface pressure and area during measurements, the cables connecting the trough with its control unit are drawn from the experimental hutch to the control hutch. Similarly, the cables for controlling the illumination device are installed. The illumination device, consisting of two arrays of each three LEDs of 365 nm and 455 nm, is placed on top of the Langmuir trough. The visible and UV light then shines through the quartz glass in the trough lid onto the sample. By this, the light can be controlled manually and remotely from the control hutch enabling *in situ* measurements. Moreover, the surface pressure and area values are recorded and saved as ASCII files. During a scan the values can be additionally saved as metadata with the raw detector files. By monitoring the surface pressure during measurements, the stability of the Langmuir monolayer is verified and the light-induced surface pressure changes can be followed.

Laser pump - X-ray probe setup

For the laser pump - X-ray probe experiments, the ErUM-Pro funded fs laser Pharos from LightConversion was used. This laser is permanently placed at the beamline and maintained by members of the LISA group of PD Dr. Bridget M. Murphy, Kiel University. The laser beam is directed to the sample and impacts the surface with an angle of about 30° from the surface normal as shown schematically in Fig. 4.4a. The laser generates infrared laser radiation with a wavelength of 1030 nm, repetition rate between 100 kHz and 1 MHz and laser pulse length from 251 fs to 10 ps. The maximum pulse energy lies between 150 µJ and 15 µJ for 100 kHz and 1 MHz, respectively. In addition to the laser, the harmonics generator HIRO and optical parametric amplifier ORPHEUS, both from LightConversion, are available. The HIRO module is optimised for an incoming laser beam with a pulse length of 251 fs and a pulse repetition rate of 130 kHz and produces the second, third and forth harmonics. The maximum pulse energies and laser spot diameters are listed in Tab. 1 in [PSH 2] in Sec. 7.1. In comparison to the fixed harmonics, ORPHEUS can generate a broad spectrum from 210 nm to 2600 nm. Moreover, the ORPHEUS is optimised for a repetition rate of 1 MHz and pulse lengths of 251 fs. The pulse energy varies for the different wavelength and its highest is obtained for 700 nm with about 1.3 µJ. A picture of the laser setup is presented in Fig. 4.4b.

To perform time-resolved measurement in the pump - probe measurement mode, the phase of the laser oscillator frequency is synchronised to the reference 499.6655 MHz

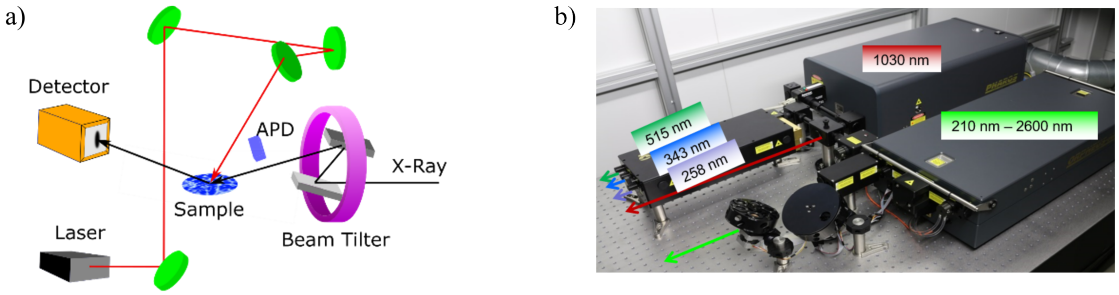

Figure 4.4: a) Schematic of the LISA and laser setup installed at P08 with the laser and X-ray beam paths indicated in red and black, respectively, from [183] reproduced with permission of the International Union of Crystallography. b) Picture of the Pharos laser (top) and the harmonics generator HIRO (left) and the optical parametric amplifier ORPHEUS (right) together with labels listing the wavelengths generated by them taken from [189] with permission.

radio frequency (RF) of the PETRA III storage ring as described in detail in [183].

At the beamline, the laser beam is guided over several mirrors from the laser in the laser hutch onto the sample stage in the experimental hutch (see Fig. 7.1 in Sec. 7.1). In this laser path lenses for focusing, spot size enlargement and diffractive optical elements can be placed to modify the beam profile and spot size. To enlarge the beam spot size, the Keplerian or the Galilean telescope design as shown in Fig. 4.5 can be used. Both designs have advantages and disadvantages. The Keplerian telescope uses two convex lenses with their focusing points between the lenses which allows large magnification factors. However, the magnified image is projected upside-down. This is in contrast to the Galilean telescope with a set of two lenses, one plan-convex and one plan-concave lens, which creates erect images. The focusing points of the lenses are behind the second lens. In this setup, the field of view is extremely narrow, which restricts the magnification factor. For the magnification of the laser spot size in the laser setup at P08, the Galilean telescope concept is beneficial. The main advantage of this concept is the absence of a focus point in the beam path. If the Keplerian telescope is used, the laser beam is focused on one point which results in very high intensities that can ignite or damage objects in the beam path easily.

The Gaussian beam profile (TEM_{00} mode) shape is preserved during magnification and focusing of the beam. To achieve a homogenous intensity distribution over the beam profile, the laser beam needs to pass through a beam shaper. Such a beam shaper is a diffractive optical element (DOE) that is especially designed for certain wavelengths, spot sizes and input profiles to produce the desired output profile. By

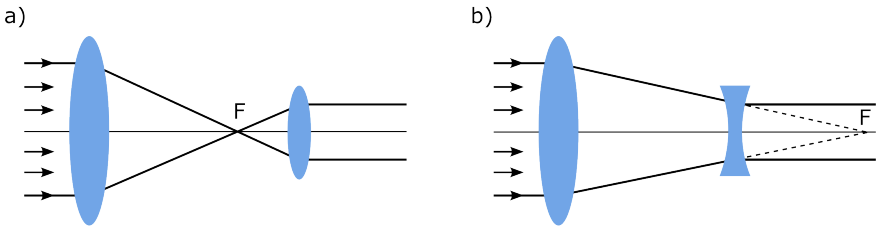

Figure 4.5: Schematics of the principle of the a) Keplerian and b) Galilean telescope.

this, a circular beam spot with a Gaussian intensity distribution can be shaped to a rectangular beam shape with a homogenous intensity distribution, a so called flat top.

Acquisition of X-ray reflectivity data

The XRR curves were recorded over an angular q range from 0.018 to 1.0 Å^{-1}. To accommodate the reduction in reflected intensity ($I \propto q_z^{-4}$) for increasing q wavevector, the absorber factor is reduced in steps during the reflectivity. While the direct beam is attenuated by a factor of 10^6, the beam is not attenuated for angles above $q_z = 0.2\,\text{Å}^{-1}$. Thus, multiple scans with different attenuation factors and counting times are taken to record the whole reflectivity curve. The specular intensity is extracted by defining a ROI on the detector image and summing the intensity of each pixel in this region. Typically, an ROI with a dimension of 30×30 is used. For the background correction, two ROIs of the same size are placed next to the ROI of the specular intensity and their intensities are averaged and subtracted from the specular intensity. This intensity extraction is done for every scan and the intensity values are saved together with the corresponding q_z values. Another extraction step is the construction of the reflectivity curve. As the attenuation factor is changed for the scans, this change in intensity has to be normalised. Normalisation is done by matching the intensity of q point in overlapping q-ranges. The extraction script is available under [184].

Acquisition of laser pump - X-ray probe data

Laser pump - X-ray probe measurements were collected on different time scales and in single pump - single probe and continuous pump - continuous probe mode. By synchronising the laser oscillator frequency to the reference radio frequency of the storage ring, time-resolved measurements on timescales of few picoseconds up to seconds is possible. For the single pump - single probe studies, the detector was

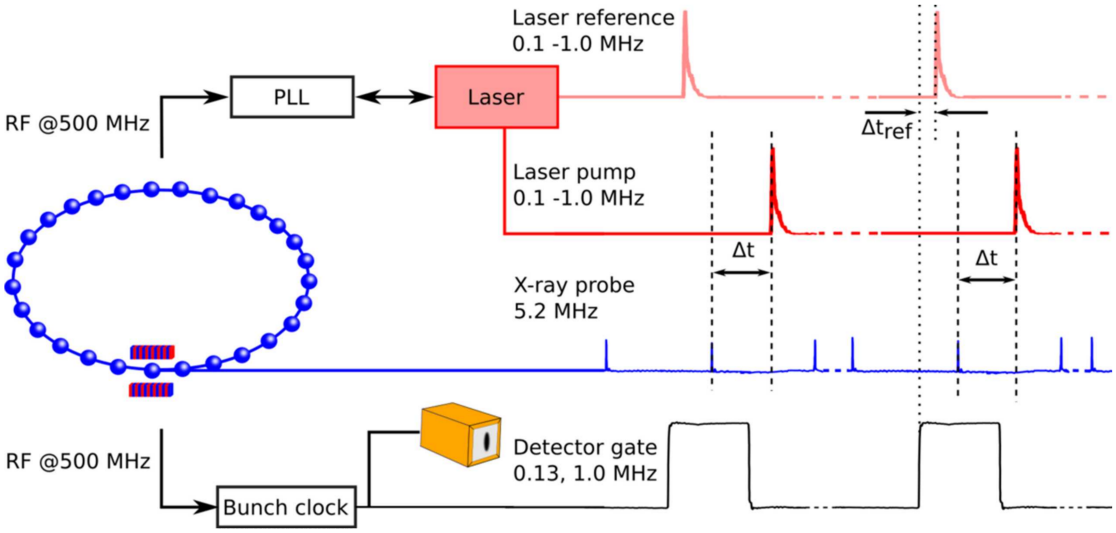

Figure 4.6: Graphical presentation of oscilloscope traces showing the detector gate signal generated from the bunch clock (black), the laser reference signal (light red) produced by one of the photodiodes in the Pharos laser unit and the laser signal (red) and X-ray bunch signal (blue) measured with a photodiode at the sample position from [183] reproduced with permission of the International Union of Crystallography.

gated to only count the photons belonging to one selected X-ray pulse as shown in Fig. 4.6. By this, a time resolution of 38 ps can be achieved [183]. By varying the phase of the laser and moving the detector gating signal to another X-ray pulse, the time delay between the laser and X-ray pulses can be varied. In contrast, in the continuous pump - continuous probe mode the laser pulses accumulate and the burst mode of the detector is used. The burst mode reduces the 24-bit mode to a 12-bit read out mode and allows continuous data acquisition with simultaneous reading and writing. Thus, the acquired data is taken in real time without any dead time between the single images. The images can be recorded with a frequency of up to 1 kHz. Since data is acquired with a minimum recording time of 1 ms multiple laser pulses hit the surface of the sample and the accumulated heating or electronic effect is investigated.

Acquisition of X-ray fluorescence near total reflection data

For the XRFNTR measurements the liquid cell described in section 4.3 was used together with a fluorescence detector as shown in Fig. 4.7. The fluorescence data was recorded with the XR100 FAST-SDD Amptek detector under X-ray incident angles

between 0.016 to 0.13° probing a sample volume from 5 nm to 21 µm (see Fig. 2.11). The intensity of the elastic peak at 18 keV was used as reference to normalise the spectra to each other at different incident angles. Further, the energy channels were calibrated by fitting the Ar and elastic peak from a reference data set, which was taken without any sample and only contains scattering from the atoms in the air atmosphere. The measured fluorescence peaks were assigned to the K- and L-shell emission lines by comparison with literature values [190]. Each scan consist of a series of collected spectra at different incident angles. The scans were performed before, during and after laser irradiation to investigate the change in ion concentration at the surface induced by the laser irradiation. The analysis routine of the collected data is described in section 4.6.4.

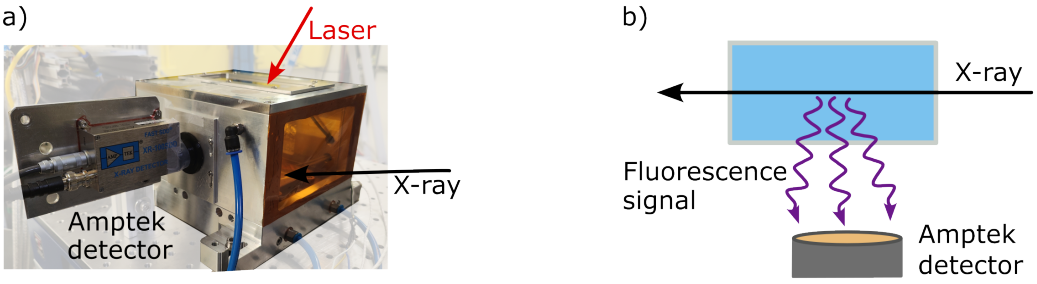

Figure 4.7: a) Photography of the fluorescence detector attached to the liquid cell at the sample stage of the LISA endstation at P08, PETRA III and b) schematic drawing of the setup with a top view.

4.5.2 ID 10, ESRF

The European Synchrotron Radiation Facility (ESRF) is a joint research facility in France and a 4th generation synchrotron radiation source. At the soft interface and coherent scattering beamline ID10 [191] the double-crystal deflector is coupled to a 6 + 2 axes diffractometer to perform high-resolution XRR and GID measurements on liquid and solid interfaces. The X-ray energy can be tuned between 7 kV and 30 kV. For the beamtime SC-5497 in September 2023, an energy of 22.5 keV and a beam size of 20 µm × 20 µm was chosen. As sample cell, the Langmuir trough setup of the beamline was used. Our custom made LED illumination device was integrated into the beamline system to allow time-resolved XRR and GID measurements. The raw data is available under [192]. At the beginning of the beamtime, multiple XRR measurements were taken to reduce beam damage on the sample. Based on this initial tests, the exposure times, absorber values and necessary movement on the sample were defined. All following XRR and GID measurement were performed on

fresh sample spots. The Langmuir trough was flushed with wet helium to reduce the oxygen level to below 2 %. For the XRR measurement, the auto attenuator available at the beamline was used. This changes the attenuator value during the XRR to keep the intensity of the reflected beam between 5000 and 60000 counts. The XRR curves were taken up to a wavevector $q_z = 1.0\,\text{Å}^{-1}$. As detectors, the Maxipix 1x5 developed by ESRF and mythen2 detector from Dectris (Baden-Daettwil Switzerland) were used for the XRR and GID measurements. The extraction of the reflectivity curve follows the procedure described in detail above for the XRR measurements at the LISA instrument. For the analysis of the reflectivity data, the Python package `refnx` was used as discussed in Sec. 4.6.1.

4.5.3 BL16 SOFIA, J-PARC

The research reactor at Japan Proton Accelerator Research Complex (J-PARC) is a proton accelerator which creates neutrons, neutrinos and hadrons to perform research in the field of materials, life science and particle and nuclear physics. The beamline BL16 Soft Interface Analyzer (SOFIA) [193, 194] offers a horizontal type reflectometer to investigate soft matter samples such as lipid monolayers at the water-air interface. NR measurements were performed in June 2023 using the Langmuir trough available at the beamline. This Langmuir trough is a Japanese fabrication and has a trough area of 80 mm × 255.87 mm and total volume of 100 mL. The surface tension is measured utilising a filter paper Wilhelmy plate. The 2-dimensional scintillation counter detector was placed 17.9 m from the sample. Data was collected under the three incident angles θ of 0.4°, 1.0° and 2.22°. The slit size was changed accordingly to the angle between 0.3226 mm and 8.0 mm. This results in an angle dependent q-resolution of 1.3 %, 5.1 % and 3.0 % for the different angles. For the data binning during extraction, a constant resolution of $\mathrm{d}q/q = 2\,\%$ was chosen. As samples, three contrasts were chosen. The contrast of D_2O and tail-deuterated DPPC lipids was chosen to match the SLD of the deuterated tail group with the water sub phase and to highlight the head group of the lipids. Further NR data was taken from hydrogenous DPPC on D_2O to feature the whole molecule. The third contrast was tail-deuterated DPPC on non-reflective water (NRW) which was mixed from D_2O and H_2O directly before the measurement. The same contrasts were applied for the mixed monolayer with 10 % of AZGL-C16. The photoswitchable lipid was not deuterated.

Each NR curve was reconstructed by stitching the parts measured at the three incident angles together with a package extension for the IGOR Pro software provided by the beamline team. Analysis of the reflectivity curves was done with the Python based analysis package `refnx` [195] and is described in more detail in Sec. 4.6.1.

4.5.4 BL2, DELTA

SAXS measurements were performed at the beamline BL2 [196] of the 3rd synchrotron source Dortmund Electron Accelerator (DELTA). This storage ring is operated by members of the TU Dortmund University and offers 12 endstations for in-house and external user research. Two beamtimes, in March and December 2022, were conducted at BL2 which is a beamline dedicated to SAXS measurements and operates at an energy of 12 keV. The data was collected with the MAR345 2D image plate detector (marXperts, Norderstedt, Germany) and by utilising a beam size of 0.6 mm×0.6 mm. The samples were filled into quartz capillaries and placed into a simple capillary sample holder for *in situ* measurements at room temperature or in the temperature-controlled cell from Linkam Scientific Instruments Ltd for temperature dependent scans at temperatures between 17 °C and 55 °C.

For the *in situ* measurements, the LED illumination device was placed above the capillary holder at a distance of 10 cm. The samples were illuminated for 5 min with either 365 nm or 455 nm before collecting the scattering signal. The acquisition time was 80 s for each detector image. No beam-induced sample degradation could be observed for this long exposure time. The collected detector images were processed with the software *FIT2D* [197–200] and transformed from real to reciprocal space. After the application of pixel mask and correction of the detector orientation, the intensity was integrated azimuthally to receive the reduced 1D scattering pattern in q-space. The typical q-range is 0.25 nm^{-1} to 3 nm^{-1}. The calibration of the detector distance and orientation was done with a standard silver behenate powder sample. The analysis of the extracted 1D scattering pattern is described in section 4.6.3 in detail.

4.5.5 P12, EMBL

For time-resolved SAXS measurements, one beamtime was performed at beamline P12 at PETRA III operated by the European Molecular Biology Laboratory (EMBL). This beamline is optimised for the structure analysis of biological samples and offers an automatic sample change system. The samples are filled in tubes and placed into the auto sampler. The capillary is then filled automatically with about 50 µL of the sample, the scattering data is collected and afterwards the capillary is flushed with detergent and water. During the beamtime in November 2023, the data was collected with the PILATUS 6M detector from Dectris (Baden-Daettwil, Switzerland) at an energy of 10 keV and with a beam size of 0.2 mm×0.12 mm. Due to the high brilliance of the PETRA III source, the exposure time could be reduced to 0.1 s at a transmission of 80 %. This setting reduced the beam damage significantly and up

to 4 frames with an exposure time of 0.1 s each could be collected before sample degradation was observed. At the beamline an automated data processing pipeline is available that reduces the 2D detector images to 1D scattering patterns and automatically performs background correction with the collected puffer scattering pattern. The saved 1D data was analysed using self-written Python scripts. The analysis process is described in detail in section 4.6.3.

The fast data exposure time allowed time-resolved measurements to record the kinetics of the mesophase transitions observed in mixed lyotropic liquid crystals containing photoswitchable amphiphiles (see Sec. 6.6). To realise the *in situ* illumination, the LEDs were placed on top of the quartz window facing the sample capillary. As only the volume inside the capillary could be illuminated, the measurements were performed in no-flow mode to prevent measuring non-illuminated sample volume. The automatic sample loading was stopped and the capillary was loaded manually before starting the illumination with either 365 nm or 455 nm. After a defined illumination time, the data was collected. Then the sample was replaced by fresh volume from the sample holder. The loading and illumination process was repeated with different illumination times to follow the temporal evolution. During the illumination time, the fast shutter was kept closed to avoid beam damage.

4.6 Data availability and analysis

The data analysis, storage and handling was performed following the FAIR principles [186] and metadata standards proposed by DAPHNE4NFDI [188, 187]. All publicised data is available under CC-BY 4.0 licence under open access in data repositories hosted by Kiel University. The corresponding links to the raw, extracted and fit data and the analysis scripts can be found in the respective publications under the data availability section. Further, all samples were registered with an International Generic Sample Number (IGSN) in the sample data bank from the international consortium DataCite using the IGSN service provided at Kiel University (`https://igsn.uni-kiel.de/de`). Furthermore, all analysis scripts used in this thesis are made publicly available [184]. In the following sections the analysis procedures for the XRR, NR, GID, SAXS and XRFNTR data are described in more detail.

4.6.1 X-ray and neutron reflectivity

The reflectivity data, both X-ray and neutron, were fitted using the Python package `refnx` [195] based on the Parratt formalism [144]. The structure of the sample is described with a model consisting of slabs of uniform SLDs. Each slap is defined by

Table 4.1: X-ray and neutron scattering lengths calculated for the DPPC, AZOL-C16, AZGL-C16 and AZLL-C16 mimetics in Å.

molecule		X-ray	neutron
DPPC	$C_{40}H_{80}NO_8P$	0.011441	0.000275
d_{62}-DPPC	$C_{40}H_{18}NO_8PD_{62}$		0.006730
AZOL-C16	$C_{56}H_{91}N_5O_9$	0.015056	0.001308
AZGL-C16	$C_{62}H_{101}N_5O_{14}$	0.017482	0.001623
AZGL-C16*	$C_{62}H_{90}N_5O_{14}D_{11}$		0.002456
AZLL-C16	$C_{68}H_{111}N_5O_{19}$	0.019907	0.001938

three properties, its thickness l, SLD and the roughness σ at the interface to the next slab. For a pure water solution, the model consist of two slabs, one for the water and one for the air. Both layers have infinite thickness and only the SLD of the water slab and its roughness to the air interface is fitted. Meanwhile the structure of a lipid monolayer at the water-air interface is described with two additional layers, one for the hydrophilic head and one for the hydrophobic tail group. The head layer possesses as additional parameter a solvent factor, to account for water molecules surrounding the lipid head groups. The parameter space was narrowed down by setting boundaries based on physical properties such as the maximum extent the layer can physically obtain or the SLD values. In addition to the boundaries, the parameters can be constrained to other parameters or conditions. For example, the the SLD and thickness of the head and tail layers have to result in the same number of lipids inside the layer. This condition can be parametrised by calculating the scattering lengths for the whole molecule. The scattering lengths b of a molecule were derived with Eq. 2.18 and are listed in Tab. 4.1. Further, the scattering lengths b_{total} of the mixed monolayer is then calculated by the relative amount of each molecule. In the fit procedure, the ratio a of the azobenzene mimetics is fitted as a parameter. Thus, b_{total} is derived with

$$b_{\text{total}} = a \cdot b_{\text{azo}} + (1 - a) \cdot b_{\text{dppc}} \tag{4.1}$$

where b_{azo} and b_{dppc} are calculated based on the chemical composition of the molecules. Moreover, the SLD of the head group is constraint to the function

$$\texttt{SLD}_{\text{head}} = \left(\frac{b_{\text{total}}}{A_{mol}} - \texttt{SLD}_{\text{tail}} \cdot l_{\text{tail}} \right) / l_{\text{head}} \tag{4.2}$$

with the fitted parameters l_{head}, l_{tail}, $\texttt{SLD}_{\text{tail}}$ and A_{mol}.

The fitting with `refnx` was performed using a Markov Chain Monte Carlo (MCMC) approach with 200 walkers. Each walker represents an independent Markov chain

initialised with random starting points. After the first 1000 steps, the chains converged towards the target distribution and 2000 additional samples per walker were collected to estimate the posterior distributions of the model parameters.

4.6.2 Grazing incidence diffraction

The 2D detector images collected during the GID measurements are analysed with self-written Python scripts. As a first step, the 2D image is transformed into the reciprocal space by assigning each pixel the corresponding reciprocal space values q_{xy} and q_z. These values are calculated by first determining the distance from the primary beam ($q_{xy} = 0$ and $q_z = 0$) in real space and then transforming these distances into the reciprocal space. This transformation is done with a script available in the group. The following analysis steps are performed with scripts written by myself.

By analysing the GID images, structural information on the packing and orientation of the molecule in the in-plane direction and the tilt angle of the acyl chains together can be determined. These parameters are calculated based on the position and width of the Bragg peaks and the intensity distribution along the Bragg rod. For this, the intensity profiles are fitted with Gaussian curves. To reduce the influence of background scattering, a reference measurement of a pure water/solvent interface is subtracted from the 2D image from the sample. Further, all images are smoothened by interpolating an area of 3×3 pixel. The background corrected images are then integrated along the q_{xy} or q_z direction as shown exemplarily in Fig. 4.8 for GID images from a DPPC monolayer measured at the LISA endstation at P08, PETRA III.

For a precise determination of the peak positions, the range for the integration is limited to a region around the peak, preferably with no other peak inside that region. From the number, position and widths of the Bragg peaks and rods the structural information can be derived. First, the Bragg peaks and Bragg rods are assigned using the Miller indices. In the case of this dataset, the peaks belong to the (0,1), (1,0) and (1,$\overline{1}$) reflections. The superimposition of the (1,0) and (0,1) peak is evidence for a distorted hexagonal lattice structure of the acyl chains with the lattice length $a = b$ (see Sec. 2.3.3). Each peak is fitted with a Gaussian curve in the q_{xy} and q_z direction. The fitted positions and widths of the Bragg peak and rod are listed in table Tab. 4.2.

The lattice parameters a and b and angle γ can be calculated from the fitted q_{xy} values using Eq. 2.21 to

$$a = b = 5.358\,\text{Å}$$
$$\gamma = 116.6^\circ$$

Table 4.2: GIXD results of DPPC monolayer shown in Fig. 4.8 with the Bragg peak and Bragg rod positions and the respective FWHM.

	$q_{xy,(0,1),(1,0)}$/ (Å^{-1})	$q_{z,(0,1),(1,0)}$/ (Å^{-1})	$q_{xy,(1,-1)}$/ (Å^{-1})	$q_{z,(1,-1)}$/ (Å^{-1})
position	1.312 ± 0.008	0.744 ± 0.008	1.463 ± 0.008	0.020 ± 0.008
width	0.078 ± 0.004	0.392 ± 0.004	0.023 ± 0.004	0.602 ± 0.004

and the tilt angle τ of the tail group and thickness D of the crystalline layer using Eq. 2.22 to

$$\tau = 29.6^\circ$$
$$D = 22.14\,\text{Å}.$$

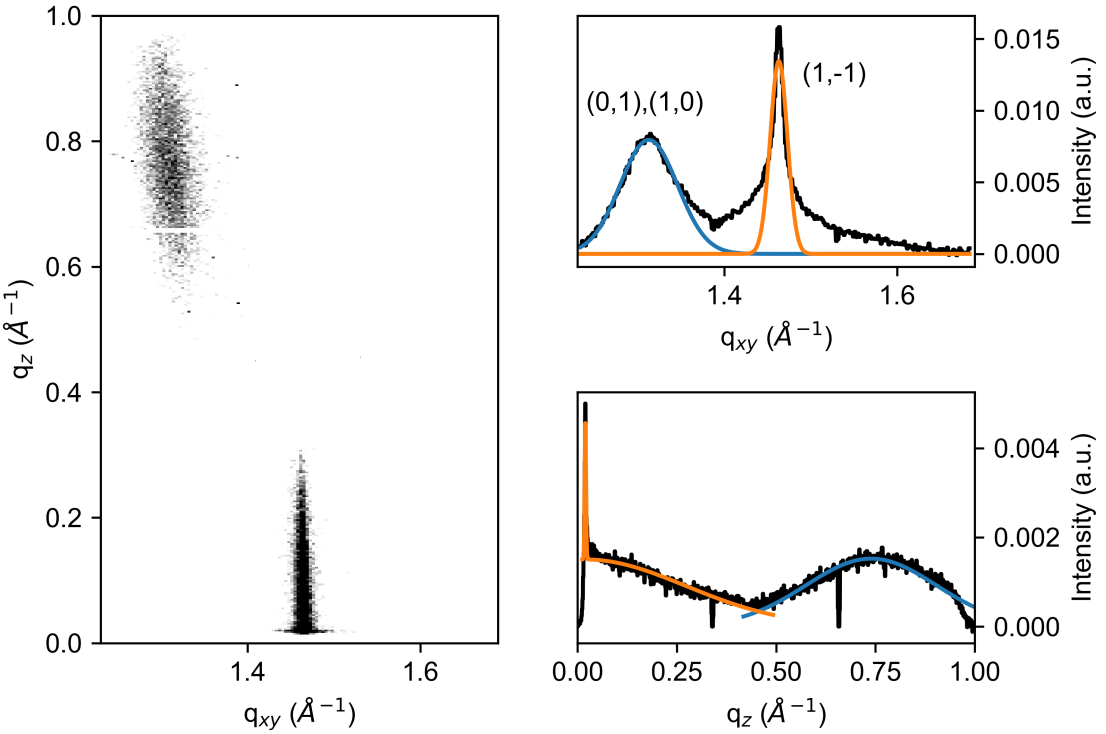

Figure 4.8: GID images of a pure DPPC monolayer at the water-air interface with a surface pressure of 18 mN m^{-1} and the integrated intensity spectra along the q_{xy} and q_z direction with the fits of the Bragg peaks and Bragg rod.

4.6.3 Small angle X-ray scattering

The reduced 1D scattering pattern are analysed with self-written Python scripts to determine the structure and repeating distance (d-spacing) of the lipid aggregates. The fit routine is a step-wise process. As first steps, models of possible structures are generated with multiple Gaussian-functions

$$f(q) = \sum_{\mathrm{i}}^{\mathrm{n}} a_{\mathrm{i}} e^{-\frac{(q-p_{\mathrm{i}})^2}{2\sigma_{\mathrm{i}}^2}} \tag{4.3}$$

with variable peak amplitude a_{i}, width σ_{i} and position p_{i}. For each mesophase, the theoretical positions of the peaks [201] can be calculated from the d-spacing value as exemplarily shown in Fig. 4.9 for a d-spacing value of 6 nm. These models are first compared visually and then fitted to the measured data to find the best match. After identifying the matching structure, the model is fitted to the data again, allowing small deviations δ_{i} of the peak position to consider small defects and distortions in

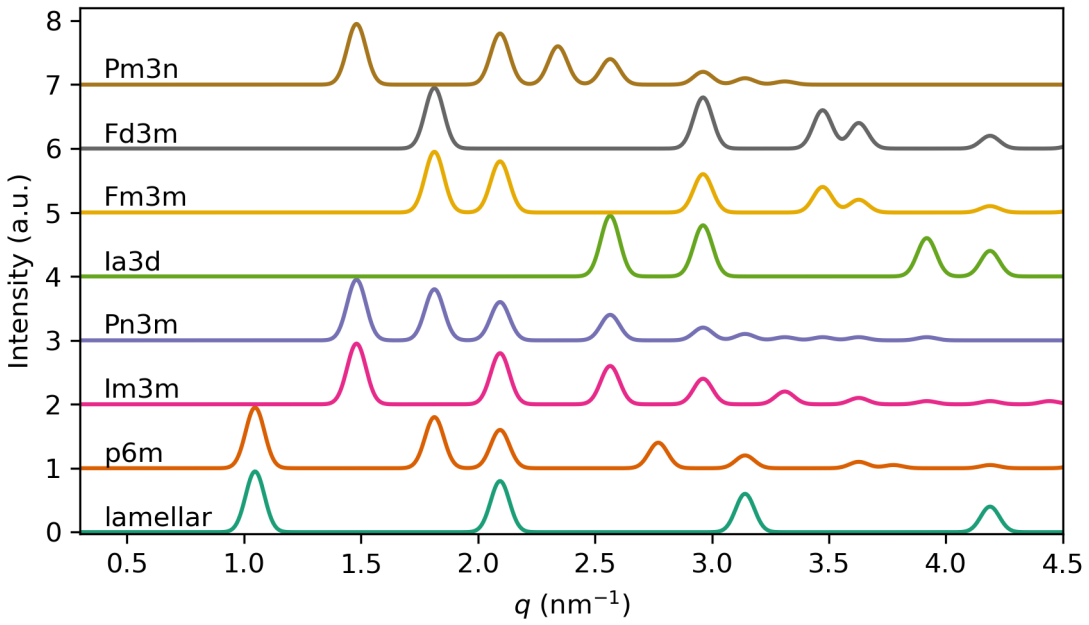

Figure 4.9: Computed scattering models for different lipid mesophases with the same d-spacing value of 6 nm and decreasing peak intensities for the higher order peaks. The models are composed by a series of Gaussian peaks as described in Eq. 4.3.

the sample structure. Thus, the model function is extended to

$$f(q) = \sum_{\mathrm{i}}^{\mathrm{n}} a_{\mathrm{i}} e^{-\frac{(q-(p_{\mathrm{i}}+\delta_{\mathrm{i}}))^2}{2\sigma_{\mathrm{i}}^2}} \tag{4.4}$$

with a maximum allowed deviation of $\pm 0.06\,\mathrm{nm}$ during the fitting. Following this fitting step, the d-spacing value is recalculated for each position $p_{\mathrm{i}} + \delta_{\mathrm{i}}$ and averaged. The error for d-spacing is determined from the deviations between the recalculated values.

This fit routine is extended for scattering data, for which a single mesophase cannot describe the observed structure. In those cases a superposition of two or more models is used to fit the data. The steps described above are performed for all combinations of two (or three) of the eight models. The resulting best matching models are evaluated on the quality of the fit and the physical possibility.

4.6.4 X-ray fluorescence near total reflection

The collected XRFNTR scans consist of a series of images at incident angles α between 0.016 to 0.13° around the critical angle α_c taken following the measurement description in section 4.5.1. Each image contains the energy resolved intensity spectrum of the fluorescence signal as shown exemplarily in Fig. 4.10. The detected fluorescence peaks can be assigned to the specific energy level transitions of chemical elements. An exemplary classification of the detected emission lines from an aqueous 4 M NaI solution is shown in Fig. 4.10. The fluorescence peaks at energies between 3.7 to 4.9 keV originate from the L_α, $L_{\beta,1}$, $L_{\beta,2}$ and L_γ emission lines of the iodide ions (I^-) in the solution. The four peaks with much lower intensity at energies between 2 to 3.7 keV are the escape peaks of the I^- L-emission lines. These escape peaks occur when the emitted photon (e.g. belonging to the L_α transition) hits the silicon (Si) chip of the fluorescence detector and loses energy by exciting an Si atom. This loss in energy corresponds to the $K_\alpha = 1.74\,\mathrm{keV}$ transition of Si. Thus, the energy of the detected photon is 1.74 keV lower than originally. Whereas the I^- emission peaks could be identified, the peak at 5 keV could not be assigned. It could originate from multi-photon counting, which means that the detector counts two arriving photons as one and adds their energy. In addition to the I^- emission peaks, copper (Cu), nickel (Ni) and zinc (Zn) peaks are observed. Their presence indicate that partial scattering from the sample cell occurs. The peaks at highest energy, arise from the elastic scattering peak at 18 keV and at slightly lower energy the inelastic Compton scattering. Though the I^- atoms in the solution could be detected, no peaks belonging to the Na^+ ions are found. This indicates that the Na^+ ions, in contrast to the I^- ions, are not present at the surface.

Next step in the analysis is the fitting of the L emission peaks of the I^-. The peaks are fitted with a series of Gaussians functions. As the peaks are slightly overlapping, all peaks in the range of 3.7 to 4.9 keV are fitted simultaneously with one fit function containing five Gaussian curves. Following this fit, the fit values for the intensity of the L_α peak are plotted against the incident angle and analysed further. The shape of this intensity profile allows conclusions on the structure of the interfacial region of the surface (see Sec. 2.3.5). The critical angle is determined by fitting the intensity profile with Eq. 2.26. From this the critical angle α_c is directly derived and the electron density SLD is calculated with $\mathtt{SLD} = q_c^2/16\pi = \sin(\alpha_c)^2 \cdot \pi/\lambda$ using the X-ray wavelength λ.

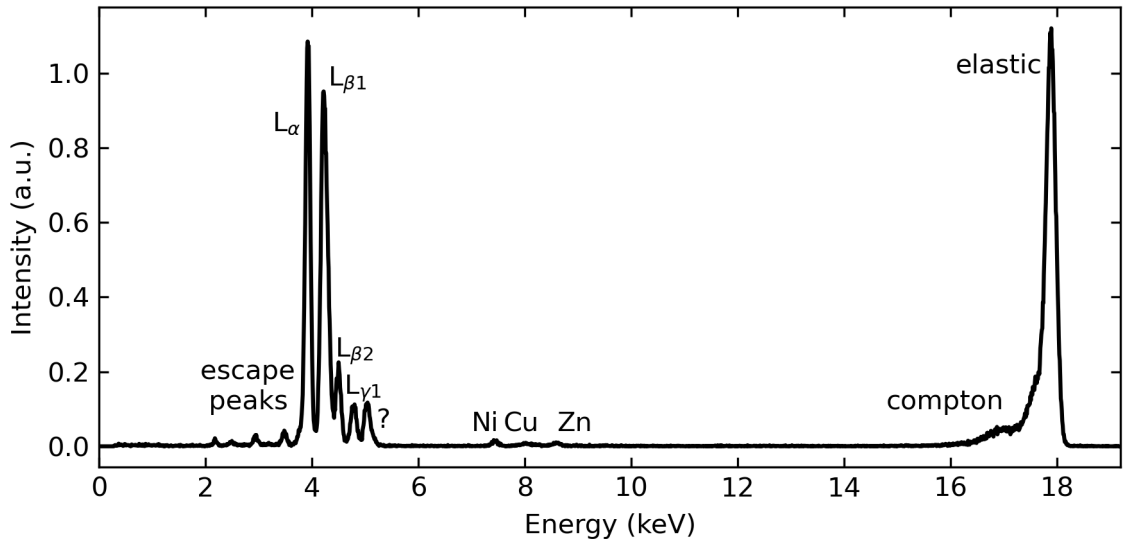

Figure 4.10: Fluorescence spectra collected under grazing X-ray incidence angle of $\alpha = 0.06°$ from a 4 M NaI solution with an X-ray energy of 18 keV and the assigned fluorescence peaks. The L_α, $L_{\beta,1}$, $L_{\beta,2}$ and $L_{\gamma,1}$ and escape peaks originate from the I^- ions in the solution.

5

Controlling the orientation and morphology of glycolipids in lipids monolayers with light

Glycolipids play a fundamental role in lipid membranes and are responsible for cell signalling and attachment of proteins, bacteria and other cells. Studies on proteins and bacteria attaching to glycolipids discovered a selectivity on the type and orientation of the carbohydrate group. Therefore, identifying and controlling the orientation of the carbohydrate group has high potential to influence the protein and bacteria activity. In the study presented in the following section, synthetic photoswitchable glycolipids are incorporated into Langmuir monolayers to characterise their influence on the monolayer structure and to identify the orientation of the glycan head group. Further, the structural changes upon switching the photoswitchable glycolipid between its *trans* and *cis* isomer are investigated with Langmuir isotherm, grazing incidence diffraction (GID) and X-ray reflectivity (XRR) measurements. The results are presented in the manuscript [MSH 3] in Sec. 5.1. In addition to the manuscript, a summary of collaborative and complementary measurements and their results related to the Langmuir monolayer studies on mixed monolayers composed of photoswitchable glycolipids and phospholipids is given in Sec. 5.2.

5.1 Light-induced reorientation of the sugar head group of photoswitchable glycolipids in phospholipid monolayers

The following manuscript discusses the Langmuir isotherm, XRR, NR and GID results on photoinduced structural changes and reorientation of carbohydrate groups in Langmuir monolayers containing azobenzene amphiphiles. The data of mixed monolayers with on of three different azobenzene amphiphiles are compared to conclude on the influence of the type of carbohydrate group attached to the head group. The XRR and GID measurements were performed at the LISA endstation at P08, PETRA III, (see Sec. 4.3) and the complementary NR data was taken at the BL16 beamline at J-PARC (see Sec. 4.5.3). Compared to the nomenclature in this thesis, the azobenzene mimetics AZOL-C16, AZGL-C16 and AZLL-C16 are referred to as **1**, **2** and **3**, respectively, in the following article (compare Fig. 3.1 with Fig. 1 in the article).

Light-induced reorientation of the sugar head group of photoswitchable glycolipids in phospholipid monolayers

Svenja C. Hövelmann[1,2], Jonas E. Warias[1], Jule Kuhn[1], Karin Hansen[1], Lukas Petersdorf[1,2], Nicolas Hayen[1,2], Andrea Sartori[1,†], Philipp Jordt[1,2], Rajendra P. Giri[1,‡], Franziska Reise[3], Norifumi L. Yamada[4], Adrian R. Rennie[5], Thomas Arnold[6], Thisbe K. Lindhorst[3], and Bridget M. Murphy[1,2]

[1]**Institute of Experimental and Applied Physics, Kiel University, Leibnizstraße 19, 24118 Kiel, Germany**
[2]**Ruprecht Haensel Laboratory, Deutsches Elektronen-Synchrotron (DESY), Notkestraße 85, 22607 Hamburg, Germany**
[3]**Otto Diels Institute of Organic Chemistry, Kiel University, Otto-Hahn-Platz 3-4, 24118 Kiel, Germany**
[4]**Institute of Materials Structure Science, High Energy Accelerator Research Organization, Tsukuba, Ibaraki 305-0801, Japan**
[5]**Centre for Neutron Scattering & Macromolecular Chemistry, Department of Chemistry Angström, Uppsala University, Box 538, 75121 Uppsala, Sweden**
[6]**European Spallation Source ERIC, BOX 176, SE-221 00 Lund, Sweden**
[†]**ALBA SYNCHROTRON LIGHT SOURCE, Carrer de la Llum 2-26, 08290, Cerdanyola del Vallès, Barcelona, Spain**
[‡]**Department of Physics, Indian Institute of Technology (ISM) Dhanbad, Jharkhand 826004, India**

ABSTRACT

Glycolipids play a fundamental role in cell membrane structure and for cell signalling and attachment of proteins, bacteria and other cells. Studies on proteins and bacteria attaching to glycolipids discovered a selectivity on the type and orientation of the carbohydrate group. In this study artificial photoswitchable glycolipids with no sugar, a glucose or lactose group are incorporated into Langmuir monolayers. Their response to optical stimuli is investigated to characterise their influence on the monolayer structure and to identify the orientation of the glycan head group. X-ray and neutron scattering measurements combined with *in situ* Langmuir isotherms confirm the location of the head group in the water and reveal that the photoswitching of the glycolipids induce a reorientation of the head group of the glycolipids and affects the head group ordering. Significant structural changes are observed in the thickness and the roughness of the monolayer. An additional phase transition for both *trans* and *cis* isomers and bidirectional surface pressure change is seen in the Langmuir isotherms.

Keywords: Photoswitching, X-ray and neutron scattering, Glycolipids

INTRODUCTION

Cell membranes consist of a variety of lipids, proteins, nucleic acids and sugars and the composition of these components defines the physical properties of the membrane such as its rigidity, fluidity and functionality [1; 2; 3]. Membrane components are responsible for vital physical and chemical processes at the membrane interface and across the membrane such as glycolipids for cell signalling [4; 5] and attachment of proteins and other cells [6; 7]. Glycolipids have a carbohydrate group in the head group allowing selective attachment of proteins and cells [8; 9]. Not only the type of carbohydrate group, but also its orientation is key for successful binding of the proteins or cells to the glycolipid. Changes in the orientation of the glycan head can result in detachment of proteins [10; 11] and bacteria [12] from the glycolipid, potentially resulting in deactivation. Controlling the spatial orientation of the glycoligands by means of photoswitchable glycoconjugates [13; 14] for turning bacterial and protein adhesion on and off [15; 16] has received increasing interest. Photoswitches such as the azobenzene

group in azobenzene mimetics [17; 18; 19] with their reversible E/Z isomerisation show high reproducibility and stability. In addition to the focus on controlling bacterial and protein adhesion, many recent studies on membranes containing synthetic azobenzene amphiphiles concentrate on light induced structural changes in the membrane thickness [20; 21; 22; 23] and rheology of vesicles [24]. Also the functionalisation of proteins [25; 17; 26], nanoparticles[27] and surfaces [28] has been shown.

To induce both structural changes of the lipid monolayer morphology and the orientation of the carbohydrate group at the water-air interface the artificial photoswitchable glycolipids **1** (no sugar), **2** (glucose) and **3** (lactose) (see Fig. 1) are embedded in Langmuir monolayers. The photoswitchable glycolipids contain an azobenzene switch between the carbohydrate head groups and the acyl chain tail group. These azobenzene mimetics can be switched between their *trans* and *cis* isomer with visible (455 nm) and UV (365 nm) light as schematically shown in Fig. 1. As model membranes, Langmuir monolayers containing one of the three azobenzene mimetics **1**, **2** and **3** and the phospholipid 1,2-Dipalmitoyl-*sn*-glycero-3-phosphocholine (DPPC) in a ratio of 1:9 are investigated. Complementary *in situ* grazing incidence diffraction (GID) [29; 30], X-ray reflectivity (XRR) [31; 32] and neutron reflectivity (NR) [33; 34] measurements were performed to determine the monolayer thickness, electron density, roughness and tilt angle of the head and tail groups[35; 36]. Combining these measurements with Langmuir isotherm[37] investigations allows to study the structure in the liquid expanded and liquid condensed phase of the monolayer. Further, the switching behaviour is analysed with time-resolved surface pressure measurements during illumination with visible and UV light to capture the kinetics of the structural changes. Understanding and controlling the orientation of the carbohydrate group at lipid monolayers interfaces has the potential to design bespoke model systems to induce structural changes in the monolayer and to (de-)activate protein and bacteria attachment with light.

METHODS AND MATERIALS

Material

The phospholipids DPPC and 1,2-Dipalmitoyl-d62-*sn*-glycero-3-phosphocholine (d_{62}DPPC) were purchased from Avanti Polar lipids (Alabaster, AL) with each a purity of $> 99\,\%$ and the photoswitchable mimetics **1**, **2** and **3**, synthesised based on the published protocol [38] and provided by the group of Prof. Dr. Thisbe K. Lindhorst, University Kiel, were dissolved in chloroform ($> 99\,\%$ purity and ethanol as stabilser burchased from Sigma-Aldrich) with a concentration of 1 mM. For the compression isotherms, XRR and NR studies, compositions with a mol/mol concentration ratio of 90:10 DPPC:azobenzene mimetic were prepared.

Isomerisation

The azobenzene mimetics were photoswitched between their *cis* and *trans* isomers with an illumination device consisting of LEDs with an wavelength of 365 nm (Nichia, NCSU033B(T)) and 455 nm (Osram, LD CQ7P), respectively. The illumination device was placed on the quartz glass window of the Langmuir trough and at the monolayer position fluencies of $1.1\,\mathrm{mW\,cm^{-2}}$ and $1.0\,\mathrm{mW\,cm^{-2}}$ for both wavelengths during the X-ray scattering measurements and neutron reflectivity measurements, respectively.

Langmuir isotherms and time resolved surface pressure measurements

The Langmuir isotherms collected during the X-ray scattering measurements, a temperature controlled Riegler & Koch Langmuir trough (Potsdam, Germany) was used to collect Langmuir compression isotherms at 21 °C. The isotherms from the pure DPPC and mixed monolayers with the mimetics **1** and **2** were measured with a compression rate of $22.8(5)\,\mathrm{cm^2\,min^{-1}}$ and the mixed monolayer with the mimetic **3** with a compression rate of $31.8(5)\,\mathrm{cm^2\,min^{-1}}$. The lipid solutions were spread on the water surface with a gas-tight microsyringe (Hamilton). The surface pressure was measured by a film balance with a filter paper as Wilhelmy plate. For the time-resolved surface pressure measurements, the monolayer was compressed to the desired surface pressure with a compression rate of $10.2(5)\,\mathrm{cm^2\,min^{-1}}$ and the area was kept constant while illuminating the monolayer alternating with 365 nm and 455 nm for each 5 min while recording the surface pressure change.

X-ray reflectivity and grazing incidence X-ray diffraction

The X-ray measurements were performed at the Liquid Interface Scattering Apparatus (LISA) [39] at P08 [40] of PETRA III at DESY at a photon energy of 18 keV and with a beam size of $100\,\mu\mathrm{m} \times 400\,\mu\mathrm{m}$ (vertical $\times$ horizontal). A Lambda GaAs 750 k detector (X-Spectrum, Hamburg Germany) with a pixel size of $55\,\mu\mathrm{m} \times 55\,\mu\mathrm{m}$

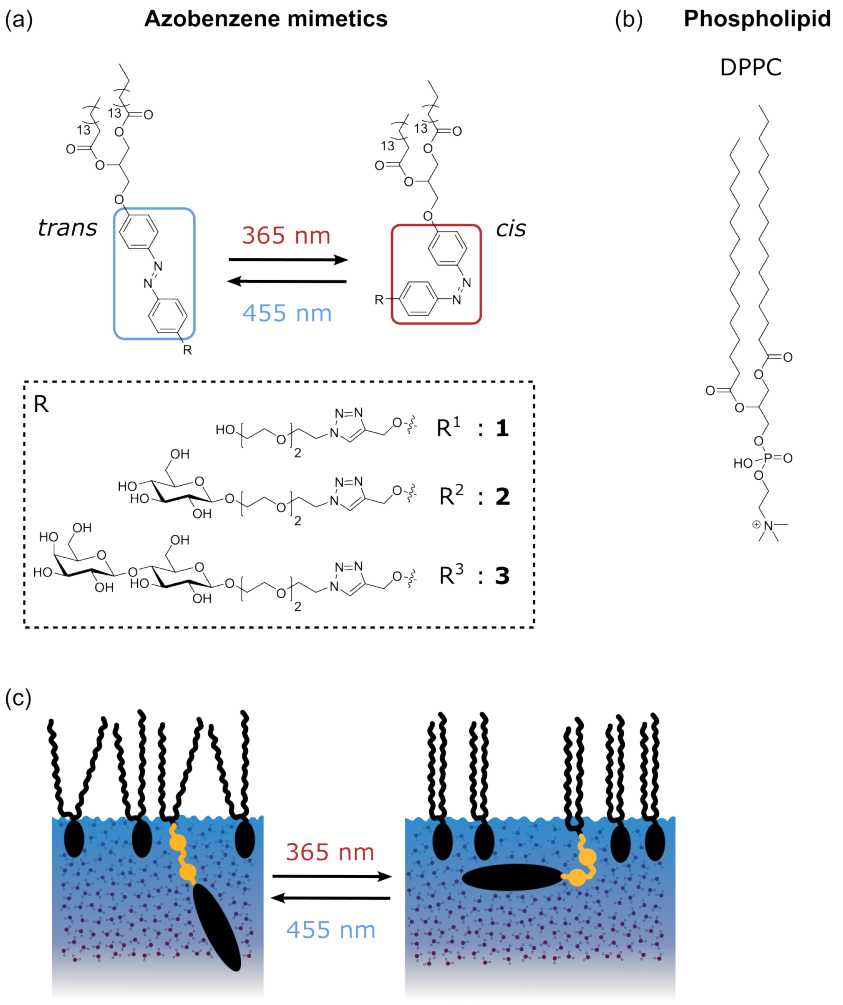

Figure 1. Chemical structure of (a) both the *trans* (blue) and *cis* (red) isomers of the azobenzene amphiphiles **1**-**3** [38] and (b) DPPC. In (c) the model of the photoswitching affecting the monolayer is shown.

was placed at a distance of 1.113 m from the sample to record 2D images. At the beginning of each beamtime beam damage test were performed to ensure high data quality and reproducibility of the XRR and GID data. Beam damage tests included collecting XRR and GID data while modifying the absorber values to reduce the flux of the X-ray beam and counting times until two consecutive measured XRR and GID curves. The box surrounding the Langmuir trough was flushed with helium to reduce the background scattering and oxygen induced radiation damage. Further, after each XRR and GID measurement the sample position was changed by a transverse increment to allow measuring from a fresh sample spots. For the extraction of the XRR the intensity, a region of interest of 30×30 pixels was chosen to integrate the specular intensity resulting in a angular resolution in q_z direction of 0.085°. Background was reduced by subtracting the average background intensity calculated from two regions next to the region of the specular intensity in q_{xy} direction.

Together with the XRR measurements, GID data were collected from the monolayers at a grazing incidence angle of 0.058° and a slit with a gap size of 0.5 mm was placed 0.550 m from the sample. For background correction, GID images from the pure solvent were taken.

Neutron reflectivity

The NR data were collected at beamline BL16 [41; 42] at the Japan Proton Accelerator Research Complex (J-PARC) MLF neutron facility and three incident angles 0.4°, 1.0° and 2.22°. The q-resolution of increasing incident angle was 1.3 %, 5.1 % and 3.0 %. Data were measured for monolayers composed of combinations of the azobenzene mimetic **2** with either hydrogenous DPPC or tail-deuterated d_{62}DPPC on D_2O to highlight the whole molecule or the head group of the molecule, respectively. The third contrast was tail-deuterated d_{62}DPPC and mimetic **2** on non-reflective water (NRW). The NRW was prepared by mixing D_2O and H_2O directly before the measurement. The mimetic **2** was not deuterated. The data were extracted with a constant resolution $dq/q = 2\,\%$ and the reflectivity curve was reconstructed with a package extension for the IGOR Pro software provided by the beamline team.

Reflectometry fitting

The extracted X-ray and neutron reflectivity data were fitted with the Python package `refnx` [43] based on the Parratt formalism [44]. The monolayer was described with a two-slab model parametrised with the slab thickness, scattering length density `SLD` and roughness σ at the interface between the slabs. Another parameter for the head layer was the solvent volume fraction to allow for the water molecules surrounding the heads of the lipids. The scattering lengths of the head and tail regions were calculated from the fitted `SLD` values, layer thickness and area per molecule and compared to the total scattering lengths of the molecules for the different compositions. The areas per molecule were taken from the Langmuir isotherm measurements.

Grazing incidence X-ray diffraction analysis

The 2D detector images were transformed into reciprocal space by assigning each pixel q_{xy} and q_{z} values. For the analysis of the position and width of the Bragg peaks, intensity profiles of the peaks along the two scattering directions q_{xy} and q_{z} were determined by integration over of the directions in a defined region around the respective peaks. The regions were chosen for each peak to enclose the whole peak but to exclude any scattering from other peaks. The derived 1D curves were fitted with a Gaussian function to determine the peak position and width of the Bragg peaks. Further, the intensity distribution along the Bragg rods was analysed. From the q_{xy} and q_z position of the Bragg peaks, the lengths of the lattice vectors $\vec{a}$ and $\vec{b}$, the tilt angle τ of the acyl chains of the tail groups and the area occupied by the chains were calculated [33].

RESULTS AND DISCUSSION

Langmuir isotherm studies on the switching kinetics

The light induced switching behaviour in mixed monolayers is characterised with Langmuir isotherm and time resolved surface pressure measurements. In Fig. 2a, the compression isotherms of the three mixed 9:1 DPPC:**1** (no sugar), DPPC:**2** (glucose) and DPPC:**3** (lactose) monolayers are plotted together with the pure DPPC isotherm. The isotherm of the pure DPPC monolayer presents the typical and expected liquid-expanded (LE) and liquid-condensed (LC) phase transitions together with the LE-LC coexistence phase [45; 46; 37]. Meanwhile for the mixed monolayers, an additional phase transition to *LC′* is observed. The nomenclature as *LC′* follows the naming in the previous publication, in which Langmuir isotherms of mixed 95:5 DPPC:**2** monolayers [23] were investigated. In addition to the observed *LC′* phase transition solely in the *trans* state of

the 95:5 DPPC:**2** monolayer, the presented compression isotherms for the mixed monolayers with the higher percentage of 10 % azobenzene mimetics show an additional LC' transition also in the *cis* state. These additional LC' phases, LC'_{trans} and LC'_{cis}, have been identified by calculating the compressibility C as described in section S1 in the Supplementary Information. The individual isotherms and calculated values for the compressibility for all three mixed monolayer are shown in Fig. S1, S2 and S3.

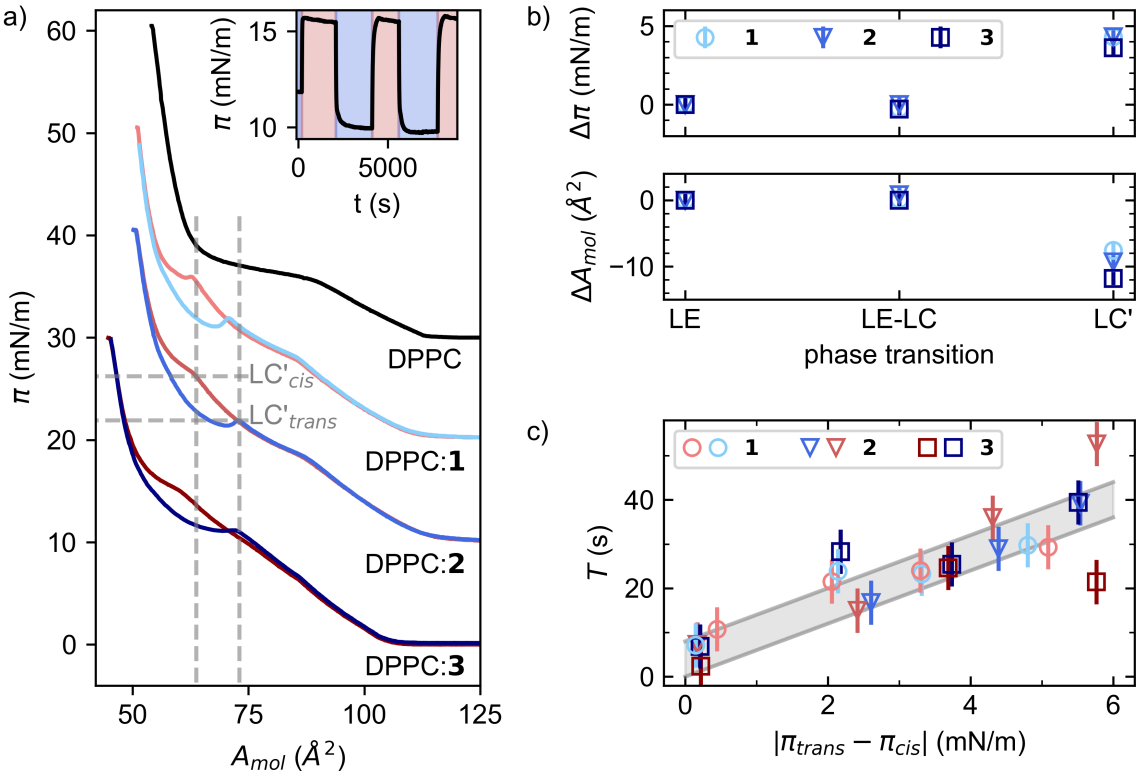

Figure 2. a) Langmuir isotherms of the pure DPPC (black) and mixed 9:1 DPPC:**1** (no sugar), DPPC:**2** (glucose) and DPPC:**3** (lactose) (coloured light, medium and dark) monolayer in their *trans* (blue) and *cis* (red) state. For the DPPC:**2** monolayer, the additional phase transition LC' for the *trans* and *cis* state are marked with horizontal and vertical lines and b) the differences in surface pressure $\Delta\pi$ and area per molecule ΔA_{mol} between the *trans* and *cis* state for the phase transition LE, L-LC and LC' . As inset in a), the surface pressure changes upon illumination with 455 nm (red) and 365 nm (blue) light for the 9:1 DPPC:**2** monolayer at an area per molecule of 0.2 Å^2. c) The fitted time constants T to reach equilibrium surface pressure after switching from the *trans* state to the *cis* state (red) and vice versa (blue) at various area per molecules for the three mixed monolayers plotted against the relative surface pressure change. The individual fits and pressure vs. time plots are shown in S1. The region of most data points is highlighted in grey.

In Fig. 2a the additional LC'_{trans} and LC'_{cis} transitions are marked at the corresponding surface pressures and area per molecules for the mixed DPPC:**2** monolayer. The LC'_{cis} phase transition occurs at a smaller area per molecule and higher surface pressure than the LC'_{trans} phase transition. Further, the surface pressure presents a dynamic jump at the phase transition LC'_{trans} where the surface pressure drops directly after the transition point. This jump in surface pressure is associated with the formation of non-equilibrium domain textures that often form fractal or dendritic shapes [47]. These unstable and non-equilibrium domains relax to the equilibrium domain structure. Multiple factors such as temperature and compression speed define how pronounced this jump is visible in the isotherms [47]. Interestingly, this surface pressure jump is observed in all *trans* isotherms independent of the kind of azobenzene mimetic while in the *cis* isotherm, this non-equilibrium dynamics is only found for the sugar-free mimetic **1**. To characterise the size and physical form of possible domains, Brewster-angle microscopy [48] measurements with a KSV NIMA MicroBAM microscope were performed on mixed monolayer of DPPC and mimetic **2**. No domain formation was observed during the measurements. If domains form, their size is

below the resolution of 12 µm of the Brewster-angle microscope.

Comparing the surface pressures and area per molecules in Fig. 2b at which the additional phase transitions LC' occur, reveals that the relative difference in surface pressure is the same for all three mixed monolayers while the difference in the area per molecule increases for the mimetics **2** (glucose) and **3** (lactose) with larger head groups. Though the presence of the LC' phase is directly influenced by the isomerisation of the azobenzene amphiphiles, the LE and LE-LC phase transitions show no dependency on the isomer. With the existence of the additional LC' phase transition, the *trans* and *cis* isotherms of the mixed monolayers show a large deviation from each other in the region of these LC' points and great potential to induce structural changes within the monolayer upon illumination. To investigate the dynamics within these regions, the monolayers are compressed to various surface pressures/area per molecules around and within this region. For the monolayers with the mimetics **1** and **2**, the surface pressures 9 mN m^{-1}, 12 mN m^{-1}, 15 mN m^{-1} and 18 mN m^{-1} were approached. Additionally, switching at a surface pressure of 27 mN m^{-1} was recorded for the mimetic **2**. Meanwhile, for the mixed monolayer with the derivate **3**, the surface pressures were chosen slightly lower with 8 mN m^{-1}, 10.5 mN m^{-1}, 15 mN m^{-1} and 18 mN m^{-1} as the additional phase transition LC'_{trans} occurs at lower surface pressure compared to the other two mixed monolayers.

After compressing to the desired surface pressure, the area is kept constant during the alternating illumination of the monolayers with light of 365 nm and 455 nm for 5 min to switch between the *trans* and *cis* states while recording the surface pressure. Upon switching the azobenzene mimetics in the monolayers, a change of surface pressure as shown in the inset in Fig. 2a and Fig. S1, S2 and S3 is observed. For the surface pressures below LC'_{trans}, the surface pressure decreases upon switching to the *cis* state. Meanwhile, the surface pressure increases upon *cis* isomerisation for all surface pressures above LC'_{trans}. This bidirectional switching behaviour is consistent with to the behaviour studied previously in 95:5 DPPC:**2** monolayers [23].

The dynamics of the surface pressure changes upon illumination can be described with an exponential function with the time constant T at which the surface pressure reached $1/\mathrm{e}$ of the absolute surface pressure change. For the fit procedure the following expressions were used:

$$\begin{aligned} f(t) &= \pi_0 && t < t_0 \\ f(t) &= \pi_0 + \Delta\pi \cdot \left(1 - \mathrm{e}^{-\frac{t-t_0}{T}}\right) && t_0 < t \end{aligned} \tag{1}$$

with the starting surface pressure π_0, the time t_0 when the surface pressure starts to change and the relative surface pressure change $\Delta\pi$. The derived fit values for the time constants T are plotted in Fig. 2c against the relative surface pressure change and the respective times T for the different mixed monolayer agree well with each other. The relation between all times T and the corresponding relative surface pressure difference can be approximated for the majority of the data points with a linear function as $T(\Delta\pi) = 6\,\mathrm{s}/(\mathrm{mN/m}) \cdot \Delta\pi + 4\,\mathrm{s}$ with an error of $\pm 2\,\mathrm{s}/(\mathrm{mN/m})$ and $\pm 4\,\mathrm{s}$ as shown in Fig. 2c with the grey coloured area. This indicates, that the relaxation time depends mainly on the relative pressure change and is not significantly influenced by the number of sugar groups in the head group.

Identifying the orientation of the carbohydrate head group with grazing incidence X-ray diffraction

To determine the in-plane structure GID measurements were performed on pure DPPC and mixed 9:1 DPPC:**1**, DPPC:**2** and DPPC:**3** monolayers. In various lipid monolayers a two-dimensional in-plane ordering of the lipids at the water-air interface, especially of the hydrophobic acyl chains, is observed. This quasi long-range order of the lipids can be described analogue to a crystalline-like structure by the lattice vectors $\vec{a}$ and $\vec{b}$ defining the primitive unit cell. Furthermore, the acyl chains of the lipid tail groups can be described as cylinders standing on the surface or being tilted with an angle τ from the surface normal. Due to the grazing incidence angle of the incoming beam, the scattering signal of the GID measurements holds information on the lattice structure.

In the top row of Fig. 3, GID detector images from the mixed 9:1 DPPC:**2**-*trans* monolayer recorded at area per molecules of 82.4 Å^2, 63.0 Å^2, 60.1 Å^2 and 56.4 Å^2 are shown and for comparison in the bottom row, images taken after photoswitching to the *cis* isomer. The first point to notice is that for all surface pressures and states a distorted hexagonal lattice is observed with the $(1,-1)$ diffraction around $q_{xy}, q_z = (1.46), (0)$ and the superimposed $(1,0)$ and $(0,1)$ peaks around $q_{xy}, q_z = (1.3), (0.7)$ in the wide angle range. Further peaks are observed in the scattering patterns at around $q_{xy}, q_z = (1.38), (0.55), (1.41), (0.51)$ and $(1.67), (0.08)$ from the mixed monolayers in the *trans* state at 60.1 Å^2 (12.39 mN m^{-1}) and 56.4 Å^2 (17.05 mN m^{-1}) revealing

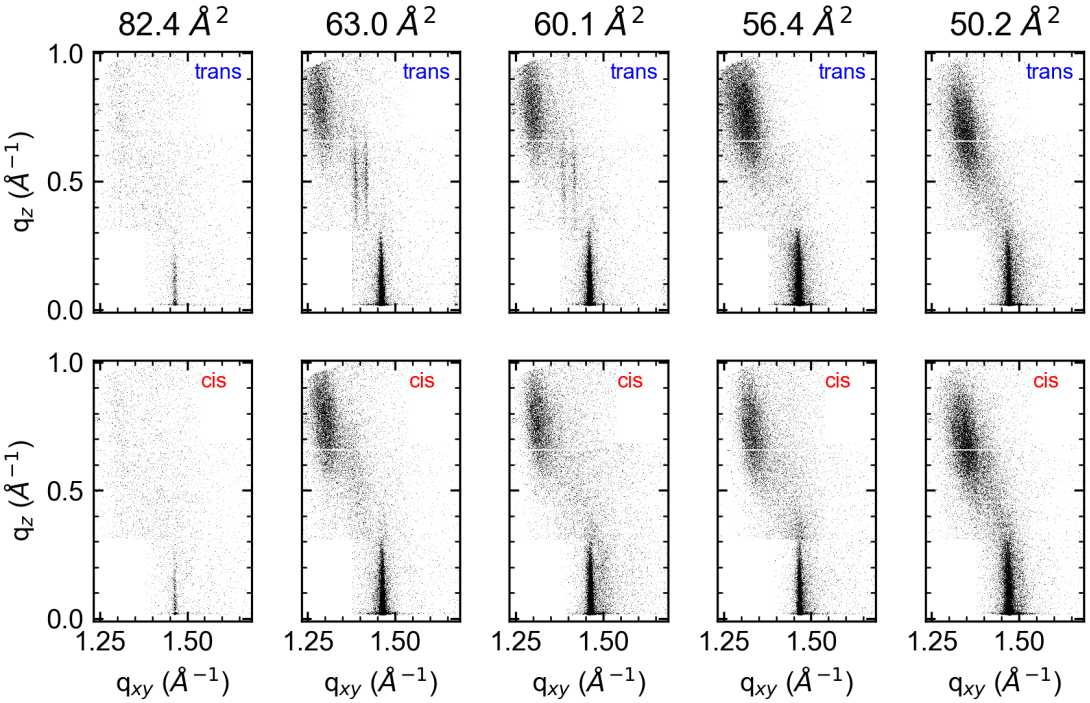

Figure 3. GID images taken from a monolayer made of 9:1 DPPC:**2** at various area per molecules for the *trans* and *cis* states of the azobenzene mimetic **2**.

an additional ordering of the head groups. All fitted peak positions and widths are summarised in S in the Supplementary information and the calculated lattice parameters are listed in Tab. 1 and plotted in Fig. 3. The lattice lengths a and b, the angle γ between these lattice vectors, the tilt angle τ and areas A_{xy} and A_0 were calculated as described in the Supplementary Information in detail.

Focusing first on the hexagonal lattice structure at surface pressures above 10 mN m^{-1} and comparing the lattice parameters of the monolayers in the trans state, a decrease of the tilt angle τ and of the lattice lengths a and b with increasing surface pressure and decreasing area per molecule is observed. This indicates a tighter packing of the acyl chains with increasing surface pressure, which is a behaviour also found for the reference monolayer consisting purely of DPPC and has been reported previously for various amphiphilic lipid monolayers [33; 49; 50]. A close packing is further associated with the liquid-condensed phase of the lipids in the monolayer. Comparing the area per molecules and surface pressures at which the GID images were taken with the isotherm measurements, the points of measurement lie in the region of the liquid condensed phase and above the addition phase transition LC'_{trans}.

Switching the mimetic **2** to its *cis* isomer by illuminating the monolayer with 365 nm at surface pressure above 10 mN m^{-1}, results in a tightening of the lattice packing with a decrease of the lattice length a and decrease of the tilt angle τ. This tightening is also observable in the increase of surface pressure. These structural changes are induced fully by the conformational change of the photoswitchable mimetic **2** as the total area of the trough is kept constant during and after the illumination, thus the barrier is not moved during the measurement. Comparing the lattice parameters determined for the monolayers with the **2**-*trans* and **2**-*cis* mimetics with the parameters of the pure DPPC monolayer, the values show great agreements between each other when related to the surface pressure as shown in Fig. 4.

Thus, by illuminating the monolayer at a fixed area per molecule, the monolayer structure can be switched between two orientation and ordering states with different areas per molecule. This can be explained by a conformational change of the azobenzene derivatives and the subsequent difference in space requirement. The increased extension of the azobenzene mimetic results in a reduction of the space for the DPPC lipids in the monolayer, which corresponds to a decrease of the mean area per molecule determined with the Langmuir

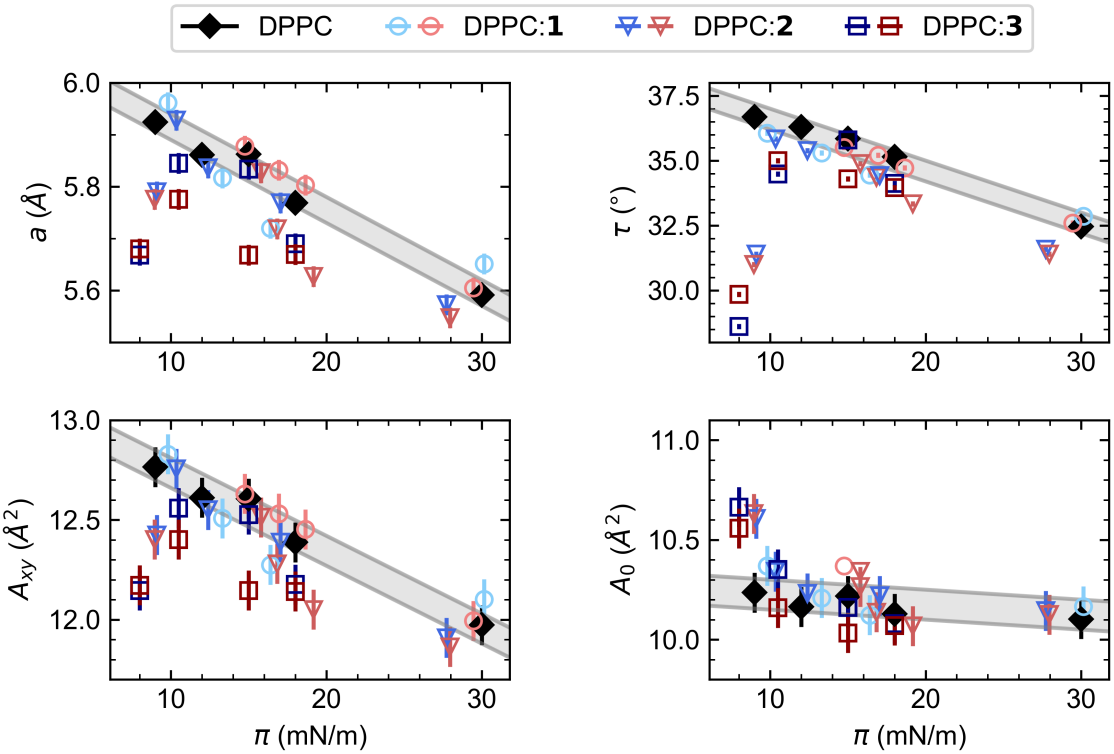

Figure 4. Lattice parameters calculated from the Bragg peak positions from a pure DPPC monolayer (grey highlighted) and mixed monolayers of 9:1 DPPC:**1** (no sugar), DPPC:**2** (glucose) and DPPC:**3** (lactose) at various surface pressures and for the *trans* (blue) and *cis* (red) states of the azobenzene mimetics **1**, **2** and **3** plotted in dependency of the surface pressure with the Wilhelmy plate during the measurements. The lattice parameters are the lattice lengths $a = b$, the tilt angle τ of the acyl chains, the area A_{xy} occupied by the acyl chains and the cross-section area A_0 of the cylinder describing the acyl chains.

isotherms. Meanwhile, the difference of the cross-section A_0 of the acyl chains is insignificant over the range of studied surface pressures, which means that the acyl chains do not change their orientation or formation upon compression of the monolayer or switching between the *trans* and *cis* state at surface pressures above 10 mN m^{-1}.

In contrast, at the lowest investigated surface pressure of 9 mN m^{-1} slightly below the additional phase transition LC'_{trans}, a deviation between the structure of the pure DPPC monolayer at 9 mN m^{-1} and the mixed monolayers with the mimetics **2** and **3** is found. For the mixed monolayer with the mimetic **1** no data were collected at this low surface pressure. While the tail groups of the pure DPPC monolayer are tightly packed and only possess a cross-section of 10.2 Å, the cross-section area of the acyl chains in the mixed monolayer is 10.6 Å, suggesting a less ordered structure. However, the smaller tilt angle τ and the smaller lattice lengths a and b suggest that the chains are closer in distance to each other than in the pure DPPC layer and also at surface pressure above the LC'_{trans}. This contradiction could be explained by the existence of the additional phase transition, which is associated with the photoswitchable mimetics' presence in the monolayer and their reorientation in the film. At surface pressures below that phase transition, the azobenzene mimetics are still in a LE comparable phase, which is associated with a loose packing of the acyl chains and a more lying, elongated orientation of the azobenzene mimetics almost parallel to the surface plane. This horizontal orientation is proposed on the basis of the XRR measurements and from previous studies on similar mixed monolayer systems [23].

At the phase transition, the lipids descend into their LC phase, straighten up and integrate them more ordered into the two-dimensional lattice order. This leads to a decrease of the space occupied by the azobenzene mimetics and consequently a relaxation of the packing for the other DPPC lipids in the monolayer. This relaxation is observable in the increase of lattice lengths a and b of the unit cell and the increase of the tilt angle τ of the tail groups.

Investigating the GID scattering pattern from the mixed monolayers in the *trans* state at 60.1 Å^2 (12.39 mN m^{-1})

Table 1. GID results of pure DPPC and mixed monolayers at 21 °C: Lattice parameters a, γ, chain tilt τ from the surface normal, in plane area per acyl chain A_{xy} and chain cross-sectional area A_0. The uncertainties for the areas A_{mol}, A_{xy} and A_0 are 0.1 Å^2, for the surface pressure π 0.01 mN m^{-1}, for the lattice lengths a 0.01 Å and for the angles γ, τ and ϕ are 0.1°.

A_{mol} / Å^2	π / mN m^{-1}	state	a / Å^{-1}	γ / °	*tau* / °	ϕ/ °	A_{xy} / Å^2	A_0/ Å^2
DPPC								
56.4	9		5.92	124.5	36.7	185.0	12.8	10.2
53.2	12		5.86	124.3	36.3	185.1	12.6	10.2
52.7	15		5.86	124.3	35.9	185.2	12.6	10.2
51.1	18		5.77	123.9	35.2	185.7	12.4	10.1
48.2	30		5.59	123.1	32.5	186.7	12.0	10.1
DPPC:**1** (no sugar)								
59.6	9.80	*trans*	5.96	124.7	36.1	185.4	12.8	10.4
59.6	14.75	*cis*	5.88	124.4	35.5	185.5	12.6	10.3
55.6	13.31	*trans*	5.82	124.1	35.3	185.5	12.5	10.2
55.6	16.94	*cis*	5.83	124.2	35.2	186.1	12.5	10.2
53.9	16.39	*trans*	5.72	123.7	34.4	186.1	12.3	10.1
53.9	18.65	*cis*	5.80	124.1	34.7	186.1	12.5	10.2
52.1	30.15	*trans*	5.65	123.4	32.9	186.2	12.1	10.2
52.1	29.45	*cis*	5.61	123.2	32.6	186.1	12.0	10.1
DPPC:**2** (glucose)								
82.4	9.10	*trans*	5.79	124.0	31.4	186.8	12.4	**10.6**
82.4	8.95	*cis*	5.78	123.9	31.0	187.1	12.4	10.6
63.0	10.35	*trans*	**5.93**	124.6	**35.8**	185.3	12.8	**10.3**
63.0	15.80	*cis*	**5.83**	124.2	**34.9**	185.6	12.5	10.3
60.1	12.39	*trans*	**5.84**	124.2	**35.4**	185.5	12.6	10.2
60.1	16.83	*cis*	**5.72**	123.7	**34.4**	185.9	12.3	10.1
56.4	17.05	*trans*	**5.77**	123.9	**34.4**	186.1	12.4	10.2
56.4	19.17	*cis*	**5.63**	123.3	**33.3**	185.9	12.1	10.1
50.2	27.72	*trans*	5.57	123.1	31.6	187.3	11.9	10.1
50.2	27.95	*cis*	5.55	123.0	31.4	187.4	11.9	10.1
DPPC:**3** (lactose)								
80.6	7.74	*trans*	5.67	123.5	28.6	187.5	12.1	10.7
80.6	7.52	*cis*	5.58	123.5	29.8	187.4	12.2	10.6
61.3	8.79	*trans*	5.84	124.2	34.5	185.6	12.6	10.4
61.3	14.30	*cis*	5.78	123.9	35.0	185.6	12.4	10.2
51.2	12.92	*trans*	5.83	124.2	35.8	185.4	12.5	10.2
51.2	16.86	*cis*	5.67	123.5	34.3	186.0	12.1	10.0
48.5	16.93	*trans*	5.69	123.6	34.1	185.3	12.2	10.1
48.5	19.20	*cis*	5.67	123.5	34.0	186.2	12.1	10.1

and 56.4 Å^2 (17.05 mN m^{-1}), additional peaks at around $q_{xy}, q_z = (1.38), (0.55), (1.41), (0.51)$ and $(1.67), (0.08)$ are found. In contrast to the peaks, belonging to the distorted hexagonal structure associated with the chain structure, discussed before, these additional peaks indicate an ordering of the entire molecule including at least parts of the head group. This superior ordering of the entire molecule can be described with a superlattice structure. An ordering of the complete head group or parts of it has been previously reported for a variety of sugar groups [47]. The driving force for this orientation is the strong intermolecular hydrogen bonds between the glycan groups. Interestingly, this superior ordering disappears when switching to the *cis* state at both area per molecules suggesting a dissociation of the glucose groups or the azobenzene switches from each other. As the only force acting on the head group of the mimetics during illumination originates from the conformational change of the azobenzene switch, the driving force for the uncoupling must be induced by the conformational change.

In a similar way, GID measurements (see Fig. S5 and S6) were conducted and structural changes derived for the mixed 9:1 DPPC:**1** and DPPC:**3** monolayers. For both systems, the changes of the tail groups in-plane structural upon switching resemble the difference between the lattice parameters for the corresponding surface pressures as shown in Fig. 4. Therefore, the head group composition of the three investigated mimetics **1**, **2** and **3** does not significantly influence the packing of the acyl chains. Meanwhile, a difference in the existence of the head group ordering is found for the monolayer with the mimetic **3**. Similar to the 9:1 DPPC:**2** monolayer, the monolayers containing the mimetics **1** and **3** show Bragg peaks belonging to a superimposed lattice structure in the *trans* state of the mimetics for surface pressures above the pressure of the LC'_{trans} transition phase. However, a difference in the scattering intensity of the additional Bragg peaks is observed. The scattering signal intensity increases for monolayers with the mimetic **2** and even further for the mimetic **2** compared to mimetic **1**. The existence of a superimposed head group structure in the monolayer with the mimetic **1** implies that the head group ordering originates at least partially from the intermolecular bonds of the azobenzene switches. Nevertheless, the increase in intensity of the scattering signal suggests a higher degree of ordering and thus stronger bonding of the headgroups for the monolayer with the mimetics **2** and **3**. Hence, the strongest bonding would be present for the lactose head group. This strong intermolecular bonding for the lactose head group could explain why the ordering of the head groups would not be decoupled upon switching to the *cis* state as observed for the two measurements at area per molecules of 51.2 Å^2 and 48.5 Å^2.

To conclude, the results derived from the GID measurements imply that the switching of the azobenzene mimetics affects mainly the head group orientation and depending on the glycan group in the head group a reorientation of the carbohydrate group can be induced.

Characterising the monolayer morphology with X-ray and neutron reflectivity

X-ray reflectivity (XRR) and neutron reflectivity (NR) are powerful methods to determine the structure of lipid monolayer in the direction of the surface normal. For reference, reflectivity measurements from the pure DPPC monolayers were taken in addition to the data from the mixed Langmuir monolayer (see Fig. S7 and Tab. S6). The *in situ* XRR and NR data were collected at 21 °C during irradiation of the mixed monolayers with UV and visible light at various areas per molecule. The data are shown in Fig. 5 together with the model and the derived `SLD` profiles. The fit values for the water, head and tail layer thickness l, scattering length density `SLD` and roughness σ at the interface are listen in Tab. 2.

The XRR data in Fig. 5 show the specular reflectivity intensity curves collected from mixed DPPC:**2** monolayers normalised by the Fresnel reflectivity for an ideal surface with no roughness to highlight the oscillations (Kiessig fringes) originating from the scattering at the slab interfaces. With higher surface pressures and smaller area per molecules, the fringe minima shift to lower momentum transfer vector q_z. A shift to lower q_z corresponds to an increase of the total layer thickness $l_{total} = l_{tail} + l_{head}$ and is associated with a closer packing of the molecules.

Upon illumination of the mixed monolayer with UV light (365 nm) and the subsequent photoswitching of the mimetics **2** to its *cis* state, a shift of the fringe minimum is observed in the XRR data at area per molecules of 63.0 Å^2 and 60.1 Å^2. These areas correspond to the region above the LC'_{trans} phase transition and close to the LC'_{cis} phase transition. The fitted values listed in Tab. 2 show at an increase of the tail layer thickness of up to 2.75 Å upon switching to the *cis* state that indicates a straightening of the tail group. This corresponds well with the determined increase of the tilt angle τ of the tail groups in the GID data shown in Fig. 4.

However, a decrease of the head layer thickness by up to 3.21 Å and a decrease of the roughness by 0.83 Å at the interface between the bulk water and the head groups is also seen. In sum, the opposed thickness changes of the head and tail layer result in no significant change of the total thickness. Yet, the significant decrease of

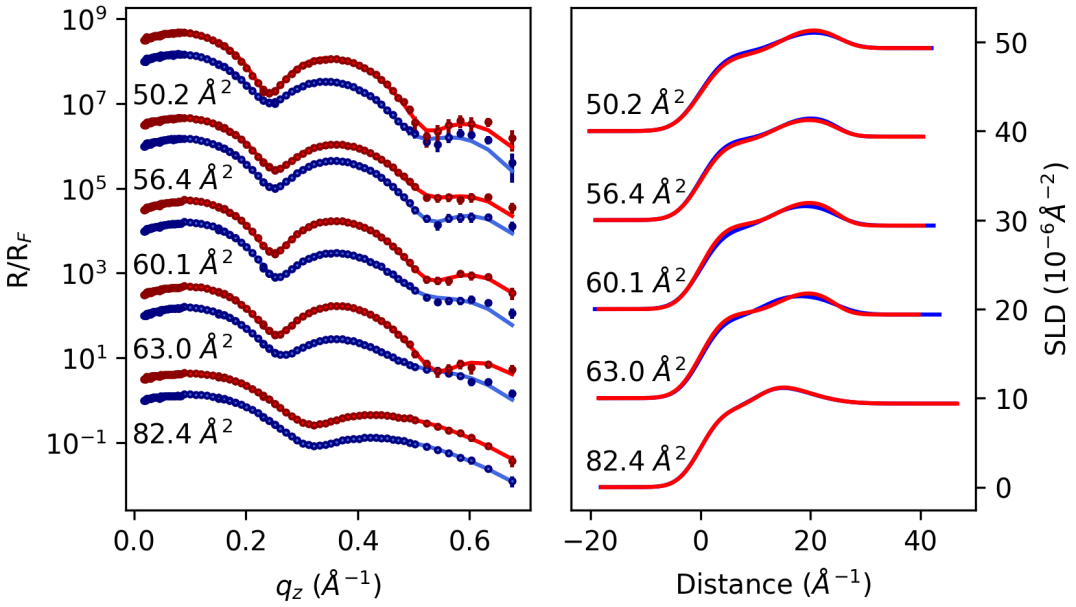

Figure 5. XRR data normalised by the Fresnel reflectivity for an ideal interface with no roughness from the mixed 9:1 DPPC:**2** (glucose) monolayer with the model fit (left) and the derived SLD for the *trans* and *cis* isomer of the mimetic **2** at various area per molecules.

Table 2. Fit parameters for the pure DPPC and mixed DPPC:**2** (glucose) monolayers obtained from fits of the XRR data modelled with a two-slab model. Listed are values of the layer thickness l, the scattering length density SLD for each slab and the roughness σ at the interface of the slab for the water, head and tail layer. The SLD for the water layer was fitted to 9.39 10^{-6}Å^{-2}. The uncertainties of the fitted values are 0.3 Å^2 for the thicknesses l, are 0.11×10^{-6} Å^{-2} for the SLD and 0.1 Å for the roughness σ.

A_{mol} / Å^2	π / mNm^{-1}	state	l_{total} / Å	l_{head} / Å	l_{tail} / Å	SLD_{head} / 10^{-6}Å^{-2}	SLD_{tail} / 10^{-6}Å^{-2}	σ_{water} / Å	$\sigma_{\text{head/tail}}$ / Å
82.4	9.10	*trans*	18.94	8.48	10.46	12.08	8.76	5.59	3.28
82.4	8.95	*cis*	18.59	7.39	10.66	12.68	8.78	5.76	3.26
63.0	10.35	*trans*	24.74	13.32	11.42	12.59	9.06	3.42	3.34
63.0	15.80	*cis*	24.29	10.11	14.17	13.40	9.57	2.59	3.38
60.1	12.39	*trans*	24.79	12.31	12.48	13.10	9.02	3.14	3.55
60.1	16.38	*cis*	24.75	10.71	14.03	13.11	9.50	2.68	3.38
56.4	17.05	*trans*	24.78	10.80	13.98	13.55	9.06	2.56	3.49
56.4	19.17	*cis*	24.74	11.61	13.24	13.66	8.77	2.69	3.53
50.2	27.72	*trans*	25.71	11.61	14.11	12.15	8.81	2.82	3.76
50.2	27.95	*cis*	25.16	10.70	14.46	13.26	8.53	2.88	3.80

the head layer thickness and the reduction of surface roughness suggests that the head group of the mimetic **2** changes its orientation. Compared to the DPPC molecules, the azobenzene mimetic **2** is much longer, especially the extent of the head group (see Fig. 1). Considering a more vertical alignment of the derivative **2**-*trans* in the monolayer, the photoswitching and the subsequently conformation of the mimetic **2** to its *cis* state, would result in a 90° angle at the azo group and either the tail group or the head group would tilt away from the surface normal. In both cases, the tilting of either part leads to an increase of the area taken up by the mimetic **2** and consequently a decrease of the area for the other DPPC molecules. With this reduction of the effective area per molecule, the molecules have to moved close to each other that is observed by the rise of the surface pressure and an increase of the tail layer thickness. However, a tilting of the tail group would not explain the decrease of the head group and is also not supported from the GID measurements for which the tail group cross-section is unchanged upon switching. In contrast, a tilting of the elongated mimetic **2** head groups away from the surface normal towards the surface parallel direction results in a decrease of the layer thickness.

To investigate the relative position of the two isomers of the azobenzene mimetic **2** compared to the DPPC molecules in the mixed monolayers in more detail, complementary NR data were collected as described in the methods and materials section with contrast for the total scattering of the molecules. The total scattering length of the individual lipids, d_{62}DPPC, DPPC and **2**, were calculated by summing over the atom specific scattering lengths [51] for each molecule. The derived scattering lengths are 0.006 73 Å, 0.000 27 Å and 0.001 62 Å for d_{62}DPPC, DPPC and **2**, respectively. Considering deuterium enrichment of the glucose hydrogen atoms [52] in the D_2O solvent and the replacement of eleven hydrogen atoms with deuterium atoms, the scattering length for the partially deuterated **2** mimetic would be 0.002 76 Å. The monolayers were compressed to an initial surface pressures just above LC'_{trans} before keeping the area per molecule constant and collecting the data for the *trans* isomer. Subsequently, the monolayer were illuminated for 5 min to switch to the *cis* state before taking the *cis* data. The NR data are shown in Fig. 6 together with the model fit and the corresponding `SLD` profiles. The fit values are summaries in Tab. 3. Similar to the XRR data, an asynchronous increase of the tail layer and decrease of the head layer thickness is observed.

From the fitted values that describe the head and tail layer properties, the scattering lengths b for those regions are calculated as $b = \mathtt{SLD} \cdot l \cdot A_{\mathrm{mol}}$ and summarised in Tab. 4. The scattering lengths b_{tail} increase and b_{head} decrease upon switching from the *trans* to *cis* state for the contrasts which d_{62}DPPC on D_2O and NRW. Whereas, for the contrast with the hydrogenous DPPC the b_{tail} decreases and b_{head} increases.

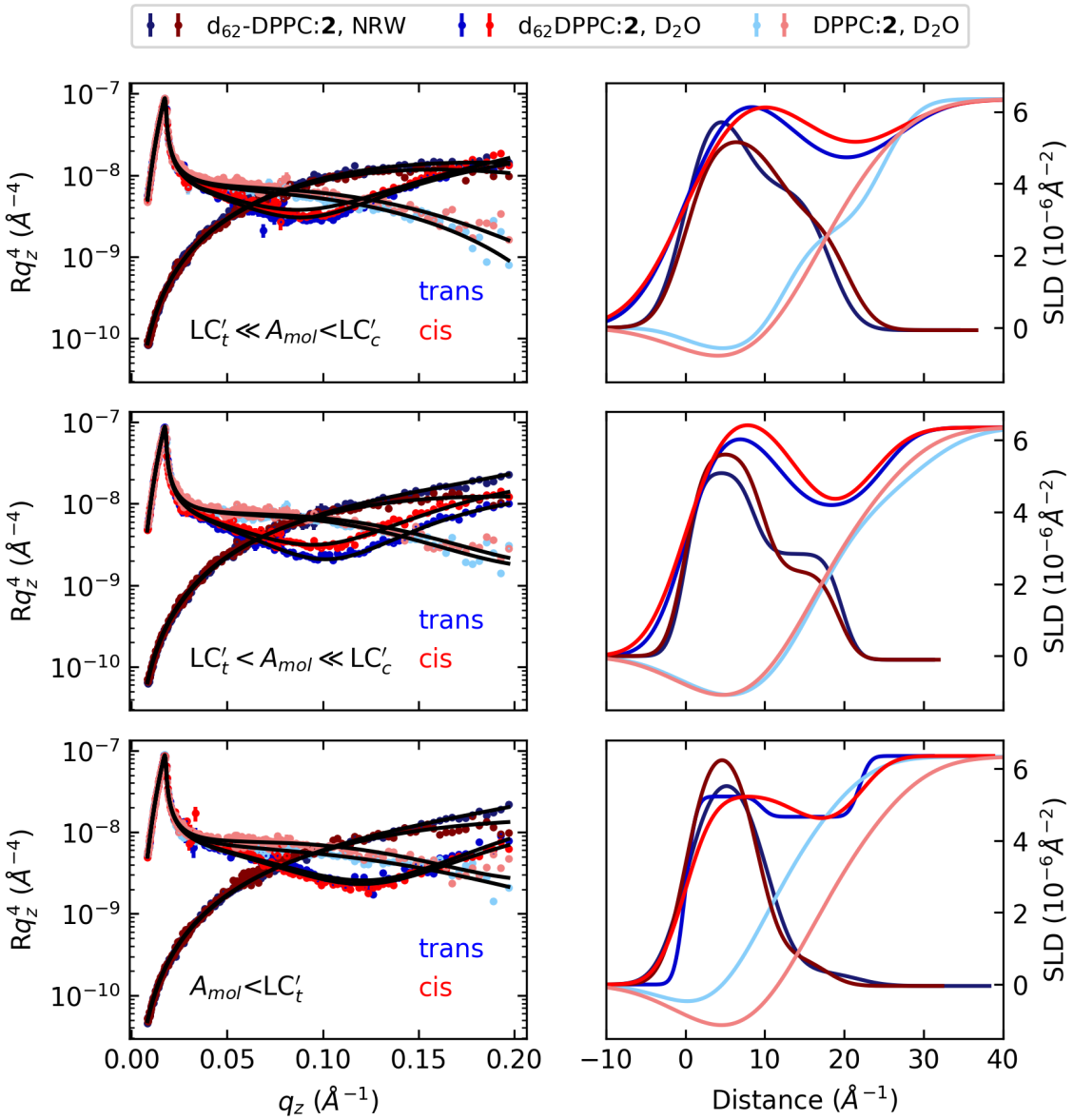

Figure 6. NR data from the mixed 9:1 DPPC:**2** (glucose) monolayer on D_2O at an area per molecule of 41.02 Å^2, d_{62}DPPC:**2** monolayer on D_2O at 49.86 Å^2 and DPPC:**2** monolayer on NRW at 43.51 Å^2 with the model fits (left) and the derived SLD profiles for the *trans* (blue) and *cis* (red) isomer of the mimetic **2**. The data were collected area per molecules A_{mol} below and between the areas of the additional phase transitions LC'_{trans} and LC'_{cis} determined from the Langmuir isotherms shown in Fig. S8.

Table 3. Fit parameters for the mixed DPPC:**2** (glucose) monolayers on D_2O and the mixed d_{62}DPPC:**2** on D_2O and NRW at different surface areas obtained from fits of the NR data modelled with a two-slab model. Listed are values of the layer thickness l, the scattering length density SLD for each slab and the roughness σ at the interface of the slab for the water, head and tail layer. The roughness of the water, tail and head layer were constraint and are given as σ. The uncertainties of the fitted values are 0.3 Å^2 for the thicknesses l, are 0.13×10^{-6} Å^{-2} for the SLD and 0.1 Å for the roughness σ.

contrast	A_{mol} / Å^2	π / mN m^{-1}	state	l_{total} / Å	l_{head} / Å	l_{tail} / Å	SLD_{water} / 10^{-6}Å^{-2}	SLD_{head} / 10^{-6}Å^{-2}	SLD_{tail} / 10^{-6}Å^{-2}	σ / Å
$A_{mol} < LC'_{trans}$										
d_{62}DPPC:**2** NRW	53.05	13.06	*trans*	21.7	11.4	10.3	-0.04	4.92	5.95	2.9
d_{62}DPPC:**2** NRW	53.05	13.57	*cis*	17.7	8.6	9.08	-0.04	6.66	6.60	2.4
d_{62}DPPC:**2** D_2O	61.42	11.40	*trans*	21.9	12.4	9.6	6.35	4.30	5.22	1.0
d_{62}DPPC:**2** D_2O	61.42	13.11	*cis*	22.3	8.7	13.5	6.35	5.25	5.25	2.9
DPPC:**2** D_2O	54.99	8.02	*trans*	18.2	9.8	8.50	6.33	2.24	-1.44	5.2
DPPC:**2** D_2O	54.99	10.99	*cis*	24.8	10.5	14.3	6.33	3.30	-1.77	5.9
$LC'_{trans} < A_{mol} \ll LC'_{cis}$										
d_{62}DPPC:**2** NRW	43.51	15.60	*trans*	19.67	11.11	8.56	-0.10	8.93	5.11	1.6
d_{62}DPPC:**2** NRW	43.51	18.9	*cis*	19.26	9.60	9.66	-0.10	9.1	5.64	1.9
d_{62}DPPC:**2** D_2O	48.96	13.96	*trans*	24.97	13.13	11.84	6.35	3.99	6.30	3.3
d_{62}DPPC:**2** D_2O	48.96	18.15	*cis*	23.41	9.54	13.87	6.35	3.47	6.77	4.0
DPPC:**2** D_2O	45.48	10.98	*trans*	29.6	13.7	16.0	6.35	2.56	-1.48	5.2
DPPC:**2** D_2O	45.48	15.23	*cis*	25.5	10.93	14.58	6.35	3.25	-1.64	5.8
$LC'_{trans} \ll A_{mol} < LC'_{cis}$										
d_{62}DPPC:**2** NRW	37.48	18.83	*trans*	18.2	11.1	7.1	-0.07	10.79	6.534	2.8
d_{62}DPPC:**2** NRW	37.48	21.70	*cis*	20.3	8.7	11.6	-0.07	12.02	5.29	2.8
d_{62}DPPC:**2** D_2O	42.34	17.12	*cis*	26.8	13.9	12.8	6.34	4.32	6.97	5.1
d_{62}DPPC:**2** D_2O	42.34	20.41	*cis*	25.8	9.9	15.9	6.34	4.27	6.74	5.7
DPPC:**2** D_2O	41.02	14.27	*trans*	24.92	12.44	12.48	6.35	1.70	-0.67	3.45
DPPC:**2** D_2O	41.02	17.63	*cis*	24.12	9.36	14.76	6.35	3.39	-1.28	6.0

Table 4. Calculated scattering lengths b from the fitted values in Tab. 3 with an uncertainty of $\pm 0.000\,10$ Å for the head and tail layer of the mixed monolayers with the mimetic **2** (glucose) shown in Fig. 6

contrast	A_{mol} Å^2	π / mN m^{-1}	state	b_{head} / Å	b_{tail} / Å	b_{total} / Å
$A_{\mathrm{mol}} < LC'_{trans}$						
d_{62}DPPC:**2** NRW	53.05	13.06	*trans*	0.00297	0.00325	0.00622
d_{62}DPPC:**2** NRW	53.05	13.57	*cis*	0.00304	0.00318	0.00622
d_{62}DPPC:**2** D_2O	61.42	11.40	*trans*	0.00327	0.00307	0.00633
d_{62}DPPC:**2** D_2O	61.42	13.11	*cis*	0.00196	0.00437	0.00633
DPPC:**2** D_2O	54.99	8.02	*trans*	0.00120	-0.00067	0.00052
DPPC:**2** D_2O	54.99	10.99	*cis*	0.00191	-0.00139	0.00052
$LC'_{trans} < A_{\mathrm{mol}} \ll LC'_{cis}$						
d_{62}DPPC:**2** NRW	43.51	15.60	*trans*	0.00431	0.00190	0.00622
d_{62}DPPC:**2** NRW	43.51	18.9	*cis*	0.00385	0.00237	0.00622
d_{62}DPPC:**2** D_2O	48.96	13.96	*trans*	0.00257	0.00365	0.00622
d_{62}DPPC:**2** D_2O	48.96	18.15	*cis*	0.00162	0.00460	0.00622
DPPC:**2** D_2O	45.48	10.98	*trans*	0.00159	-0.00107	0.00052
DPPC:**2** D_2O	45.48	15.23	*cis*	0.00161	-0.00109	0.00052
$LC'_{trans} \ll A_{\mathrm{mol}} < LC'_{cis}$						
d_{62}DPPC:**2** NRW	37.48	18.83	*trans*	0.00449	0.00173	0.00622
d_{62}DPPC:**2** NRW	37.48	21.70	*cis*	0.00392	0.00230	0.00622
d_{62}DPPC:**2** D_2O	42.34	17.12	*cis*	0.00255	0.00379	0.00633
d_{62}DPPC:**2** D_2O	42.34	20.41	*cis*	0.00179	0.00454	0.00633
DPPC:**2** D_2O	41.02	14.27	*trans*	0.00087	-0.00034	0.00052
DPPC:**2** D_2O	41.02	17.63	*cis*	0.00130	-0.00077	0.00052

CONCLUSION

With the combination of Langmuir isotherm, X-ray and neutron reflectivity and grazing incidence X-ray diffraction, light-induced structural changes in Langmuir monolayers at the water-air interface with a mixture of 9:1 DPPC and the photoswitchable mimetics **1**, **2** and **3** are identified. They revealed repeatable and reversible changes in the surface pressure and vertical and in-plane structure of the lipid monolayers. An additional phase transition, allocated to the photoswitchable mimetics, is seen for both *trans* and *cis* isomers of the azobenzene derivatives **1**, **2** and **3**, generating a division in which the structure of the monolayer can be altered at fixed area per molecule with light. This is the first observation of this additional phase transition for the *cis* isomer. The time to switch between the surface pressures in the *trans* and *cis* state depends linearly on the absolute surface pressure change and shows no dependence on the carbohydrate in the head group of the photoswitchable glycolipid. Although the azobenzene mimetic molecules only make up 10 % of the lipids in the monolayer, their light-induced conformation changes upon isomerisation lead to a general increase of few $\mathrm{mN\,m^{-1}}$ in surface pressure and a closer packing of the molecules. Furthermore, an ordering of the head groups primarily for the *trans* isomers of the mimetic **1** and **2** is found. This ordering is disrupted upon illumination and switching to the *cis* isomer. It is notable that this change of orientation allows manipulation of the glucose head group of the mimetic **2** within the monolayer. Therefore, mimetic **2** is a good candidate for a controlled switching of the glucose group orientation and for bespoke model systems for light-controlled attachment and detachment systems for proteins or bacteria.

ACKNOWLEDGMENTS

We acknowledge DESY (Hamburg, Germany), a member of the Helmholtz Association HGF, for the provision of experimental facilities. This research was carried out at PETRA III beamline P08 via proposals ProposalID H-20010009, I-20190953 EC, I-20200343. We would like to thank Florian Betram, Chen Shen and René Kirchhof for assistance at P08 and Milena Lippman for chemistry lab support. The neutron experiment at the Materials and Life Science Experimental Facility of the J-PARC was performed under a user program (Proposal No. 2023A0098). We want to thank Masako Yamada and Hideki Seto for their support and assistence.

FUNDING SOURCES

We acknowledge funding from Bundesministerium fuer Bildung und Forschung, ErUM-Pro (grant No. BMBF 05K19FK2 and BMBF 05K22FK3) for the LISA instrument. We further acknowledge financial support from the Center for Molecular Water Science (CMWS). This publication was written in the context of the work of the consortium DAPHNE4NFDI in association with the German National Research Data Infrastructure (NFDI) e.V. NFDI is financed by the Federal Republic of Germany and the 16 federal states and the consortium is funded by the Deutsche Forschungsgemeinschaft (DFG, German Research Foundation) - project number 460248799. The authors would like to thank for the funding and support. Furthermore, thanks go to all institutions and actors who are committed to the association and its goals.

REFERENCES

[1] J. A. Op den Kamp. Lipid asymmetry in membranes. *Annual Review of Biochemistry*, 48(1979):47–71, 1979. doi: 10.1146/annurev.bi.48.070179.000403.

[2] P. L. Yeagle. *The Structure of Biological Membranes: 2nd Edition*. CRC Press, 2004. ISBN 9780429120640.

[3] Aleš Iglič, Michael Rappolt, and Patricia Losada Perez. *Advances in biomembranes and lipid self-assembly*. Advances in biomembranes and lipid self-assembly. Academic Press, London, United Kingdom, 2024.

[4] Sen-itiroh Hakomori and Yasuyuki Igarashi. Functional role of glycosphingolipids in cell recognition and signaling. *The Journal of Biochemistry*, 118(6):1091–1103, 1995.

[5] M. Manna, T. Róg, and I. Vattulainen. The challenges of understanding glycolipid functions: An open outlook based on molecular simulations. *Biochimica et Biophysica Acta*, 1841(8):1130–1145, 2014. doi: 10.1016/j.bbalip.2013.12.016.

[6] O. Ces and X. Mulet. Physical coupling between lipids and proteins: a paradigm for cellular control. *Signal Transduction*, 6(2):112–132, 2006. doi: 10.1002/sita.200500079.

[7] B. Nepal and K. J. Stine. Monolayers of carbohydrate-containing lipids at the water- air interface. In Radwa Ali Mehanna, editor, *Cell Culture*. IntechOpen, 2019. ISBN 978-1-78984-866-3.

[8] G. W. Jones and R. E. Isaacson. Proteinaceous bacterial adhesins and their receptors. *Critical Reviews in Microbiology*, 10(3):229–260, 1983. doi: 10.3109/10408418209113564.

[9] N. Sharon and H. Lis. Lectins as cell recognition molecules. *Science*, 246(4927):227–234, 1989. doi: 10.1126/science.2552581.

[10] G. A. Cross. Glycolipid anchoring of plasma membrane proteins. *Annual Review of Cell Biology*, 6(1):1–39, 1990. doi: 10.1146/annurev.cb.06.110190.000245.

[11] S. V. Evans and C. R. MacKenzie. Characterization of protein-glycolipid recognition at the membrane bilayer. *Journal of Molecular Recognition*, 12(3):155–168, 1999. doi: 10.1002/(SICI)1099-1352(199905/06)12:3¡155::AID-JMR456¿3.0.CO;2-S.

[12] J. P. Renou, J. B. Giziewicz, I. C. Smith, and H. C. Jarrell. Glycolipid membrane surface structure: orientation, conformation, and motion of a disaccharide headgroup. *Biochemistry*, 28(4):1804–1814, 1989. doi: 10.1021/bi00430a057.

[13] J. Volarić, W. Szymanski, N. A. Simeth, and B. L. Feringa. Molecular photoswitches in aqueous environments. *Chemical Society Reviews*, 50(22):12377–12449, 2021. doi: 10.1039/d0cs00547a.

[14] G. Despras, V. Poonthiyil, and T. K. Lindhorst. *Photochromic Carbohydrate Conjugates*. Molecular Photoswitches. Wiley, 2022. ISBN 9783527351046.

[15] Theresa Weber, Vijayanand Chandrasekaran, Insa Stamer, Mikkel B. Thygesen, Andreas Terfort, and Thisbe K. Lindhorst. Switching of bacterial adhesion to a glycosylated surface by reversible reorientation of the carbohydrate ligand. *Angewandte Chemie International Edition*, 53(52):14583–14586, 2014. doi: 10.1002/anie.201409808.

[16] Yu Fan, Ahmed El Rhaz, Stéphane Maisonneuve, Emilie Gillon, Maha Fatthalla, Franck Le Bideau, Guillaume Laurent, Samir Messaoudi, Anne Imberty, and Juan Xie. Photoswitchable glycoligands targeting pseudomonas aeruginosa leca. *Beilstein journal of organic chemistry*, 20:1486–1496, 2024. doi: 10.3762/bjoc.20.132.

[17] Andrew A. Beharry and G. Andrew Woolley. Azobenzene photoswitches for biomolecules. *Chemical Society Reviews*, 40(8):4422–4437, 2011. doi: 10.1039/c1cs15023e.

[18] H. M. D. Bandara and S. C. Burdette. Photoisomerization in different classes of azobenzene. *Chemical Society Reviews*, 41(5):1809–1825, 2012. doi: 10.1039/c1cs15179g.

[19] Mitsuaki Yamauchi, Miho Okaji, Naoki Aratani, Hiroko Yamada, and Sadahiro Masuo. Reversible photoluminescence control of azobenzene crystals by light and heat stimulation. *ChemPhotoChem*, 6(5), 2022. doi: 10.1002/cptc.202100301.

[20] P. Urban, S. D. Pritzl, M. F. Ober, C. F. Dirscherl, C. Pernpeintner, D. B. Konrad, J. A. Frank, D. Trauner, B. Nickel, and T. Lohmueller. A lipid photoswitch controls fluidity in supported bilayer membranes. *Langmuir*, 36(10):2629–2634, 2020. doi: 10.1021/acs.langmuir.9b02942.

[21] Stefanie D. Pritzl, David B. Konrad, Martina F. Ober, Alexander F. Richter, James A. Frank, Bert Nickel, Dirk Trauner, and Theobald Lohmüller. Optical membrane control with red light enabled by red-shifted photolipids. *Langmuir*, 38(1):385–393, 2022. doi: 10.1021/acs.langmuir.1c02745.

[22] Martina F. Ober, Adrian Müller-Deku, Anna Baptist, Benjamin Ajanović, Heinz Amenitsch, Oliver Thorn-Seshold, and Bert Nickel. Saxs measurements of azobenzene lipid vesicles reveal buffer-dependent photoswitching and quantitative z→e isomerisation by X-rays. *Nanophotonics*, 11(10):2361–2368, 2022. doi: 10.1515/nanoph-2022-0053.

[23] J. E. Warias, F. Reise, S. C. Hövelmann, R. P. Giri, M. Röhrl, J. Kuhn, M. Jacobsen, K. Chatterjee, T. Arnold, C. Shen, S. Festersen, A. Sartori, P. Jordt, O. M. Magnussen, T. K. Lindhorst, and B. M. Murphy. Photoinduced bidirectional switching in lipid membranes containing azobenzene glycolipids. *Scientific reports*, 13(1):11480, 2023. doi: 10.1038/s41598-023-38336-x.

[24] Mina Aleksanyan, Andrea Grafmüller, Fucsia Crea, Vasil N. Georgiev, Naresh Yandrapalli, Stephan Block, Joachim Heberle, and Rumiana Dimova. Photomanipulation of minimal synthetic cells: Area increase, softening, and interleaflet coupling of membrane models doped with azobenzene-lipid photoswitches. *Advanced science (Weinheim, Baden-Wurttemberg, Germany)*, 10(31):e2304336, 2023. doi: 10.1002/advs.202304336.

[25] K. G. Yager and C. J. Barrett. Novel photo-switching using azobenzene functional materials. *Journal of Photochemistry and Photobiology A: Chemistry*, 182(3):250–261, 2006. doi: 10.1016/j.jphotochem.2006.04.021.

[26] E. H. G. Backus, J. M. Kuiper, J. B. F. N. Engberts, B. Poolman, and M. Bonn. Reversible optical control of monolayers on water through photoswitchable lipids. *The Journal of Physical Chemistry B*, 115(10):2294–2302, 2011. doi: 10.1021/jp1113619.

[27] M.-M. Russew and S. Hecht. Photoswitches: from molecules to materials. *Advanced materials (Deerfield Beach, Fla.)*, 22(31):3348–3360, 2010. doi: 10.1002/adma.200904102.

[28] Ulrich Jung, Jens Kubitschke, Rainer Herges, and Olaf Magnussen. Studies of the molecular switching of azobenzene-functionalized platform adlayers on au(111) by chronoamperometry. *Electrochimica Acta*, 112: 869–880, 2013. doi: 10.1016/j.electacta.2013.06.123.

[29] Jens Als-Nielsen and Kristian Kjær. X-ray reflectivity and diffraction studies of liquid surfaces and surfactant monolayers. In *Phase Transitions in Soft Condensed Matter*, NATO ASI Series, pages 113–138. Springer US, Boston, MA, 1990. ISBN 978-1-4613-0551-4. doi: 10.1007/978-1-4613-0551-4_11.

[30] Jaroslaw Majewski and Boguslaw Stec. X-ray scattering studies of model lipid membrane interacting with purothionin provide support for a previously proposed mechanism of membrane lysis. *European Biophysics Journal*, 39(8):1155–1165, 2010. doi: 10.1007/s00249-009-0568-0.

[31] P. S. Pershan. Liquid surface order: X-ray reflectivity. *Physica A: Statistical Mechanics and its Applications*, 231(1-3):111–116, 1996. doi: 10.1016/0378-4371(95)00456-4.

[32] K. Kjaer. Some simple ideas on X-ray reflection and grazing-incidence diffraction from thin surfactant films. *Physica B: Condensed Matter*, 198(1-3):100–109, 1994. doi: 10.1016/0921-4526(94)90137-6.

[33] J. Als-Nielsen, D. Jacquemain, K. Kjaer, F. Leveiller, M. Lahav, and L. Leiserowitz. Principles and applications of grazing incidence X-ray and neutron scattering from ordered molecular monolayers at the air-water interface. *Physics Reports*, 246(5):251–313, 1994. doi: 10.1016/0370-1573(94)90046-9.

[34] S. Dietrich and A. Haase. Scattering of X-rays and neutrons at interfaces. *Physics Reports*, 260(1-2):1–138, 1995. doi: 10.1016/0370-1573(95)00006-3.

[35] K. Kjaer, J. Als-Nielsen, C. A. Helm, L. Laxhuber, and H. Möhwald. Ordering in lipid monolayers studied by synchrotron X-ray diffraction and fluorescence microscopy. *Physical Review Letters*, 58(21):2224–2227, 1987. doi: 10.1103/PhysRevLett.58.2224.

[36] Cristina Stefaniu, Gerald Brezesinski, and Helmuth Möhwald. Langmuir monolayers as models to study processes at membrane surfaces. *Advances in Colloid and Interface Science*, 208:197–213, 2014. doi: 10.1016/j.cis.2014.02.013.

[37] A. Blume. Lipids at the air–water interface. *ChemTexts*, 4(1), 2018. doi: 10.1007/s40828-018-0058-z.

[38] F. Reise, J. E. Warias, K. Chatterjee, N. R. Krekiehn, O. Magnussen, B. M. Murphy, and T. K. Lindhorst. Photoswitchable glycolipid mimetics: Synthesis and photochromic properties of glycoazobenzene amphiphiles. *Chemistry A European Journal*, 24(66):17497–17505, 2018. doi: 10.1002/chem.201803112.

[39] B. M. Murphy, M. Greve, B. Runge, C. T. Koops, A. Elsen, J. Stettner, O. H. Seeck, and O. M. Magnussen. A novel X-ray diffractometer for studies of liquid-liquid interfaces. *Journal of Synchrotron Radiation*, 21(Pt 1):45–56, 2014. doi: 10.1107/S1600577513026192.

[40] O. H. Seeck, C. Deiter, K. Pflaum, F. Bertam, A. Beerlink, H. Franz, J. Horbach, H. Schulte-Schrepping, Bridget M. Murphy, M. Greve, and O. Magnussen. The high-resolution diffraction beamline P08 at PETRA III. *Journal of Synchrotron Radiation*, 19(Pt 1):30–38, 2012. doi: 10.1107/S0909049511047236.

[41] N. L. Yamada, N. Torikai, K. Mitamura, H. Sagehashi, S. Sato, H. Seto, T. Sugita, S. Goko, M. Furusaka, T. Oda, M. Hino, T. Fujiwara, H. Takahashi, and A. Takahara. Design and performance of horizontal-type neutron reflectometer sofia at j-parc/mlf. *The European Physical Journal Plus*, 126(11):1–13, 2011. doi: 10.1140/epjp/i2011-11108-7.

[42] K. Mitamura, N. L. Yamada, H. Sagehashi, N. Torikai, H. Arita, M. Terada, M. Kobayashi, S. Sato, H. Seto, S. Goko, M. Furusaka, T. Oda, M. Hino, H. Jinnai, and A. Takahara. Novel neutron reflectometer sofia at j-parc/mlf for in-situ soft-interface characterization. *Polymer Journal*, 45(1):100–108, 2013. doi: 10.1038/pj.2012.156.

[43] A. R. J. Nelson and S. W. Prescott. refnx: neutron and X-ray reflectometry analysis in python. *Journal of Applied Crystallography*, 52(Pt 1):193–200, 2019. doi: 10.1107/S1600576718017296.

[44] L. G. Parratt. Surface studies of solids by total reflection of X-rays. *Physical Review*, 95(2):359–369, 1954. doi: 10.1103/PhysRev.95.359.

[45] Cary W. McConlogue and T. Kyle Vanderlick. A close look at domain formation in dppc monolayers. *Langmuir*, 13(26):7158–7164, 1997. doi: 10.1021/la970898e.

[46] Heidi M. Mansour and George Zografi. Relationships between equilibrium spreading pressure and phase equilibria of phospholipid bilayers and monolayers at the air-water interface. *Langmuir*, 23(7):3809–3819, 2007. doi: 10.1021/la063053o.

[47] D. Vollhardt and V. B. Fainerman. Kinetics of two-dimensional phase transition of langmuir monolayers. *The Journal of Physical Chemistry B*, 106(2):345–351, 2002. doi: 10.1021/jp012798u.

[48] D. Vollhardt. Brewster angle microscopy: A preferential method for mesoscopic characterization of monolayers at the air/water interface. *Current Opinion in Colloid & Interface Science*, 19(3):183–197, 2014. doi: 10.1016/j.cocis.2014.02.001.

[49] V. M. Kaganer, I. R. Peterson, R. M. Kenn, M. C. Shih, M. Durbin, and P. Dutta. Tilted phases of fatty acid monolayers. *The Journal of Chemical Physics*, 102(23):9412–9422, 1995. doi: 10.1063/1.468809.

[50] H. Haas, W. Caetano, G. P. Borissevitch, M. Tabak, M. I. Mosquera Sanchez, O. N. Oliveira, Enrico Scalas, and Michel Goldmann. Interaction of dipyridamole with phospholipid monolayers at the air–water interface: Surface pressure and grazing incidence X-ray diffraction studies. *Chemical Physics Letters*, 335(5-6): 510–516, 2001. doi: 10.1016/S0009-2614(00)01464-0.

[51] V. F. Sears. Neutron scattering lengths and cross sections. *Neutron News*, 3(3):26–37, 1992.

[52] Maciek R. Antoniewicz, Joanne K. Kelleher, and Gregory Stephanopoulos. Measuring deuterium enrichment of glucose hydrogen atoms by gas chromatography/mass spectrometry. *Analytical Chemistry*, 83(8):3211–3216, 2011. doi: 10.1021/ac200012p.

SUPPLEMENTARY INFORMATION

S1 Langmuir isotherms, compressibility and time resolved surface pressure

While performing the XRR and GID measurements at the LISA end station at P08, the surface pressure was recorded constantly to monitor any surface pressure changes and to correlated these to the observed structural changes. The isotherms shown in Fig. S1, Fig. S2 and Fig. S3 were collected before starting the XRR and GID measurements to verify the successful formation of a Langmuir monolayer and to detect the surface pressures of interest around the additional phase transitions LC' . The compressibility C is derived from the slope of the compression isotherm by

$$C = -\frac{1}{A}\left(\frac{\delta A}{\delta \pi}\right) \tag{2}$$

with the area per molecule A and the surface pressure π. For the isotherms shown in Fig. S1, Fig. S2 and Fig. S3, the compressibility was calculated with Eq. 2 by determining the gradient for every ten data point. This corresponds to a binning of the data to 10 s intervals as the data were collected with one data point per second. The horizontal lines mark the LC' phase transitions.

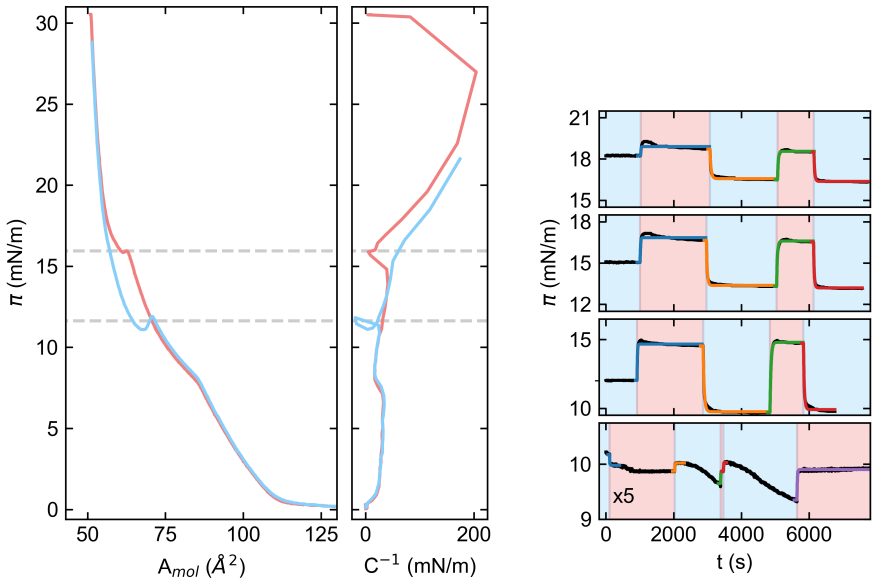

Figure S1. Left: Langmuir isotherm of mixed 9:1 DPPC:**1** (no sugar) monolayer for its *trans* (blue) and *cis* (red) state and the calculated compressibility marking the phase transitions. On the right the time resolved surface pressure change upon illumination with 365 nm (red) and 455 nm nm (blue coloured background) and their fits (varicoloured) to determine the time constant τ.

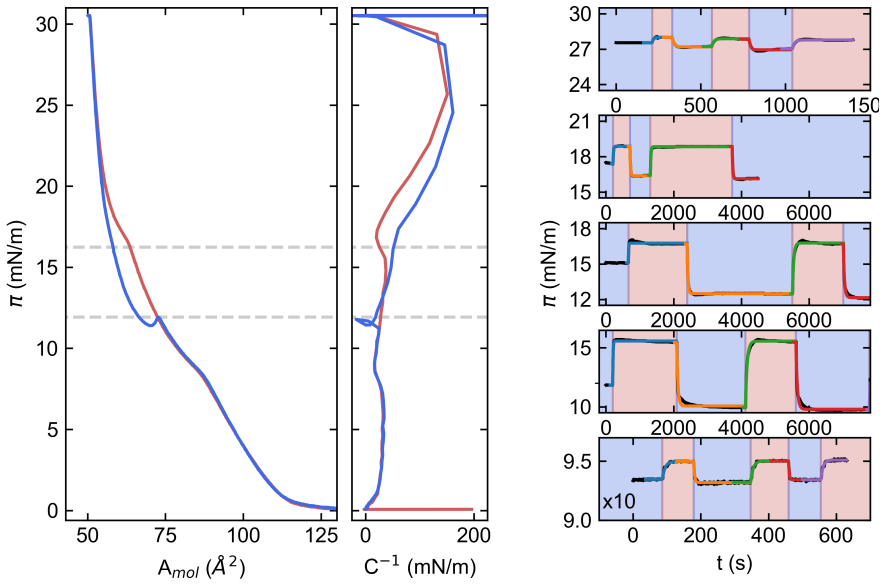

Figure S2. Left: Langmuir isotherm of mixed 9:1 DPPC:**2** (glucose) monolayer for its *trans* (blue) and *cis* (red) state and the calculated compressibility marking the phase transitions. On the right the time resolved surface pressure change upon illumination with 365 nm (red) and 455 nm nm (blue coloured background) and their fits (varicoloured) to determine the time constant τ.

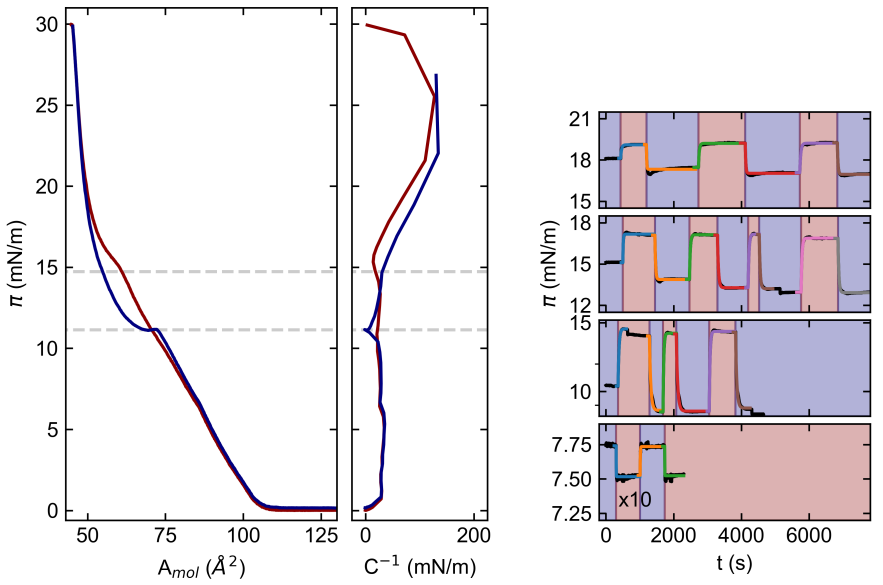

Figure S3. Left: Langmuir isotherm of mixed 9:1 DPPC:**3** (lactose) monolayer for its *trans* (blue) and *cis* (red) state and the calculated compressibility marking the phase transitions. On the right the time resolved surface pressure change upon illumination with 365 nm (red) and 455 nm nm (blue coloured background) and their fits (varicoloured) to determine the time constant τ.

S2 Grazing incidence X-ray diffraction images and results

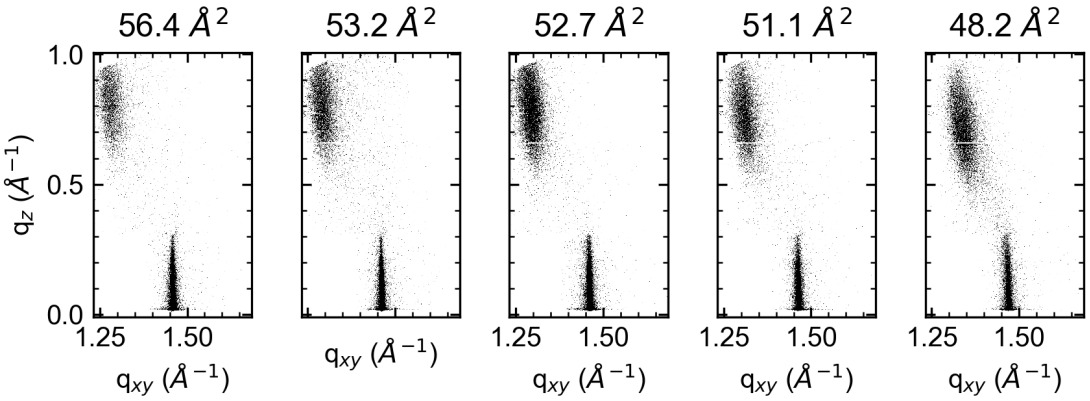

Figure S4. GID images taken from a pure DPPC monolayer at various area per molecules.

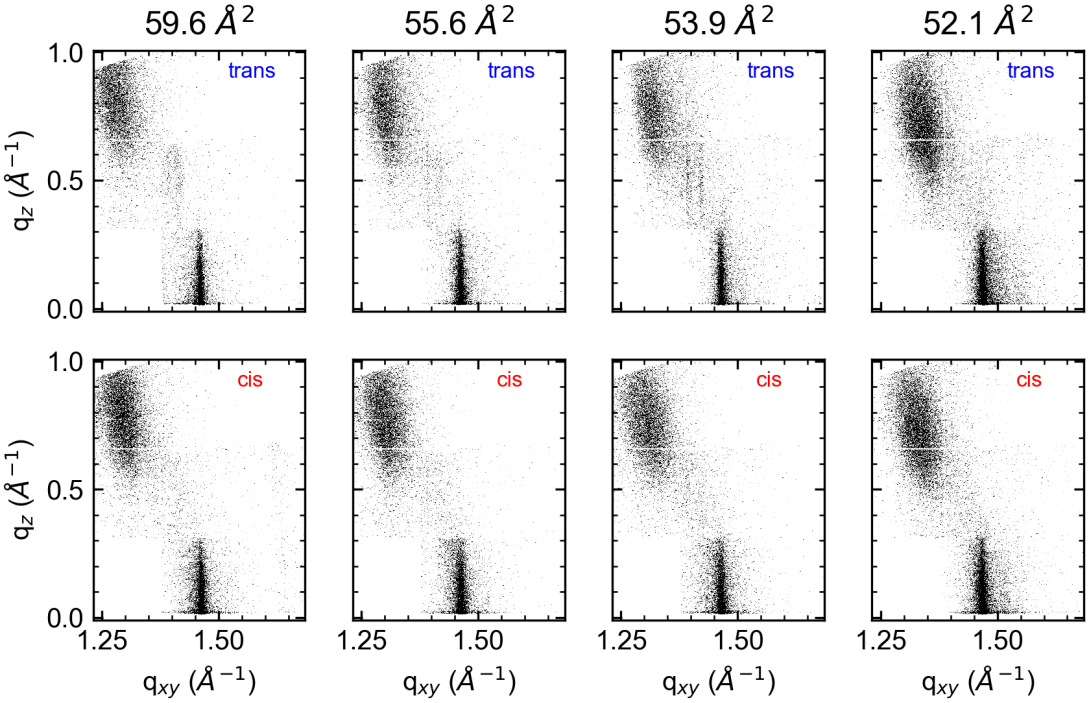

Figure S5. GID images taken from a monolayer made of 9:1 DPPC:**1** (glucose) at various area per molecules for the *trans* and *cis* states of the azobenzene mimetic **1**.

Table S1. GID results of pure DPPC monolayers at 21 °C: Bragg peak and Bragg rod positions (upper row) and the respective widths (lower row).

A_{mol} / Å^2	π / mN m^{-1}	state	$q_{xy,01/10}$ / Å^{-1}	$q_{z,01/10}$/ Å^{-1}	$q_{xy,1-1}$ / Å^{-1}	$q_{z,1-1)}$/ Å^{-1}
DPPC						
56.4	9		1.287(2)	0.787(2)	1.458(2)	0.095(3)
			0.080(1)	0.330(5)	0.012(1)	0.233(7)
53.2	12		1.297(2)	0.784(2)	1.460(2)	0.096(3)
			0.072(1)	0.32(5)	0.012(1)	0.243(9)
52.7	15		1.297(2)	0.771(2)	1.461(2)	0.096(3)
			0.076(1)	0.339(5)	0.012(1)	0.238(9)
51.1	18		1.312(2)	0.763(2)	1.463(2)	0.102(3)
			0.078(1)	0.346(5)	0.015(1)	0.235(1)
48.2	30		1.342(2)	0.710(2)	1.467(2)	0.109(4)
			0.084(1)	0.367(5)	0.021(1)	0.245(12)

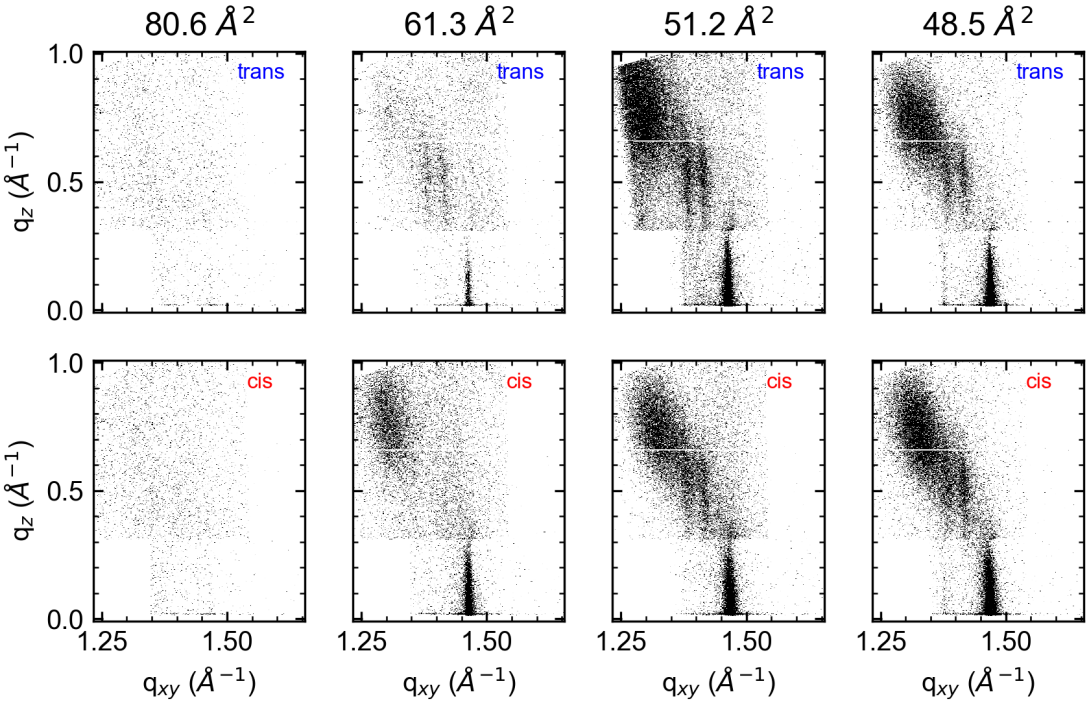

Figure S6. GID images taken from a monolayer made of 9:1 DPPC:**3** (lactose) at various area per molecules for the *trans* and *cis* states of the azobenzene mimetic **3**.

Table S2. GID results of mixed 9:1 DPPC:**1** (no sugar) monolayers at 21 °C: Bragg peak and Bragg rod positions (upper row) and the respective widths (lower row).

A_{mol} / Å^2	π / mN m^{-1}	state	$q_{xy,01/10}$ / Å^{-1}	$q_{z,01/10}$/ Å^{-1}	$q_{xy,1-1}$ / Å^{-1}	$q_{z,1-1)}$/ Å^{-1}
DPPC:**1**						
59.6	9.80	*trans*	1.282(2) 0.099(2)	0.764(2) 0.386(5)	1.460(2) 0.011(1)	0.100(3) 0.221(9)
59.6	14.75	*cis*	1.295(2) 0.085(1)	0.759(2) 0.353(5)	1.462(2) 0.012(1)	0.100(3) 0.243(9)
55.6	13.31	*trans*	1.304(2) 0.084(1)	0.761(2) 0.379(5)	1.461(2) 0.014(1)	0.100(3) 0.226(9)
55.6	16.94	*cis*	1.302(2) 0.089(1)	0.756(2) 0.381(5)	1.462(2) 0.016(1)	0.109(4) 0.25(12)
53.9	16.39	*trans*	1.320(2) 0.069(1)	0.749(2) 0.349(5)	1.464(2) 0.014(1)	0.107(3) 0.231(9)
53.9	18.65	*cis*	1.307(2) 0.097(1)	0.746(2) 0.372(5)	1.464(2) 0.016(1)	0.107(4) 0.252(12)
52.1	30.15	*trans*	1.332(2) 0.083(1)	0.717(2) 0.367(5)	1.467(2) 0.014(1)	0.102(3) 0.257(9)
52.1	29.45	*cis*	1.340(2) 0.079(1)	0.713(2) 0.370(5)	1.468(2) 0.013(1)	0.100(3) 0.235(9)

Table S3. GID results of mixed 9:1 DPPC:**2** (glucose) at 21 °C: Bragg peak and Bragg rod positions (upper row) and the respective widths (lower row).

A_{mol} / Å^2	π / mN m^{-1}	state	$q_{xy,01/10}$ / Å^{-1}	$q_{z,01/10}$/ Å^{-1}	$q_{xy,1-1}$ / Å^{-1}	$q_{z,1-1)}$/ Å^{-1}
82.4	9.10	*trans*	1.309(2) 0.082(5)	0.658(7) 0.419(19)	1.464(2) 0.011(1)	0.108(6) 0.252(19)
82.4	8.95	*cis*	1.311(2) 0.089(5)	0.649(8) 0.405(21)	1.463(2) 0.012(1)	0.110(7) 0.261(21)
63.0	10.35	*trans*	1.287(2) 0.080(16)	0.762(2) 0.334(5)	1.460(2) 0.012(1)	0.097(4) 0.245(9)
63.0	15.80	*cis*	1.303(2) 0.079(2)	0.748(2) 0.337(5)	1.463(2) 0.012(1)	0.099(7) 0.233(9)
60.1	12.39	*trans*	1.301(2) 0.077(2)	0.761(2) 0.323(5)	1.461(2) 0.013(1)	0.099(3) 0.235(9)
60.1	16.83	*cis*	1.320(2) 0.077(2)	0.747(2) 0.323(5)	1.463(2) 0.012(1)	0.103(3) 0.25(9)
56.4	17.05	*trans*	1.312(2) 0.101(2)	0.742(2) 0.384(5)	1.463(2) 0.017(1)	0.107(3) 0.240(9)
56.4	19.17	*cis*	1.336(2) 0.065(2)	0.719(2) 0.294(5)	1.467(2) 0.013(1)	0.233(3) 0.294(5)
50.2	27.72	*trans*	1.346(2) 0.086(2)	0.688(2) 0.363(5)	1.470(2) 0.018(1)	0.115(4) 0.363(5)
50.2	27.95	*cis*	1.350(2) 0.093(2)	0.686(2) 0.363(5)	1.469(2) 0.021(1)	0.116(4) 0.266(12)

Table S4. GID results of mixed 9:1 DPPC:**3** (lactose) monolayers at 21 °C: Bragg peak and Bragg rod positions (upper row) and the respective widths (lower row).

A_{mol} / Å^2	π / mN m^{-1}	state	$q_{xy,01/10}$ / Å^{-1}	$q_{z,01/10}$/ Å^{-1}	$q_{xy,1-1}$ / Å^{-1}	$q_{z,1-1)}$/ Å^{-1}
80.6	7.74	*trans*	1.329(2) 0.054(7)	0.60(2) 0.306(50)	1.466(2) 0.012(9)	0.105(2) 0.306(50)
80.6	7.52	*cis*	1.327(2) 0.068(5)	0.630(2) 0.377(50)	1.466(2) 0.009(12)	0.109(2) 0.283(5)
61.3	8.79	*trans*	1.300(2) 0.054(5)	0.735(4) 0.184(9)	1.462(2) 0.013(1)	0.098(4) 0.252(5)
61.3	14.30	*cis*	1.311(2) 0.073(2)	0.758(2) 0.318(5)	1.463(2) 0.016(1)	0.100(4) 0.264(12)
51.2	12.92	*trans*	1.302(1) 0.094(2)	0.773(2) 0.412(5)	1.463(2) 0.014(1)	0.099(3) 0.226(7)
51.2	16.86	*cis*	1.329(2) 0.083(2)	0.752(2) 0.308(5)	1.466(2) 0.021(1)	0.105(3) 0.258(1)
48.5	16.93	*trans*	1.326(2) 0.087(2)	0.745(2) 0.308(5)	1.468(2) 0.013(1)	0.092(3) 0.231(7)
48.5	19.20	*cis*	1.329(2) 0.085(2)	0.742(2) 0.325(5)	1.467(2) 0.021(1)	0.106(3) 0.252(9)

Table S5. GID results of mixed monolayers at 21 °C: Bragg peak and Bragg rod positions (upper row) and the respective widths (lower row) from the additional peaks belonging to the head group ordering.

A_{mol} / Å^2	π / mN m^{-1}	state	$q_{xy,1}$ / Å^{-1}	$q_{z,1}$/ Å^{-1}	$q_{xy,2}$ / Å^{-1}	$q_{z,2}$/ Å^{-1}	$q_{xy,3}$ / Å^{-1}	$q_{z,3}$/ Å^{-1}
DPPC:**1**								(no sugar)
59.6	9.80	*trans*	1.394(2)	0.535(6)	1.418(2)	0.477(6)	1.682(2)	0.07(2)
			0.007(2)	0.492(16)	0.006(1)	0.398(16)	0.006(2)	0.235(7)
55.6	13.31	*trans*	1.391(2)	0.552(7)	1.420(2)	0.46(1)	1.674(2)	0.04(3)
			0.004(1)	0.553(19)	0.006(1)	0.518(24)	0.008(2)	0.188(7)
53.9	16.39	*trans*	1.391(2)	0.575(5)	1.421(2)	0.45(1)	1.675(2)	0.10(2)
			0.006(2)	0.466(12)	0.006(1)	0.542(24)	0.004(1)	0.188(9)
DPPC:**2**								(glucose)
63.0	10.35	*trans*	1.386(2)	0.545(5)	1.415(2)	0.504(5)	1.673(2)	0.078(6)
			0.021(1)	0.391(12)	0.017(1)	0.341(12)	0.009(1)	0.132(19)
60.1	12.39	*trans*	1.385(2)	0.570(5)	1.416(2)	0.513(6)	1.674(2)	0.087(9)
			0.031(2)	0.396(12)	0.024(1)	0.412(16)	0.008(1)	0.188(5)
DPPC:**3**								(lactose)
61.3	8.79	*trans*	1.381(2)	0.540(5)	1.414(2)	0.491(5)		
			0.035(5)	0.379(12)	0.035(5)	0.363(12)		
51.2	12.92	*trans*	1.377(2)	0.567(3)	1.414(2)	0.515(4)		
			0.049(5)	0.502(9)	0.384(2)	0.462(9)		
51.2	16.86	*cis*	1.375(2)	0.588(3)	1.415(2)	0.504(3)		
			0.064(5)	0.398(7)	0.047(5)	0.433(9)		
48.5	16.93	*trans*	1.378(3)	0.582(2)	1.414(2)	0.512(3)		
			0.045(9)	0.367(7)	0.033(2)	0.332(7)		
48.5	19.20	*cis*	1.374(2)	0.580(2)	1.414(2)	0.505(3)		
			0.073(12)	0.377(5)	0.038(2)	0.353(7)		

S3 X-ray and neutron reflectivity results

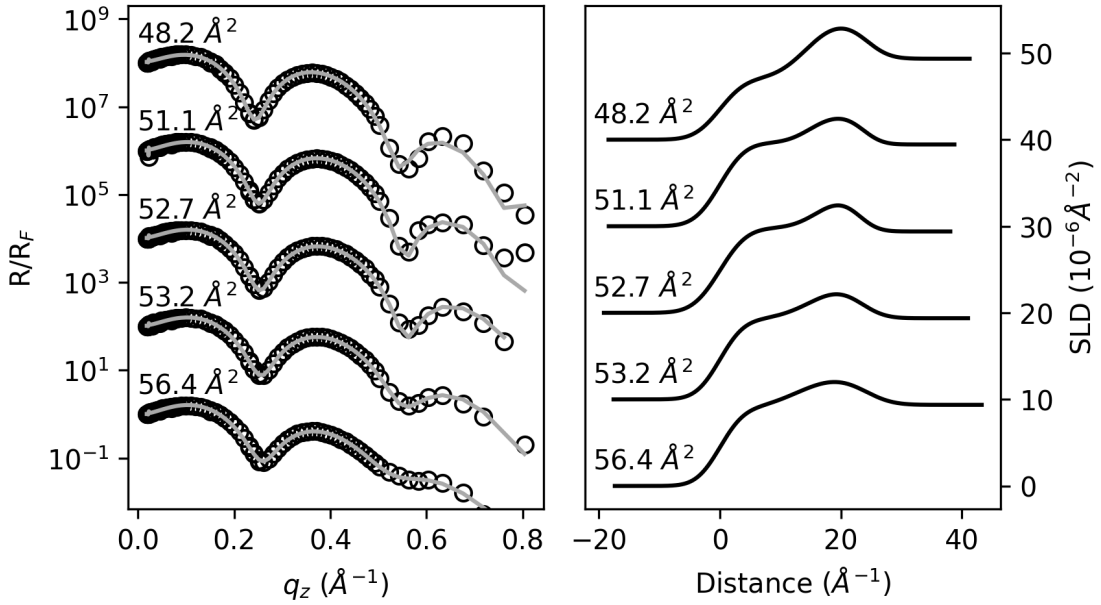

Figure S7. XRR data normalised by the Fresnel reflectivity for an ideal interface with no roughness from the pure DPPC monolayer with the model fit (left) and the derived SLD profiles at various area per molecules. The data are offset for clarity.

Table S6. Fit parameters for the pure DPPC monolayer obtained from fits of the XRR data modelled with a two-slab model. Listed are values of the layer thickness l, the scattering length density SLD for each slab and the roughness σ at the interface of the slab for the water, head and tail layer. The SLD for the water layer was fitted to 9.39 10^{-6}Å^{-2}. The uncertainties of the fitted values are 0.3 Å^2 for the thicknesses l, are 0.10×10^{-6} Å^{-2} for the SLD and 0.1 Å for the roughness σ.

A_{mol}	π / mN m^{-1}	l_{total} / Å	l_{head} / Å	l_{tail} / Å	SLD_{head} / 10^{-6}Å^{-2}	SLD_{tail} / 10^{-6}Å^{-2}	σ_{water} / Å	$\sigma_{head/tail}$ / Å
56.4	9	23.84	10.98	12.86	13.09	8.87	3.61	5.15
53.2	12	22.92	6.91	16.00	14.78	9.19	3.28	5.22
52.7	15	22.87	6.66	16.20	14.17	9.80	2.56	3.50
51.1	18	23.67	8.74	14.92	14.09	9.63	2.53	3.21
48.2	30	24.15	9.95	14.20	13.80	7.05	3.04	4.01

Langmuir isotherms

During the NR beamtime, Langmuir isotherms with a compression speed of 31.8(5) cm^2 min^{-1} were collected as shown in Fig. S8. The isotherms shift to higher surface pressure for the mixed monolayers with the deuterated d_{62}DPPC compared to the DPPC containing monolayer. The area per molecules for the measurements were chosen based on the appearance of the additional phase transitions LC'_{trans} and LC'_{cis}.

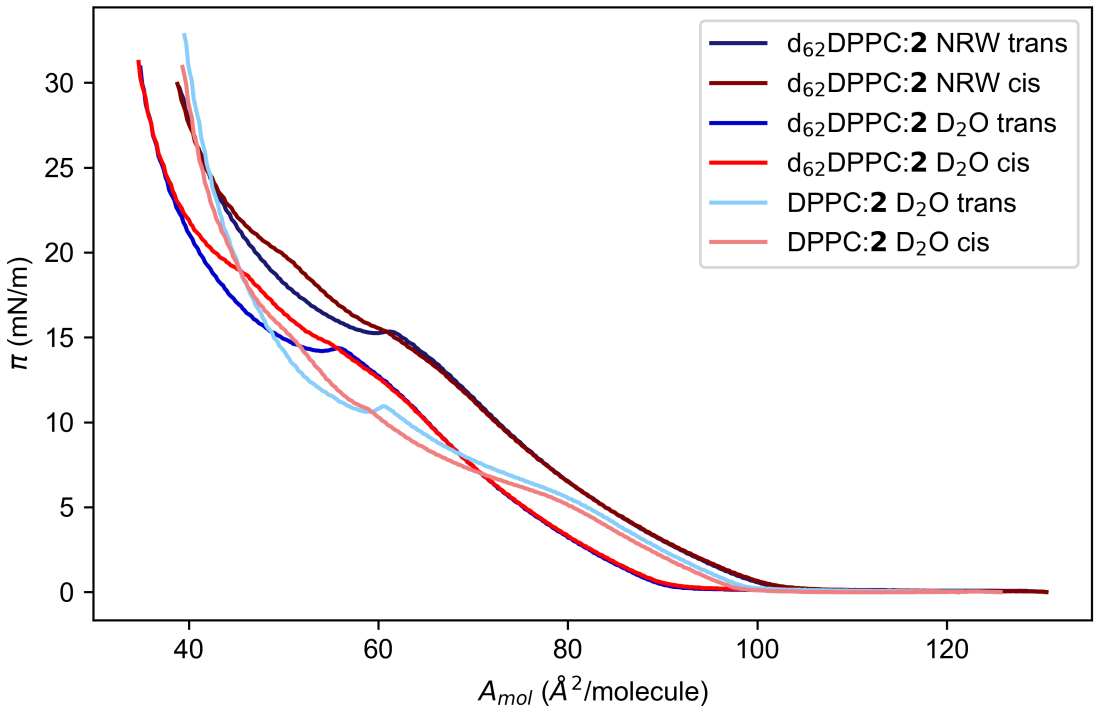

Figure S8. Langmuir isotherms of the mixed 9:1 DPPC:**2** (glucose) monolayer on D_2O , d_{62}DPPC:**2** monolayer on D_2O and DPPC:**2** monolayer on NRW for the *trans* (blue) and *cis* (red) isomer of the mimetic **2**.

5.2 Further continuative and collaborative work on Langmuir monolayers

Within the scope of this work, a number of bachelor theses investigating different aspects of influences on the switching behaviour in Langmuir monolayers were supervised.

Karin Hansen, Kiel University, investigated the influence of the intensity of the light used to switch the lipids between their *trans* and *cis* state [202]. Langmuir isotherm measurements were performed and the surface pressure change upon switching in dependency to different light intensities was collected. These measurements showed that the time to reach 63 % of the maximum pressure difference after starting the illumination with either 365 nm or 455 nm is proportional to a power function of the light intensity.

Another research question studied by Sonja Reinheimer, Kiel University, was how the switching behaviour induced by the azobenzene amphiphiles differs in monolayers with one of the alternative phospholipids 1,2-Dipalmitoyl-*sn*-glycero-3-phosphate (DPPA), 1,2-Dipalmitoyl-*sn*-glycero-3-phosphoglycerol (DPPG) and 1,2-Dipalmitoyl-*sn*-glycero-3-phosphoethanolamine (DPPE) [203] instead of the phospholipid DPPC that is used in this work. For all combinations of the mixed monolayers, a light-induced switching behaviour was observed. However, the findings suggest that the phospholipid DPPC is the best choice concerning pressure stability, short switching and illumination durations, solubility and the existence of all phases, from gaseous, liquid expanded and liquid condensed phase at 21 °C.

In the third bachelor thesis, the temperature influence on the switching behaviour in Langmuir monolayers with the observed and in this work discussed mesophase transition in lyotropic liquid crystals consisting of 80 % DPPC and 20 % of the AZOL-C16 mimetic was investigated by Ella Dieball, Kiel University [204]. The Langmuir monolayer measurements for pure DPPC and mixed monolayers with 20 % of the AZOL-C16 at temperatures between 21 °C and 45 °C showed a shift of the phase transitions to a lower surface area and a higher surface pressure with increasing temperature. Furthermore, at all temperatures, a light-induced surface pressure change could be observed. This is in contrast to the disappearance of light-induced phase transitions at higher temperatures than 37 °C in the corresponding lyotropic liquid crystals.

Further bachelor theses on similar Langmuir monolayers by Katharina Steinkirchner, Kiel University, [205] and Gesa Frahm, Kiel University, [206] were supported during the measurements and data analysis and discussion. Being part of the physical

chemistry group of Prof. Dr. Gernot Friedrichs, Gesa Frahm performed complementary vibrational sum frequency generation (VSFG) studies on Langmuir monolayers made of DPPC and AZGL-C16 with varied ratios of the azobenzene amphiphiles. With VSFG measurements the orientation of the molecules can be investigated. The studies verified that the alkyl chains of the AZGL-C16 molecules straighten up upon isomerisation from the *trans* state to the *cis* state in monolayers containing 5, 10, 50 and 100 % of the AZGL-C16 mimetics. The decrease of the tilt angle from the surface normal is in good agreement with the GID measurements in the manuscript [MSH 3]. In addition to the tail group orientation, the orientation of parts of the head group of the AZGL-C16 mimetic was investigated in mixed monolayers with a ratio of 50 %. For lower ratios of the AZGL-C16 mimetic, the signal intensity was too low to distinguish the vibration signal originating from the azo group of the azobenzene mimetic. Nevertheless, the measurements on the monolayer with 50 % of the AZGL-C16 mimetics support the hypothesis of a vertically orientated azobenzene group and a loss of the ordering upon the compression of the layer to lower surface areas or switching to the *cis* state. A similar trend has been seen in the GID measurements on the mixed monolayer with 10 % of the azobenzene mimetics (see [MSH 3]), for which a head group orientation for the *trans* isomers but not for the *cis* isomer was detected.

6
Photo-induced mesophase transitions in lyotropic liquid crystals

Understanding and controlling mesophase transitions in lipid aggregates are of high interest for drug delivery systems in pharmaceutical applications and to investigate membrane fusion processes. In the following sections, the studies on lyotropic liquid crystals with different composition of phospholipids and azobenzene mimetics showing light and temperature induced mesophase transitions and structural changes are presented. First, the results from the preparation measurements are given in Sec. 6.1 followed by an overview on the collected data and summary of the determined mesophases in Sec. 6.1. Next, the unpublished results from the SAXS measurements of samples containing the reference molecules are discussed in Sec. 6.3 and 6.4.

The chapter is concluded with the publication [PSH 1] and the manuscript [MSH 1] on light and temperature induced mesophase transitions from lamellar to bicontinuous cubic $Pn3m$ phase in compositions of the phospholipid DPPC and the AZOL-C16 mimetic and the time-resolved SAXS measurements revealing the kinetic of the light-induced mesophase transition. The reprint of [PSH 1] is included in Sec. 6.5 and the preprint of [MSH 1] in Sec. 6.6.

6.1 First preparation of lyotropic liquid crystals

In preparation for the synchrotron radiation beamtimes on the lyotropic liquid crystals, initial SAXS experiments were performed at a Bruker AXS Nanostar lab source at Helmholtz-Zentrum Hereon (HEREON) to verify successful sample preparation. During this time, the focus lay on the preparation of unilamellar vesicleunilamellar vesicles (ULVs) which are formed by extrusion of the hydrated samples through a membrane. These first tests were done in cooperation with the master student Jule Kuhn within the framework of her master lab course (official

name: Forschungspraktikum). The process and documentation of preparation steps as well as the challenges faced are noted down in the lab report [207]. After these first SAXS measurements, we refined and finalised our sample preparation protocol to the procedure described in Sec. 4.2. The successful preparation of vesicles and liquid crystals was proven during DSC measurements prior to the first SAXS measurements at BL2, DELTA. At DELTA, both non-extruded and extruded suspensions were measured to check their scattering intensity. Two main factors led to the suspension of ULVs during the measurements: firstly the scattering pattern of the extruded suspension (ULVs) was very faint and secondly the extrusion of mixed suspensions with higher ratio of azobenzene amphiphiles than phospholipids showed separation of the lipids and water solution upon pushing the suspension trough the membrane. Therefore, all following experiments were performed on hydrated samples without extrusion and thus not with ULVs.

6.2 Overview of the studied lyotropic liquid crystals

Combinations of the phospholipids DPPC or DLPC with one of the seven azobenzene amphiphiles or seven reference amphiphiles presented in Fig. 3.1 were investigated with different ratios between the phospholipids and azobenzene mimetics. Each combination and ratio was illuminated for 5 min with 365 nm or 455 nm light to collect the SAXS data for their *cis* and *trans* state, respectively. In Fig. 6.1 the observed mesophases for all lipid combinations are summarised. A light-induced mesophase transition is found in AZOL-C12, AZOL-C16 and AZ-R containing crystals in combination with DPPC. These three azobenzene mimetics have no sugar group attached at the head group. In contrast, for all other azobenzene mimetics with a glycan head group either a change in d-spacing or no light-induced change is observed. The publication [PSH 1], in Sec. 6.5, focuses on the observed light and temperature induced mesophase transitions in liquid crystals containing the AZOL-C16 derivative and the phospholipid DPPC. Motivated by the observation of a light-induced mesophase transition, the kinetics of this transition was studied with time-resolved SAXS measurements. These results on the kinetic are presented in the manuscript [MSH 1] in Sec. 6.6 together with the structures of a variety of aggregates containing combinations of either DPPC or DLPC phospholipids with one of the azobenzene mimetics AZOL-C12, AZGL-C12, AZGL-C16, AZLL-C12 and AZLL-C16.

In addition to the published results, SAXS data on crystals made of combinations

of the phospholipid DPPC with the mimetics AZ-R, a precursor in the synthesis of the azobenzene, and the reference mimetics without the azobenzene switch (see Fig. 3.1) were collected during the beamtimes at BL2, DELTA and at EMBL beamline P12, PETRA III. For these additional mimetics, only single ratios between the lipids were studied for comparison and proof of concept. The results of these unpublished data are discussed in Sec. 6.3 and Sec. 6.4.

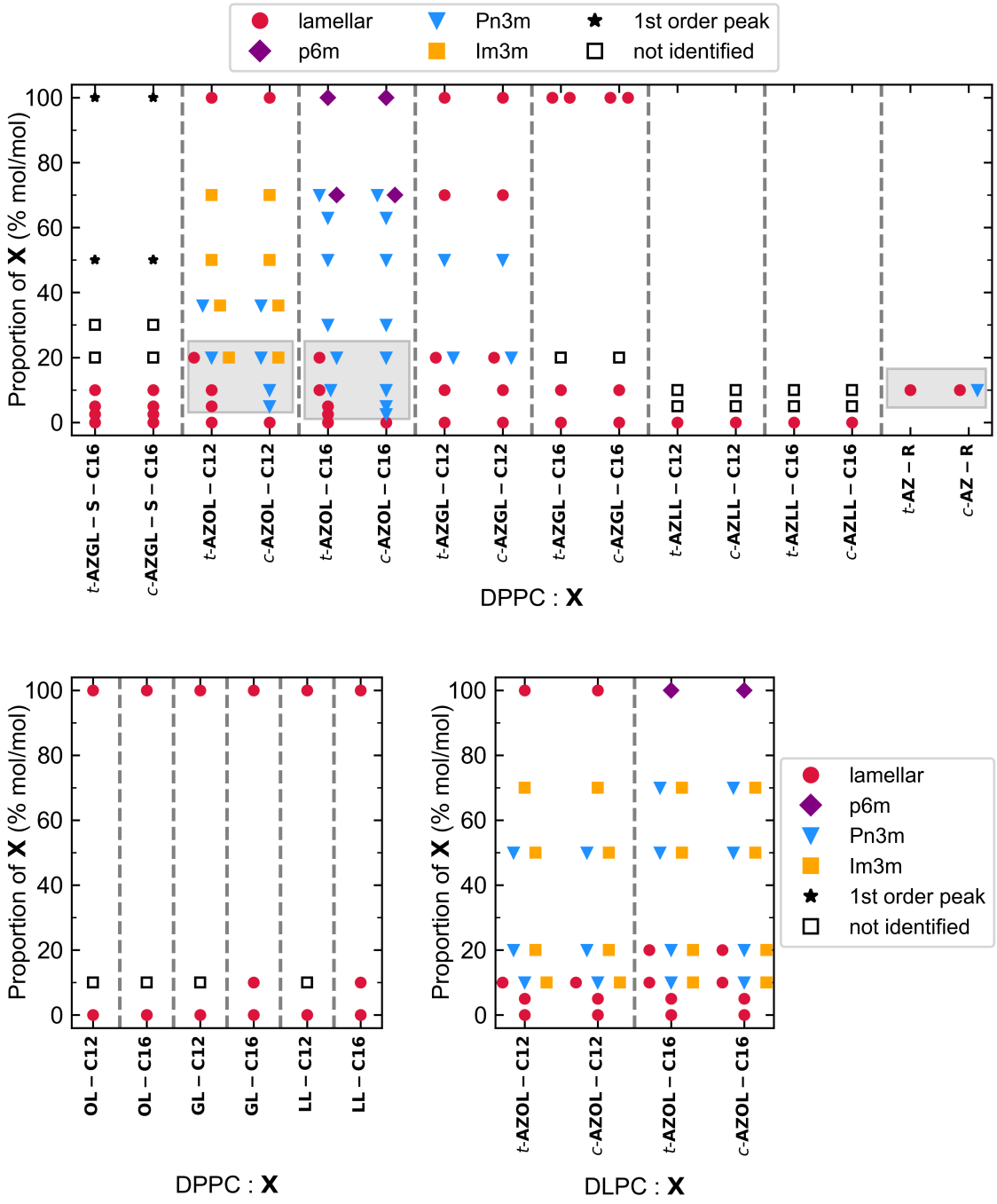

Figure 6.1: Mesophases for mixtures of DPPC or DLPC with the azobenzene amphiphiles shown in Fig. 3.1 for their *trans* (t) and *cis* (c) isomer. The grey highlighted combinations show a light-induced mesophase transition in the gel phase. This overview is based on the summary of mesophases in [MSH 1] and is completed with the results from [PSH 1] and the unpublished data of the AZ-R and reference mimetics.

6.3 Light-induced mesophase transition in aggregates containing the AZ-R mimetic

During the synthesis of the photoswitchable glycolipids the mimetic AZ-R, a precursor in the synthesis of the azobenzene mimetics (see Sec. 3.2), was collected for reference and testing measurements. One sample, an aggregate consisting of 10 % of the AZ-R derivative and 90 % of the phospholipid DPPC, was prepared following the sample preparation description in Sec. 4.2 and was measured during the first beamtime at BL2, DELTA using the *in situ* sample setup (see Sec. 4.5.4). The collected SAXS scattering signal is shown in Fig. 6.2 for the *trans* and *cis* state of the mixed aggregate together with the scattering signal of pure DPPC vesicles. Fitting of the scattering signal identified a lamellar phase for the *trans* state and a coexistence of the lamellar and bicontinuous cubic *Pn3m* phase in the *cis* state.

This light-induced mesophase transition from lamellar to cubic *Pn3m* is analogue to the investigated transition in crystals containing AZOL-C12 and AZOL-C16 (see Sec. 6.5 and 6.6). The fitted *d*-spacing value of (6.37 ± 0.03) nm for the AZ-R mimetic containing crystals in the *trans* state is almost the same as the lamellar distance of (6.35 ± 0.01) nm in DPPC multilamellar vesiclemultilamellar vesicles (MLVs). This suggests, that the AZ-R mimetic does not add to the bilayer thickness significantly.

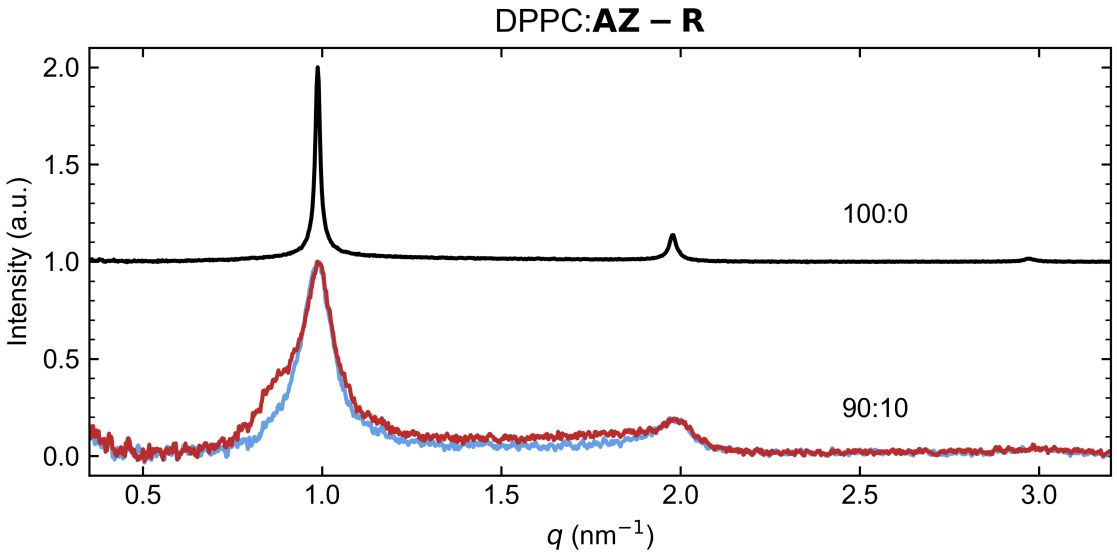

Figure 6.2: SAXS data of pure DPPC aggregates (black) and the 90:10 mixture of DPPC and the AZ-R mimetic (see Fig. 3.1) for the *trans* (blue) and *cis* (red) state. For clarity, the DPPC data has an offset.

This is in contrast to the determined *d*-spacings for the crystals containing 10 % AZOL-C12 or AZOL-C16. For these mimetics, an increase of the lamellar spacings by (0.45 ± 0.08) nm and (0.20 ± 0.03) nm, respectively, were found (see Sec. 6.5 and 6.6). Similar, the *d*-spacing for the *cis* isomers of the mixed crystals with AZ-R is smaller with a fit value of (10.1 ± 0.2) nm than the fitted values of (11.2 ± 0.4) nm and (11.2 ± 1.0) nm for AZOL-C12 and AZOL-C16, respectively. The reduced lamellar *d*-spacing for the AZ-R mimetic containing aggregates can be explained by the much smaller length of the mimetic compared to the other azobenzene mimetics (see Tab. 3.1).

However, there is one significant difference between the switching behaviours. Whereas for the aggregates containing the AZOL-C12 and AZOL-C16 mimetics the lamellar phase disappears completely upon switching to the *cis* state, a coexistence of the lamellar and cubic *Pn3m* phase is observed for the AZ-R-*cis* crystals. Further, the *d*-spacing of the lamellar phase is the same for the *trans* and *cis* state within the measurement uncertainty. The absence of a change in the *d*-spacing upon switching could be explained by an inhomogeneous distribution of the AZ-R mimetic among the liquid crystals. Some crystals do not contain the AZ-R mimetics and therefore do not change their structure upon illumination. In contrast, the AZ-R mimetic containing aggregates, show the mesophase transition to the cubic *Pn3m* phase. Due to the comparably large X-ray beam and superposition of the scattering signals from the differently composed aggregates, both phases are detected. Another explanation would be, that the AZ-R mimetic does not get integrated into the membrane. The azobenzene switch itself is slightly polar and thus the overall molecule can be considered hydrophilic. Yet, as a hydrophobic tail group is missing, the AZ-R mimetic is not amphiphilic and therefore the molecules are not self assembling at water interfaces. This could lead to only a partial integration of the mimetics in the aggregates. For a final conclusion on the origin of the different switching behaviour, further investigations would be needed. As the main focus in this work lies on photoswitchable amphiphiles and their influence on the membrane structure, the investigations on the AZ-R mimetic may be an interesting topic for future studies.

6.4 Structure of crystals containing the reference mimetics without the azobenzene switch

One of the research questions discussed in Chap. 5 and Sec. 6.6 is the question how the sugar group at the head group influences the switching behaviour of photoswitchable glycolipids in lipid membranes. To disentangle the influence of the sugar group and the azobenzene switch, aggregates containing the reference mimetics without the azobenzene switch but otherwise the same head and tail group (see Fig. 3.1) were investigated. The samples were prepared as described in Sec. 4.2 and measured at the EMBL beamline P12, PETRA III (see Sec. 4.5.5). The scattering data and the corresponding fitted *d*-spacing values are shown in Fig. 6.3. For all crystals consisting purely of the reference molecules a lamellar phase could be determined. The *d*-spacings of these MLVs increase with increasing head group size and length of the acyl chain in the tail group. For the mimetics with shorter acyl chain (C12) an increase of the *d*-spacings by (0.3 ± 0.3) nm and (0.7 ± 0.3) nm for the mimetics possessing a glucose or lactose group, respectively, compared to the spacing for the mimetics without sugar group in the head group is observed. This increase is only half of the difference of (0.5 ± 0.3) nm and (1.4 ± 0.3) nm found for the mimetics with longer acyl chain (C16). Comparing the *d*-spacing for the specific head groups but different tail lengths, the difference in *d*-spacing for the longer and shorter mimetics with no sugar, glucose and lactose head group are quite close with (1.3 ± 0.3) nm, (1.5 ± 0.3) nm and (1.9 ± 0.3) nm. This difference is slightly larger than the expected length difference of (1.0 ± 0.6) nm based on the determined lengths for the mimetics with 12 and 16 carbon atoms listed in Tab. 3.1.

One of the main findings from these reference measurements was that all reference mimetics form MLVs. This is in contrast to their corresponding azobenzene containing mimetic. A lamellar phase was only detected for aggregates made of either the AZOL-C12, AZGL-C12 or AZGL-C16 mimetics. In addition, the crystals consisting of the AZOL-C16 mimetic show a hexagonal *p6m* structure. Whereas, for the azobenzene mimetics with the lactose head group (AZLL-C12 and AZLL-C16) no crystals could be produced. During the sample preparation, large chunks of lipids formed which could not be broken up by either freeze-cycles, heated water baths, vortexing or ultra sonic baths. This led to the first hypothesis, that the lactose in the head group would prevent the formation of crystals. However, this hypothesis was rebutted by the successful preparation of the lactose containing reference molecules.

In addition to vesicles consisting of 100 % reference mimetics, mixtures of 90 %

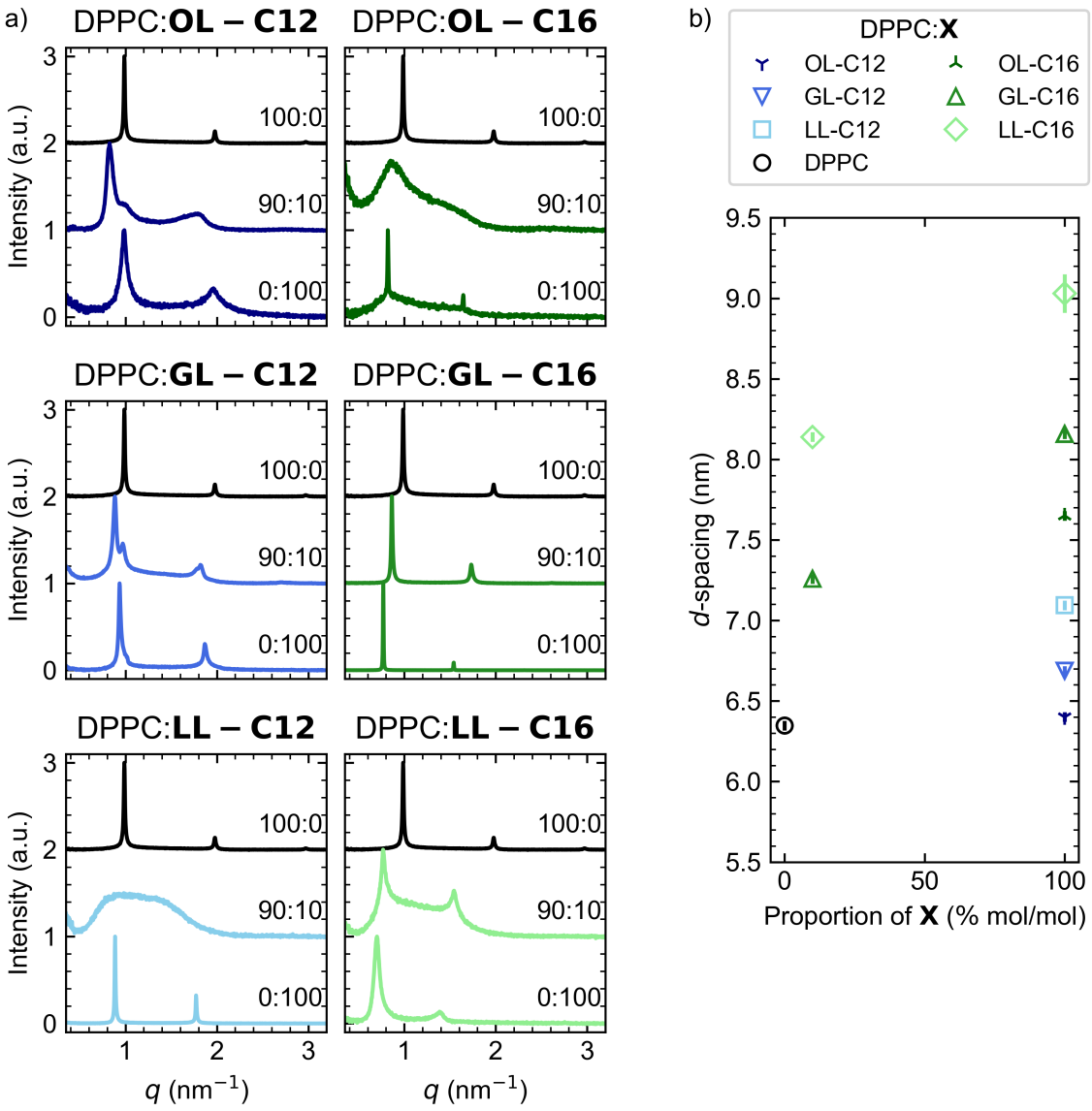

Figure 6.3: a) SAXS data for crystals containing the reference mimetics without azobenzene switch (see Fig. 3.1) with different ratios of the mimetics and b) the fitted *d*-spacing values.

DPPC and 10 % reference mimetics were investigated. Different to the MLVs found for 100 % of the reference molecules, the geometric structure and the corresponding mesophase could not be determined for all mixtures. The scattering signals of the mixtures with OL-C16 and LL-C12 only show a broad peak with no clear features, which makes it impossible to identify the structure. For the OL-C12 and GL-C12 mimetics containing mixtures, distinguished peaks were collected. However, fitting of these peak positions did not lead to a final conclusion on the geometric

structure. None of the structures belonging to the superposition of two lamellar phases, hexagonal phase or cubic phases (*Pn3m*, *Im3m*, *Pm3n*, *Fm3m*, *Fd3m* or *Ia3d*) gave a reasonable good fit result. Considering the peak around $0.9\,\text{Å}^{-1}$ and $1.8\,\text{Å}^{-1}$ are the first and second order peaks, respectively, the corresponding repeating distances are $(7.60 \pm 0.01)\,\text{nm}$, $(6.38 \pm 0.05)\,\text{nm}$ (1^{st} order) and $(7.2 \pm 0.3)\,\text{nm}$ (2^{nd} order) and $(7.12 \pm 0.01)\,\text{nm}$, $(6.49 \pm 0.02)\,\text{nm}$ (1^{st} order), $(7.08 \pm 0.02)\,\text{nm}$ and $(6.88 \pm 0.02)\,\text{nm}$ (2^{nd} order), respectively, for the mixed OL-C12 and GL-C12 aggregates. Meanwhile, a lamellar phase in mixtures with GL-C16 and LL-C16 were found. These fitted d-spacing values are between the values for pure DPPC and pure GL-C16 or LL-C16, respectively, as shown in Fig. 6.3b.

6.5 [PSH 1] Photoinduced bidirectional mesophase transition in vesicles containing azobenzene amphiphiles

The following publication [PSH 1] on photoinduced bidirectional mesophase transition in vesicles containing azobenzene amphiphiles was published in July 2024 as a research letter in the journal IUCrJ and is part of the online special issue of collected articles from the IUCr 2023 Congress in Melbourne, Australia. In this article, the structure of lyotropic liquid crystals consisting of DPPC and the photoswitchable AZOL-C16 are investigated with SAXS and DSC. These measurements revealed a light-induced mesophase transition between the MLV phase in the *trans* state to the bicontinuous cubic $Pn3m$ phase in the *cis* state in crystals containing up to 20 % of AZOL-C16 at room temperature. Similarly, temperature dependent measurements show a mesophase transition for crystals in the *trans* state during the gel-to-liquid crystalline phase transition at around 33 °C. Whereas for crystals in the *cis* state, no such transition was observed. Furthermore, illuminating the sample to switch between the *trans* and *cis* isomer at temperatures above 33 °C showed no structural difference between the two isomers. This discovery of a reversible and repeatable light-induced phase transition in aggregates containing photoswitchable glycolipids indicates first steps to create model systems to design drug delivery systems and study membrane fusion processes.

The SAXS measurements were conducted at beamline BL2, DELTA (see Sec. 4.5.4) and the DSC measurements at P08, DESY. Compared to the nomenclature in this thesis, the azobenzene mimetic AZOL-C16 is referred to as mimetic **1** in the following article (compare Fig. 3.1 with Fig. 1 in the article).

The article is available under `https://doi.org/10.1107/S2052252524004032` and is reproduced with permission of the International Union of Crystallography.

research letters

IUCrJ
ISSN 2052-2525
PHYSICS | FELS

Photoinduced bidirectional mesophase transition in vesicles containing azobenzene amphiphiles

Svenja C. Hövelmann,[a,b,c] Ella Dieball,[a] Jule Kuhn,[a] Michelle Dargasz,[d] Rajendra P. Giri,[a]‡ Franziska Reise,[e] Michael Paulus,[f] Thisbe K. Lindhorst[e] and Bridget M. Murphy[a,c]*

[a]Institute of Experimental and Applied Physics, Kiel University, Leibnizstraße 19, 24118 Kiel, Germany, [b]Deutsche Elektronen-Synchrotron DESY, Notkestraße 85, 22607 Hamburg, Germany, [c]Ruprecht Haensel Laboratory, Olshausenstraße 40, 24098 Kiel, Germany, [d]Department Physik, Universität Siegen, Walter-Flex-Strasse 3, 57072 Siegen, Germany, [e]Otto Diels Institute of Organic Chemistry, Kiel University, Otto-Hahn-Platz 3-4, 24118 Kiel, Germany, and [f]Fakultät Physik/DELTA, TU Dortmund, 44221 Dortmund, Germany. *Correspondence e-mail: murphy@physik.uni-kiel.de

Received 6 March 2024
Accepted 2 May 2024

Edited by F. Maia, Uppsala University, Sweden

This article is part of a collection of articles from the IUCr 2023 Congress in Melbourne, Australia, and commemorates the 75th anniversary of the IUCr.

‡ Present address: Department of Physics, Indian Institute of Technology (ISM) Dhanbad, Jharkhand 826004, India.

Keywords: lipid mesophase; photoswitches; azobenzene; vesicles; small-angle X-ray scattering; light-induced mesophase transformations; temperature-induced mesophase changes; structure determination; solution scattering; structural biology; SAXS.

Supporting information: this article has supporting information at www.iucrj.org

The functionality and efficiency of proteins within a biological membrane are highly dependent on both the membrane lipid composition and the physiochemical properties of the solution. Lipid mesophases are directly influenced by changes in temperature, pH, water content or due to individual properties of single lipids such as photoswitchability. In this work, we were able to induce light- and temperature-driven mesophase transitions in a model membrane system containing a mixture of 1,2-dipalmitoyl-phosphatidylcholine phospholipids and azobenzene amphiphiles. We observed reversible and reproducible transitions between the lamellar and *Pn3m* cubic phase after illuminating the sample for 5 min with light of 365 and 455 nm wavelengths, respectively, to switch between the *cis* and *trans* states of the azobenzene N=N double bond. These light-controlled mesophase transitions were found for mixed complexes with up to 20% content of the photosensitive molecule and at temperatures below the gel-to-liquid crystalline phase transition temperature of 33°C. Our results demonstrate the potential to design bespoke model systems to study the response of membrane lipids and proteins upon changes in mesophase without altering the environment and thus provide a possible basis for drug delivery systems.

1. Introduction

Lipid membranes are a fundamental part of biological cells and contain various components such as phospholipids, cholesterol and proteins. Phospholipids are the main component of bilayer membranes and their composition determines the membrane properties and mesophase (Shah *et al.*, 2001; Yang *et al.*, 2012; Cavalcanti *et al.*, 2006; van Meer *et al.*, 2008). The lipid mesophase is of great interest for efficient drug transportation and release of pharmaceuticals because of the possibility of opening the water channel via phase changes, or due to its influence on membrane protein activity and efficiency (Shah *et al.*, 2001; Sagalowicz *et al.*, 2006; Cournia *et al.*, 2015; Hirlekar *et al.*, 2010). Lipid mesophases have multiple geometric shapes and structures which evolve when amphiphilic lipids such as phospholipids come in contact with water. The explicit geometric shape depends on multiple properties such as temperature, pH, salinity, volume concentration (% *w*/*w*) and lipid curvature, which can be quantified by the critical packing parameter *CPP* (McManus *et al.*, 2003; Di Cola *et al.*, 2016; Shah *et al.*, 2001). Changes in these properties can lead to structural changes and even a transition into another

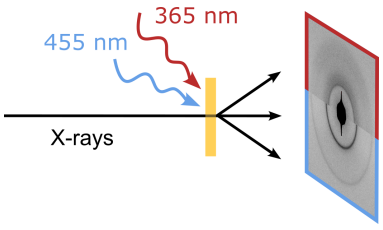

mesophase. These transitions can be used in bio-hybrid microsystems as biological actuators and sensors (Carlsen & Sitti, 2014). Different approaches to induce phase transitions have been studied extensively for application in drug delivery systems or for manipulation of proteins. Previous approaches employ temperature and water content (% *w*/*w*) (Shah *et al.*, 2001; Kulkarni, 2012), pH (Ribeiro *et al.*, 2019) or salinity (Muir *et al.*, 2012; Kalvodova *et al.*, 2005) to induce a mesophase transition. Light-induced structural changes (Basílio & García-Río, 2017) are mostly studied on lipid monolayers (Backus *et al.*, 2011; Warias *et al.*, 2023) and bilayers at the water–gas interface, or on small unilamellar vesicles (Urban *et al.*, 2020; Oh *et al.*, 2013; Ober *et al.*, 2022) and giant unilamellar vesicles (Pfeffermann *et al.*, 2021; Georgiev *et al.*, 2018; Pernpeintner *et al.*, 2017), inducing reversible modification of the layer thickness. Light-induced mesophase transitions studied by Wang *et al.* (2011) showed an irreversible transition from multilamellar vesicles to worm-like micelles. In liquid crystals, light-driven isomerization (Wuckert *et al.*, 2015), thermotropic phase transitions and structural reorientation (Bisoyi & Li, 2016; Yelamaggad *et al.*, 2012) are also observed.

In this study, we introduce a bilayer model system consisting of lipid mixtures of phospholipid 1,2-dipalmitoylphosphatidylcholine (DPPC) and synthetic photoswitchable lipid mimetics (Reise *et al.*, 2018) and use light to trigger phase transitions. Previous investigations by the authors into the structural response of mixed 95%/5% mol/mol Langmuir monolayers of DPPC and azobenzene amphiphile moieties under illumination revealed bidirectional, repeatable and fully reversible changes of the layer thickness and surface pressure (Warias *et al.*, 2023). The switching stability and repeatability found in these monolayers make the azobenzene amphiphiles ideal candidates for bilayer studies.

The selected azobenzene amphiphile is photosensitive and its N═N double bond switches between the straight *trans* and bent *cis* isomers on illumination with light of 365 and 455 nm wavelengths, respectively [see Fig. 1(*b*) for schematic representation]. In the employed synthetic azobenzene amphiphiles, the azobenzene moiety is attached on one side to a triethylene glycol linker forming the hydrophilic head group and on the other side to the hydrophobic tail group consisting of diacylglycerol esterified with two fatty acids containing 16 carbon atoms, similar to the DPPC tail.

In order to identify the lipid structures formed by mixtures of the azobenzene amphiphiles and DPPC with proportions from 0 to 100% in water, small-angle X-ray scattering (SAXS) investigations were performed. SAXS is commonly employed to identify mesophases of lyotropic liquid crystals and to determine their scattering length profiles, sizes and shapes (Kikhney & Svergun, 2015; Kornmueller *et al.*, 2018; Hyde, 2001). In the following, we identify the mesophases and the light-induced phase transitions for the *trans* and *cis* isomers of the azobenzene amphiphile, herein referred to as **1**. Furthermore, temperature-dependent SAXS measurements for selected proportions are analysed and complemented by differential scanning calorimetry (DSC) (McElhaney, 1982; Privalov & Plotnikov, 1989; Chiu & Prenner, 2011) measurements to determine the phase transition temperatures from gel to the liquid crystalline phase.

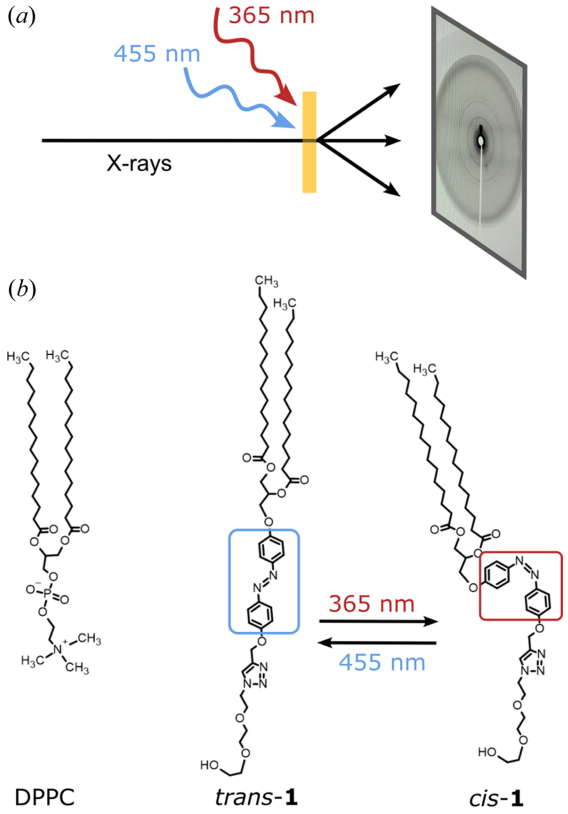

Figure 1
Schematic of (*a*) the transmission SAXS measurement setup and (*b*) the chemical structure of DPPC and both the *trans* and the *cis* isomers of azobenzene amphiphile **1**.

2. Experimental

2.1. Sample preparation

DPPC was purchased from Avanti Polar lipids (Alabaster, AL). The azobenzene amphiphile **1** was synthesized in accordance with our previously published synthesis route (Reise *et al.*, 2018). The lipids were dissolved in chloroform (Sigma–Aldrich) at a concentration of 10 m*M* and mixed at various proportions of DPPC and **1**. All following preparation steps were done for the stable *trans* form of **1**. These mixtures were dried to thin films with a BÜCHI Rotavapor R-300 at a bath temperature of 45°C and a pressure of 16 mbar for at least 1 h. These dried films were stored in the fridge at <10°C prior to the measurements. All samples were freshly prepared on the day of the measurements by adding warm Milli-Q water onto the film and then rotating and shaking the solution in a water bath above 45°C until a homogenous solution was formed. Larger lipid lumps were broken up using a vortex mixer and ultrasonic water bath. The hydrated samples were stored in the fridge at the beamline. Right before the measurements, the hydrated solutions were left for 1 h outside of the fridge to reach room temperature. Roti PreMix PBS salt

(Carl Roth) (0.14 *M* NaCl, 2.7 m*M* KCl, 10 m*M* phosphate) was initially used as buffer to adjust the pH to 7.4 and later Milli-Q water was added. All measurements were performed no more than 24 h after the sample hydration.

2.2. Isomerization

A custom-made illumination device consisting of a row of three 365 nm LEDs [Nichia, NCSU033B(T)] and three 455 nm LEDs (Osram, LD CQ7P) was used to switch **1** from the *trans* to the *cis* isomer and back. Prior UV–Vis measurements on the azobenzene mimetics revealed that 96% of the molecules switch to the *cis* and 82% to *trans* conformation (Warias *et al.*, 2023). Illumination and isomerization of the samples were carried out prior to both the DSC and the temperature-controlled SAXS measurements as the housing and sample holder, respectively, did not allow *in situ* illumination. The time following illumination between measurements was kept as short as possible to minimize back switching (see Section S1 of the supporting information). For the *in situ* SAXS measurements at room temperature, the illumination device was mounted above the capillary sample holder at a distance of about 10 cm. At the sample position, fluencies of 2.0 mW cm^{-2} for 365 and 455 nm were measured during the first beam time and 1.6 mW cm^{-2} during the second.

2.3. Differential scanning calorimetry

DSC measurements were carried out at a MicroCal Peaq-DSC (Malvern Panalytical, Northampton, MA) at P08 of PETRA III at DESY. After initial cleaning and reference measurements of pure and buffered Milli-Q water, sample solutions with 1 m*M* l^{-1} concentration were studied between 25 and 70°C at a heating rate of 12°C h^{-1} and a cooling rate of 60°C h^{-1}. The heating and cooling scan was repeated three times. The data were recorded in high-feedback mode.

2.4. Small-angle X-ray scattering

All SAXS measurements were performed at BL2 of DELTA, Dortmund (Dargasz *et al.*, 2022) and at a concentration of 10 m*M* l^{-1}. Two different sample setups were used to study temperature- and light-induced structural changes *in situ*. The schematic measurement setup is shown in Fig. 1(*a*). Temperature-dependent measurements were performed for lipid proportions of 0:100, 10:90 and 20:80 **1**:DPPC in the temperature range 17–65°C with a temperature-controlled cell (Linkam Scientific Instruments Ltd). In favour of *in situ* isomerization, a simple capillary sample holder was used for all other measurements at room temperature. The room temperature was monitored and varied between 18 and 27°C with a mode temperature of 25°C. For clarity, 25°C is given for all measurements between 18 and 27°C as the measured structures were identical in this range. The samples were filled in 1 and 2 mm diameter capillaries for the Linkam stage and simple sample holder, respectively. At DELTA, a photon energy of 12 keV, beam size of about 0.6 × 0.6 mm and a MAR345 2D image plate detector were used. The 2D detector images were processed with the software *FIT2D* (Hammersley *et al.*, 1995, 1996; Hammersley, 1997, 2016) including pixel mask application, transformation from real to reciprocal space, detector orientation correction and angular integration to receive the reduced 1D scattering pattern in *q*-space. Calibration of the detector distance and orientation were done with a standard silver behenate sample. The typical measurement time for the data collection was 180 s followed by a detector read out time of another 180 s.

2.5. Analysis software

A self-written Python script was used for background correction of the reduced 1D SAXS pattern and resaving the corrected pattern in the NeXus file format with the associated metadata (Wilkinson *et al.*, 2016). Following the metadata standards determined by DAPHNE4NFDI (Barty *et al.*, 2023), the newly generated NeXus file contains, in addition to the background-corrected pattern and the uncorrected signal, information on the background reduction as well as the detector, beamline and sample-specific metadata. The DSC data were also analysed with a self-written Python script and stored as simple ASCI files. Further information on the data and script accessibility are given in Data Availability.

3. Results and discussion

3.1. Light-induced mesophase changes at room temperature

SAXS measurements on the hydrated samples for different proportions between 0 and 100% of DPPC and **1** in the *q*-range 0.5–3.2 nm^{-1} are shown in Fig. 2(*a*). A range of different mesophases are observed. At each concentration, we illuminated with 365 and 455 nm to measure the structures for the *cis* and *trans* states of **1**. Changes are observed between proportions of 2.5–20% of **1**.

For pure DPPC vesicles, the well studied multilamellar phase with a lamellar *d*-spacing of 6.34 ± 0.03 nm was found in agreement with previous studies (Soloviov *et al.*, 2012; Kornmueller *et al.*, 2018). Focusing on the *trans* isomer of **1**, a multilamellar vesicle (MLV) structure was also found for low proportions up to a molar percentage of 10% with an increase of the lamellar *d*-spacing up to 6.55 ± 0.03 nm. Increasing the proportion of **1** further, we observed a transformation to the cubic phase *Pn*3*m* for proportions between 20 and 70%, as shown in Fig. 2(*a*). At 70%, we found a coexistence of the previous cubic phase at low proportions and the hexagonal phase determined by fitting at 100%. Example raw detector images are presented in Fig. S1(*b*) of the supporting information, showing scattering from different mesophases.

Following *in situ* illumination of the mixed samples for 3–5 min with 365 nm, we could study the light-induced structural changes between the *trans* and *cis* isomer of **1**. Time-resolved measurements were not possible at DELTA, as the dynamics were faster than the counting and detector readout time. For proportions above 30% **1**, no light-induced change was observed. In contrast, we found a change in mesophase for proportions of **1** up to 20%. The lamellar phase with a lamellar

d-spacing of 6.55 ± 0.03 nm for the *trans* isomer transformed to the bicontinuous cubic diamond *Pn3m* phase with a *d*-spacing of 11.2 ± 1.0 nm for the *cis* isomer is presented in Fig. 2(*b*) for the 10% proportion. This phase transformation was reversible by illumination with 455 nm light and was highly reproducible, as demonstrated for at least three illumination cycles (see Fig. S1). Based on the *Pn3m* phase identified for the *cis* isomer at 10 and 20% **1**, a coexistence of the lamellar and *Pn3m* phases was found for the corresponding *trans* isomer of **1** with *Pn3m* fractions of 59 ± 1% and 76 ± 1%, respectively. This coexistence was found for repetitive illuminations, showing a stable phase formation. By increasing the proportion of **1** to 30%, the *Pn3m* phase with *d*-spacings of 11.4 ± 0.6 and 10.7 ± 1.0 nm was found for both the *trans* and the *cis* isomers, respectively. At even higher proportions of 50 and 63%, not only the *Pn3m* phase but also the bicontinuous cubic *Im3m* structure give a reasonable fit, as described in Section S3 of the supporting information. The different mesophases revealed and *d*-spacing depending on the proportions between DPPC and **1** are shown in Fig. 2(*c*) and are summarized in Table 1.

The transformation to a cubic phase for a high content of **1** can be explained by an increase in the curvature of the monolayers, resulting in a rearrangement of the 3D structure. To quantify the curvature and the resulting self-assembled lipid geometry, the critical packing parameter (*CPP*) can be used to predict the phase, as introduced by Israelachvili *et al.* (1976) and Tanford (1973):

$$CPP = \frac{v_{\mathrm{chain}}}{a_{\mathrm{head}}\, l_{\mathrm{chain}}},$$

where v_{chain} and l_{chain} are the volume and length of the hydrophobic chain, respectively, and a_{head} is the effective area of the hydrophilic headgroup. If $CPP \simeq 1.0$, the molecule can be considered to be cylindrical. A deviation of *CPP* from 1.0 indicates a positive or negative curvature which causes a cone-shape of the lipids and reformation into cubic, hexagonal or micellar structures, or their reversed correspondent. Flexible lipid bilayers are found for *CPP* values between 1.0 and 0.5, which can form both vesicles and cubic phases. When $0.3 < CPP < 0.5$, the hexagonal structure is observed, and below 0.3

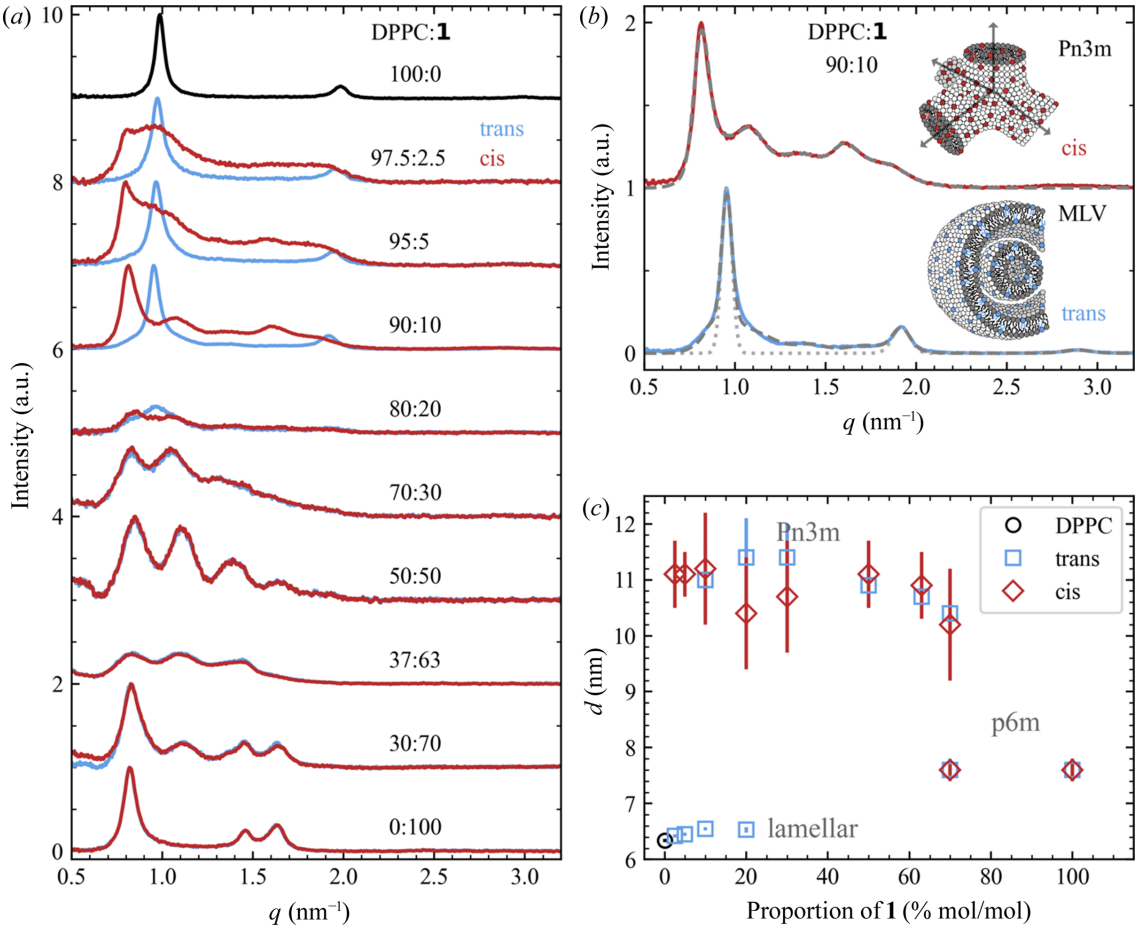

Figure 2
Scattering data of DPPC and **1** mixtures with varying proportions of **1** for both *trans* and *cis* isomers. (*a*) Pure DPPC (in black), mixed *trans*-**1** (in blue) and *cis*-**1** (in red) data. The curves with different proportions are offset vertically for clarity. (*b*) *Trans* and *cis* isomers of the mixture with 10% **1** and the structure fits (in grey) for the multilamellar vesicle (MLV) and *Pn3m* structure, respectively. For *trans*, the fits for the single lamellar (dotted), combined lamellar and *Pn3m* (dashed) phases are shown. The *d*-spacing values and mesophases derived from the fits are summarized in (*c*).

Table 1
Mesophases and *d*-spacing parameters (*d*) derived from the SAXS data for pure DPPC vesicles and mixed lipid structures.

The error for all estimated *CPP* values is ±0.002.

T (°C)	DPPC:**1**	Mesophase	*d* (nm)	*CPP*
25	100:0	Lamellar	6.34 ± 0.03	0.6†
37	100:0	Lamellar	7.17 ± 0.05	
45	100:0	Lamellar	6.58 ± 0.01	
55	100:0	Lamellar	6.49 ± 0.01	

		Trans			*Cis*		
T (°C)	DPPC:**1**	Mesophase	*d* (nm)	*CPP*	Mesophase	*d* (nm)	*CPP*
25	97.5:2.5	Lamellar	6.42 ± 0.03	0.597	*Pn3m*	11.1 ± 0.6	0.596
25	95:5	Lamellar	6.45 ± 0.03	0.594	*Pn3m*	11.1 ± 0.4	0.592
25	90:10	Lamellar, *Pn3m*	6.55 ± 0.03, 11.0 ± 0.7	0.589	*Pn3m*	11.2 ± 1.0	0.584
25	80:20	Lamellar, *Pn3m*	6.53 ± 0.05, 11.4 ± 0.7	0.577	*Pn3m*	10.4 ± 1.0	0.568
25	70:30	*Pn3m*	11.4 ± 0.6	0.566	*Pn3m*	10.7 ± 1.0	0.552
25	50:50	*Pn3m*	10.9 ± 0.4	0.543	*Pn3m*	11.1 ± 0.6	0.52
25	37:63	*Pn3m*	10.7 ± 0.4	0.528	*Pn3m*	10.9 ± 0.6	0.499
25	30:70	*Pn3m*, *p6m*	10.4 ± 0.7, 7.6 ± 0.2	0.520	*Pn3m p6m*	10.2 ± 1.0 7.6 ± 0.2	0.488
25	0:100	*p6m*	7.6 ± 0.2	0.486	*p6m*	7.6 ± 0.2	0.440
25	90:10	Lamellar, *Pn3m*	6.55 ± 0.03, 11.0 ± 0.7		*Pn3m*	10.9 ± 1.2	
37	90:10	*Pn3m*	11.1 ± 0.7		*Pn3m*	10.6 ± 1.0	
45	90:10	Lamellar	6.64 ± 0.03		Lamellar	6.69 ± 0.03	
55	90:10	Lamellar	6.62 ± 0.03		Lamellar	6.63 ± 0.03	
25	80:20	Lamellar, *Pn3m*	6.49 ± 0.01, 11.9 ± 0.8		*Pn3m*	11.1 ± 0.9	
37	80:20	*Pn3m*	10.6 ± 0.4		*Pn3m*	10.6 ± 0.4	
45	80:20	Lamellar	6.67 ± 0.01		Lamellar	6.64 ± 0.01	

† Reference value for DPPC was taken from Kobierski *et al.* (2022).

micelles are observed (Iakimov *et al.*, 2021; Charles Tanford, 1973; Nagarajan, 2002).

Theoretical values for the *CPP* factors of DPPC and **1**, in both the *trans* and the *cis* states, were estimated following the approach by Kobierski *et al.* (2022) and Oremusová *et al.* (2019). The detailed calculations and parameters are listed in Section S4 of the supporting information. In contrast to DPPC, **1** has *CPP* values of about 0.486 ± 0.002 and 0.440 ± 0.002 for the *trans* and *cis* isomers, respectively, suggesting a rod-like shape forming a hexagonal structure for pure **1**. Assuming the *CPP* values for the mixtures of DPPC and **1** can be calculated proportionally (König *et al.*, 2023), we observe a decrease in the *CPP* value with increasing concentration of **1** (see Table 1), which is in good agreement with the experimentally observed phases and the conversion from flexible bilayers to hexagonal structures at proportions of 70% **1**. Comparing the *CPP* values for *trans*-**1** and *cis*-**1**, the *cis* isomer is only slightly more curved, which could hint at favouring the cubic phase. Nevertheless, the *CPP* values for the *trans* and *cis* states are very close at low proportions and cannot be the only driving factor for the structural reorientation. Similar conclusions were drawn in recent molecular dynamic studies, where they revealed a lamellar-to-hexagonal transition on changes in temperature but with neglectable changes in the *CPP* value (Mochizuki, 2023).

3.2. Temperature-induced mesophase changes

Samples were illuminated *ex situ* and later temperature-controlled measurements were performed using the Linkam stage. Two capillaries were filled from the same stock solution and both were illuminated with 365 nm light for 5 min for *tans–cis* isomerization. Afterwards, one capillary was illuminated with 455 nm to transform back to the *trans* state. The *cis* isomer was measured first, followed by the thermally stable *trans* form. The temperature was increased from room temperature (25°C) in steps up to 55°C at a heating rate of 10°C min^{-1}. After reaching the desired temperature, a 10 min waiting time was introduced before starting each SAXS measurement. These temperature-dependent measurements were carried out for mixtures of 10 and 20% **1** and pure DPPC, and the data are presented in Fig. 3(*a*). The observed Bragg peak shifts and calculated lamellar *d*-spacing for pure DPPC are in good agreement with other studies of multilamellar DPPC vesicles (Almeida *et al.*, 2018), except for the rippled phase expected at 37°C, which was absent. The reason for not observing the rippled phase for pure DPPC could be due to a temperature offset between the set temperature and the sample temperature (typically between 0.5 and 1°C) or due to not waiting long enough to allow the formation of the rippled phase.

Comparing the heating series for the *trans* and *cis* isomers of 10% **1**, the mesophases are identical for both isomers at temperatures higher than 37°C [see Fig. 3(*a*)]. A clear difference between the lamellar (*trans*) and *Pn3m* (*cis*) phase was only observed at room temperature. The fitted structures and *d*-spacings match the *in situ* measurements in Fig. 2(*a*). At 37°C, we found a *Pn3m* structure for both isomers, *trans* and *cis*, with a slightly decreased *d*-spacing of 11.1 ± 0.7 and 10.6 ± 1.0 nm [see Table 1 and Fig. 3(*b*)]. When the temperature was

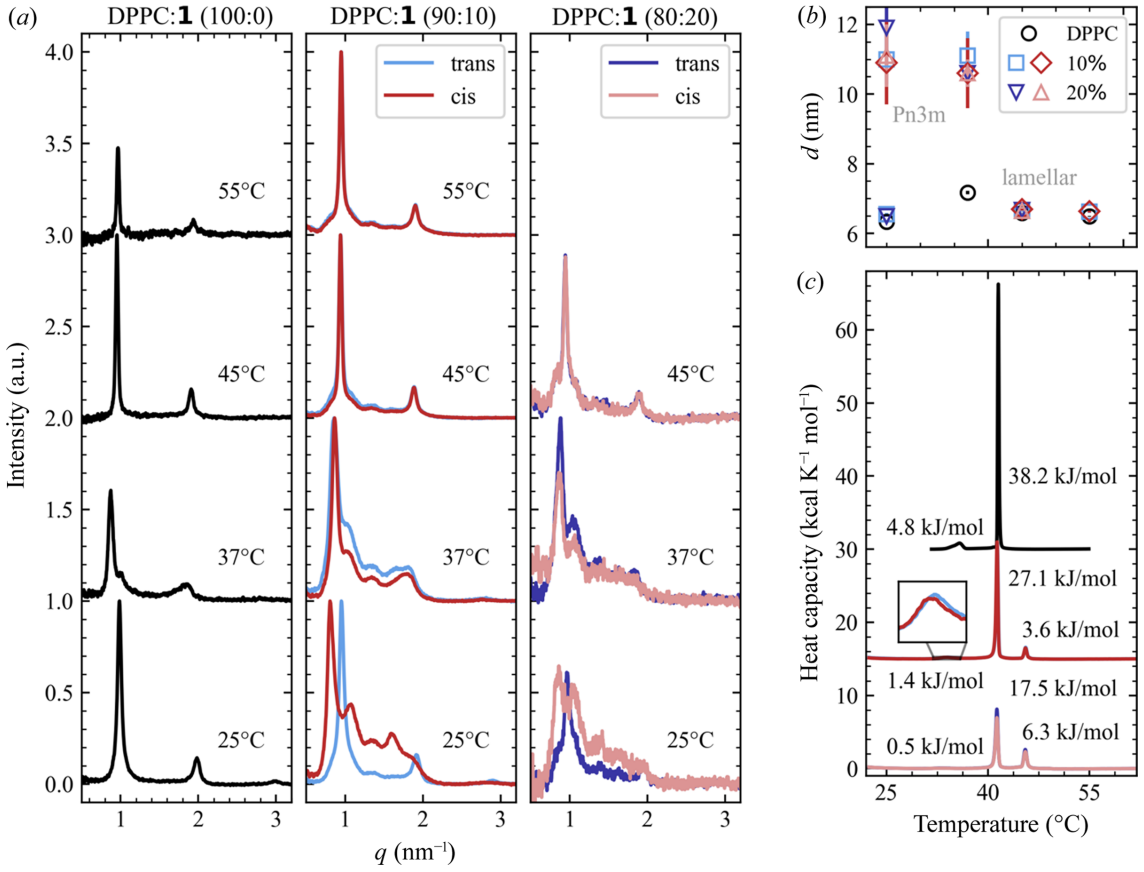

Figure 3
(*a*) SAXS data at different temperatures for mixed DPPC and **1** structures with proportion of 0, 10 and 20% **1**. The curves are shifted vertically and on the left the data from pure DPPC vesicles are shown. In the middle and right, respectively, the 10 and 20% mixtures of DPPC and **1** for both the *trans* (blue) and the *cis* states (red) are illustrated. The fitted *d*-spacing parameters and mesophases are summarized in (*b*) and complementary DSC data are shown in (*c*) for pure DPPC and mixtures of 10 and 20% **1** in the *trans* (blue) and *cis* states (red).

increased above the main phase transition to 45 and 55°C, a transition back to the lamellar phase occurred with lamellar *d*-spacings of 6.64 ± 0.03 and 6.62 ± 0.03 nm, respectively, for the *trans* isomer. This back transition could be attributed to the higher flexibility of the tails in the liquid crystalline phase, causing the tail length to appear shorter, which results in an increased *CPP* value.

Analogue transitions were observed for 20% **1** in *trans* and *cis* [see Figs. 3(*a*) and 3(*b*)]. In contrast to the *trans* isomer, the *cis* isomer only shows two phase transitions as the *Pn3m* structure is already present at room temperature. Complementary DSC measurements showed three phase transitions for 10 and 20% **1** [see Fig. 3(*c*)], supporting the phase transitions observed in the SAXS data. For 20%, the pre-transition peak at 33.1 ± 0.3°C, belonging to the DPPC molecules, was hardly observable with an enthalpy of only 0.5 ± 0.1 kJ mol^{-1}. A decrease in the enthalpy is typically found for mixed systems with increasing proportions of the second compound, as shown by Almeida *et al.* (2018) for mixed DPPC and cholesterol vesicles. Generally, a reduction in the enthalpy for each phase transition, a shift towards lower temperatures and an emerging additional phase transition peak at around 45.5°C were found on increasing the proportion of **1** [see Fig. 3(*c*)]. Meanwhile, the difference between the *trans* and *cis* phase transition temperatures is negligibly small and within the measurement error for the phase transitions at 41.3 ± 0.3 and 45.5 ± 0.3°C. The shift of 0.3°C between the pre-phase transition temperatures 33.7 ± 0.3°C and 44.0 ± 0.3°C for 10% **1** in *trans* and *cis*, respectively, is close to the measurement accuracy.

4. Conclusions

In summary, from the SAXS investigation on mixed DPPC and the photoswitchable azobenzene amphiphile **1** in aqueous solutions, we could confirm reversible light-induced switching between mesophases. Photoswitching was observed for concentrations up to 20% of the photosensitive molecule **1** and for temperatures from 18 to 27°C which correspond to the lipid gel phase. The mesophase could be switched reversibly, repeatedly and reproducibly between its lamellar structure in the *trans* state and its cubic *Pn3m* structure in the *cis* state. For proportions higher than 20% **1**, the cubic *Pn3m* and at even higher proportions such as 70% a hexagonal structure was favoured for both the *trans* and the *cis* states equally, showing the sensitivity of the lipid structures to the lipid composition.

DSC measurements identified the phase transition temperatures. Complementary temperature-dependent SAXS

measurements for mixtures containing 10% **1** in the *trans* state showed a mesophase transition from lamellar to cubic *Pn*3*m* at the 34.0 ± 0.3°C phase transition and a mesophase transition from *Pn*3*m* back to lamellar at the main phase transition at 41.4 ± 0.3°C. Interestingly, no mesophase transition was observed at 33.7 ± 0.3°C for the *cis* state, which is already present in the *Pn*3*m* phase at room temperature, but similar to the *trans* state displays a transition to lamellar at 41.3 ± 0.3°C. At temperatures above 34°C, no photoswitching was observed, as here both the *trans* and the *cis* forms are present in the same mesophase.

These findings indicate a useful temperature and concentration range for photoswitching applications. The first steps to create model systems for the study of membrane protein response to mesophase changes due to external stimuli without altering the environment are shown. Further, such systems may have potential as a basis for drug delivery applications.

5. Data availability

Raw data, fit parameters and analysis scripts are available under: https://doi.org/10.57892/100-49 International Generic Sample Numbers (IGSNs): DPPC:**1** 100:0 (https://doi.org/10.60578/gucn-en2h); DPPC:**1** 97.5:2.5 (https://doi.org/10.60578/kw2n-ouv5); DPPC:**1** 95:5 (https://doi.org/10.60578/dg1l-5gebr); DPPC:**1** 90:10 (https://doi.org/10.60578/reqz-rk9v); DPPC:**1** 80:20 (https://doi.org/10.60578/r2j8-grzb); DPPC:**1** 70:30 (https://doi.org/10.60578/l7hw-iao2); DPPC:**1** 50:50 (https://doi.org/10.60578/p1fg-n3tw); DPPC:**1** 37:63 (https://doi.org/10.60578/g7n3-wkj3); DPPC:**1** 30:70 (https://doi.org/10.60578/q7j3-sid5); DPPC:**1** 0:100 (https://doi.org/10.60578/xke5-nz1u).

6. Related literature

The following references are cited in the supporting information: Ishiwatari *et al.* (2024); Khalil & Zarari (2014); SzymaŃski *et al.* (2013); Tanford, C. (1972).

Acknowledgements

The authors thank the DELTA machine group for providing synchrotron radiation, and Dr Christian Sternemann and Sonja Reinheimer for their support during the beam times in March and December 2022. Parts of this research were carried out at PETRA III and we would like to thank Dr Chen Shen for their assistance in using the Buchi R300 rotary evaporator and MicroCal DSC at P08.

Funding information

We acknowledge financial support from Deutsche Forschungsgemeinschaft (grant Nos. DAPHNE4NFDI; SFB 677); Bundesministerium für Bildung und Forschung, ErUM Pro (grant Nos. 05K22FK3; 05K19FK2). We acknowledge DESY (Hamburg, Germany), a member of the Helmholtz Association HGF, for the provision of experimental facilities and support of SH via the Center of Molecular Water Science.

References

Almeida, P. F., Carter, F. E., Kilgour, K. M., Raymonda, M. H. & Tejada, E. (2018). *Langmuir*, **34**, 9798–9809.
Backus, E. H. G., Kuiper, J. M., Engberts, J. B. F. N., Poolman, B. & Bonn, M. (2011). *J. Phys. Chem. B*, **115**, 2294–2302.
Barty, A., Gutt, C., Lohstroh, W., Murphy, B., Schneidewind, A., Grunwaldt, J.-D., Schreiber, F., Busch, S., Unruh, T., Bussmann, M., Fangohr, H., Görzig, H., Houben, A., Kluge, T., Manke, I., Lützenkirchen-Hecht, D., Schneider, T. R., Weber, F., Bruno, G., Einsle, O., Felder, C., Herzig, E. M., Konrad, U., Markötter, H., Rossnagel, K., Sheppard, T. & Turchinovich, D. (2023). *DAPHNE4NFDI – Consortium Proposal.*. https://doi.org/10.5281/ZENODO.8040606; https://www.daphne4nfdi.de.
Basílio, N. & García-Río, L. (2017). *Curr. Opin. Colloid Interface Sci.* **32**, 29–38.
Bisoyi, H. K. & Li, Q. (2016). *Chem. Rev.* **116**, 15089–15166.
Carlsen, R. W. & Sitti, M. (2014). *Small*, **10**, 3831–3851.
Cavalcanti, L. P., Konovalov, O. & Torriani, I. L. (2006). *Eur. Biophys. J.* **35**, 431–438.
Charles Tanford (1973). *The Hydrophobic Effect: Formation of Micelles and Biological Membranes*. New York: Wiley.
Chiu, M. H. & Prenner, E. J. (2011). *J. Pharm. Bioall. Sci.* **3**, 39–59.
Cournia, Z., Allen, T. W., Andricioaei, I., Antonny, B., Baum, D., Brannigan, G., Buchete, N.-V., Deckman, J. T., Delemotte, L., Del Val, C., Friedman, R., Gkeka, P., Hege, H.-C., Hénin, J., Kasimova, M. A., Kolocouris, A., Klein, M. L., Khalid, S., Lemieux, M. J., Lindow, N., Roy, M., Selent, J., Tarek, M., Tofoleanu, F., Vanni, S., Urban, S., Wales, D. J., Smith, J. C. & Bondar, A.-N. (2015). *J. Membr. Biol.* **248**, 611–640.
Dargasz, M., Bolle, J., Faulstich, A., Schneider, E., Kowalski, M., Sternemann, C., Savelkouls, J., Murphy, B. & Paulus, M. (2022). *J. Phys. Conf. Ser.* **2380**, 012031.
Di Cola, E., Grillo, I. & Ristori, S. (2016). *Pharmaceutics*, **8**, 10.
Georgiev, V. N., Grafmüller, A., Bléger, D., Hecht, S., Kunstmann, S., Barbirz, S., Lipowsky, R. & Dimova, R. (2018). *Adv. Sci.* **5**, 1800432.
Hammersley, A. P. (2016). *J. Appl. Cryst.* **49**, 646–652.
Hammersley, A. P., Svensson, S. O., Hanfland, M., Fitch, A. N. & Hausermann, D. (1996). *High. Press. Res.* **14**, 235–248.
Hammersley, A. P., Svensson, S. O., Thompson, A., Graafsma, H., Kvick, Å. & Moy, J. P. (1995). *Rev. Sci. Instrum.* **66**, 2729–2733.
Hammersley, A. P. (1997). *FIT2D: An Introduction and Overview*. ESRF Internal Report, ESRF97HA02T.
Hirlekar, R., Jain, S., Patel, M., Garse, H. & Kadam, V. (2010). *Curr. Drug Deliv.* **7**, 28–35.
Hyde, S. T. (2001). *Handbook of Applied Surface and Colloid Chemistry*, edited by Krister Holmberg, pp. 299–327. John Wiley & Sons.
Iakimov, N. P., Zotkin, M. A., Dets, E. A., Abramchuk, S. S., Arutyunian, A. M., Grozdova, I. D. & Melik-Nubarov, N. S. (2021). *Colloid Polym. Sci.* **299**, 1543–1555.
Ishiwatari, Y., Yokoyama, T., Kojima, T., Banno, T. & Arai, N. (2024). *Mol. Syst. Des. Eng.* **9**, 20–28.
Israelachvili, J. N., Mitchell, D. J. & Ninham, B. W. (1976). *J. Chem. Soc. Faraday Trans. 2*, **72**, 1525.
Kalvodova, L., Kahya, N., Schwille, P., Ehehalt, R., Verkade, P., Drechsel, D. & Simons, K. (2005). *J. Biol. Chem.* **280**, 36815–36823.
Khalil, R. A. & Zarari, A. A. (2014). *Appl. Surf. Sci.* **318**, 85–89.
Kikhney, A. G. & Svergun, D. I. (2015). *FEBS Lett.* **589**, 2570–2577.
Kobierski, J., Wnętrzak, A., Chachaj-Brekiesz, A. & Dynarowicz-Latka, P. (2022). *Colloids Surf. B Biointerfaces*, **211**, 112298.
König, M., de Vries, R., Grünewald, F., Marrink, S. J. & Pezeshkian, W. (2023). *bioRxiv*:2023.12.15.571845.

Kornmueller, K., Lehofer, B., Leitinger, G., Amenitsch, H. & Prassl, R. (2018). *Nano Res.* **11**, 913–928.
Kulkarni, C. V. (2012). *Nanoscale*, **4**, 5779–5791.
McElhaney, R. N. (1982). *Chem. Phys. Lipids*, **30**, 229–259.
McManus, J. J., Rädler, J. O. & Dawson, K. A. (2003). *J. Phys. Chem. B*, **107**, 9869–9875.
Meer, G. van, Voelker, D. R. & Feigenson, G. W. (2008). *Nat. Rev. Mol. Cell Biol.* **9**, 112–124.
Mochizuki, K. (2023). *J. Colloid Interface Sci.* **631**, 17–21.
Muir, B. W., Zhen, G., Gunatillake, P. & Hartley, P. G. (2012). *J. Phys. Chem. B*, **116**, 3551–3556.
Nagarajan, R. (2002). *Langmuir*, **18**, 31–38.
Ober, M. F., Müller-Deku, A., Baptist, A., Ajanović, B., Amenitsch, H., Thorn-Seshold, O. & Nickel, B. (2022). *Nanophotonics*, **11**, 2361–2368.
Oh, H., Javvaji, V., Yaraghi, N. A., Abezgauz, L., Danino, D. & Raghavan, S. R. (2013). *Soft Matter*, **9**, 11576.
Oremusová, J., Vitková, Z., Vitko, A., Tárník, M., Miklovičová, E., Ivánková, O., Murgaš, J. & Krchňák, D. (2019). *Molecules*, **24**, 651.
Pernpeintner, C., Frank, J. A., Urban, P., Roeske, C. R., Pritzl, S. D., Trauner, D. & Lohmüller, T. (2017). *Langmuir*, **33**, 4083–4089.
Pfeffermann, J., Eicher, B., Boytsov, D., Hannesschlaeger, C., Galimzyanov, T. R., Glasnov, T. N., Pabst, G., Akimov, S. A. & Pohl, P. (2021). *J. Photochem. Photobiol. B*, **224**, 112320.
Privalov, P. L. & Plotnikov, V. V. (1989). *Thermochim. Acta*, **139**, 257–277.
Reise, F., Warias, J. E., Chatterjee, K., Krekiehn, N. R., Magnussen, O., Murphy, B. M. & Lindhorst, T. K. (2018). *Chem. A Eur. J.* **24**, 17497–17505.
Ribeiro, I. R., Immich, M. F., Lundberg, D., Poletto, F. & Loh, W. (2019). *Colloids Surf. B Biointerfaces*, **177**, 204–210.
Sagalowicz, L., Mezzenga, R. & Leser, M. E. (2006). *Curr. Opin. Colloid Interface Sci.* **11**, 224–229.
Shah, J. C., Sadhale, Y. & Chilukuri, D. M. (2001). *Adv. Drug Deliv. Rev.* **47**, 229–250.
Soloviov, D. V., Gorshkova, Y. E., Ivankov, O. I., Zhigunov, A. N., Bulavin, L. A., Gordeliy, V. I. & Kuklin, A. I. (2012). *J. Phys. Conf. Ser.* **351**, 012010.
SzymaŃski, W., Yilmaz, D., Koçer, A. & Feringa, B. L. (2013). *Acc. Chem. Res.* **46**, 2910–2923.
Tanford, C. (1972). *J. Phys. Chem.* **76**, 3020–3024.
Urban, P., Pritzl, S. D., Ober, M. F., Dirscherl, C. F., Pernpeintner, C., Konrad, D. B., Frank, J. A., Trauner, D., Nickel, B. & Lohmueller, T. (2020). *Langmuir*, **36**, 2629–2634.
Wang, D., Dong, R., Long, P. & Hao, J. (2011). *Soft Matter*, **7**, 10713.
Warias, J. E., Reise, F., Hövelmann, S. C., Giri, R. P., Röhrl, M., Kuhn, J., Jacobsen, M., Chatterjee, K., Arnold, T., Shen, C., Festersen, S., Sartori, A., Jordt, P., Magnussen, O. M., Lindhorst, T. K. & Murphy, B. M. (2023). *Sci. Rep.* **13**, 11480.
Wilkinson, M. D., Dumontier, M., Aalbersberg, I. J. J., Appleton, G., Axton, M., Baak, A., Blomberg, N., Boiten, J.-W., da Silva Santos, L. B., Bourne, P. E., Bouwman, J., Brookes, A. J., Clark, T., Crosas, M., Dillo, I., Dumon, O., Edmunds, S., Evelo, C. T., Finkers, R., Gonzalez-Beltran, A., Gray, A. J. G., Groth, P., Goble, C., Grethe, J. S., Heringa, J., 't Hoen, P. A. C., Hooft, R., Kuhn, T., Kok, R., Kok, R., Lusher, S. J., Martone, M. E., Mons, A., Packer, A. L., Persson, B., Rocca-Serra, P., Roos, M., van Schaik, R., Sansone, S., Schultes, E., Sengstag, T., Slater, T., Strawn, G., Swertz, M. A., Thompson, M., van der Lei, J., van Mulligen, E., Velterop, J., Waagmeester, A., Wittenburg, P., Wolstencroft, K., Zhao, J. & Mons, B. (2016). *Sci Data*, **3**, 160018.
Wuckert, E., Harjung, M. D., Kapernaum, N., Mueller, C., Frey, W., Baro, A., Giesselmann, F. & Laschat, S. (2015). *Phys. Chem. Chem. Phys.* **17**, 8382–8392.
Yang, P.-W., Lin, T.-L., Hu, Y. & Jeng, U.-S. (2012). *Chin. J. Phys.* **50**, 349–356.
Yelamaggad, C. V., Krishna Prasad, S. & Li, Q. (2012). *Liquid Crystals Beyond Displays*, edited by Quan Li, pp. 157–211, John Wiley & Sons.

IUCrJ

Volume 11 (2024)

Supporting information for article:

Photoinduced bidirectional mesophase transition in vesicles containing azobenzene amphiphiles

Svenja C. Hövelmann, Ella Dieball, Jule Kuhn, Michelle Dargasz, Rajendra P. Giri, Franziska Reise, Michael Paulus, Thisbe K. Lindhorst and Bridget M. Murphy

S1. *Cis* stability tests

During the DSC and SAXS measurements possible thermal back isomerisation was minimised by keeping the time between the measurement and illumination as short as possible. For the SAXS measurements, we made a prior test on the *cis* stability of the mixture with 20% of **1** at 37°C. For that, we illuminate the sample for three illumination cycles (UV-blue-UV-blue) and kept the sample in the temperature controlled Linkam stage at 37°C. The LED Box was positioned in front of the sample holder window (5 mm diameter) for the X-ray beam for about 5 minutes. After removing the LED Box and searching the hutch (below 1 minute), the SAXS pattern was measured immediately. This procedure was repeated at 45°C for one illumination cycle. No difference in the SAXS signals were observed after the illumination. For the 10% of **1** SAXS data, the sample was illuminated for 5 minutes before starting the temperature run 2 minutes later. The three-step temperature run from 37°C to 55°C took about 90 minutes. In the case of DSC measurements, the time between illumination and the start of the measurement was about 90 minutes and the measuring time was about 105 minutes.

S2. Multiple illumination cycles and raw detector images

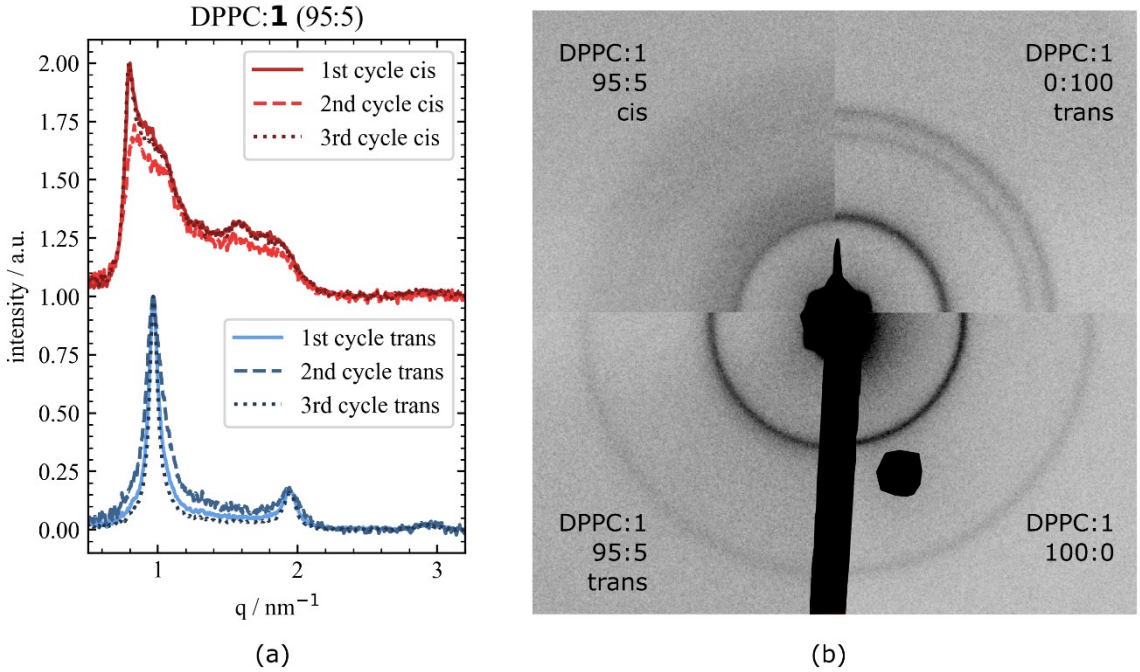

Figure S1 a) SAXS data obtained from the DPPC and 5 % **1** mixtures for its *trans* and *cis* isomers after iterative illumination of 365 nm and 455 nm, respectively, to switch three times between *cis*-**1** and *trans*-**1**. b) Detector images from 95:5 DPPC:**1** *cis*-state (top left) and *trans*-state (bottom left), 100% *trans*-**1** (top right) and 100% DPPC (bottom right).

S3. Fitting different mesophases

All SAXS data was fitted using a two-step approach to determine the mesophase structure. In the first step the fit model consisted of multiple Gaussian-functions with variable amplitude $a_{1,2,\ldots,\mathrm{n}}$, width $\sigma_{1,2,\ldots,\mathrm{n}}$ and d-spacing d.

$$f(q) = a_1\, e^{-\frac{(q-p_1)^2}{2\sigma_1^2}} + \cdots + a_\mathrm{n}\, e^{-\frac{(q-p_\mathrm{n})^2}{2\sigma_\mathrm{n}^2}}$$

The positions $p_{1,2,\ldots,\mathrm{n}}$ of the Gaussian peaks were calculated using the d-spacing parameter d for the lamellar, hexagonal p6m and the bicontinuous cubic phases Pn3m, Im3m, Ia3d, Fm3m, Pm3n and Fd3m as for example for the lamellar phase: $p_\mathrm{n} = \frac{2\pi}{d}n$, or for the hexagonal p6m phase: $p_1 = \frac{2\pi}{d}\sqrt{1}$, $p_2 = \frac{2\pi}{d}\sqrt{3}$, $p_3 = \frac{2\pi}{d}\sqrt{4}$, ... The space groups are taken from (Hyde, 2001).

A visual check was introduced to choose the best match. In most cases only one phase was in good agreement with the measured data. This phase was then selected for the second step, small deviations $\delta_{1,2,\ldots,\mathrm{n}}$ of the peak positions for each peak in the scattering data was allowed.

$$f(q) = a_1\, e^{-\frac{(q-(p_1+\delta_1))^2}{2\sigma_1^2}} + \cdots + a_\mathrm{n}\, e^{-\frac{(q-(p_\mathrm{n}+\delta_\mathrm{n}))^2}{2\sigma_\mathrm{n}^2}}$$

For all positions $p_\mathrm{n} + \delta_\mathrm{n}$, the d-spacing parameters were recalculated and averaged. The error for the d-spacing value was then calculated from the deviations. The fit results are accessible with the raw data (see Data Availability).

For some ratios of **1**, such as for 50% and 63 %, either the Pn3m or Im3m phase give a good fit to the data as shown in Fig. S2. For lower ratios such as 30 % of **1**, the Pn3m fit shows better accordance than the Im3m structure (see Fig. S2).

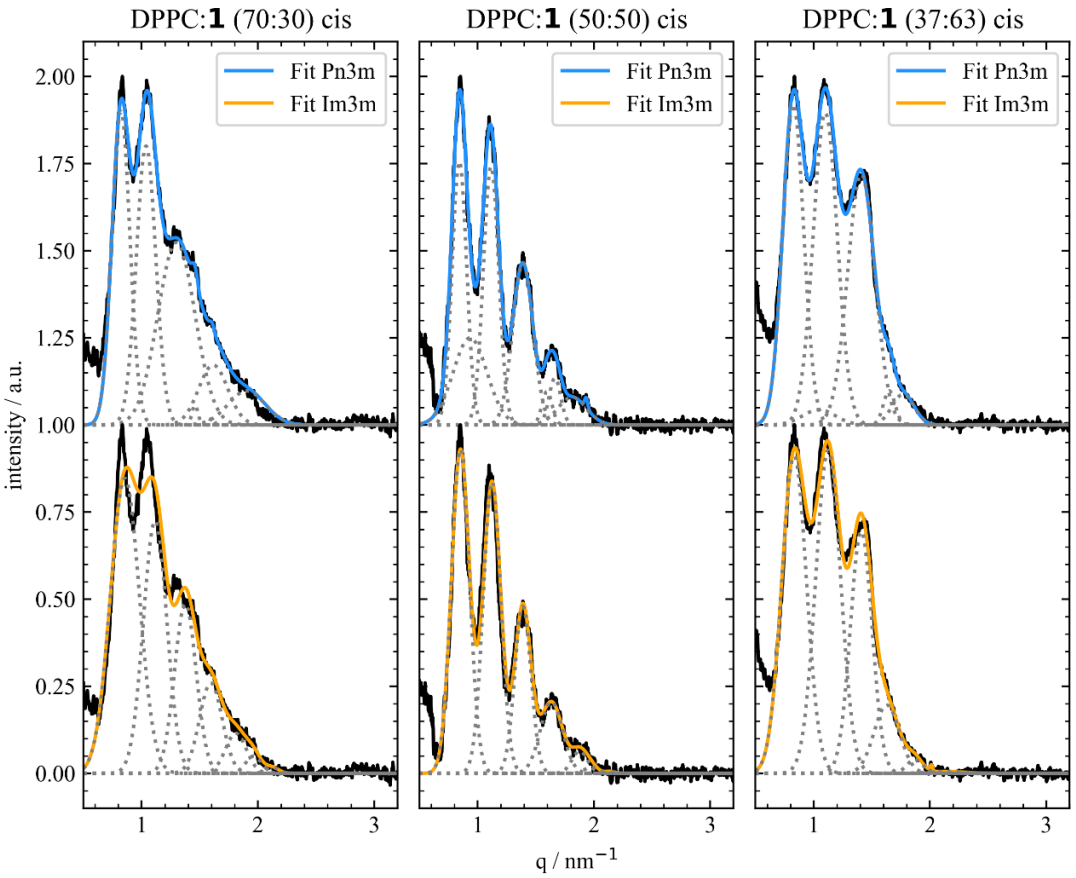

Figure S2 SAXS data obtained from the mixed DPPC with 30 % (left), 50 % (middle) and 63 % (right), respectively, *cis*-**1** shown twice with the fits for the Pn3m structure (top) and Im3m structure (bottom).

S4. Calculation of critical packing parameter

For the estimation of the maximum alkyl chain length l_{chain} and volume v_{chain} the following equations were used: (Tanford, 1972)

$$l_{\mathrm{chain}} \leq l_{\mathrm{max}} = 1.5 + 1.265 * n \,[\text{Å}]$$

$$v_{\mathrm{chain}} = 54.3 + 27.05 * 2n \,[\text{Å}^3]$$

where n represents the number of carbon atoms in one acyl chain. For both, DPPC and **1**, the acyl chain consists of 16 carbon atoms, resulting in $l_{\mathrm{chain}} = 21.74$ Å and $v_{\mathrm{chain}} = 919.9$ Å^3. As the acyl chains are not fully stretched in reality, values from a molecular dynamic simulation by (Kobierski *et al.*, 2022) at 20°C are used to get a more accurate estimation: $l_{\mathrm{chain}} = 19.22$ Å and $v_{\mathrm{chain}} = 722.57$ Å^3. They calculated the hydrophobic head area to 62.71 Å^2 and a resulting critical packing parameter CPP value of 0.6 for pure DPPC.

Calculating the area of hydrophilic head group is not trivial and different experimental and theoretical approaches report different values. New molecular models are used also in combination with machine learning to get a better understanding and more accurate values. (Kobierski *et al.*, 2022; Ishiwatari *et al.*, 2024; Khalil & Zarari, 2014) In this work, molecular modulations of our specific molecule **1** were not possible and therefore only an approximation of the hydrophilic head group area a_{head} is presented. To estimate a_{head} for the **1** isomer, the observed difference in area per molecule for the LE-LC phase transitions determined in Langmuir monolayer studies of mixed 90:10 DPPC:**1** at 21°C were taken. A difference of (14.7 ± 0.2) Å^2 and (22.8 ± 0.2) Å^2 between the LE-LC phase transition of DPPC and **1** *trans* and *cis*, respectively, were observed. Adding these values to the theoretical head group area of 62.71 Å^2 for DPPC the following values could be derived:

$$a_{\mathrm{head},\mathbf{1},\mathrm{trans}} = (77.4 \pm 0.2)\ \text{Å}^2$$

$$a_{\mathrm{head},\mathbf{1},\mathrm{cis}} = (85.5 \pm 0.2)\ \text{Å}^2.$$

Under the assumption, that the hydrophobic tail packing is independent of the polar head group, the chain length and volume modelled for DPPC can be assumed for **1** as well. This results in CPP values of 0.486 ± 0.002 and 0.440 ± 0.002 for the *trans*-**1** and *cis*-**1** isomer, respectively. The decrease of the CPP value upon cis isomerisation agrees with other studies on photoisomerisation molecules (Szymański *et al.*, 2013; Wang *et al.*, 2011).

References

Hyde, S. T. (2001). *Handbook of Applied Surface and Colloid Chemistry*, edited by Krister Holmberg, pp. 299–327, John Wiley & Sons, Ltd.

Ishiwatari, Y., Yokoyama, T., Kojima, T., Banno, T. & Arai, N. (2024). *Mol. Syst. Des. Eng.* **9**, 20–28, doi:10.1039/D3ME00151B.

Khalil, R. A. & Zarari, A. A. (2014). *Applied Surface Science*. **318**, 85–89, doi:10.1016/j.apsusc.2014.01.046.

Kobierski, J., Wnętrzak, A., Chachaj-Brekiesz, A. & Dynarowicz-Latka, P. (2022). *Colloids and surfaces. B, Biointerfaces*. **211**, 112298, doi:10.1016/j.colsurfb.2021.112298.

Szymański, W., Yilmaz, D., Koçer, A. & Feringa, B. L. (2013). *Accounts of chemical research*. **46**, 2910–2923, doi:10.1021/ar4000357.

Tanford, C. (1972). *The Journal of Physical Chemistry*. **76**, 3020–3024, doi:10.1021/j100665a018.

Wang, D., Dong, R., Long, P. & Hao, J. (2011). *Soft Matter*. **7**, 10713, doi:10.1039/C1SM05949A.

6.6 [MSH 1] Kinetics of light-induced mesophase transitions in azobenzene amphiphiles containing lyotropic liquid crystals

Continuing the study of light-induced bidirectional mesophase transitions in lyotropic liquid crystals, SAXS measurements of aggregates consisting of DPPC or DLPC phospholipids and one of the photoswitchable mimetics were performed to identify combinations of lipids that show light-induced structural changes. A light-induced mesophase transition is found in combinations of DPPC phospholipids and the photoswitchable mimetic AZOL-C12. For the combinations of DPPC with either AZGL-C12, AZGL-C16, AZLL-C12 or AZLL-C16 and of DLPC with either AZOL-C12 or AZOL-C16 no mesophase phase transition was observed. For some of the aggregates, a light-induced shift of the repeating distance was found. In addition to the static measurements, time-resolved *in situ* SAXS measurements revealed a time scale of multiple tens of seconds for the switching kinetics in crystals containing DPPC and either AZOL-C12 or AZGL-S-C16. As the following article is the first publication on the azobenzene amphiphile AZGL-S-C16, its synthesis route is presented in the Supporting Information. This lipid was synthesised by Michael Röhrl, Kiel University, and he wrote the description of the synthesis route.

In this article, the azobenzene mimetics are referred to as **1** to **7**. This nomenclature corresponds to the following assignment: **1** - AZGL-S-C16, **2** - AZOL-C12, **3** - AZOL-C16, **4** - AZGL-C12, **5** - AZGL-C16, **6** - AZLL-C12 and **7** - AZLL-C16 (compare Fig. 3.1 with Fig. 1 in the paper).

The data on the lipid mixtures were partially collected at beamtime BL2, DELTA (see Sec. 4.5.4) and the EMBL beamline P12 (see Sec. 4.5.5). The short exposure time at P12 allowed to perform time-resolved SAXS measurements to study the kinetics of the observed light-induced structural changes in mixtures with the azobenzene mimetics AZGL-S-C16 (**1** in the paper) and AZOL-C12 (**2** in the paper).

The manuscript [MSH 1] had been submitted and was under review at the time of submission of this work. The below reprinted article is now available under `https://doi.org/10.1107/S1600576725004923` and is reproduced with permission of the International Union of Crystallography.

research papers

JOURNAL OF APPLIED CRYSTALLOGRAPHY

ISSN 1600-5767

Received 25 February 2025
Accepted 30 May 2025

Edited by J. Keckes, Montanuniversität Leoben, Austria

‡ Present address: Department of Physics, Indian Institute of Technology (ISM) Dhanbad, Jharkhand 826004, India.

Keywords: kinetics; photoswitching; azobenzene; lipid mesophases; vesicles; small-angle X-ray scattering; structure determination; solution scattering; structural biology.

Supporting information: this article has supporting information at journals.iucr.org/j

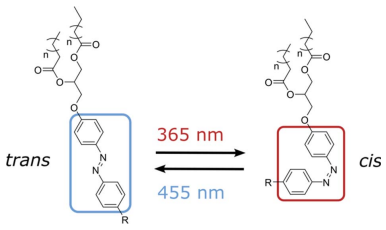

Kinetics of light-induced mesophase transitions in azobenzene amphiphiles containing lyotropic liquid crystals

Svenja C. Hövelmann,[a,b]* Michael Röhrl,[c] Ella Dieball,[a] Michelle Dargasz,[d] Jule Kuhn,[a] Rajendra P. Giri,[a]‡ Franziska Reise,[c] Dmytro Soloviov,[e] Clement E. Blanchet,[e] Michael Paulus,[f] Thisbe K. Lindhorst[c] and Bridget M. Murphy[a]*

[a]Institute of Experimental and Applied Physics, Kiel University, Leibnizstraße 19, 24118 Kiel, Germany, [b]Ruprecht Haensel Laboratory, Deutsche Elektronen-Synchrotron DESY, Notkestraße 85, 22607 Hamburg, Germany, [c]Otto Diels Institute of Organic Chemistry, Kiel University, Otto-Hahn-Platz 3-4, 24118 Kiel, Germany, [d]Department Physik, Universität Siegen, Walter-Flex-Straße 3, 57072 Siegen, Germany, [e]European Molecular Biology Laboratory, Hamburg Site, c/o DESY, Notkestraße 85, 22607 Hamburg, Germany, and [f]Fakultät Physik/DELTA, TU Dortmund, 44221 Dortmund, Germany. *Correspondence e-mail: hoevelmann@physik.uni-kiel.de, murphy@physik.uni-kiel.de

This study focuses on the kinetics of light-induced mesophase transitions in lyotropic liquid crystals containing a mixture of phospholipids and azobenzene amphiphiles. Lipid membranes organize in a wide range of morphologies, directly influencing their functionality and the efficiency of associated components such as proteins. Transitions between mesophases occur naturally during membrane fusion and can also be triggered by multiple factors, such as pH, salinity, temperature and light. Employing light to isomerize artificial photoswitchable lipids in mixed model membranes containing 1,2-dipalmitoylphosphatidylcholine or 1,2-didecanoylphosphatidylcholine revealed light-induced structural changes including mesophase transitions from a lamellar to a cubic *Pn*3*m* phase. Performing time-resolved small-angle X-ray scattering measurements, the kinetics of the change in membrane repeat distance and the transition from a lamellar to a bicontinuous cubic phase could be captured on the timescale of tens of seconds. The results demonstrate new possibilities for investigating intermediate states during mesophase transitions that are important to understand membrane fusion, and they highlight the potential of photoswitchable lipids for designing bespoke drug delivery systems.

1. Introduction

Controlling the geometric shape of lyotropic lipid crystals allows one to define their structure, activity and functionality as a whole and as individual parts inside their membrane, and subsequently to influence components embedded in or interacting with the membrane structure. Natural lipid membranes are built up from a multitude of components such as phospho- and glycolipids, cholesterol, and proteins. Each cell membrane is composed of a specific combination of lipids defining its elasticity, viscosity and lipid mesophase optimized for its functional purpose in the body (Op den Kamp, 1979; Devaux, 1991; Kelley *et al.*, 2020; Lorent *et al.*, 2020). Phospholipids, as the main component of bilayer membranes, define the membrane mesophase of natural membranes. Upon contact with water, amphiphile lipids self-assemble and form aggregates with multiple geometric shapes and structures depending on various properties such as lipid curvature, pressure, pH, salinity or volume concentration. These self-assembled geometric shapes range from micelles, hexagonal structures and lamellar bilayers to twisted bilayers forming

cubic mesophases (Yeagle, 2004). Bicontinuous cubic structures, with their ability to create separated water channels, are of special interest for creating ion channels (Ichikawa *et al.*, 2007), designing pharmaceutical drug delivery systems (Shah *et al.*, 2001; Hirlekar *et al.*, 2010; Martiel *et al.*, 2013) and embedding proteins to reduce their activity (Cournia *et al.*, 2015), to protect them from physical and chemical degradation (Rizwan *et al.*, 2010) or to act as an environment for protein crystallization (Cherezov *et al.*, 2002), and they are found in organelles (Walde & Ichikawa, 2021) and in cells during endo- and exocytosis (Luzzati, 1997). Each cubic structure displays distinct diffusion coefficients and modes (Zabara & Mezzenga, 2014). Therefore, controlling the lipid mesophase and its geometric shape opens new possibilities to design functional materials for pharmaceutical, food and cosmetic applications and bio-hybrid actuators and sensors (Carlsen & Sitti, 2014).

To understand the complexity of the interactions between membrane components, model membranes are employed to investigate interactions between single components. Multiple factors have been identified that can be utilized to induce a mesophase transition from a lamellar to a cubic phase and between cubic phases. Pressure (Winter *et al.*, 1998; Winter, 2002), pH (Ribeiro *et al.*, 2019) and salinity (Muir *et al.*, 2012; Kalvodova *et al.*, 2005) have been successfully employed so far. However, changing the physical or chemical properties requires specially designed sample cells, and often no reversibility between the mesophases could be reached. Therefore, we introduced in our recent study (Hövelmann *et al.*, 2024) a model system of the phospholipid 1,2-dipalmitoylphosphatidylcholine (DPPC) and a photoswitchable mimetic using light as the controlling element to induce a reversible and repeatable mesophase transition between the multilamellar and bicontinuous cubic *Pn*3*m* structures.

We present an array of model systems comprising one of seven distinct photoswitchable lipid mimetics (Reise *et al.*, 2018) in combination with the phospholipids DPPC or 1,2-didecanoylphosphatidylcholine (DLPC) to identify the structures of aggregates formed by mixing azobenzene amphiphiles and phospholipids in ratios varying from 0 to 100% for both components in water. In particular, the mesophase and possible light-induced mesophase transitions are of increasing interest (Fig. 1). The aggregate structures were characterized using small-angle X-ray scattering (SAXS), and time-resolved SAXS measurements were performed to investigate the evolution of the structural changes and mesophase transitions.

This research will help to design model systems for studying the influence of mesophase transitions on lipid–lipid/lipid–protein interactions and protein functionality in a light-controlled, reversible and repeatable way.

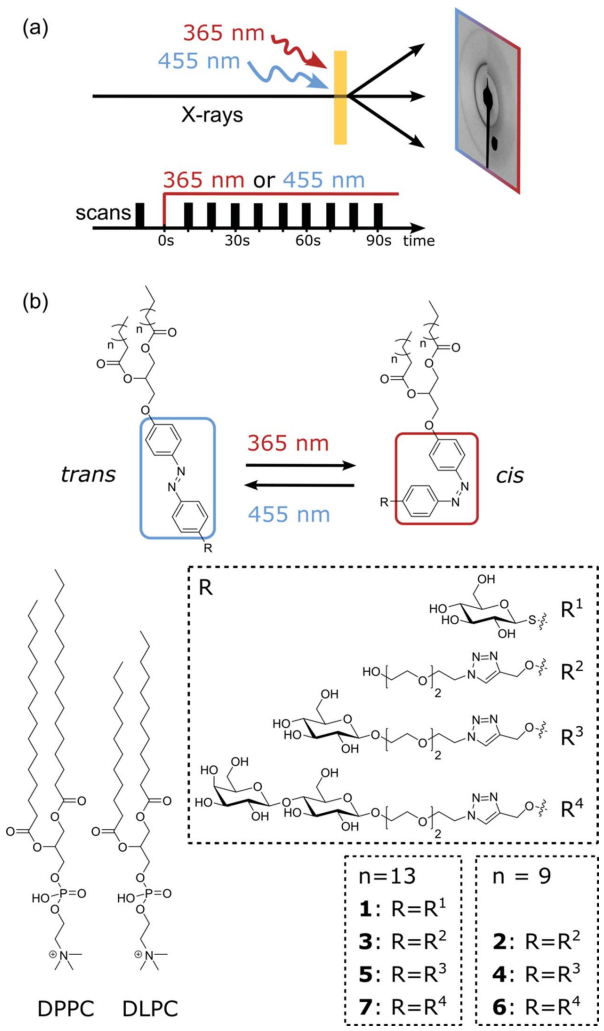

Figure 1
(*a*) Schematic diagram of the static (Hövelmann *et al.*, 2024) and kinetic transmission SAXS measurement setup. For the kinetic measurements, the structures were probed at various times after starting to illuminate the sample continuously as indicated. (*b*) Chemical structures of DPPC, DLPC, and both the *trans*- and *cis*-isomers of azobenzene amphiphiles **1** to **7**. The length of the double acyl chains of the azobenzene amphiphiles corresponds to either 12 (n = 9) or 16 (n = 13) carbon atoms.

2. Experimental details

2.1. Azobenzene mimetics

Seven azobenzene amphiphiles, referred to as **1** to **7** hereafter as shown in Fig. 1(*b*), were investigated. Lipids **2** to **7** were synthesized in accordance with our previously published synthesis route (Reise *et al.*, 2018) and differ in the number and type of carbohydrate moieties attached (none, glucose, lactose) to the head group and in the length of the acyl chain. This being the first publication on the azobenzene amphiphile with a glucose-based head group **1**, the synthesis route for **1** is presented in the supporting information Section S1, together with the UV–Vis absorption spectra in Fig. S10. In contrast to **2** to **7**, the glucosyl head group of **1** is linked via a sulfur atom directly to the azobenzene photoswitch.

2.2. Sample preparation

DPPC and DLPC were bought from Avanti Polar lipids (Alabaster, Alabama, USA). The phospholipid and azobenzene amphiphile mixtures were dissolved in 1 ml of

chloroform (Sigma Aldrich) with cumulative lipid concentrations amounting to 5 or 10 m*M* and were prepared with incrementally varying ratios of the azobenzene amphiphiles. The mixtures were then subjected to a drying process, whereby they were reduced to thin films, using a Rotavapor R-300 from Büchi Labortechnik GmbH (Essen, Germany). The drying was conducted at a bath temperature of 45°C and a pressure of 16 mbar for a duration of at least 1 h. Subsequent to the drying process, the dried films were stored within a refrigeration unit maintained at a temperature below 10°C. On the day of the measurements, all samples were prepared by adding warm Milli-Q water to the film and then rotating and shaking the suspension in a water bath at a temperature above 45°C until a homogenous solution was formed. Larger lipid lumps were broken up using a vortex mixer and ultrasonic water bath. The pH was adjusted to 7.4 with Roti PreMix PBS salt (Carl Roth) (0.14 *M* NaCl, 2.7 m*M* KCl, 10 m*M* phosphate) for the measurement on beamline P12 at EMBL, DESY, and one of the two beamtimes on BL2 at DELTA. The hydrated samples were stored in the refrigerator at the beamline. Prior to the measurements, the hydrated solutions were allowed to reach room temperature by leaving them outside of the refrigerator for 1 h. The SAXS measurements were performed within 24 h of sample hydration. In this time frame the SAXS patterns from tested samples were identical, confirming structural stability. Samples prepared in this way are referenced as ratio lipid:number of photoswitchable mimetic, for example: 95:5 DPPC:**1**, 80:20 DPLC:**3**.

2.3. Isomerization

Custom-made illumination devices with rows of 365 nm LEDs [Nichia, NCSU033B(T)] and 455 nm LEDs (Osram, LD CQ7P) were employed to isomerize the azobenzene amphiphiles from *trans* to *cis* and back. A remote connection to the illumination device was set up and the samples were illuminated for at least 5 min to switch between the *trans* and *cis* states. On beamline BL2 at DELTA, the illumination device was mounted above the capillary sample holder at a distance of about 10 cm with fluxes for 365 and 455 nm of 2.0 mW cm^{-2} in the first beamtime and 1.6 mW cm^{-2} in the second beamtime. On beamline P12 at EMBL, the illumination device was placed on top of the quartz window of the standard flow cell setup available on the beamline. A direct power measurement at the flow cell position could not be performed due to the chamber design. However, the estimated distance of 7 cm between the illumination device and the capillary would correspond to a flux of 7 mW cm^{-2}. To distinguish between the *trans* and *cis* isomers, we use the naming convention *trans*-**1** and *cis*-**1**.

2.4. Small-angle X-ray scattering

In situ SAXS measurements were performed on BL2 at DELTA (Dargasz *et al.*, 2022) and on P12 at EMBL (Blanchet *et al.*, 2015) at concentrations of 10 and 5 m*M*, respectively. The corresponding mass per volume concentrations are listed in Table S1. On BL2 a simple capillary sample holder with 2 mm diameter quartz capillaries was used under an ambient atmosphere and at a room temperature of about 25°C. A photon energy of 12 keV, a beam size of about 0.6 × 0.6 mm and a MAR345 2D image-plate detector (marXperts, Norderstedt, Germany) were employed. Standard silver behenate powder was used to calibrate the detector distance and orientation. Using the *FIT2D* software (Hammersley *et al.*, 1995; Hammersley *et al.*, 1996; Hammersley, 1997; Hammersley, 2016), the 2D detector images were processed by applying a pixel mask and detector orientation correction. The data were then transformed from real to reciprocal space and an angle integration was performed to provide reduced 1D scattering patterns in q space [$q = (4\pi/\lambda)\sin\theta$, where θ is half the scattering angle and λ is the wavelength of the incident radiation]. The typical exposure time was 180 s for the data collection followed by a detector read-out time of an additional 120 s.

On the P12 EMBL BioSAXS beamline at DESY, the automated auto-sampler setup was used in combination with a PILATUS 6M detector from Dectris (Baden-Daettwil, Switzerland). Measurements were performed at 10 keV with a beam size of 0.2 × 0.12 mm. On this beamline, a flow mode for the sample is available which allows fresh sample from the stock solution to be flushed through the measurement capillary at a continuous flow rate to exchange the sample volume and reduce beam-induced damage in the sample. However, for the time-resolved measurements, the sample had to be illuminated *in situ* while being in the capillary for multiple tens of seconds. Due to the limited area of illumination, a constant sample volume was used to ensure measurement on the illuminated part. After the illumination and measurement, the sample was exchanged. After the start of the measurement, the routine was stopped during the loading process to allow manual loading of the capillary and illumination of the sample before data collection with an exposure time of 0.1 s at a transmission of 80%. Following beam damage assessment to avoid sample degradation, four frames, each with an exposure time of 0.1 s, were chosen for optimal data quality. The 2D detector images were processed automatically on the beamline and reduced 1D scattering patterns in q space were saved.

2.5. Time-resolved small-angle X-ray scattering

Time-resolved measurements were performed on the P12 EMBL BioSAXS beamline. The samples were filled into the automatic sample changer in the thermally stable *trans* state. After the sample had been loaded into the quartz capillary, there was a waiting/illumination time using the remote-controlled LEDs at either 365 or 455 nm, varying from 2 to 180 s. For the *cis* to *trans* isomerization, the sample was illuminated first at 365 nm for 60 s and then at 455 nm. During the illumination the samples were protected from X-ray damage using the fast shutter. Subsequently, the fast shutter was opened and X-ray measurements were carried out while continuing the illumination. After each scan, the capillary was rinsed automatically before being refilled for the next time delay. At each time delay, data were collected with an

exposure time of 0.4 s to exclude X-ray-induced beam damage. Thus, the time resolution was set to 400 ms.

2.6. Analysis software

The data collected on BL2 at DELTA were analysed using a purpose-written Python script for background correction of the reduced 1D SAXS pattern and resaving the corrected pattern in the NeXus file format with associated metadata (Wilkinson *et al.*, 2016). Following the metadata standards proposed by DAPHNE4NFDI (Barty *et al.*, 2023; Lohstroh *et al.*, 2024), the newly generated NeXus file contains the background-corrected pattern, the uncorrected signal, information on the background reduction, and detector-, beamline- and sample-specific metadata. For the background reduction, reference measurements on pure water and buffer solutions were collected. The P12 data were taken as extracted by the automatic analysis pipeline of the beamline, including a background subtraction from the solvent reference measurement. Structure analysis of the BL2 and P12 data was done with custom Python scripts to determine the mesophase and *d* spacing. All SAXS data were fitted using a two-step approach, described in detail in Section S2 and by Hövelmann *et al.* (2024). The data and script are accessible from Hövelmann & Murphy (2025) and further information on their accessibility is given in the section *Data availability*.

3. Results and discussion

3.1. Tuning the mesophases

Investigating various combinations of DPPC or DLPC with the azobenzene amphiphiles **1** to **7** [Fig. 1(*b*)] at 21 and 25°C with *in situ* SAXS measurements performed in the *q* range of 0.5–4.5 nm^{-1} (Fig. 2), multiple mesophases could be identified following the fitting routine described in detail in Section S2. Generally, it can be summarized that, for mixtures containing more than 20% of azobenzene amphiphiles **2** to **7**, a bicontinuous cubic mesophase was found. For low lipid percentages, especially 2.5 and 5% of the azobenzene amphiphiles **1** to **5**, a lamellar mesophase was observed, which corresponds to only a small deviation from the lamellar phase of pure DPPC and DLPC. For DPPC and DLPC, lamellar *d* spacings of 6.34 ± 0.03 nm and 5.89 ± 0.01 nm, respectively, were determined, which are in good agreement with previous studies (Soloviov *et al.*, 2012; Kornmueller *et al.*, 2018; Shafieenezhad *et al.*, 2023). All *d*-spacing values are listed in Table S1.

In mixtures of DPPC:**1** and DPPC:**2** a light-induced change in the multilayer repeat distance (*i.e. d* spacing) and switching between mesophases, respectively, were found. Upon switching from the *trans* state to the *cis* state the mesophase transition from a multilamellar phase to a bicontinuous cubic phase *Pn3m* was observed for DPPC:**2** (the mimetic without glycan). The kinetics of this transition are discussed below and

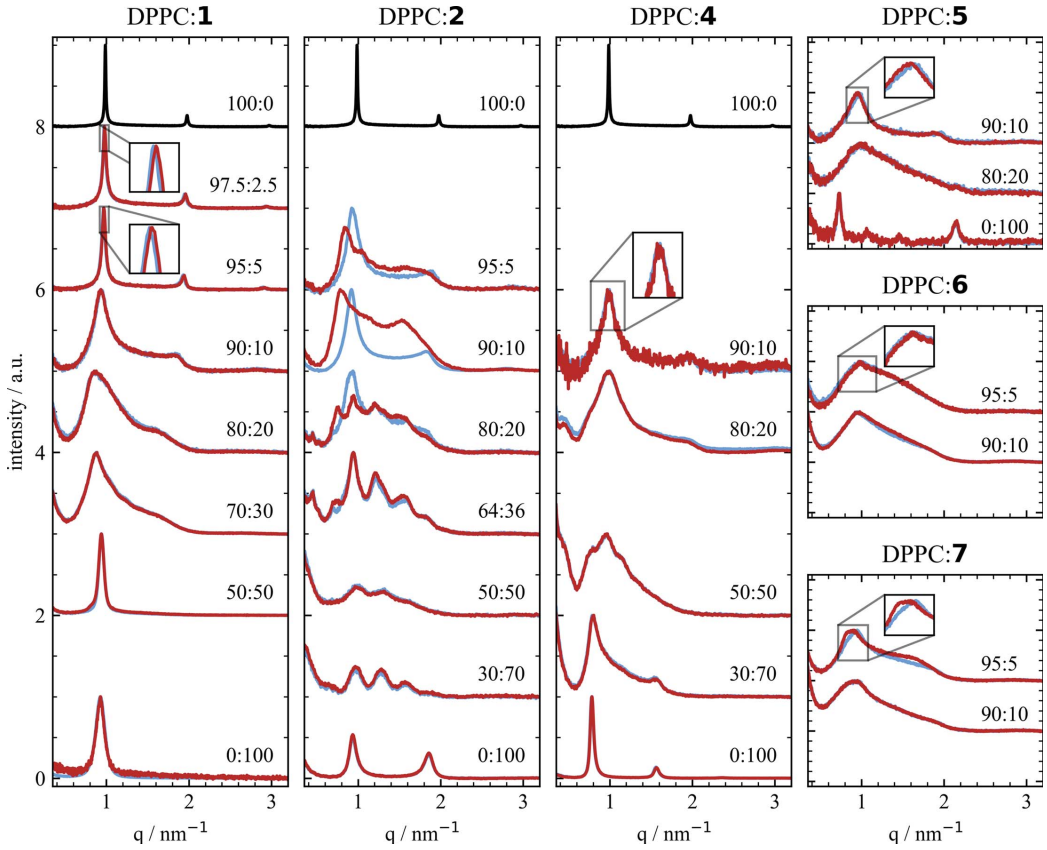

Figure 2
SAXS data for pure DPPC (black) and mixtures of DPPC and the azobenzene amphiphiles **1**, **2** and **4** to **7** [Fig. 1(*b*)] in *trans* (blue) and *cis* (red) states for all mixtures in their annotated ratios. All scattering patterns shown here are background subtracted using reference measurements of the pure solution.

research papers

Table 1
Mesophases and *d* spacings derived from the SAXS data for pure DPPC vesicles and mixed azobenzene amphiphile structures.

T (°C)	DPPC:**1**	Mesophase	*d* (nm)
25	100:0	Lamellar	6.35 ± 0.01

		trans		*cis*	
T (°C)	DPPC:**1**	Mesophase	*d* (nm)	Mesophase	*d* (nm)
21	97.5:2.5	Lamellar	6.44 ± 0.01	Lamellar	6.40 ± 0.02
21	95:5	Lamellar	6.51 ± 0.01	Lamellar	6.47 ± 0.02
21	90:10	Lamellar	6.71 ± 0.04	Lamellar	6.75 ± 0.04

		trans		*cis*	
T (°C)	DPPC:**2**	Mesophase	*d* (nm)	Mesophase	*d* (nm)
25	95:5	Lamellar	6.7 ± 0.09	*Pn3m*	10.4 ± 0.2
25	90:10	Lamellar	6.8 ± 0.08	*Pn3m*	11.2 ± 0.4
21	80:20	*Im3m*	12.7 ± 0.3	*Im3m*	12.6 ± 0.4
		Pn3m	11.6 ± 0.3	*Pn3m*	11.7 ± 0.2
		Lamellar	6.9 ± 0.09		

		trans		*cis*	
T (°C)	DPPC:**3**	Mesophase	*d* (nm)	Mesophase	*d* (nm)
25	97.5:2.5	Lamellar	6.42 ± 0.03†	*Pn3m*	11.1 ± 0.6†
25	95:5	Lamellar	6.45 ± 0.03†	*Pn3m*	11.1 ± 0.4†
25	90:10	Lamellar	6.55 ± 0.03†	*Pn3m*	11.2 ± 1.0†
		Pn3m	11.0 ± 0.7†		
25	80:20	Lamellar	6.53 ± 0.05†	*Pn3m*	10.4 ± 1.0†
		Pn3m	11.4 ± 0.7†		

† Reference values for DPPC:**3** from Hövelmann *et al.* (2024).

shown in Fig. 5. The mesophase transition shows great reversibility upon switching back to the *trans* state and high reproducibility through multiple switching cycles. This finding is similar to the mesophase transition observed from a lamellar to a *Pn3m* phase for DPPC:**3** mixtures reported in our previous study (Hövelmann *et al.*, 2024). The azobenzene amphiphiles **2** and **3** only differ in the length of the acyl chain [Fig. 1(*b*)]. For both DPPC:**2** and DPPC:**3**, the lamellar phase is dominant up to a content of 10% of *trans*-**2** and *trans*-**3**. On increasing the ratio of the photoswitchable lipid to 20%, cubic phases evolve in addition to the lamellar phase. For comparison, the *d* spacings and mesophases for up to 20% of **2** and **3** are listed in Table 1. While for DPPC:**3** only the additional bicontinuous cubic phase *Pn3m* was determined for 20% of *trans*-**3**, a coexistence of two bicontinuous cubic phases, *Pn3m* and *Im3m*, in addition to the lamellar phase was identified for DPPC:**2** for 20% of *trans*-**2**. Switching from the *trans* to the *cis* state results in the disappearance of the lamellar phase peaks and an increase in intensity of the peaks belonging to the *Pn3m* structure, while the intensity and position of the *Im3m* peaks remain constant. This suggests that the mesophase transition only takes place between the lamellar and *Pn3m* structured parts, while the sections structured in *Im3m* are unaffected by the conformational change of **2**. Identification of the phases has been performed by checking combinations of different phases to match the peaks visible in the SAXS data (Fig. S11). At percentages higher than 36% of **2**, no difference between the *trans* and *cis* states was observed and the mesophase was identified to be a coexistence of *Pn3m* and *Im3m*

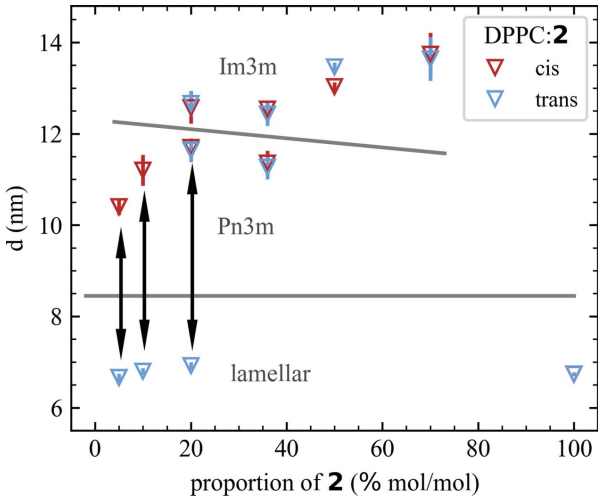

Figure 3
Fitted values of the *d* spacing for *trans* (blue) and *cis* (red) DPPC:**2** data. Note the increase in *d* spacing by 50% to 60% and the mesophase transition by switching from the *trans* to the *cis* state (and *vice versa*) for 95:5, 90:10 and 80:20 DPPC:**2** (highlighted by the black arrows). The grey lines are inserted as points of reference to differentiate between the different mesophases. The *d*-spacing error is estimated from the deviations of the peak positions as described in Section S2.

phases. At 70% of **2**, while both the *Pn3m* and *Im3m* phases give a reasonable fit (Fig. S12), the fitted values for the *Im3m* phase are more reasonable as the *d* spacing is close to that for the *Im3m* structure observed at 50% and below (Table S1). Therefore, in Fig. 3 only the fitted value for the *Im3m* structure is included. Increasing the percentage of *trans*-**2** to 100% reveals the formation of multilamellar vesicles with a spacing of 6.74 ± 0.05 nm. The *d*-spacing values are shown graphically in Fig. 3 to visualize the switching-induced mesophase transition and change in *d* spacing.

Whereas DPPC:**2** and DPPC:**3** both show light-induced mesophase transitions, combinations of DPPC with the sugar-containing azobenzene amphiphiles **1**, **5** and **7** display an increase or decrease in the *d* spacing upon switching. In contrast, for combinations of DPPC with the shorter chain sugar-containing mimetics **4** and **6** no light-induced structural change could be observed. Both 90:10 DPPC:**5** and 95:5 DPPC:**7** mixtures show a shift of the first- and second-order peaks to smaller *q* upon switching to the *cis* state, corresponding to an increase in the *d* spacing and an expansion of the structure from 6.42 ± 0.08 nm to 6.57 ± 0.08 nm for the 90:10 DPPC:**5** sample. For 100% of **5**, two lamellar lipid phases with *d* spacings of 8.63 ± 0.01 nm and 5.89 ± 0.02 nm are found. Unfortunately, the exact geometric structure for 80:20 DPPC:**5** could not be determined, as the lack of clear peaks leads to reasonable fits for multiple cubic structures and any combination thereof. The same issue occurs for the data of DPPC:**6** and DPPC:**7**. Nevertheless, all identified structures and *d* spacings are listed in Table S1. In contrast to the increase in *d* spacing for 90:10 DPPC:**5** and 95:5 DPPC:**7**, the data for both 97.5:2.5 and 95:5 DPPC:**1** show a decrease in the lattice parameter by 0.04 nm upon switching to the *cis* state. Having both a glucose-based head group and the same acyl

chain length, **1** and **5** differ in the linker between the azobenzene and glucose groups [Fig. 1(*b*)]. Above 10% no difference between the *trans*-**1** and *cis*-**1** states is observed. At higher percentages than 20% of **1**, another structure adds to the lamellar phase structure, and from 50% upwards only a first-order peak with a repeat distance of 6.67 ± 0.01 nm and no higher-order peaks are detected.

Overall, the data illustrate the strong dependency of the mesophase on the structure of the azobenzene amphiphile and show that mixtures with shorter azobenzene amphiphiles form more defined mesophases. Especially for the longest, lactose-containing, azobenzene amphiphiles **6** and **7**, the solubility during sample preparation decreases greatly at higher percentages and the scattering signal is less defined, with the absence of clear peaks complicating the mesophase determination. Further, we found that a small but visible change in structure upon switching was observed for **5** and **7**, although the comparable molecules **4** and **6**, with a shorter acyl chain but identical head group, showed no structural difference. Also, the percentage up to which a switching could be observed decreases with the length of the photoswitchable molecule. While photoswitching was detected for percentages of up to 20% of **2** and **3** (both with no sugar), for **5** (glucose) and **7** (lactose) a difference between the *trans* and *cis* states was only found up to 10% and 5%, respectively.

To identify the effect of the phospholipid present in the liquid crystal on the light-induced mesophase transition, we investigated mixtures of DLPC with **2** and **3**. Compared with DPPC, DLPC possesses shorter acyl chains [Fig. 1(*b*)], and it is in the liquid crystalline phase at room temperature as its phase transition temperature of −2°C (Mabrey & Sturtevant, 1976) is much lower than that for DPPC (41°C; Biltonen & Lichtenberg, 1993).

Similar to the mixtures with DPPC, the DLPC mixtures show a lamellar mesophase for low percentages of **2** and **3** as shown in Fig. 4(*a*). The lamellar *d* spacings for 95:5 DLPC:**2** and 95:5 DLPC:**3** are 6.00 ± 0.01 nm and 5.93 ± 0.01 nm, respectively, smaller than their DPPC-containing counterparts. Yet the absolute increase in the *d* spacing upon adding 5% of **2** and **3** is comparable for DLPC and DPPC. At 10%, coexisting cubic phases *Pn*3*m* and *Im*3*m* emerge and above 20% only cubic phases are present. Despite the similarities, only a very small increase in the lateral structural parameter within the error bars is observed for 5% of **2**, while for all higher percentages of **2** and all percentages measured of **3** no structure difference upon switching is found. Most likely, the lack of a structural change upon illumination stems from the difference in phase of the phospholipids. Being in the liquid crystalline phase, the DLPC molecules are more flexible and their fluidity is higher than the DPPC molecules, suggesting

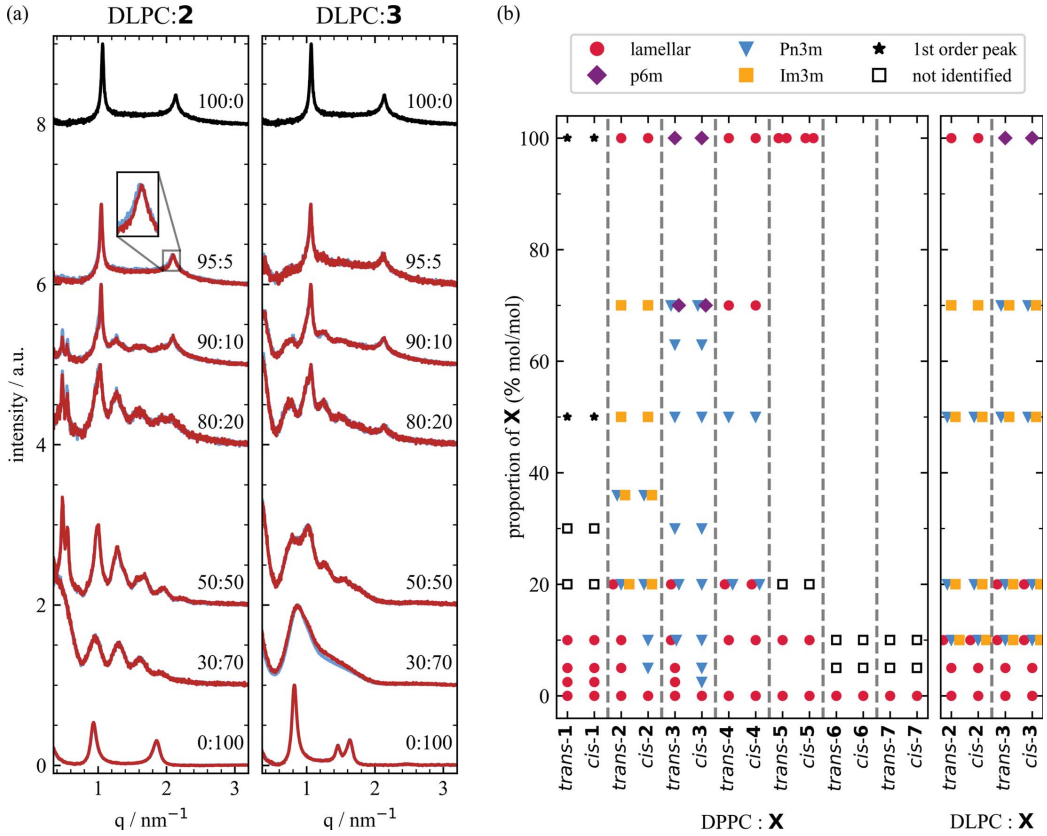

Figure 4
(*a*) SAXS data for pure DLPC (black) and mixtures of DLPC and the azobenzene amphiphiles **2** and **3** in *trans* (blue) and *cis* (red) states. (*b*) Mesophases for mixtures of DPPC, DLPC and the azobenzene amphiphiles **1** to **7** [Fig. 1(*b*)]. Mesophases for DPPC:**3** are taken from Hövelmann *et al.* (2024).

research papers

that photoswitching does not result in an observable change of the mesophase. In previously conducted measurements at temperatures above the phase transition of DPPC, no structural change was observed for DPPC:**3** mixtures either (Hövelmann *et al.*, 2024), strongly endorsing the dependence of the observed mesophase change on the lipid phase. The diversity of mesophases found for all the mixtures of liquid crystals reported here is summarized graphically in Fig. 4(*b*).

3.2. Kinetics of switching

Time-resolved measurements were performed on 97.5:2.5 and 95:5 DPPC:**1** and 80:20 DPPC:**2** samples on the EMBL beamline P12. Utilizing the automatic sample changer on the beamline, the sample was pre-illuminated at 365 and 455 nm to bring the sample to the *trans* or *cis* state, respectively. To achieve a time delay between illumination and X-ray irradiation, the sample was loaded manually into the sample capillary, as described in the experimental details of the time-resolved SAXS measurements, Section 2.5. For each sample, two runs with multiple measurements were performed to capture the light-induced structure change *in situ* for both transitions from *trans* to *cis* and *vice versa*. A selection of scans for 95:5 DPPC:**1** and 80:20 DPPC:**2** are shown in Figs. 5(*a*1) and Fig. 5(*b*1), respectively. All scans were fitted with the same parameters as for the structures found from the static measurements. For DPPC:**1**, a decrease and increase in the *d* spacing can be observed upon switching from *trans* to *cis* and *vice versa*. While the lamellar mesophase stays constant, the *d* spacing increases and decreases by about 0.03 nm for 2.5:97.5 and 5:95 DPPC:**1**. The thickness starts to change within the first 5 s of illumination at 455 and 365 nm, and reaches the final thickness for the *trans* and *cis* states after 50 s for 2.5% of **1**. Similarly, for 5% of **1** the *cis* state is reached after 40 s, while

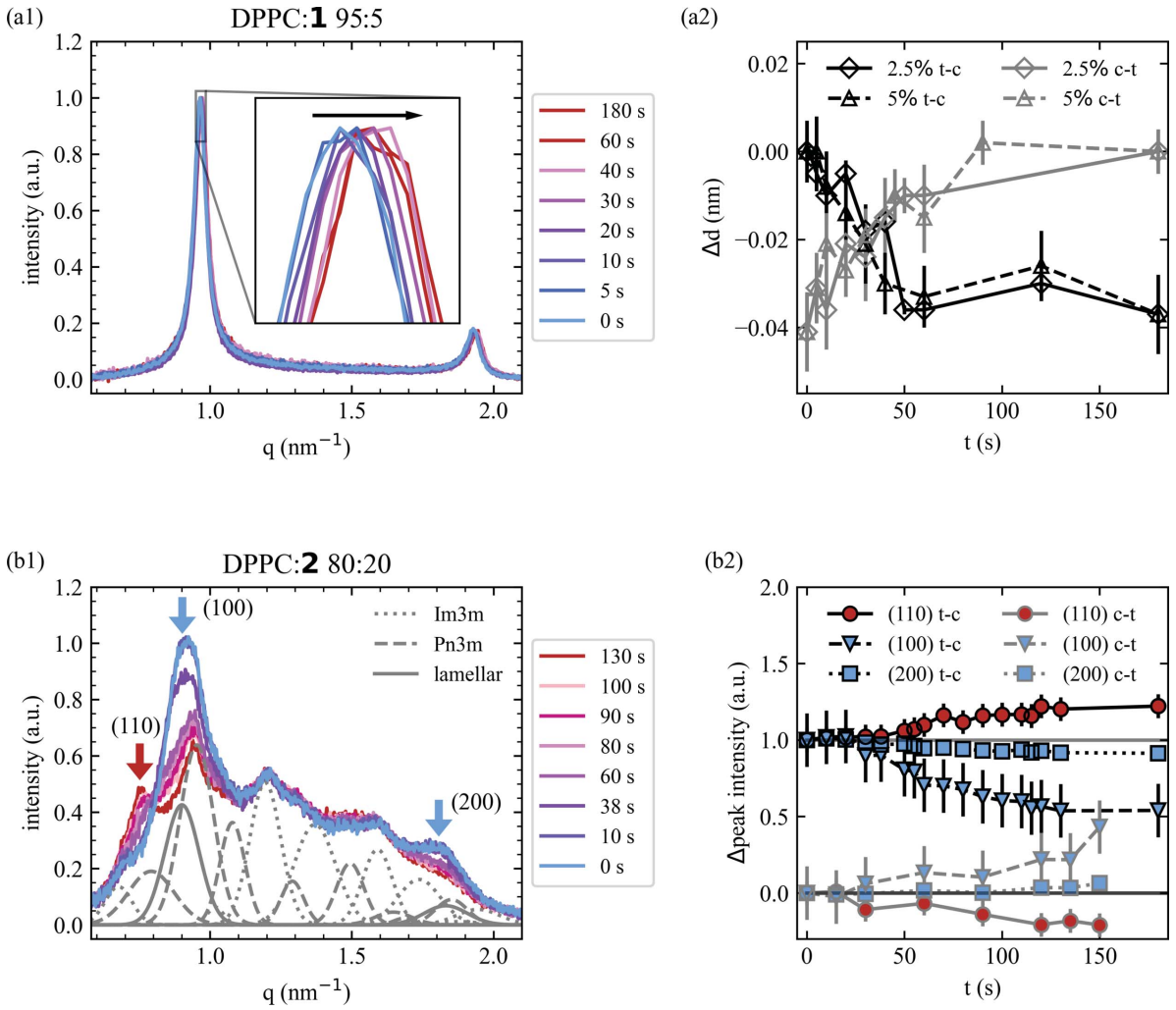

Figure 5
Time-resolved SAXS data for azobenzene amphiphile mixtures of (*a*1) 95:5 DPPC:**1** and (*b*1) 80:20 DPPC:**2** from the *trans* state (blue) to the *cis* state (red) after illuminating the sample for the given number of seconds. In addition to the measured scattering data, the Gaussian curves belonging to the fitted lamellar (blue), *Pn3m* (red/grey solid lines) and *Im3m* (grey dotted lines) phases for the *trans* state at 0 s are shown underneath the data in panel (*b*1) (the fits for the *cis* state are shown in Fig. S11). (*a*2) Fitted values of the *d* spacing for 95:5 and 97.5:2.5 DPPC:**1**. (*b*2) Comparison of the intensity of the lamellar phase 100 and 200 peaks and *Pn3m* 110 peak [marked by arrows in panel (*b*1)] of 80:20 DPPC:**2** for the *trans* to *cis* (t-c) and *cis* to *trans* (c-t) isomerization.

switching back to the *trans* state takes about 90 s. The fitted *d* spacings are shown in Fig. 5(*a*2).

In contrast to the instantaneous induced thickness increase and decrease observed for both DPPC:**1** samples, the light-induced mesophase transition found in 80:20 DPPC:**2** does not occur immediately. The first observable change in structure takes place after 30 s of illuminating the sample. For the *trans* state, peaks belonging to three mesophases were identified, namely the lamellar, cubic *Pn*3*m* and *Im*3*m* phases as listed in Table 1. The fits revealed that the *d* spacings for all three phases stayed constant during isomerization within the error bars (Table S2). Comparing the peaks of the *trans* and *cis* states, the peaks belonging to the *Im*3*m* structure do not change in either position or relative intensity. This suggests that the *Im*3*m* structure is unaffected by the structural re-arrangement and the switching only happens between the lamellar and cubic *Pn*3*m* structures. Therefore, each scan was normalized to the *Im*3*m* 211 peak intensity. In the *trans* state the first- (100) and second-order (200) peaks belonging to the lamellar phase are prominent but they disappear when switching to the *cis* state. Meanwhile, the 110 peak of the *Pn*3*m* structure evolves strongly upon switching to the *cis* state [Fig. 5(*b*1)]. To follow the temporal development of the phase transition, the intensities of the 100, 200 and 110 peaks are visualized in Fig. 5(*b*2). Isomerizing from the *trans* to the *cis* state, the first changes in intensity of the 100 and 200 peaks are observed after 30 s of illumination at 365 nm. Meanwhile, the intensity of the 110 peak stays constant and starts to increase at 50 s. Though the start of the appearance of the 110 peak is delayed compared with the disappearance of the 100 and 200 peaks, all peaks reach their final intensity after 120 s. This suggests that a certain number of molecules have to be isomerized before a phase transition is induced. Switching back from the *cis* to the *trans* state, the change in peak intensity is observed after 30 s of illumination at 455 nm for all three peaks simultaneously. This suggests the mesophase transition from *Pn*3*m* to a lamellar phase upon isomerization back to the *trans* state is faster and may have a different mechanism. Nevertheless, the mesophase transition takes 120 s to reach equilibrium.

4. Conclusion

In this work, we confirmed with small-angle X-ray scattering that visible and UV light is able to induce reversible and repeatable structural changes in lyotropic liquid crystals. The crystals consist of mixtures of DPPC, DLPC and photo-switchable azobenzene amphiphiles, named **1** to **7**, in aqueous solutions. Generally, photoswitching of the mesophase was observed for percentages up to 20% of azobenzene molecules **2** without a carbohydrate group, **1** and **5** both with glucose, and **7** with lactose attached to the headgroup in combination with DPPC at room temperature. Similarly to our previous investigation on the combination of DPPC and mimetic **3** without a carbohydrate head group (Hövelmann *et al.*, 2024), a light-induced mesophase transition from a lamellar structure in the *trans* state to a cubic *Pn*3*m* structure in the *cis* state was observed for DPPC:**2** mixtures for a percentage of up to 20% of **2**. For sugar-containing mimetics **1**, **5** and **7**, small changes in the lamellar *d* spacing were detected up to lipid percentages of 5%, 10% and 5%, respectively. All structural changes and mesophase transitions could be switched reversibly, repeatedly and reproducibly. While structural changes were observed for multiple combinations with DPPC, lyotropic liquid crystals consisting of DLPC and photoswitchable molecules showed no light-induced changes, suggesting that the overall membrane properties influenced by the phospholipids play a vital role in whether a structural change is observed upon isomerization of the azobenzene amphiphile.

Performing time-resolved SAXS measurements allowed the kinetics of the light-induced structural changes to be observed *in situ* for DPPC:**1** and DPPC:**2** mixtures. For the glucose-containing DPPC:**1**, the lamellar *d* spacing starts to change within seconds of the initial illumination and reaches its final value within 90 s. Meanwhile, the light-induced mesophase transition from a lamellar to a *Pn*3*m* phase in 80:20 DPPC:**2** (no sugar) happened on the minute timescale. The transition was tracked by comparing the intensities of the 100 and 200 peaks belonging to the lamellar phase and the cubic *Pn*3*m* 110 peak. While the intensity of the lamellar peaks starts to decrease after 30 s of illumination for isomerization into the *cis* state, the *Pn*3*m* peak only rises after 50 s of illumination. Meanwhile, during *trans* isomerization, the *Pn*3*m* peak and lamellar peaks change their intensity simultaneously after 30 s. After 120 s the isomerization is complete for both the isomerization from *cis* to *trans* and back.

These findings indicate that the combination of DPPC and azobenzene amphiphiles in lyotropic liquid crystals is optimal to observe light-induced mesophase transitions at room temperature. The type of induced structural changes depends on the specific azobenzene amphiphile. The timescale for light-induced mesophase transitions has been identified as being in the multiple tens of seconds. Investigating these phase transitions and the timescale of their kinetics furthers the understanding of cellular fusion processes and allows for the design and evaluation of membrane systems for drug delivery and protein folding.

5. Related literature

For further literature related to the supporting information, see Bruneau *et al.* (2015), Dams *et al.* (2013) and Leriche *et al.* (2010).

Acknowledgements

Time-resolved synchrotron SAXS data were collected on beamline P12 operated by EMBL Hamburg at the PETRA III storage ring (DESY, Hamburg, Germany). The authors also thank the DELTA machine group for providing synchrotron radiation, and Dr Christian Sternemann and Sonja Reinheimer for their support during the beam times in March and December 2022. We would like to thank Dr Chen Shen for

assistance in using the Büchi R300 rotary evaporator. Open access funding enabled and organized by Projekt DEAL.

Conflict of interest

There are no conflicts of interest.

Data availability

Raw data, fit parameters and analysis scripts are available via https://doi.org/10.57892/100-112. International generic sample numbers (IGSNs): DPPC (https://doi.org/10.60578/x2ep-qgqj); DPPC:**1** 97.5:2.5 (https://doi.org/10.60578/pmzq-9at9); DPPC:**1** 95:5 (https://doi.org/10.60578/s4fn-nmc1); DPPC:**1** 90:10 (https://doi.org/10.60578/k080-8a1z); DPPC:**1** 80:20 (https://doi.org/10.60578/32vk-hk7k); DPPC:**1** 70:30 (https://doi.org/10.60578/na1d-eqhc); DPPC:**1** 50:50 (https://doi.org/10.60578/yf0e-mqt6); DPPC:**1** 0:100 (https://doi.org/10.60578/27sy-9a6j); DPPC:**2** 95:5 (https://doi.org/10.60578/u26c-tzwe); DPPC:**2** 90:10 (https://doi.org/10.60578/hfys-47sn); DPPC:**2** 80:20 (https://doi.org/10.60578/hr19-er73); DPPC:**2** 64:36 (https://doi.org/10.60578/wqv9-2pu7); DPPC:**2** 50:50 (https://doi.org/10.60578/3hj1-g8a4); DPPC:**2** 30:70 (https://doi.org/10.60578/a4s8-76vt); DPPC:**2** 0:100 (https://doi.org/10.60578/gs8q-11sm); DPPC:**4** 90:10 (https://doi.org/10.60578/f3dp-378u); DPPC:**4** 80:20 (https://doi.org/10.60578/64b0-d2ch); DPPC:**4** 50:50 (https://doi.org/10.60578/fzju-5yay); DPPC:**4** 30:70 (https://doi.org/10.60578/1fe1-mp5k); DPPC:**4** 0:100 (https://doi.org/10.60578/mghe-0vqg); DPPC:**5** 90:10 (https://doi.org/10.60578/51s4-vskp); DPPC:**5** 80:20 (https://doi.org/10.60578/r9qu-m53n); DPPC:**5** 0:100 (https://doi.org/10.60578/2pcd-7u3b); DPPC:**6** 95:5 (https://doi.org/10.60578/nfs5-qxw2); DPPC:**6** 90:10 (https://doi.org/10.60578/gs1e-7wrk); DPPC:**7** 95:5 (https://doi.org/10.60578/ujbp-4acv); DPPC:**7** 90:10 (https://doi.org/10.60578/6d37-2h53); DLPC (https://doi.org/10.60578/x9e6-y42z); DLPC:**2** 95:5 (https://doi.org/10.60578/pv02-4bj7); DLPC:**2** 90:10 (https://doi.org/10.60578/1ekt-pwaa); DLPC:**2** 80:20 (https://doi.org/10.60578/w37y-tubw); DLPC:**2** 50:50 (https://doi.org/10.60578/9xk4-0a1c); DLPC:**2** 30:70 (https://doi.org/10.60578/8ebr-p7hs); DLPC:**3** 95:5 (https://doi.org/10.60578/87qy-qbhc); DLPC:**3** 90:10 (https://doi.org/10.60578/pkfk-rqw6); DLPC:**3** 80:20 (https://doi.org/10.60578/2vxt-bbqh); DLPC:**3** 50:50 (https://doi.org/10.60578/vwun-1p59); DLPC:**3** 30:70 (https://doi.org/10.60578/syvh-v1wf).

Funding information

This publication was written in the context of the work of the consortium DAPHNE4NFDI in association with the German National Research Data Infrastructure (NFDI) e.V. NFDI is financed by the Federal Republic of Germany and the 16 federal states and the consortium is funded by the Deutsche Forschungsgemeinschaft (DFG, German Research Foundation) project No. 460248799. The following additional funding is acknowledged: Deutsche Forschungsgemeinschaft (grant No. SFB 677); Bundesministerium für Bildung und Forschung, ErUM Pro (grant Nos. 05K22FK3 and 05K19FK2).

References

Barty, A., Gutt, C., Lohstroh, W., Murphy, B., Schneidewind, A., Grunwaldt, J.-D., Schreiber, F., Busch, S., Unruh, T., Bussmann, M., Fangohr, H., Görzig, H., Houben, A., Kluge, T., Manke, I., Lütznekirchen-Hecht, D., Schneider, T. R., Weber, F., Bruno, G., Einsle, O., Felder, C., Herzig, E. M., Konrad, U., Markötter, H., Rossnagel, K., Sheppard, T. & Turchinovich, D. (2023). *DAPHNE4NFDI – Consortium Proposal*, https://doi.org/10.5281/zenodo.8040605.

Biltonen, R. L. & Lichtenberg, D. (1993). *Chem. Phys. Lipids* **64**, 129–142.

Blanchet, C. E., Spilotros, A., Schwemmer, F., Graewert, M. A., Kikhney, A., Jeffries, C. M., Franke, D., Mark, D., Zengerle, R., Cipriani, F., Fiedler, S., Roessle, M. & Svergun, D. I. (2015). *J. Appl. Cryst.* **48**, 431–443.

Bruneau, A., Roche, M., Hamze, A., Brion, J.-D., Alami, M. & Messaoudi, S. (2015). *Chemistry* **21**, 8375–8379.

Carlsen, R. W. & Sitti, M. (2014). *Small* **10**, 3831–3851.

Cherezov, V., Clogston, J., Misquitta, Y., Abdel-Gawad, W. & Caffrey, M. (2002). *Biophys. J.* **83**, 3393–3407.

Cournia, Z., Allen, T. W., Andricioaei, I., Antonny, B., Baum, D., Brannigan, G., Buchete, N.-V., Deckman, J. T., Delemotte, L., Del Val, C., Friedman, R., Gkeka, P., Hege, H.-C., Hénin, J., Kasimova, M. A., Kolocouris, A., Klein, M. L., Khalid, S., Lemieux, M. J., Lindow, N., Roy, M., Selent, J., Tarek, M., Tofoleanu, F., Vanni, S., Urban, S., Wales, D. J., Smith, J. C. & Bondar, A.-N. (2015). *J. Membr. Biol.* **248**, 611–640.

Dams, I., Chodyński, M., Krupa, M., Pietraszek, A., Zezula, M., Cmoch, P., Kosińska, M. & Kutner, A. (2013). *Tetrahedron* **69**, 1634–1648.

Dargasz, M., Bolle, J., Faulstich, A., Schneider, E., Kowalski, M., Sternemann, C., Savelkouls, J., Murphy, B. & Paulus, M. (2022). *J. Phys. Conf. Ser.* **2380**, 012031.

Devaux, P. F. (1991). *Biochemistry* **30**, 1163–1173.

Hammersley, A. P. (1997). *FIT2D: An Introduction and overview*. ESRF Internal Report. ESRF, Grenoble, France.

Hammersley, A. P. (2016). *J. Appl. Cryst.* **49**, 646–652.

Hammersley, A. P., Svensson, S. O., Hanfland, M., Fitch, A. N. & Hausermann, D. (1996). *High Pressure Res.* **14**, 235–248.

Hammersley, A. P., Svensson, S. O., Thompson, A., Graafsma, H., Kvick, Å. & Moy, J. P. (1995). *Rev. Sci. Instrum.* **66**, 2729–2733.

Hirlekar, R., Jain, S., Patel, M., Garse, H. & Kadam, V. (2010). *Curr. Drug Deliv.* **7**, 28–35.

Hövelmann, S. C., Dieball, E., Kuhn, J., Dargasz, M., Giri, R. P., Reise, F., Paulus, M., Lindhorst, T. K. & Murphy, B. M. (2024). *IUCrJ* **11**, 486–493.

Hövelmann, S. C. & Murphy, B. M. (2025). *SAXS data and scripts for publication: Kinetics of light-induced mesophase transitions in azobenzene amphiphiles containing lyotropic liquid crystals*, https://doi.org/10.57892/100-112.

Ichikawa, T., Yoshio, M., Hamasaki, A., Mukai, T., Ohno, H. & Kato, T. (2007). *J. Am. Chem. Soc.* **129**, 10662–10663.

Kalvodova, L., Kahya, N., Schwille, P., Ehehalt, R., Verkade, P., Drechsel, D. & Simons, K. (2005). *J. Biol. Chem.* **280**, 36815–36823.

Kelley, E. G., Butler, P. D., Ashkar, R., Bradbury, R. & Nagao, M. (2020). *Proc. Natl Acad. Sci. USA* **117**, 23365–23373.

Kornmueller, K., Lehofer, B., Leitinger, G., Amenitsch, H. & Prassl, R. (2018). *Nano Res.* **11**, 913–928.

Leriche, G., Budin, G., Brino, L. & Wagner, A. (2010). *Eur. J. Org. Chem.* **2010**, 4360–4364.

Lohstroh, W., Weber, F., Busch, S., Görzig, H., Murphy, B., Coan, P., Fahad, H., Osterhoff, M., Tymoshenko, Y., Paripsa, S., Schneidewind, A. & Herb, C. (2024). *DAPHNE4NFDI – Draft recommendations on metadata capture and specifications*, https://doi.org/10.5281/zenodo.12169109

Lorent, J. H., Levental, K. R., Ganesan, L., Rivera-Longsworth, G., Sezgin, E., Doktorova, M., Lyman, E. & Levental, I. (2020). *Nat. Chem. Biol.* **16**, 644–652.
Luzzati, V. (1997). *Curr. Opin. Struct. Biol.* **7**, 661–668.
Mabrey, S. & Sturtevant, J. M. (1976). *Proc. Natl Acad. Sci. USA* **73**, 3862–3866.
Martiel, I., Sagalowicz, L. & Mezzenga, R. (2013). *Langmuir* **29**, 15805–15812.
Muir, B. W., Zhen, G., Gunatillake, P. & Hartley, P. G. (2012). *J. Phys. Chem. B* **116**, 3551–3556.
Op den Kamp, J. A. (1979). *Annu. Rev. Biochem.* **48**, 47–71.
Reise, F., Warias, J. E., Chatterjee, K., Krekiehn, N. R., Magnussen, O., Murphy, B. M. & Lindhorst, T. K. (2018). *Chem. A Eur. J.* **24**, 17497–17505.
Ribeiro, I. R., Immich, M. F., Lundberg, D., Poletto, F. & Loh, W. (2019). *Colloids Surf. B Biointerfaces* **177**, 204–210.
Rizwan, S. B., Boyd, B. J., Rades, T. & Hook, S. (2010). *Expert Opin. Drug Deliv.* **7**, 1133–1144.
Shafieenezhad, A., Mitra, S., Wassall, S. R., Tristram-Nagle, S., Nagle, J. F. & Petrache, H. I. (2023). *Biophys. J.* **122**, 1118–1129.
Shah, J. C., Sadhale, Y. & Chilukuri, D. M. (2001). *Adv. Drug Deliv. Rev.* **47**, 229–250.
Soloviov, D. V., Gorshkova, Y. E., Ivankov, O. I., Zhigunov, A. N., Bulavin, L. A., Gordeliy, V. I. & Kuklin, A. I. (2012). *J. Phys. Conf. Ser.* **351**, 012010.
Walde, P. & Ichikawa, S. (2021). *Appl. Sci.* **11**, 10345.
Wilkinson, M. D., Dumontier, M., Aalbersberg, I. J. J., Appleton, G., Axton, M., Baak, A., Blomberg, N., Boiten, J.-W., da Silva Santos, L. B., Bourne, P. E., Bouwman, J., Brookes, A. J., Clark, T., Crosas, M., Dillo, I., Dumon, O., Edmunds, S., Evelo, C. T., Finkers, R., Gonzalez-Beltran, A., Gray, A. J. G., Groth, P., Goble, C., Grethe, J. S., Heringa, J., 't Hoen, P. A. C., Hooft, R., Kuhn, T., Kok, R., Kok, R., Lusher, S. J., Martone, M. E., Mons, A., Packer, A. L., Persson, B., Rocca-Serra, P., Roos, M., van Schaik, R., Sansone, S., Schultes, E., Sengstag, T., Slater, T., Strawn, G., Swertz, M. A., Thompson, M., van der Lei, J., van Mulligen, E., Velterop, J., Waagmeester, A., Wittenburg, P., Wolstencroft, K., Zhao, J. & Mons, B. (2016). *Sci. Data* **3**, 160018.
Winter, R. (2002). *Biochim. Biophys. Acta* **1595**, 160–184.
Winter, R., Erbes, J., Czeslik, C. & Gabke, A. (1998). *J. Phys. Condens. Matter* **10**, 11499–11518.
Yeagle, P. L. (2004). *The structure of biological membranes*. Boca Raton: CRC Press.
Zabara, A. & Mezzenga, R. (2014). *J. Controlled Release* **188**, 31–43.

JOURNAL OF APPLIED CRYSTALLOGRAPHY

Volume 58 (2025)

Supporting information for article:

Kinetics of light-induced mesophase transitions in azobenzene amphiphiles containing lyotropic liquid crystals

Svenja C. Hövelmann, Michael Röhrl, Ella Dieball, Michelle Dargasz, Jule Kuhn, Rajendra P. Giri, Franziska Reise, Dmytro Soloviov, Clement E. Blanchet, Michael Paulus, Thisbe K. Lindhorst and Bridget M. Murphy

S1. Synthesis route of 1

S1.1. General Information

S1.1.1. Chemicals

The reagents employed in the described syntheses are commercially available unless otherwise noted. (4-Hydroxyphenyl)(4'-iodophenyl)diazene (**8**) (Leriche *et al.*, 2010), solketal tosylate (**9**) (Dams *et al.*, 2013) and 1-thio-β-D-glucopyranose (**10**) (Bruneau *et al.*, 2015) were synthesized according to the literature procedures annotated. Dry solvents were either purchased directly (1,4-dioxane, DMF), or in the case of chloroform dried over molecular sieves 4 Å according to standard procedures. For extractions and column chromatography, technical grade solvents were used, which were purified by distillation before use.

S1.1.2. NMR spectroscopy

^{1}H and ^{13}C NMR spectra were recorded on a Bruker Avance (600 MHz) NMR spectrometer at 298 K. The ^{1}H NMR shifts were determined using the solvent peaks as reference: $CDCl_3$ (^{1}H = 7.26 ppm, ^{13}C 77.2 ppm) or DMSO-d_6 (^{1}H = 2.50, ^{13}C = 39.5 ppm). Data are presented in the following format: chemical shift, multiplicity (s = singlet, d = doublet and m = multiplet), coupling constant *J* in Hertz (Hz) and integration. Structural assignment of signals was performed utilizing 2D-NMR spectroscopy (COSY, HSQC, HMBC).

S1.1.3. Infrared spectroscopy

The infrared (IR) spectra were measured with a PerkinElmer FT-IR Spectrum Two (UATR) spectrometer and are reported in cm^{-1}.

S1.1.4. Thin layer chromatography (TLC)

TLC was performed on silica gel plates (GF 254, Merck). Visualization was achieved by either a vanillin-(3.0 g vanillin and 0.5 mL H_2SO_4 in 100 mL EtOH) or $KMnO_4$-based staining solution (1.5 g $KMnO_4$, 10 g K_2CO_3 and 1.25 mL 10% NaOH solution (aq.) in 200 mL water) followed by heat treatment at approximately 200 °C.

S1.1.5. Flash chromatography

The products were purified by flash chromatography on silica gel columns (Merck, 230–400 mesh, particle size 0.040–0.063 mm) or by automated flash chromatography using a puriFlash450 or puriFlash5.020 device (Interchim®).

S1.1.6. MALDI/ESI MS spectrometry

HR-ESI mass spectra were recorded on a ThermoFischer Orbitrap mass spectrometer. Samples were prepared using a solvent mixture of acetonitrile/ water (4:1) containing ammonium formate as an additive in a concentration of 1.3 mM.

S1.2. Synthesis

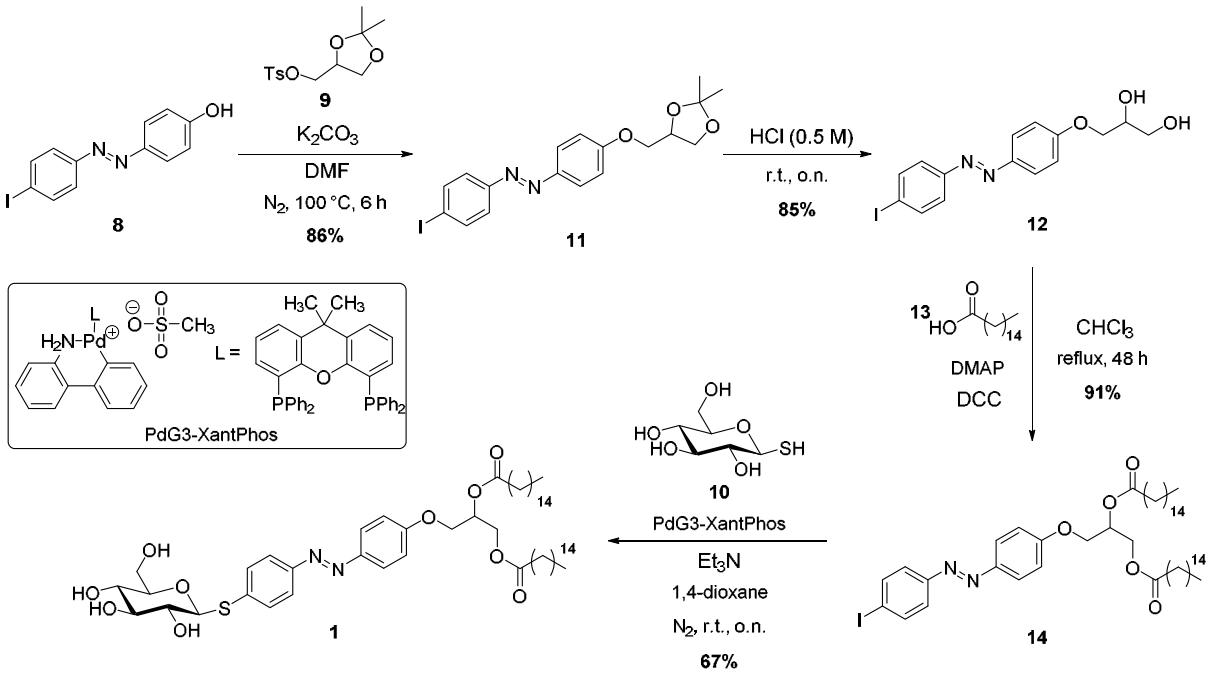

Figure S1 Synthetic overview for the preparation of the photoswitchable glycolipid mimetic **1**. Starting from (4-hydroxyphenyl)(4'-iodophenyl)diazene (**8**) the glycerol moiety is introduced in the form of the tosyl-activated solketal **9**, followed by deprotection of the isopropylidene protecting group to result in the azobenzene glycerol derivate **12**. The lipid tail of the mimetic is completed by esterification with hexadecanoic acid (**13**) resulting in the diacyl glycerol **14**. In the final step, a modified Buchwald-Hartwig-Migita coupling derived from a method published by (Bruneau *et al.*, 2015) was performed to introduce the hydrophilic head group 1-thio-β-D-glucopyranose (**10**) resulting in target glycolipid mimetic **1**. DCC: *N*,*N*′-dicyclohexylcarbodiimide; DMAP: *N*,*N*-dimethylpyridin-4-amine; DMF: *N*,*N*-dimethylformamide.

1-*O*-(4-(4-Iodophenyldiazenyl)benzene)-2,3-di-*O*-isopropylidene-*rac*-glycerol (**11**):

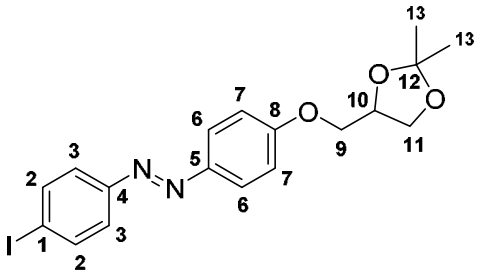

(4-Hydroxyphenyl)(4'-iodophenyl)diazene (**8**) (2.00 g, 6.17 mmol, 1.00 equiv) was dissolved in dry DMF under N_2-atmosphere. Solketal tosylate (**9**) (1.80 g, 6.29 mmol, 1.02 equiv) and potassium carbonate (2.03 g, 14.7 mmol, 2.38 equiv) were added. The reaction mixture was heated to 100 °C for 6 h under stirring and monitored by TLC. The solvent was removed under reduced pressure. The residue was taken up in ethyl acetate (300 mL) and the organic phase washed with water (100 mL) and brine (100 mL). The organic phase was dried over $MgSO_4$, it was filtered and the solvent removed under reduced pressure. The product was purified by column chromatography (cyclohexane/ ethyl acetate 8:1). 1-*O*-(4-(4-Iodophenyldiazenyl)benzene)-2,3-di-*O*-isopropylidene-*rac*-glycerol (**11**) (2.32 g, 5.29 mmol, 86% yield) was isolated as an orange solid.

R_f = 0.53 (cyclohexane/ ethyl acetate 4:1).

IR (ATR): $\tilde{\nu}$ = 2973, 2893, 1602, 1584, 1041, 838, 543.

^{1}H NMR (600 MHz, $CDCl_3$) δ 7.92 – 7.88 (m, 2H, H-6), 7.86 – 7.82 (m, 2H, H-2), 7.63 – 7.59 (m, 2H, H-3), 7.05 – 7.01 (m, 2H, H-7), 4.52 (dddd, $^3J_{H\text{-}10–H\text{-}11a}$ = 6.5 Hz, ^3J = 5.7, 5.7, 5.7 Hz, 1H, H-10), 4.19 (dd, $^2J_{H\text{-}11a–H\text{-}11b}$ = 8.5 Hz, $^3J_{H\text{-}11a–H\text{-}10}$ = 6.4 Hz, 1H, H-11a), 4.14 (dd, $^2J_{H\text{-}9a–H\text{-}9b}$ = 9.5 Hz, $^3J_{H\text{-}9a–H\text{-}10}$ = 5.4 Hz, 1H, H-9a), 4.04 (dd, $^2J_{H\text{-}9b–H\text{-}9a}$ = 9.5 Hz, $^3J_{H\text{-}9b–H\text{-}10}$ = 5.8 Hz, 1H, H-9b), 3.93 (dd, $^2J_{H\text{-}11b–H\text{-}11a}$ = 8.5 Hz $^3J_{H\text{-}11b–H\text{-}10}$ = 5.8 Hz, 1H, CH_2b'), 1.48, 1.42 (each s, each 3H, 3 CH_3-13).

^{13}C NMR (151 MHz, $CDCl_3$) δ 161.4 (1C, C-8), 152.2 (1C, C-4), 147.2 (1C, C-5), 138.4 (2C, C-2), 125.1 (2C, C-6), 124.4 (2C, C-3), 115.0 (2C, C-7), 110.1 (1C, C-12), 97.0 (1C, C-1), 74.0 (1C, C-10), 69.2 (1C, C-9), 66.9 (1C, C-11), 27.0, 25.5 (2 C13).

ESI-HRMS: *m/z* = 439.05139 $[M+H]^+$ (calculated *m/z* = 439.05139).

1-*O*-(4-(4-Iodophenyldiazenyl)benzene)-*rac*-glycerol (**12**):

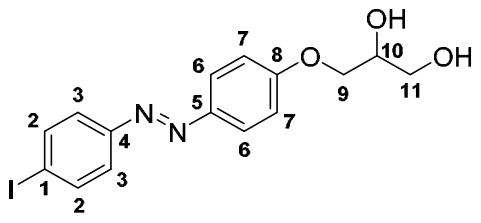

The isopropylidene-protected glycerol derivate **11** (643 mg, 1.47 mmol, 1.00 equiv) was dissolved in THF (20 mL). Aqueous hydrochloric acid (365 mg, 20.0 mL, 10.0 mmol, 0.5 M, 6.82 equiv) was added to the solution and the reaction mixture was stirred at room temperatur overnight. The reaction mixture was neutralized to pH = 7 with aq. NaOH solution (1 M). The reaction mixture was extracted with ethyl acetate (3x50 mL) and the solvent was removed under reduced pressure. The crude product was purified by column chromatography (cyclohexane/ ethyl acetate 1:1 → ethyl acetate/ methanol 1:1). 1-*O*-(4-(4-Iodophenyldiazenyl)benzene)-*rac*-glycerol (**12**) (498 mg, 1.25 mmol, 85% yield) was isolated as an orange solid.

R_f = 0.35 (cyclohexane/ ethyl acetate 1:1).

IR (ATR): $\tilde{\nu}$ =3294, 2929, 2973, 1600, 1562, 1240, 1033, 836, 549.

^{1}H NMR (600 MHz, DMSO-d$_6$) δ 7.97 – 7.92 (m, 2H, H-2), 7.92 – 7.87 (m, 2H, H-6), 7.65 – 7.60 (m, 2H, H-3), 7.17 – 7.11 (m, 2H, H-7), 5.03 (d, $^3J_{\text{OH-10–H-10}}$ = 5.1 Hz, 1H, OH-10), 4.72 (t, $^3J_{\text{OH-11–H-11}}$ = 5.7 Hz, 1H, OH-11), 4.13 (dd, $^2J_{\text{H-9a–H-9b}}$ = 9.9 Hz, $^3J_{\text{H-9a–H-10}}$ = 4.0 Hz, 1H, H-9a), 3.99 (dd, $^2J_{\text{H-9b–H-9a}}$ = 10.0 Hz, $^3J_{\text{H-9b–H-10}}$ = 6.2 Hz, 1H, H-9b), 3.87 – 3.80 (m, 1H, H-10), 3.47 (dd, $^3J_{\text{H-11–OH-11}}$ = 5.7 Hz, $^3J_{\text{H11-H10}}$ = 5.7 Hz, 2H, H-11).

^{13}C NMR (151 MHz, DMSO-d$_6$) δ 161.9 (1C, C-8), 151.3 (1C, C-4), 146.0 (1C, C-5), 138.3 (2C, C-2), 124.8 (2C, C-6), 124.1 (2C, C-3), 115.2 (2C, C-7), 97.9 (1C, C-1), 70.1 (1C, C-9), 69.8 (1C, C-10), 62.6 (1C, C-11).

ESI-HRMS: *m/z* = 399.02008 $[M+H]^+$ (calculated *m/z* = 399.02001).

1-*O*-(4-(4-Iodophenyldiazenyl)benzene)-2,3-di-*O*-hexadecanoyl-*rac*-glycerol (**14**):

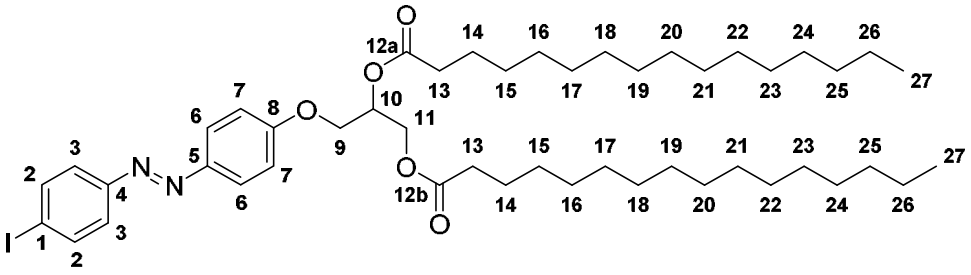

The azobenzene glycerol derivate **12** (270 mg, 678 µmol, 1.00 equiv) was dissolved in chloroform (30 mL). Hexadecanoic acid (**13**) (700 mg, 2.73 mmol, 4.03 equiv) and DMAP (85.1 mg, 697 µmol, 1.03 equiv) were added to the solution, followed by the addition of DCC (593 mg, 2.87 mmol, 4.24 equiv). The reaction mixture was heated to slight reflux (70 °C) for 48 h. The solvent was removed under reduced pressure and the crude product purified by column chromatography (cyclohexane → cyclohexane/ ethyl acetate 4:1 → ethyl acetate). 1-*O*-(4-(4-Iodophenyldiazenyl)benzene)-2,3-di-*O*-hexadecanoyl-*rac*-glycerol (**14**) (521 mg, 595 µmol, 88% yield) was isolated as a yellow powder.

R_f = 0.67 (cyclohexane/ ethyl acetate 4:1).

IR (ATR): $\tilde{\nu}$ = 2955, 2917, 2849, 1735, 1598, 1469, 1171, 840, 720, 546.

^{1}H NMR (600 MHz, $CDCl_3$) δ 7.93 – 7.88 (m, 2H, H-6), 7.86 – 7.82 (m, 2H, H-2), 7.63 – 7.59 (m, 2H, H-3), 7.03 – 6.99 (m, 2H, H-7), 5.45 – 5.40 (m, 1H, H-10), 4.48 – 4.43 (m, 1H, H-11a), 4.34 – 4.29 (m, 1H, H-11b), 4.22 – 4.18 (m, 2H, H-9), 2.39 – 2.29 (m, 4H, H-13), 1.68 – 1.58 (m, 4H, H-14), 1.38 – 1.14 (m, 48H, H-15-H-26), 0.91 – 0.85 (m, 6H, H-27).

^{13}C NMR (151 MHz, $CDCl_3$) δ 173.5 (1C, C-12b), 173.2 (1C, C-12a), 161.1 (1C, C-8), 152.2 (1C, C-3), 147.4 (1C, C-6), 138.4 (2C, C-2), 125.1 (2C, C-6), 124.4 (2C, C-3), 115.0 (2C, C-7), 97.0 (1C, C-1), 69.5 (1C, C-10), 66.5 (1C, C-9), 62.3 (1C, C-11), 34.4 (1C, C-13), 34.3 (1C, C-13), 32.1 (2C, $C_{aliphatic}$), 30.0 – 29.2 (m, 20C, $C_{aliphatic}$), 25.1 (2C, C-14), 22.9 (2C, $C_{aliphatic}$), 14.3 (2C, C-27).

C-15–C-26 are referred to as $C_{aliphatic}$ and could not be individually assigned.

ESI-HRMS: *m/z* = 875.47955 $[M+H]^+$ (calculated *m/z* = 875.47934).

1-*O*-(4-(4-(*S*-β-D-Glucopyranosyl)thiophenyldiazenyl)benzene)-2,3-di-*O*-hexadecanoyl-*rac*-glycerol (**1**):

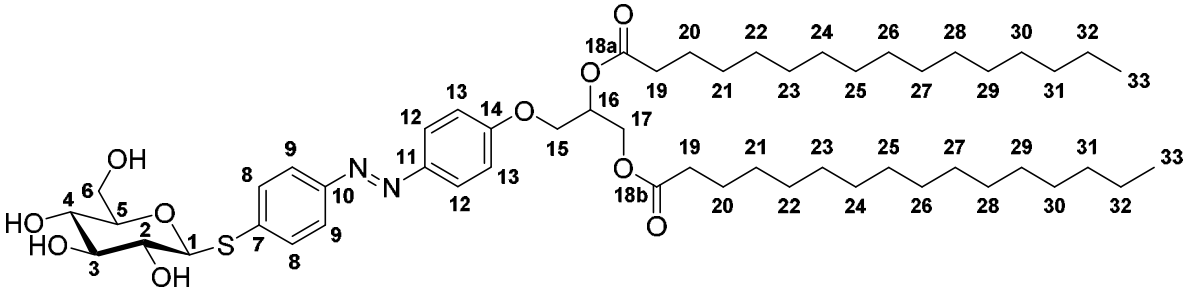

In an adaption to the protocol published by (Bruneau *et al.*, 2015), 1-thio-β-D- glucopyranose (**10**) (136 mg, 695 µmol, 3.80 equiv) was dissolved in a flame-dried round bottom flask by addition of dry 1,4-dioxane (15 mL) under N_2-atomsphere. After degassing the solution with three freeze-thaw cycles, the iodine substituted azobenzene derivative **14** (160 mg, 183 µmol, 1.00 equiv) and XantPhos Pd G3 (3.50 mg, 3.69 µmol, 0.02 equiv) were added to the flask. Triethylamine (18.9 mg, 26.0 µL, 187 µmol, 1.02 equiv) was added to the reaction mixture and the solution was stirred at room temperature overnight. Within the first minutes of the reaction, a discoloration of the reaction from yellow to reddish-brown was observed, in accordance to the observation described by Messaudi and coworkers, (Bruneau *et al.*, 2015) indicating the start of the reaction. As no complete conversion was observed, the reaction time was elongated overnight. After 18 h the reaction was extracted with brine (3x30 mL) and the solvent was removed under reduced pressure. The crude product was purified by column chromatography (cyclohexane/ ethyl acetate 1:1 → ethyl acetate). 1-*O*-(4-(4-(*S*-β-D-Glucopyranosyl)thiophenyldiazenyl)benzene)-2,3-di-*O*-hexadecanoyl-*rac*-glycerol (**1**) (116 mg, 123 µmol, 67% yield) was obtained as an orange solid.

$\mathbf{R}_f$ = 0.45 (ethyl acetate).

IR (ATR): $\tilde{\nu}$ = 3366, 2955, 2917, 2849, 1735, 1727, 1602, 1241, 1043, 841, 550.

^{1}H NMR (600 MHz, $CDCl_3$) δ 7.89 – 7.84 (m, 2H, H-12), 7.79 – 7.75 (m, 2H, H-9), 7.59 – 7.54 (m, 2H, H-8), 7.00 – 6.95 (m, 2H, H-13), 5.45 – 5.37 (m, 1H, H-16), 4.74 (d, $^3J_{H\text{-}1–H\text{-}2}$ = 9.5 Hz, 1H, H-1), 4.45 (dd, $^2J_{H\text{-}17a–H\text{-}17b}$ = 12.0 Hz, $^3J_{H\text{-}17a–H\text{-}16}$ = 3.9 Hz, 1H, H-17a), 4.30 (dd, $^2J_{H\text{-}17b–H\text{-}17a}$ = 12.0, $^3J_{H\text{-}17b–H\text{-}16}$ = 6.1 Hz, 1H, H-17b), 4.20 – 4.13 (m, 2H, H-15), 3.97 – 3.85 (m, 2H, H-6), 3.74 – 3.63 (m, 2H, H-3, H-4), 3.54 – 3.48 (m, 1H, H-2), 3.48 – 3.42 (m, 1H, H-5), 2.37 – 2.30 (m, 4H, H-19), 1.66 – 1.58 (m, 4H, H-20), 1.36 – 1.19 (m, 48H, H-21–H-32), 0.90 – 0.84 (m, 6H, H-33).

^{13}C NMR (151 MHz, $CDCl_3$) δ 173.5 (1C, C-18b), 173.2 (1C, C-18a), 161.0 (1C, C-14), 152.0 (1C, C-10), 147.4 (1C, C-11), 135.6 (1C, C-7), 131.9 (2C, C-8), 125.1 (2C, C-12), 123.4 (1C, C-9), 115.0 (1C, C-13), 88.0 (1C, C-1), 79.6 (1C, C-5), 78.0 (1C, C-3), 72.4 (1C, C-2), 69.7 (1C, C-4), 69.5 (1C, C-16), 66.5 (1C, C-15), 62.4 (1C, C-17), 62.2 (1C, C-6), 34.4 (1C, C-19), 34.2 (1C, C-19), 32.1 (2C, $C_{aliphatic}$), 30.2 – 28.8 (20C, $C_{aliphatic}$), 25.1 (2C, C20), 22.8 (2C, $C_{aliphatic}$), 14.3 (2C, C-33).

C-21–C-32 are referred to as $C_{aliphatic}$ and could not be individually assigned.

ESI-HRMS: *m/z* = 943.60757 $[M+H]^+$ (calculated *m/z* = 943.60759).

NMR spectra of synthesized compounds

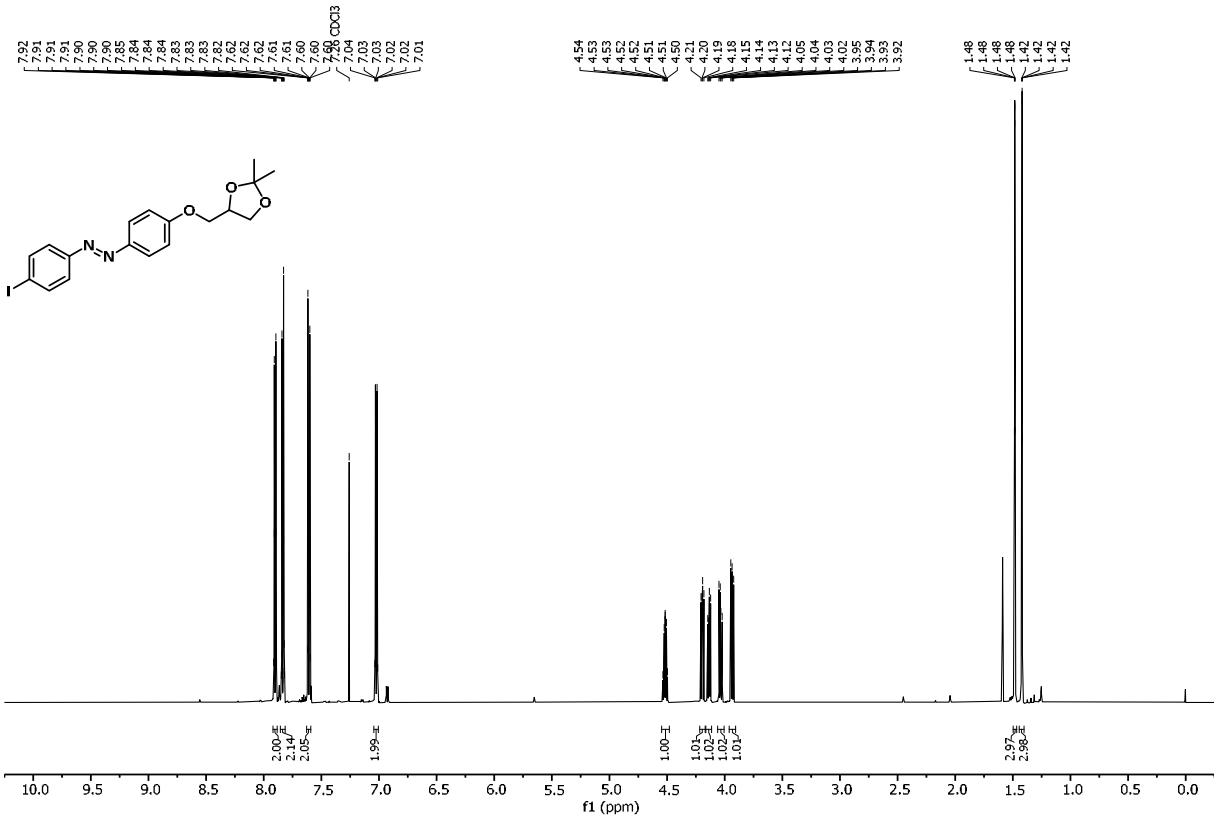

Figure S2 ^{1}H NMR spectrum of 1-*O*-(4-(4-iodophenyldiazenyl)benzene)-2,3-di-*O*-isopropylidene-*rac*-glycerol (**11**) (600 MHz, $CDCl_3$, 298 K).

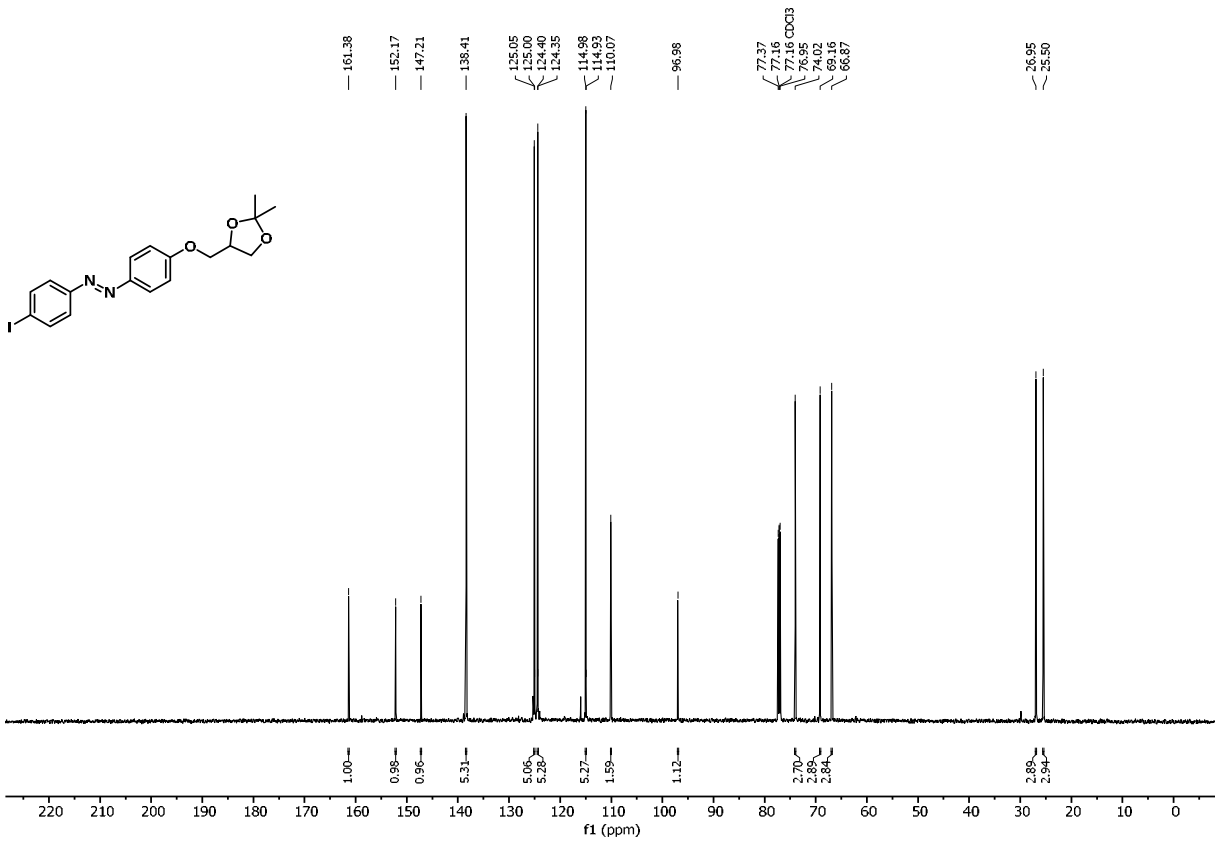

Figure S3 ^{13}C NMR spectrum of 1-O-(4-(4-iodophenyldiazenyl)benzene)-2,3-di-O-isopropylidene-rac-glycerol (**11**) (151 MHz, $CDCl_3$, 298 K).

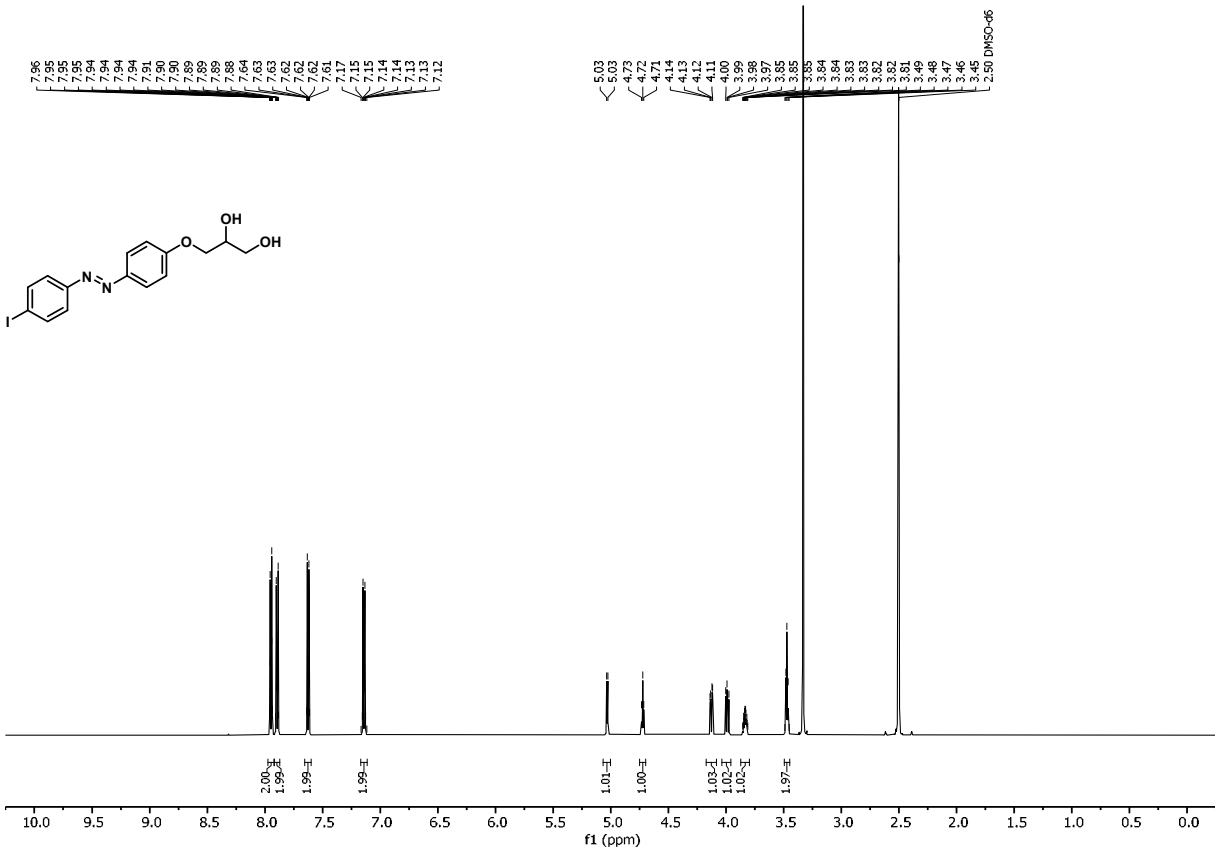

Figure S4 ^{1}H NMR spectrum of 1-*O*-(4-(4-iodophenyldiazenyl)benzene)-*rac*-glycerol (**12**) (600 MHz, DMSO-d_6, 298 K).

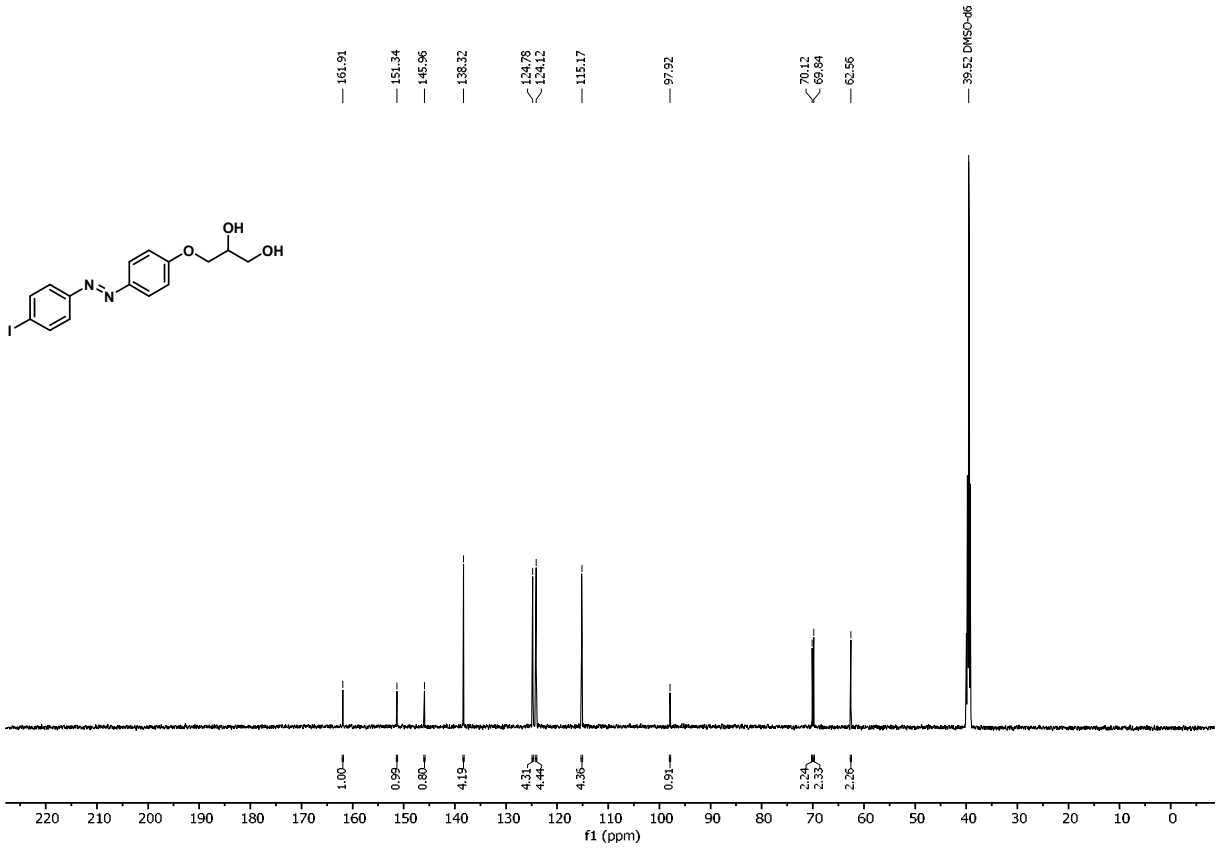

Figure S5 ^{13}C NMR spectrum of 1-*O*-(4-(4-iodophenyldiazenyl)benzene)-*rac*-glycerol (**12**) (151 MHz, DMSO-d_6, 298 K).

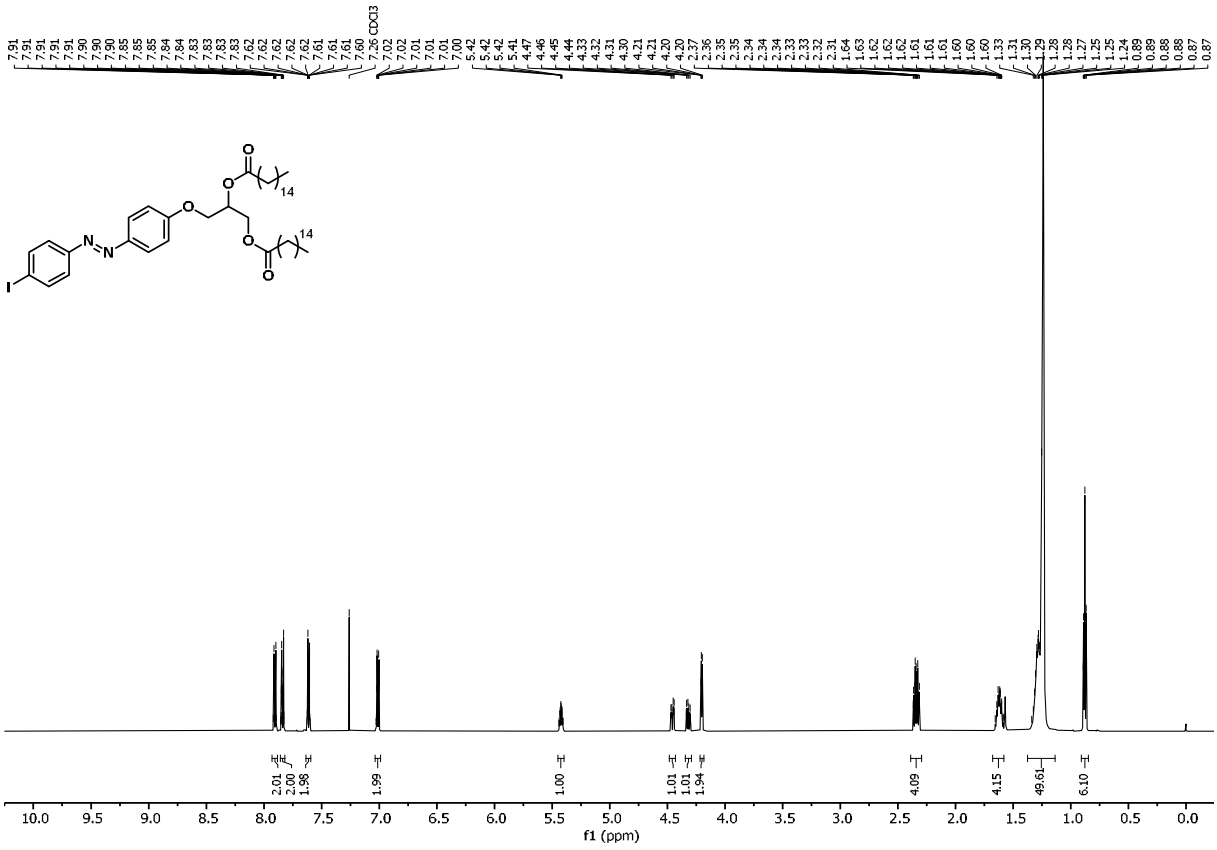

Figure S6 ^{1}H NMR spectrum of 1-*O*-(4-(4-iodophenyldiazenyl)benzene)-2,3-di-*O*-hexadecanoyl-*rac*-glycerol (**14**) (600 MHz, $CDCl_3$, 298 K).

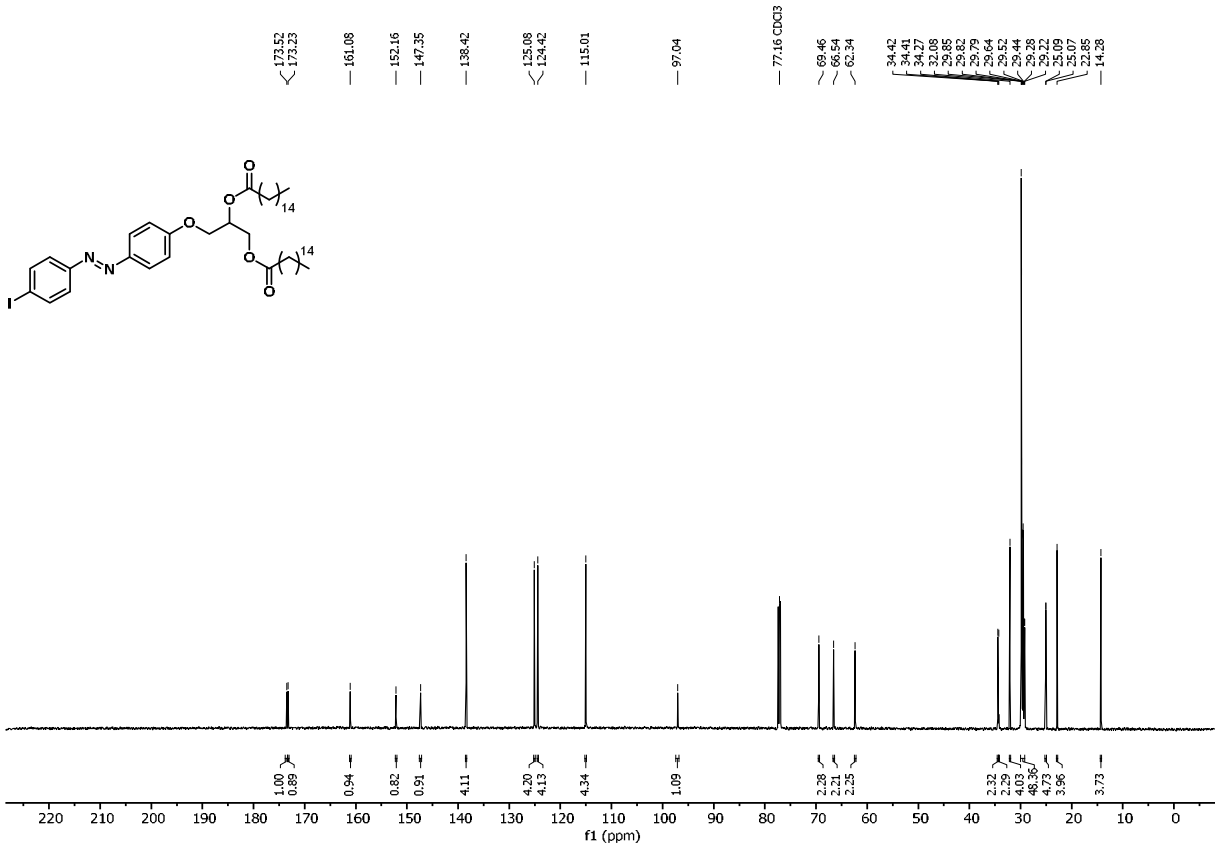

Figure S7 ^{13}C NMR spectrum of 1-*O*-(4-(4-iodophenyldiazenyl)benzene)-2,3-di-*O*-hexadecanoyl-*rac*-glycerol (**14**) (151 MHz, $CDCl_3$, 298 K).

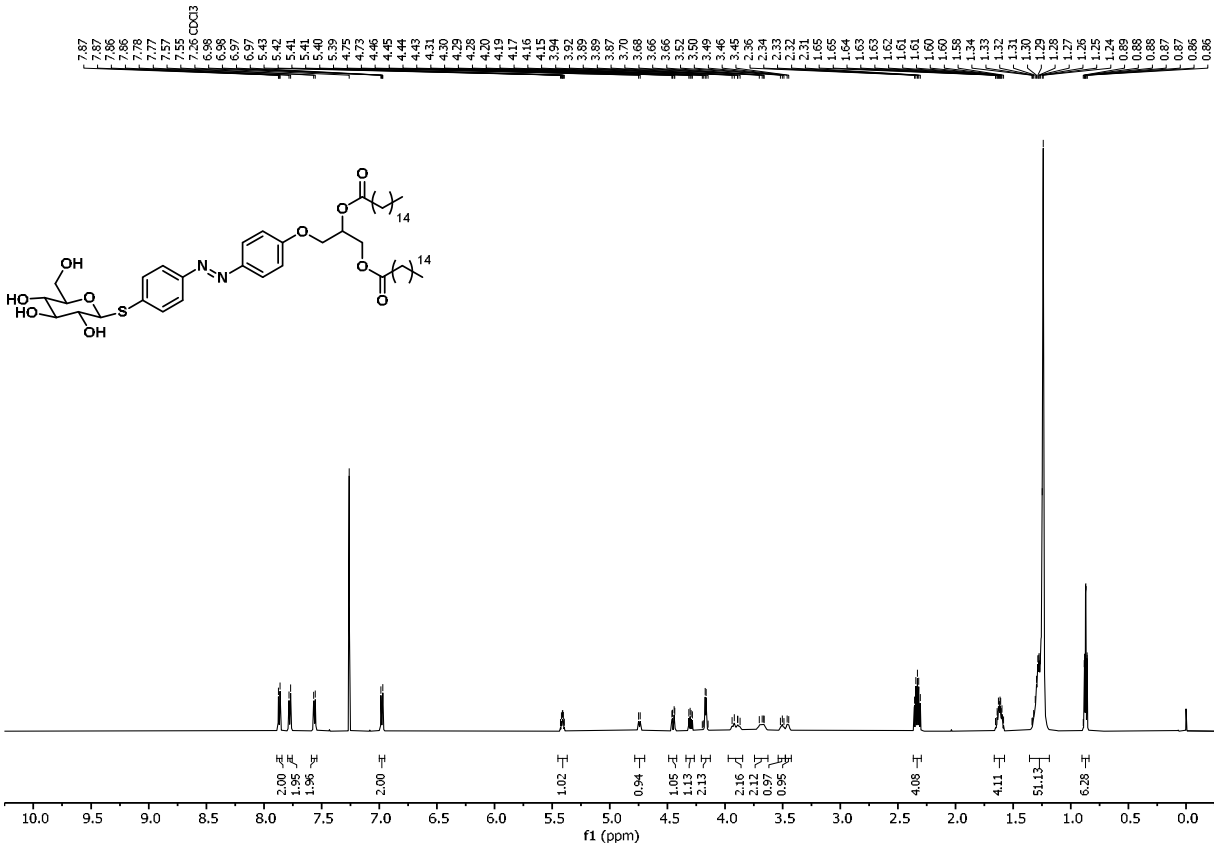

Figure S8 ^{1}H NMR spectrum of 1-*O*-(4-(4-(*S*-β-D-glucopyranosyl)thiophenyldiazenyl)benzene)-2,3-di-*O*-hexadecanoyl-*rac*-glycerol (**1**) (600 MHz, $CDCl_3$, 298 K).

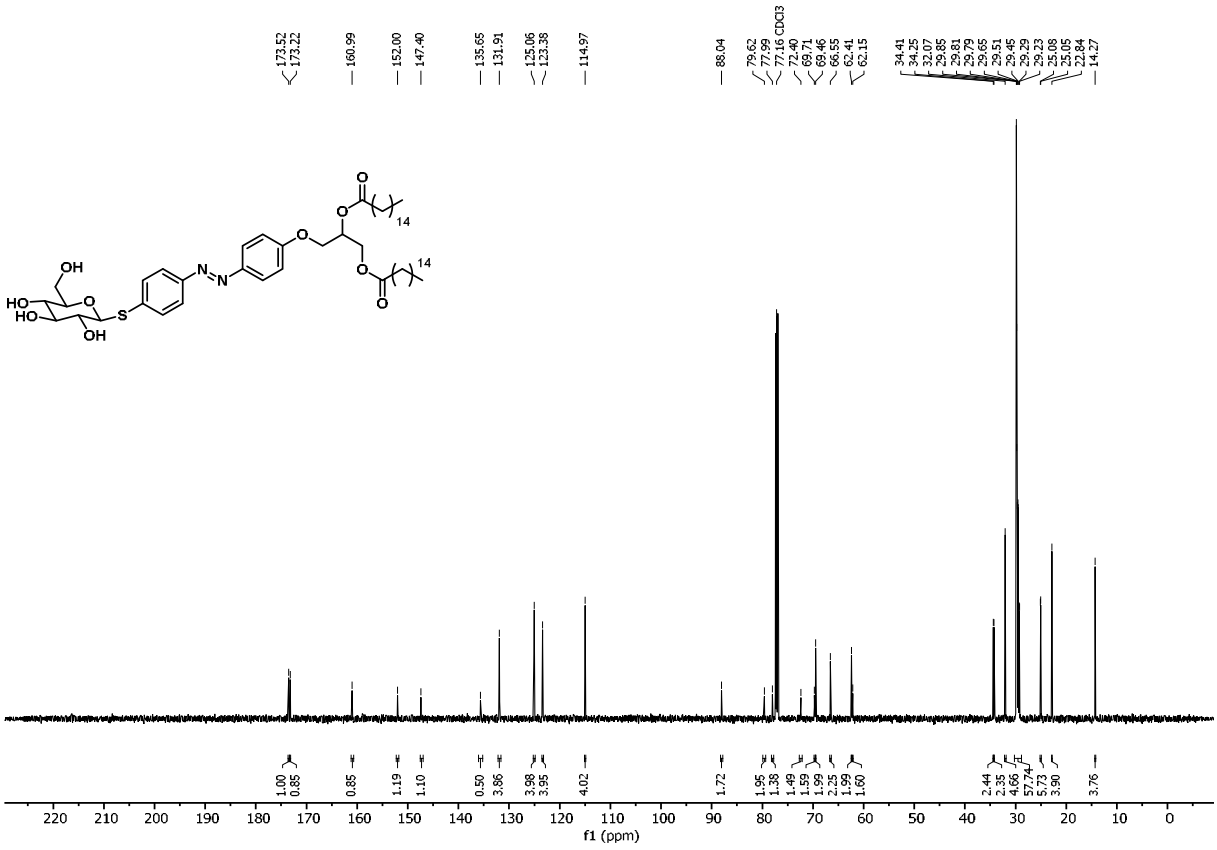

Figure S9 ^{13}C NMR spectrum of 1-*O*-(4-(4-(*S*-β-D-glucopyranosyl)thiophenyldiazenyl)benzene)-2,3-di-*O*-hexadecanoyl-*rac*-glycerol (**1**) (151 MHz, $CDCl_3$, 298 K).

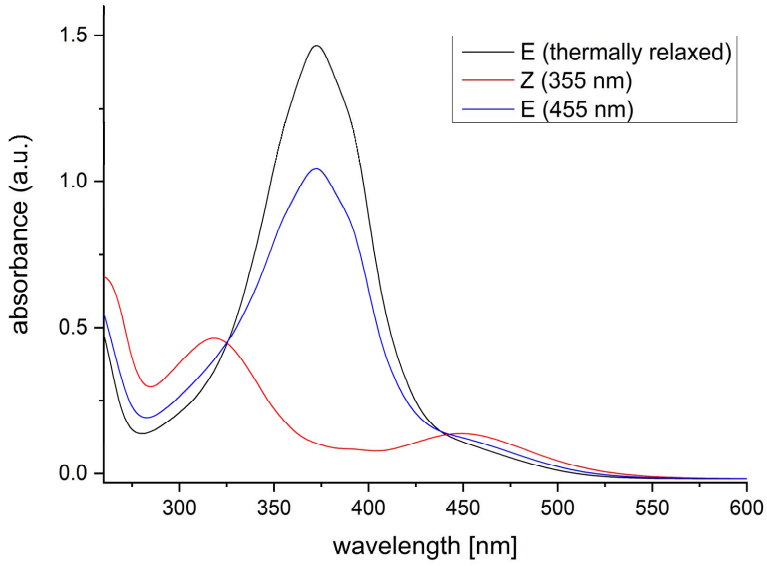

Figure S10 UV-VIS spectra of *trans*-**1** (blue) and *cis*-**1** (red) measured.

S2. Fitting different mesophases

As a first step to fit the SAXS data, a model describing possible structures, lamellar, hexagonal and bicontinuous cubic (*Pn3m*, *Im3m*, *Fm3m*, *Pm3n*, *Fd3m* and *Ia3d*), was plotted on top of the data to check visually for possible matches. The data was fitted between the wave vectors q = 0.6 and 3.5 nm^{-1}. The applied fit routine was previously used in (Hövelmann *et al.*, 2024). The model consists of multiple Gaussian-functions with variable amplitude $a_{1,2,\ldots,\mathrm{n}}$, peak width $\sigma_{1,2,\ldots,\mathrm{n}}$ and peak positions $p_{1,2,\ldots,\mathrm{n}}$ calculated based on the *d*-spacing parameter for the corresponding mesophases. The space groups are taken from (Hyde, 2001).

$$f(q) = a_1\, e^{-\frac{(q-p_1)^2}{2\sigma_1^2}} + \cdots + a_\mathrm{n}\, e^{-\frac{(q-p_\mathrm{n})^2}{2\sigma_\mathrm{n}^2}}$$

In most cases, only one matching structure was found. After identifying this best matching structure, the model was fitted again to the data allowing small deviations $\delta_{1,2,\ldots,\mathrm{n}}$ of the peak positions by maximum ± 0.06 nm^{-1} for each peak in the scattering data.

$$f(q) = a_1\, e^{-\frac{(q-(p_1+\delta_1))^2}{2\sigma_1^2}} + \cdots + a_\mathrm{n}\, e^{-\frac{(q-(p_\mathrm{n}+\delta_\mathrm{n}))^2}{2\sigma_\mathrm{n}^2}}$$

Based on the positions $p_\mathrm{n} + \delta_\mathrm{n}$ the *d*-spacing values were calculated and averages. Their deviation was used to determine the error of the *d*-spacing value.

Data such as for 90:10 or 80:20 DPPC:**2** show multiple peaks which cannot be described by a single mesophase and thus belong to different structures. In these cases, all possible combinations of two or three different mesophases were plotted on top of the data to check visually for matching peaks. The best matching combination was then fitted using the above described sequence. Thus, the overall fit consists of multiple Gaussian peaks belonging to the different mesophases as shown exemplarily in Fig. S11 for 20% of **2**.

For few data sets, both, the cubic *Pn3m* and *Im3m* structure, was found to fit the data reasonably well as for example shown in Fig. S12. In this case, the peak widths, deviations in the *d*-spacing values and the agreement with mesophases for both isomers and at other proportions were checked. In the case of 50:50 and 30:70 DPPC:**2** the *Im3m* structure was preferred as the peak widths, especially for the first peak, is smaller than for the *Pn3m* structure and the deviations in the peak positions from the theoretical positions are also smaller indicating a better match. In some cases, no unique solution of the structure could be identified as for example for the data on DPPC:**6** and DPPC:**7**. For these samples, the structure is labelled as not identified in Fig. 3 and no fit values are listed in Table S1. All other determined mesophases and their *d*-spacing are summarised in Table S1 for completeness.

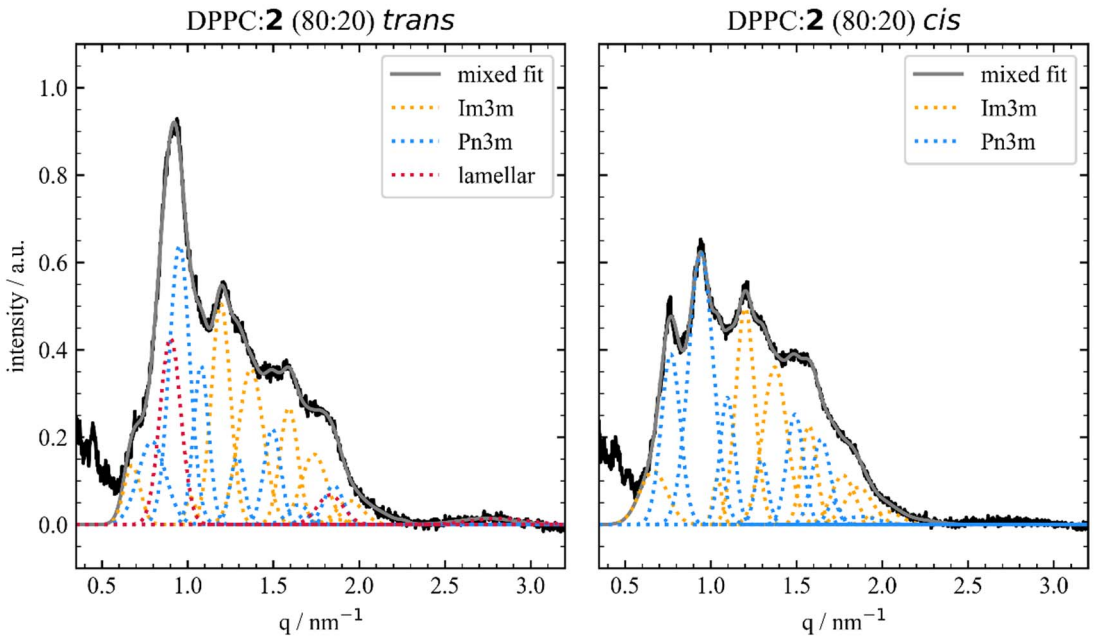

Figure S11 SAXS data obtained from 80% DPPC mixed with 20 % *trans*-**2** (left) and *cis*-**2** (right) shown with the fit (grey) of the sum of a lamellar (red), *Pn3m* (blue) and *Im3m* (orange) structure.

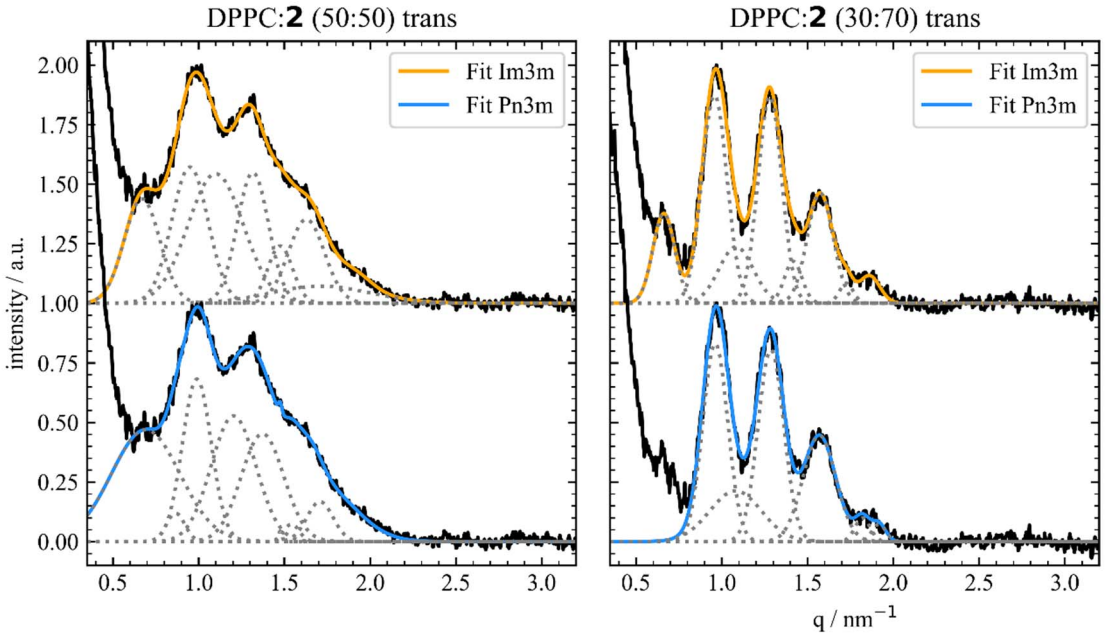

Figure S12 SAXS data obtained from DPPC mixed with *trans*-**2** in the proportion 50:50 (left) and 30:70 (right) together with the fits for the *Im3m* structure (top) and *Pn3m* structure (bottom).

Table S1 Mesophases and *d*-spacing parameters *d* derived from the SAXS data for pure DPPC and DLPC vesicles and mixed lipid aggregates together with the mass per volume with an estimated concentration error of 0.02 g/l.

T / °C	DPPC	density / g/l	mesophase	*d* / nm		
25	100	7.34	lamellar	6.34 ± 0.03		
			trans		*cis*	
T / °C	DPPC:**1**		mesophase	*d* / nm	mesophase	*d* / nm
21	97.5:2.5	3.70	lamellar	6.40 ± 0.02	lamellar	6.44 ± 0.01
21	95:5	3.72	lamellar	6.51 ± 0.01	lamellar	6.47 ± 0.02
21	90:10	3.78	lamellar	6.71 ± 0.04	lamellar	6.75 ± 0.04
21	50:50	4.19	1st order peak	6.67 ± 0.01	1st order peak	6.69 ± 0.01
21	0:100	4.72	1st order peak	6.78 ± 0.01	1st order peak	6.78 ± 0.01
			trans		*cis*	
T / °C	DPPC:**2**		mesophase	*d* / nm	mesophase	*d* / nm
25	95:5	7.41	lamellar	6.7 ± 0.09	Pn3m	10.4 ± 0.2
25	90:10	7.47	lamellar	6.8 ± 0.08	Pn3m	11.2 ± 0.4
21	80:20	3.80	lamellar	6.9 ± 0.09		
			Im3m	12.7 ± 0.3	Im3m	12.6 ± 0.4
			Pn3m	11.6 ± 0.3	Pn3m	11.7 ± 0.2
21	64:36	3.91	Im3m	12.4 ± 0.3	Im3m	12.5 ± 0.2
			Pn3m	11.3 ± 0.3	Pn3m	11.4 ± 0.3
25	50:50	8.00	Im3m	13.5 ± 0.1	Im3m	13.2 ± 0.1
25	30:70	8.27	Im3m	13.65 ± 0.5	Im3m	13.74 ± 0.5
25	0:100	8.67	lamellar	6.74 ± 0.05	lamellar	6.73 ± 0.04
			trans		*cis*	
T / °C	DPPC:**4**		mesophase	*d* / nm	mesophase	*d* / nm
25	90:10	7.64	lamellar	6.34 ± 0.05	lamellar	6.34 ± 0.05
25	80:20	7.93	lamellar	6.33 ± 0.04	lamellar	6.33 ± 0.04
			Pn3m	11.1 ± 0.2	Pn3m	11.2 ± 0.2

25	50:50	8.81	Pn3m	11.4 ± 0.1	Pn3m	11.3 ± 0.1
25	30:70	9.40	lamellar	8.0 ± 0.2	lamellar	8.0 ± 0.2
25	0:100	10.28	lamellar	8.0 ± 0.1	lamellar	8.0 ± 0.1
			trans		*cis*	
T / °C	DPPC:**5**		mesophase	*d* / nm	mesophase	*d* / nm
25	90:10	7.75	lamellar	6.42 ± 0.08	lamellar	6.57 ± 0.08
25	0:100	11.41	lamellar	8.63 ± 0.01	lamellar	8.62 ± 0.01
			lamellar	5.89 ± 0.02	lamellar	5.88 ± 0.02
T / °C	DLPC	density g/l	mesophase	*d* / nm		
25	100	3.11	lamellar	5.89 ± 0.01		
			trans		*cis*	
T / °C	DLPC:**2**		mesophase	*d* / nm	mesophase	*d* / nm
	95:5	3.17	lamellar	6.00 ± 0.01	lamellar	5.99 ± 0.01
	90:10	3.23	lamellar	6.02 ± 0.01	lamellar	6.00 ± 0.01
			Im3m	9.9 ± 0.2	Im3m	9.9 ± 0.2
			Pn3m	9.1 ± 0.2	Pn3m	9.2 ± 0.3
	80:20	3.35	Im3m	9.7 ± 0.2	Im3m	9.7 ± 0.2
			Pn3m	9.0 ± 0.1	Pn3m	9.0 ± 0.1
	50:50	3.72	Im3m	9.6 ± 0.2	Im3m	9.7 ± 0.2
			Pn3m	9.0 ± 0.1	Pn3m	9.1 ± 0.2
	30:70	3.97	Im3m	9.6 ± 0.2	Im3m	9.6 ± 0.2
	0:100	4.33	lamellar	6.74 ± 0.05	lamellar	6.73 ± 0.04
			trans		*cis*	
T / °C	DLPC:**3**		mesophase	*d* / nm	mesophase	*d* / nm
	95:5	3.20	lamellar	5.93 ± 0.01	lamellar	5.92 ± 0.01
	90:10	3.29	lamellar	5.93 ± 0.02	lamellar	5.93 ± 0.02
			Im3m	11.5 ± 0.8	Im3m	11.6 ± 0.8
			Pn3m	11.5 ± 0.7	Pn3m	11.7 ± 0.7
	80:20	3.47	lamellar	5.92 ± 0.02	lamellar	5.92 ± 0.02

		Im3m	11.6 ± 0.7	Im3m	11.5 ± 06
		Pn3m	11.1 ± 1.4	Pn3m	11.1 ± 1.4
50:50	4.00	Im3m	11.4 ± 1.2	Im3m	11.5 ± 1.6
		Pn3m	10.7 ± 1.2	Pn3m	10.8 ± 0.9
30:70	4.36	Im3m	11.2 ± 0.6	Im3m	11.0 ± 0.8
		Pn3m	11.2 ± 0.7	Pn3m	11.2 ± 0.7
0:100	4.89	p6m	7.6 ± 0.2	p6m	7.6 ± 0.2

S3. Fitting kinetics of photoswitching

Table S2 Mesophases and *d*-spacing parameters derived from the SAXS data for 97.5:2 and 95:5 DPPC:**1** at different times *t* after the start of illumination with 365 nm (*trans* to *cis*) and 455 nm (*cis* to *trans*).

		trans to cis		*cis to trans*	
t / s	DPPC:**1**	mesophase	*d* / nm	mesophase	*d* / nm
0	97.5:2.5	lamellar	6.442 ± 0.009	lamellar	6.407 ± 0.009
2	97.5:2.5	lamellar	6.445 ± 0.003		
5	97.5:2.5	lamellar	6.436 ± 0.009	lamellar	6.417 ± 0.009
10	97.5:2.5	lamellar	6.433 ± 0.008	lamellar	6.412 ± 0.010
20	97.5:2.5	lamellar	6.435 ± 0.007	lamellar	6.427 ± 0.006
30	97.5:2.5	lamellar	6.425 ± 0.008	lamellar	6.424 ± 0.010
40	97.5:2.5	lamellar	6.425 ± 0.012	lamellar	6.433 ± 0.009
50	97.5:2.5	lamellar	6.410 ± 0.005	lamellar	6.438 ± 0.005
60	97.5:2.5	lamellar	6.409 ± 0.009	lamellar	6.438 ± 0.007
120	97.5:2.5	lamellar	6.418 ± 0.004		
180	97.5:2.5	lamellar	6.407 ± 0.009		
		trans to cis		*cis to trans*	
t / s	DPPC:**1**	mesophase	*d* / nm	mesophase	*d* / nm
0	95:5	lamellar	6.512 ± 0.007	lamellar	6.475 ± 0.009
5	95:5	lamellar	6.512 ± 0.008	lamellar	6.485 ± 0.007

10	95:5	lamellar	6.504 ± 0.009	lamellar	4.495 ± 0.007
20	95:5	lamellar	6.498 ± 0.006	lamellar	4.489 ± 0.007
30	95:5	lamellar	6.491 ± 0.009	lamellar	4.497 ± 0.006
40	95:5	lamellar	6.482 ± 0.008		
45	95:5			lamellar	6.506 ± 0.006
50	95:5	lamellar	6.511 ± 0.007		
60	95:5	lamellar	6.479 ± 0.008	lamellar	6.501 ± 0.008
90	95:5			lamellar	6.518 ± 0.005
120	95:5	lamellar	6.486 ± 0.008		
180	95:5	lamellar	6.475 ± 0.009		

Table S3 Mesophases and *d*-spacing parameters derived from the SAXS data for 80:20 DPPC:**2** at different times *t* after the start of illumination with 365 nm (*trans* to *cis*) and 455 nm (*cis* to *trans*).

		trans to cis		*cis to trans*	
t / s	DPPC:**2**	mesophase	*d* / nm	mesophase	*d* / nm
0	80:20	lamellar	6.9 ± 0.2	Pn3m	11.6 ± 0.2
		Pn3m	11.6 ± 0.3	Im3m	12.6 ± 0.3
		Im3m	12.7 ± 0.3		
10	80:20	lamellar	6.9 ± 0.2		
		Pn3m	11.7 ± 0.3		
		Im3m	12.7 ± 0.3		
15	80:20			Pn3m	11.6 ± 0.3
				Im3m	12.6 ± 0.3
20	80:20	lamellar	6.8 ± 0.2		
		Pn3m	11.6 ± 0.3		
		Im3m	12.7 ± 0.3		
30	80:20	lamellar	6.9 ± 0.2	lamellar	6.9 ± 0.2
		Pn3m	11.6 ± 0.3	Pn3m	11.6 ± 0.3

		Im3m	12.6 ± 0.3	Im3m	12.6 ± 0.3
38	80:20	lamellar	6.9 ± 0.2		
		Pn3m	11.6 ± 0.3		
		Im3m	12.7 ± 0.3		
50	80:20	lamellar	6.9 ± 0.2		
		Pn3m	11.6 ± 0.3		
		Im3m	12.6 ± 0.3		
55	80:20	lamellar	6.8 ± 0.2		
		Pn3m	11.7 ± 0.3		
		Im3m	12.6 ± 0.3		
60	80:20	lamellar	6.8 ± 0.2	lamellar	6.9 ± 0.2
		Pn3m	11.8 ± 0.3	Pn3m	11.6 ± 0.3
		Im3m	12.7 ± 0.3	Im3m	12.8 ± 0.3
70	80:20	lamellar	6.9 ± 0.2		
		Pn3m	11.6 ± 0.3		
		Im3m	12.7 ± 0.3		
80	80:20	lamellar	6.9 ± 0.2		
		Pn3m	11.7 ± 0.3		
		Im3m	12.6 ± 0.3		
90	80:20	lamellar	6.8 ± 0.2	lamellar	6.8 ± 0.2
		Pn3m	11.6 ± 0.3	Pn3m	11.7 ± 0.3
		Im3m	12.6 ± 0.3	Im3m	12.7 ± 0.3
100	80:20	lamellar	6.8 ± 0.2		
		Pn3m	11.6 ± 0.3		
		Im3m	12.6 ± 0.3		
110	80:20	Pn3m	11.6 ± 0.3		
		Im3m	12.6 ± 0.2		
115	80:20	Pn3m	11.6 ± 0.2		
		Im3m	12.5 ± 0.3		
120	80:20	Pn3m	11.6 ± 0.2	lamellar	6.8 ± 0.2

		Im3m	12.6 ± 0.3	Pn3m	11.7 ± 0.3
				Im3m	12.7 ± 0.3
130	80:20	Pn3m	11.6 ± 0.3		
		Im3m	12.5 ± 0.3		
135	80:20			lamellar	6.9 ± 0.2
				Pn3m	11.7 ± 0.3
				Im3m	12.7 ± 0.3
150	80:20			lamellar	6.9 ± 0.2
				Pn3m	11.7 ± 0.3
				Im3m	12.7 ± 0.3

7
Laser induced kinetics at liquid interfaces

Laser pump - X-ray pump measurements enable studies of non-equilibrium states at interfaces on as to ns time scales. The pump - probe setup at the LISA, P08 is optimised for investigations at liquid interfaces and reaches a temporal resolution of up to 38 ps [183]. In this work, the laser beam shape was characterised, modified and optimised. Additionally, the synchronisation of the laser pulses to the X-ray pulses was improved to allow for longer time delays between laser and X-ray pulses and to enhance operability at the beamline. The publication [PSH 2] presents the detailed description of the extension of laser pump - X-ray probe setup at LISA at P08, PETRA III in Sec. 7.1. The article was accepted and will be published in the peer-reviewed Journal of Physics: Conference Series (JPCS) in June 2025.
Fields of interest for studying dynamics at liquid interfaces are the behaviour of capillary waves upon thermal or electronical excitation. Moreover, theoretical and experimental results show that specific ions, especially larger halides, are attracted to the surface and can form a layer with an enriched concentration compared to the bulk. The here presented studies were conducted on aqueous NaI solutions to investigate the enrichment or depletion of iodide ions near the surface especially under irradiation of UV light. The manuscript [MSH 2] is currently under peer-review for publishing.

7.1 Extending the laser pump - X-ray probe system at LISA, P08, PETRA III

Numerous beamlines at synchrotron radiation facilities all over the world offer laser pump - X-ray probe setups such as at the Advanced Photon Source [208], BESSY II [209], Beijing Synchrotron Radiation Facility [210], PETRA III storage ring at DESY [183], Elettra-Sincrotrone Trieste [211], ESRF [212], KIT Light Source [213], MAX IV

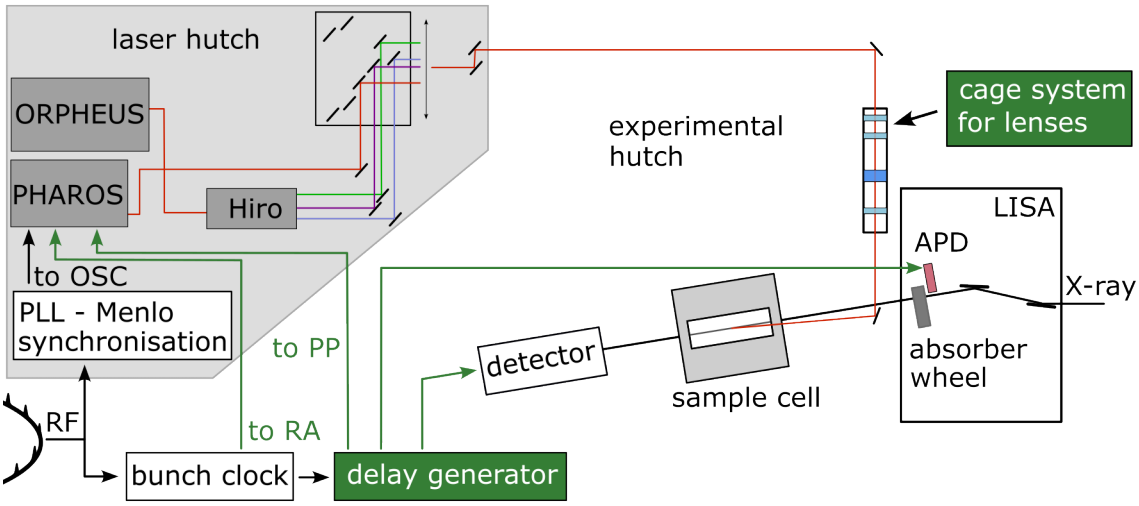

Figure 7.1: Schematic drawing of the laser and X-ray paths at LISA, P08 including the new parts planned, designed and commissioning during this work highlighted in green.

Laboratory [214], SOLEIL [215], SPring-8 [216] and Stanford Synchrotron Radiation Lightsource [217]. However, most of these beamlines focus on either bulk scattering or scattering from solid interfaces. The combination of liquid interfaces and pump - probe [183] makes the setup available at the LISA endstation unique. The ErUm-Pro funded laser pump - X-ray probe setup at the P08 beamline was constructed, commissioned and is continuously maintained and improved by members of the LISA group of PD. Dr. Bridget Murphy, Kiel University. The technical description of the original setup prior to the here described work is published in [183] and described briefly in Sec. 4.5.1. In the past years, I improved the laser setup to enhance the user experience and broaden the fields of applications for the laser pump experiments. In Fig. 7.1 the original pump - probe setup is shown together with the new parts and changes highlighted in green. On the laser beam path, two main developments were undertaken. One is the commissioning of the BEAMAGE-4M beam shape camera from Gentec-EO and the second is the integration of a beam profile shaper into the beam path. This beam shaper is a DOE purchased from HOLO/OR Ltd., Israel that transforms a Gaussian beam profile to a flat top profile. For an efficient and optimal beam profile transformation the DOEs are manufactured for a specific beam size, working distance between the DOE and the sample stage and wavelength with a 2 % bandwidth tolerance. The DOE is optimised for a wavelength of 1064 nm, which is close to the fundamental wavelength (1030 nm) of the Pharos laser. At a working distance of 2 m from the beam shaper, the beam profile is transformed to

a flat top shape with a length and width of $(5.65 \pm 0.01)\,\mathrm{mm} \times (2.44 \pm 0.01)\,\mathrm{mm}$. To obtain this final beam size, the beam coming from the Pharos laser needs to be broadened from the original $(3.72 \pm 0.01)\,\mathrm{mm} \times (3.10 \pm 0.01)\,\mathrm{mm}$ (FWHM) to about $12\,\mathrm{mm} \times 12\,\mathrm{mm}$. To avoid focusing of the laser beam, the Galilean telescope design (see Sec. 4.5.1) is used to broaden the beam with a plan-concave and a plan-convex lens. Behind the DOE, a convex lens is positioned to focus the beam onto the sample stage. As the DOE is highly sensitive to variation in the incoming beam size and position, the DOE and the lenses for the Galilean telescope are places into magnetic lens holders in a cage system from Thorlabs, Inc. in the beam path. This ensures the correct relative positioning between the lenses and beam shaper. Prior to mounting the lenses, the center of the cage system is aligned to the laser beam path.

Verification of the successful beam shape transformation and its optimisation was monitored with the beam shape camera. The camera was placed on the sample stage at the final sample position. In Fig. 7.2 two 2D images and the intensity profile along the cross lines through the centers of the profile are shown for the beam shape of the original laser beam and the flat top transformed beam. For a direct comparison of the intensities, the intensity per mm^2 is calculated for the profiles (see Appx. A.1). The intensity integrated over the whole beam spot was measured with a power meter in the beam path and corresponds to 14.4 W for the primary beam at the sample stage and 13.4 W for the flat top transformed laser beam. The difference in integrated intensity is caused by the intensity loss at the additional optical elements (three lenses and the DOE) in the beam path to transform the beam profile. Comparing the intensity profiles shown in Fig. 7.2, a lower maximum intensity of the flat top shaped beam can be noticed. Meanwhile, due to the flat top character, the intensity is almost constant over the whole beam area. This is in contrast to the high peak intensity in the Gaussian shaped profile and the fast decreasing intensity towards the edges of the beam spot. Thus, for an even heat distribution on the sample, the flat top shaped beam is of great advantage.

The quality of the transformed beam shaped is highly sensitive on the position of the lenses relative to each other and whether the laser beam passes through the center of the lenses and the DOE. A misalignment is indicated by antisymmetries of the beam profile or large intensity fluctuations and gradients. To enhance the reproducibility and quality of the beam profiles, the distances between the lenses was fixed by lens holders in the cage system built into the laser beam path. Therefore, only the position of the cage systems has to be slightly varied until an optimised beam profile is recorded. An optimal flat top shaped beam profile shows a homogeneous intensity distribution with only small deviations in the intensity as show in Fig. 7.2. The quality of the flat top is characterised with the flatness factor F_η. This is

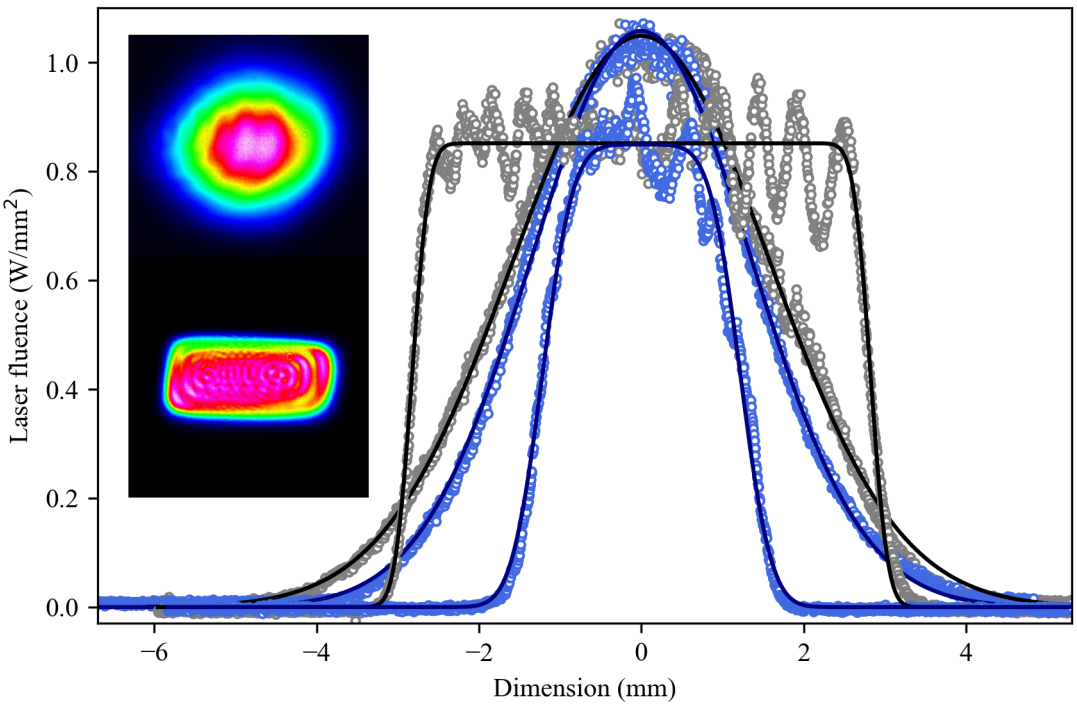

Figure 7.2: Images of the beam profile and the normalised intensity profiles (circles) along the centered horizontal (grey) and vertical (blue) cross lines together with the fits of the shape (solid lines) for the original fundamental wavelength (1030 nm) Gaussian shaped beam and the transformed flat top shaped beam.

calculated by dividing the average irradiance by the maximum irradiance [218]. The calculation of the F_η factors for three independent beam profile measurements over the course of two years is described in more detail in the accepted manuscript [PSH 2].

In addition to the developments on the laser beam path, the accessible time delays between the laser and X-ray pulses were extended with an additional delay generator integrated into the timing synchronisation in collaboration with the company TxProducts. The delay generator was purchased from TxProducts together with the software and Python scripts to allow control and communication with the beamline control system. To ensure full functionality with the previous setup, the hardware installation was done together, TxProducts and myself, and completed with an initial test of the software. Detailed performance and operation tests were conducted during two beamtimes. Both beamtimes were followed by debugging the control software and revision of the code together with TxProducts.

A further development on the laser synchronisation is the external gating of the pulse picker (PP) Pockels cell inside the Pharos laser (see 2.4.1) to reduce the effective

repetition rate of the laser pulses. In the following, the effective repetition rate refers to the time between amplified laser pulses independent of the repetition rate in the regenerative amplifier (RA) Pockels cell. By gating the PP Pockels cell, only a selection of the laser pulses is amplified. The unamplified pulses with a pulse energy of (0.15 ± 0.02) µJ are neglectable compared to the amplified pulses with energies between 12 to 110 µJ. The gate signal can be changed quickly and easily over the control system of the beamline. Modifying the repetition rate by gating the PP has multiple advantages. On one hand, the total heat load on the sample can be reduced by keeping the individual pulse intensity constant. The pulse energy is defined by the repetition rate in the RA Pockels cell and thus unaffected by gating the PP Pockels cell. On the other hand, the repetition rate of the laser pulses can be reduced to accommodate samples with a slow relaxation time. Lastly, the detector and the PP are gated by the same delay generator, which ensures that the temporal overlap between the X-ray and laser pulses is kept even by changing the repetition rate.

Another improvement was achieved on a user-optimised interface to choose and obtain a desired time delay between the X-ray and laser pulses. Previously, time delays below 192 ns were reached by shifting the phase of the oscillator with the synchronisation unit from Menlo Systems and larger time delays by jumping X-ray bunches on the 192 ns grid (as described in detail in [183] and Sec. 4.5.1). Unfortunately, shifting the phase to reach time differences of multiple tens of ns took several minutes and often the phase was lost during the shifting process which resulted in a loss of the synchronisation between laser and X-ray pulses. Restoring the synchronisation was time consuming and needed experienced and trained users. To overcome this problem, the RA Pockels cell is now triggered by a signal from the bunch clock (130.12 kHz) and by this the oscillator pulses to be amplified in the RA Pockels cell is chosen. The oscillator pulses are generated with a repetition frequency of about 83.278 kHz which corresponds to one laser pulse every 12 ns. These laser pulses enter the RA and there the laser pulses belonging to the chosen final repetition rate (e.g. 130.12 kHz) are amplified. To choose which laser pulse is amplified in the RA, the RA is triggered externally by one of the output channels of the bunch clock at P08 synchronised to 130.12 kHz. As the oscillator pulses are separated by 12 ns, the bunch clock output signal is shifted on a 12 ns grid to jump the oscillator pulses. Jumping the oscillator pulses is very fast (<ms) and showed high stability during testing, commissioning and two user beamtimes. With all these developments and improvements, time delays t_{delay} can be modified by a combinations of shifting the phase of the oscillator pulses ($t_{\mathrm{delay}} < 6$ ns), triggering the RA Pockels cell to select which oscillator pulse is amplified ($6\,\mathrm{ns} < t_{\mathrm{delay}} < 86$ ns) and jumping X-ray bunches ($86\,\mathrm{ns} < t_{\mathrm{delay}}$). For a user-friendly experience, the most

efficient combination of the delay options is calculated by the Python script, originally provided by TxProducts and jointly revised, and chosen for the desired time delay.

Following the presentation of these new developments and improvements on the 14th International Conference on Synchrotron Radiation Instrumentation (SRI) in 2024, [PSH 2] was accepted as part of the SRI 2024 Proceedings in the peer-reviewed open access volume of Journal of Physics: Conference Series (JPCS). The article was in print during submission of this work and was published under licence by IOP Publishing Ltd. with CC BY Creative Commons Attribution 4.0 licence. The article is now available under `https://doi.org/10.1088/1742-6596/3010/1/012056`.

15th International Conference on Synchrotron Radiation Instrumentation (SRI 2024) IOP Publishing
Journal of Physics: Conference Series **3010** (2025) 012056 doi:10.1088/1742-6596/3010/1/012056

Extending the laser pump X-ray probe system at LISA P08 PETRA III

S C Hövelmann[1,2], J E Warias[1], L Petersdorf[1,2], D Schmidt[3], P Gaal[3], R P Giri[1], N Hayen[1,2], P Jordt[1,2], O M Magnussen[1], C Shen[4], F Bertram[4] and B Murphy [1,2*]

[1] Institute of Experimental and Applied Physics, Kiel University, Leibnizstraße 19, 24118 Kiel, Germany
[2] Ruprecht Haensel Laboratory, Deutsche Elektronen-Synchrotron DESY, Notkestraße 85, 22607 Hamburg, Germany
[3] TXproducts UG (haftungsbeschränkt), Luruper Hauptstraße 1, 22547 Hamburg, Germany
[4] Deutsches Elektronen-Synchrotron DESY, Notkestraße 85, 22607 Hamburg, Germany

[*]E-mail: murphy@physik.uni-kiel.de

Abstract. The laser pump – X-ray probe setup at the LISA liquid interface scattering apparatus at beamline P08 at PETRA III enables investigation of photo-induced structural changes at liquid and solid interfaces with a time resolution of 38 ps. Here we report the latest upgrades on the pump – probe setup including the extension of the accessible pump-probe delay time scale and the implementation of laser beam profile transformers. The new laser optical cage system with magnetic holders allows variable laser beam sizes and flat top beam profile which can be advantageous for matching laser and X-ray beam size and profile on heat sensitive samples. The introduction of an additional delay/pulse generator now enables pump-probe measurements to be performed on all time scales from 100 picoseconds to seconds, allowing to study ultrafast and slow optical excitation and relaxation dynamics with any gap in time resolution.

1. Introduction

Liquid interfaces play a key role in atmospheric, biological, chemical and physical process influencing climate, environment and technological development [1,2,3]. Investigating the changes of local order and dynamics near the interface are constant challenges to understand phenomena such as changes in charge distribution [4,5], chemical composition [6], atmospheric chemistry [7,8] and molecular layering [9,10]. Spectroscopic studies on ultrafast dynamics at liquid interfaces identified molecular vibrations, rotations, electronic excitation [11] and formation of solvated electrons [12].

Employing X-ray reflectivity and grazing incidence scattering at liquid interfaces provides insight on interfacial structure [13] and equilibrium dynamics including capillary wave behaviour [14]. Combining these X-ray scattering techniques with pulsed laser radiation allows the study of photo-induced non-equilibrium dynamics. The laser pump – X-ray probe system [15] at the LISA liquid interface scattering apparatus [16] at beamline P08 [17] at PETRA III provides synchronised femtosecond laser pulses from the Pharos laser (Light Conversion) for pump – probe measurements with a resolution of 38 ps for a wide range of biological, solid, aqueous and liquid metal samples.

15th International Conference on Synchrotron Radiation Instrumentation (SRI 2024) IOP Publishing
Journal of Physics: Conference Series **3010** (2025) 012056 doi:10.1088/1742-6596/3010/1/012056

Here we will describe the latest instrumental developments including the extension of the pump – probe delay in the range from μs to seconds and the implementation of optical components for transforming the laser beam profile. All developments of the pump – probe system are available for experiments at both LISA and the six-circle Kohzu diffractometer on the high-resolution diffraction beamline P08 PETRA III.

2. Instrument development - Extending the pump - probe delay range

The laser pump – X-ray probe setup at P08, PETRA III, DESY and its laser and X-ray pulse synchronisation enables time resolved measurements on laser-induced phenomena at liquid and solid interfaces. The laser system consists of a PHAROS femtosecond laser from Light Conversion with a maximum output power of 15 W, fundamental wavelength of 1030 nm and TEM_{00} mode. The pulse length can be tuned between 250 fs and 10 ps and the repetition rate between 100 kHz and 1041 kHz resulting in a maximum pulse energy of 150 μJ and 14 μJ, respectively. Further wavelengths can be obtained by pumping additional Light Conversion modules with the Pharos laser. The higher harmonics generator HIRO is optimised for an input frequency of 130 kHz and pulse length of 251 fs and generates the second (515 nm), third (343 nm) and fourth (258 nm) harmonics. Meanwhile, the optical parametric amplifier ORPHEUS provides a wide wavelength range from 210 to 2600 nm at 1041 kHz and 251 fs pulse length.

To achieve synchronisation between the X-ray and laser pulses, the frequency of the laser oscillator is synchronised via phase-locked-loop (PLL) to the sixth subharmonic of the radio frequency (RF) PETRA III master clock [18] signal. Timing measurements are performed with PETRA III running in 40 bunch timing mode providing X-ray bunches with a repetition rate of 5.2 MHz, resulting in a bunch separation by 192 ns and a periodicity of 7.68 μs for all 40 bunches in the ring. This corresponds to a frequency of 130.12 kHz which is also employed as our standard laser frequency as in most experiments either the fundamental wavelength or higher harmonics generated by the HIRO module are utilised. Time delays on the range of tenth of nanoseconds between the laser pulse and X-ray bunch are realised by shifting the phase with a direct digital synthesiser from Melo Systems. More details, typical output values and first measurement results can be found in [15].

Following an upgrade of the existing above described synchronisation setup commissioned in collaboration with TXproducts, a convenient and user-friendly change of the pump-probe delay Δt between laser and X-ray pulse, the laser pulse repetition rate and the time resolution is now available. This recent development enables an easily operated pump-probe measurement setup with freely selectable delay ranges from ps up to seconds due to the addition of delay/pulse generator MOD745-OEM from BNC. The delay generator is triggered by the PETRA III bunch clock which intern is synchronised to the 499.6655 MHz (~500 MHz) RF PETRA III master clock signal. The bunch clock provides a 130.12 kHz signal which was previously used to gate the detector and monitors directly [15]. Now, the detector gate signal is produced by the delay generator.

The delay generator can generate up to eight independent output channels synchronised to the initial bunch clock trigger. These output channels are connected to the detector and monitor gate and the Pharos Pockels cell as outlined in Figure 1. Each output channel has a custom gate width and delay with respect to the trigger signal. This allows to adjust the time resolution and laser repetition rate independently. The laser repetition rate is modified by gating the Pharos Pockels cell after the regenerative amplifier with a TTL signal. This changes the effective laser repetition rate as only selected laser pulses are amplified and directed to the output aperture.

15th International Conference on Synchrotron Radiation Instrumentation (SRI 2024) IOP Publishing
Journal of Physics: Conference Series **3010** (2025) 012056 doi:10.1088/1742-6596/3010/1/012056

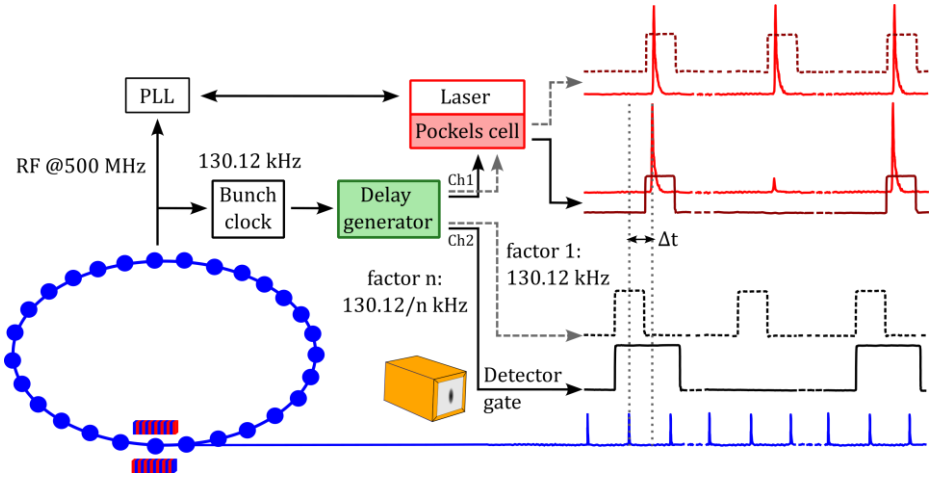

Figure 1. Schematic oscilloscope traces based on [15] including the delay generator and upgraded control schema showing the X-ray bunch (blue), detector gate (black), laser reference (red) and Pockels cell gate (dark red) signals for the maximum (dashed) and reduced (solid) repetition rate. For the reduced repetition rate an increase of the detector gate width over two bunches is shown exemplarily.

The unamplified laser pulses leaving the Pockels cell are with a pulse energy of less than < 0.15 ± 0.02 µJ and therefore neglectable. Gating the Pockels cell does not change the laser oscillator frequency or the operation frequency of the regenerative amplifier. Therefore, the pulse energy stays constant throughout changing the effective laser frequency while the total heat load on the sample is reduced. Reducing the heat load minimises sample expansion, misalignment and destruction. Moreover, for systems with a slow relaxation time after laser excitation, the time between two laser pulses can be increased to allow the system to recover to equilibrium state before the next pulse. Measuring slow dynamics on the µs to s time scale, the detector gate width can be increased to count over multiple X-ray bunches.

For user-friendly handling, the delay generator has been implemented into the beamline control system via Tango. After initial synchronisation, setting the numerous parameters for the channel widths and delays is calculated and initiated automatically when any of the three parameters delay Δt, repetition rate and resolution are changed.

3. Optical components

The optical path was upgraded with a cage system with magnetic holders in the beam path to allow fast and reproducible mounting of lenses or diffractive optical elements (DOE). Examples for the usage are mounting pairs of concave and convex lenses as telescope lenses to increase the laser spot diameter or a Flat Hat Beam Shaper. A Flat Hat Beam Shaper is a DOE that transform a Gaussian incident laser beam into a uniform-intensity spot of rectangular shape (see Figure 2). The option to modify the laser beam profile is advantageous for heat sensitive samples with a low energy damage threshold and measurements under low incident angle to match the size of the X-ray beam footprint. Further, the homogenous local heat distribution is especially beneficial during long-term measurements as small variations in the beam position are of no consequence.

15th International Conference on Synchrotron Radiation Instrumentation (SRI 2024) IOP Publishing
Journal of Physics: Conference Series **3010** (2025) 012056 doi:10.1088/1742-6596/3010/1/012056

The Flat Top Laser Beam Shaper from HOLO/OR Ltd. available at the instrument, currently only for the fundamental wavelength of 1030 nm, transforms the (3720 ± 20) x (3190 ± 10) µm FWHM Gaussian shaped beam to a (5650 ± 10) x (2440 ± 10) µm FWHM Flat Top shaped beam profile (see Figure 2). To quantify the quality of the Flat Top profile the flatness factor F_η was found by dividing the average irradiance by the maximum irradiance [19].

F_η was determined for three independent measurements of the Top Hat profile, using cross sections centered around the beam profile in 210 µm steps. Thus, the average quality factor is calculated to be $F_\eta = 0.80 \pm 0.01$ with a maximum of $F_{\eta,\max} = 0.86 \pm 0.01$ and minimum of $F_{\eta,\min} = 0.71 \pm 0.01$ along the elongated direction. For the compressed direction the average

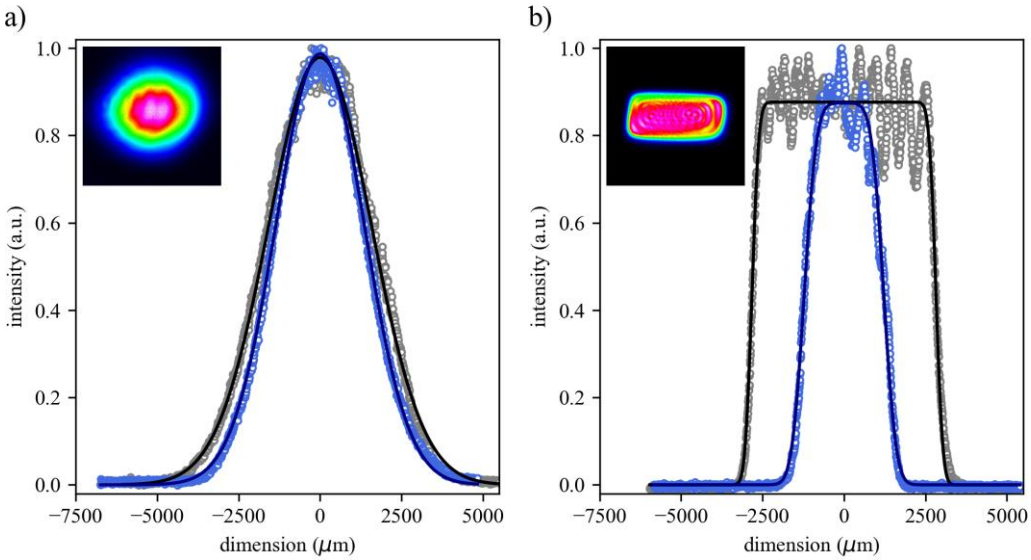

Figure 2. Laser beam profile images recorded with the beam shape camera Beamage-4M of the 1030 nm a) Gaussian and b) Top Hat beam shaped laser beam with cross section shown at the center of each beam profile.

Table 1. Laser beam parameters for the fundamental and harmonic wavelengths. The max. pulse energy and the spot size and shape were determined with the beam profile camera for a repetition rate of 130.12 kHz.

wavelength/ nm	beam shape	Spot size (FWHM)/ µm x µm	max. pulse energy/ µJ	max. deviation of center/ µm
1030	Top Hat	(5650 ± 10) x (2220 ± 10)	106.8 ± 0.4	400
1030	Gaussian	(3720 ± 10) x (3190 ± 20)	109.5 ± 0.4	50
515	Gaussian	(3120 ± 20) x (3230 ± 20)	57.6 ± 0.4	50
343	Gaussian	(3670 ± 20) x (2070 ± 20)	34.6 ± 0.4	55
258	Gaussian	(2480 ± 20) x (2140 ± 20)	7.7 ± 0.4	35

15th International Conference on Synchrotron Radiation Instrumentation (SRI 2024) IOP Publishing
Journal of Physics: Conference Series **3010** (2025) 012056 doi:10.1088/1742-6596/3010/1/012056

quality factor was determined as $F_{\eta} = 0.80 \pm 0.01$ with maximum and minimum factor $F_{\eta,\max} = 0.93 \pm 0.1$ and $F_{\eta,\min} = 0.52 \pm 0.01$.

The beam profiling camera Beamage-4M from Gentec-EO was used to determine the beam profile in 2D and 3D and beam position stability at the sample stage (see Figure 2). This is applied to precisely determine the fluency for the different wavelengths and beam shapes. Measurements of the beam position stability for the fundamental wavelength show a high beam position stability with a maximum center position deviation of 50 µm (see Table 1). The higher harmonic beam profiles are comparable with the shown primary Gaussian beam image. The additional beam parameters for the Gaussian shaped 2nd, 3rd and 4th harmonics are listed for completeness.

4. Conclusion and outlook

This laser pump – X-ray probe system at LISA P08 at PETRA III provides a valuable tool for studying photo-induced dynamics and non-equilibrium states. Implementing the latest instrumental developments, the available pump – probe time scale was extended to cover the full range from ps to seconds. The revised pump – probe delay control eases its operation for non-expert users. Moreover, for heat transfer studies an additional nanosecond laser is expected to be integrated into the existing pump – probe system to broaden the application of this setup.

5. Further Information and Acknowledgement

We acknowledge funding from Bundesministerium für Bildung und Forschung, ErUM Pro (grant No. BMBF05K19FK2 and BMBF05K22FK3). We thank Matthias Greve and Karsten Tarhouni at Kiel University for technical support. We further acknowledge DESY (Hamburg, Germany), a member of the Helmholtz Association HGF, for the provision of experimental facilities. This research was carried out at PETRA III beamline P08 via proposals II-20170014 and II-20210020. We would like to thank René Kirchhof for assistance at P08 and Milena Lippman for chemistry lab support. The authors declare no competing interests.

References

[1] Benjamin I 2006 *Chem. Rev.* **106** 1212-1233
[2] Daillant J, Mora S, Fradin C, Alba M, Braslau A, Luzet, D 2001 *Applied Surface Science* **182** 223-230
[3] Tucceri R 2004 *Surface Science Reports* **56** 85-157
[4] Jungwirth P, Tobias D J 2002 *J. Phys. Chem. B* **106** 6361-6373
[5] Petersen P B, Saykally R J 2006 *Annu. Rev. Phys. Chem.* **57** 333-364
[6] Dukhin S S, Kretzschmar G, Miller R 1995 *Dynamics of adsorption at liquid interfaces* (Amerstdam, NewYork: Elsevier)
[7] Tobias D J, Stern A C, Baer M D, Levin Y, Mundy C J 2013 *Ann. Rev. Phys. Chem.* **64** 339-359
[8] Hu, J H, Shi Q, Davidovits P, Worsnop D R, Zahniser M S, Kolb C E 1995 *J. Phys. Chem.* **99** 8768-8776
[9] Elsen A, Murphy B M, Ocko, B M, Tamam L, Deutsch M, Kuzmenko I, Magnussen O M 2010 *Phys. Rev. Lett.* **104** 105501
[10] Luo G, Bu W, Mihaylov M, Kuzmenko I, Schlossman M L, Soderholm L 2013 *J. Phys. Chem. C* **117** 19082-19090
[11] Tamarat P, Maali A, Lounis B, Orrit M 2000 *J. Phys. Chem. A* **104** 1-16
[12] Benjamin I 1996 *Chem. Rev.* **96** 1449-1475
[13] Pershan P S, Schlossman M 2012 *Liquid Surfaces and Interfaces* (Cambridge: Cambridge University Press)
[14] Runge B, Festersen S, Koops C T, Elsen A, Deutsch M, Ocko B M, Seeck O H, Murphy B M, Magnussen O M 2016 *Phys. Rev. B* **93** 165408
[15] Warias J E, Petersdorf L, Hövelmann S C, Giri R P, Lemke C, Festersen S, Greve M, Mandin P, LeBideau D, Bertram F, Magnussen O M, Murphy B M 2024 *J. Synchrotron Rad.* **31** 779-790

15th International Conference on Synchrotron Radiation Instrumentation (SRI 2024) IOP Publishing
Journal of Physics: Conference Series **3010** (2025) 012056 doi:10.1088/1742-6596/3010/1/012056

[16] Murphy B M, Greve M, Runge B, Koops, C T, Elsen, A, Stettner J, Seeck O H, Magnussen O M 2014 *J. Synchrotron Rad.* **21** 45-56
[17] Seeck O H, Deiter C, Pflaum K, Bertram F, Beerlink A, Franz H, Horbach J, Schulte-Schrepping H, Murphy B M, Greve M, Magnussen O M 2012 *J. Synchrotron Rad.* **19** 30-38
[18] Klute J, Balewski K, Delfs A, Duhme H T, Ebert M, Neumann R, Obier F 2011 *10th European Workshop on Beam Diagnostics and Instrumentation for Particle Accelerators*
[19] International Organization for Standardization 2018 *Optics and photonics -- Lasers and laser-related equipment -- Test methods for laser beam power (energy) density distribution (ISO 13694-3:2018)*

7.2 Pump - Probe studies on aqueous salt solutions

Investigations of the ion distribution in aqueous NaI salt solutions were performed at the laser pump - X-ray probe setup at LISA, P08, PETRA III with XRR and XRFNTR measurements. The fluorescence spectra hold information on the chemical composition of the solution at the surface near region. Further, XRFNTR is a very surface sensitive measurement, as it is performed under grazing incident conditions with an incident angle below and slightly above the critical angle (see Sec. 2.3.5). Therefore, combining the surface sensitive XRR and XRFNTR methods, allows identification of small variations in the electron density and surface roughness profile along the surface normal.

This surface sensitivity is used in the following studies to investigate the distribution of ions at the water-air interface. One of the research questions is whether a surface near layer is formed in aqueous NaI solutions. The second question concentrates on the influence of UV radiation on the local ion distribution. The answers to these questions are important to understand chemical reactions at water interfaces especially in the field of chemical atmosphere. In the next two subsections, first the manuscript [MSH 2] on the NaI aqueous solutions and then the additional unpublished XRFNTR results with UV radiation are presented.

7.2.1 [MSH 2] Laser excitation at the liquid-air interface of aqueous NaI solutions

In the following preprint, the data and results of the XRR and XRFNTR studies on aqueous NaI solutions are presented and discussed. This manuscript is a joined work from Dr. Julia Kobus and myself. During submission, we asked for shared first authorship to represent the equal amount of time and work contributed to the below manuscript. I planned and organised the measurement, prepared the samples and collected the XRR and XRFNTR data. Dr. Julia Kobus performed the analysis of the XRR data while I analysed the XRFNTR data. The manuscript is currently under review and is included as manuscript in this work.

Laser excitation at the liquid-air interface of aqueous NaI solutions

Julia Kobus[a,b], Svenja C. Hövelmann[a,b], Lukas Petersdorf[a,b], Philipp Jordt[a,b], Nicolas Hayen[a,b], Chen Shen[c], Florian Bertram[c], Olaf M. Magnussen[a], Rajendra Giri[a,1], Bridget M. Murphy[a,b,*]

[a] *Institute of Experimental and Applied Physics, Kiel University, Leibnizstraße 19, 24118 Kiel, Germany*
[b] *Ruprecht Haensel Laboratory, Deutsches Elektronen-Synchrotron DESY, Notkestraße 85, 22607 Hamburg, Germany*
[c] *Deutsches Elektronen-Synchrotron DESY, Notkestraße 85, 22607 Hamburg, Germany*

Abstract

Ions at liquid-air interfaces play a key role in numerous atmospheric, biological, and chemical processes, including reactions of ozone with sea-salt aerosols in the troposphere. In this X-ray study of aqueous sodium iodide solutions we investigate the ion distribution at the liquid-air interface, which is crucial for understanding fundamental surface and atmospheric chemistry.

We used complementary X-ray reflectivity and X-ray fluorescence near total reflection measurements to investigate the ion distribution at the liquid-air interface of aqueous sodium iodide solutions at concentrations ranging from 0.1 M to 4 M. A laser pump–X-ray probe setup was employed, with 258 nm UV laser irradiation used to excite the halide ions at the interface.

Our results show that both X-ray reflectivity and X-ray fluorescence near total reflection yield consistent scattering length density (SLD) values for sodium iodide solutions. These SLD values are higher than expected for the given bulk concentrations, indicating an enhanced interfacial ion concentration. This enhancement aligns with theoretical considerations of an enhancement of polarizable iodide anions at the air-liquid interface. However, no distinct layering was observed at 21 °C. Upon UV irradiation, an increase in SLD was observed, while the surface roughness remained unchanged.

*Corresponding author
Email address: murphy@physik.uni-kiel.de (Bridget M. Murphy)
[1] Present address: Department of Physics, Indian Institute of Technology (ISM) Dhanbad, Jharkhand 826004, India

Keywords: liquid-air interface, laser induced, ions, aqueous solution, surface roughness

1. Introduction

At liquid ion-containing interfaces a plethora of important and fundamental atmospheric, biological, chemical and physical processes take place and have an influence on climate and environment. In atmospheric chemistry the presence and dynamics of ions at the interface play a particularly important role to understand phenomena such as creation of molecular halogens [1, 2, 3], reactions of ozone or hydroxyl radicals with sea salt aerosols in the troposphere [4, 5] or the formation of foam after waves break in the ocean [6, 7, 8, 9, 10].

Classical thermodynamic considerations suggest that ions in aerosols should predominantly reside in the bulk phase, due to the absence of a counterbalancing image-charge in the surrounding air. However, this view has been challenged by experimental studies indicating surface-sensitive reactions and, consequently, an enhanced presence of ions at the interface. For instance, Hu et al. [1] showed that Cl^- and Br^- ions must be present at the liquid-air interface to explain the uptake of Cl_2 and Br_2 gases by aqueous salt solutions.

These findings have led to theoretical and computational efforts, particularly molecular dynamics simulations [11, 12, 13, 14, 15], which suggest that large, polarizable anions are enriched at the interface. Experimental confirmation comes from techniques such as vibrational sum-frequency spectroscopy [16, 17, 18, 19], X-ray photoelectron spectroscopy [12, 20], and X-ray reflectivity [21]. These studies consistently report a preferential accumulation of polarizable ions (e.g., I^- and Br^-) at the surface, while smaller halides (e.g., Cl^- and F^-) tend to be only weakly attracted or even repelled [22, 11]. Sloutskin et al. [21] further observed subtle surface layering in concentrated aqueous solutions of $SrCl_2$ (2.5 M) and RbBr (4.9 M) using X-ray reflectivity, whereas no such layering was found for other halide solutions.

Light from the sun, particularly in the ultraviolet (UV) range, plays a significant role in driving chemical reactions at atmospheric interfaces. UV irradiation can induce photochemical reactions and might influence the ion density at the liquid-air interface. With the depletion of the ozone layer in the stratosphere more highest-energy ultraviolet radiation (UV), especially in the UV-B range 290 nm to 315 nm, passes though the atmosphere and reacts with natural ecosystems [23, 24, 25]. Even shorter-wavelength radiation below 290 nm (UV-C) is absorbed in the atmosphere. This short-wavelength UV radiation interacts with aqueous halides and can photoinduce charge-transfer-to-solvent (CTTS) states creating solvated electrons. These aqueous halides exhibit broad

ultraviolet absorption bands which makes them ideal systems to study CTTS dynamics [26, 27, 28, 29]. Understanding how such light-driven processes affect the interfacial distribution of halide ions is therefore essential for assessing their role in atmospheric chemistry.

This study aims to gain understanding of how halide ions behave at the air–water interface under atmospherically relevant conditions. In this work, we focus on aqueous NaI solutions as iodide is atmospherically relevant, occurring in marine aerosols and playing a role in interfacial photochemistry [30, 31]. Two key questions are addressed: (1) Is the number of ions at the surface enhanced, supporting theoretical predictions of interfacial enrichment? (2) How does the ion distribution at the surface change upon UV irradiation?

To explore these questions, we studied NaI solutions with concentrations between 0.1 M to 4 M. For this purpose, we employed X-ray reflectivity (XRR) [32, 33, 34] and X-ray fluorescence near total reflection (XRFNTR) [35, 36, 37], two surface-sensitive techniques complementary to other commonly used methods such as vibrational sum-frequency spectroscopy and X-ray photoelectron spectroscopy.

XRR measurements allow probing the atomic-scale structure of fluid interfaces. Specifically, XRR enables the investigation of the surface-normal electron density profile, providing detailed insights into surface layering and the distribution of ions near the surface. This technique is highly sensitive to surface roughness and structural changes at the interface, making it ideal for studying ion concentrations at liquid-air interfaces under varying conditions, such as different concentrations of aqueous halide solutions or the influence of UV irradiation [38, 32]. In fact, XRR has proven capable of resolving complex, nonmonotonic ion-density profiles near the interface, as demonstrated for aqueous $ErCl_3$ solutions by Luo et al. [39].

XRFNTR provides complementary information to XRR by enabling element-specific detection of ions near the interface. As with XRR, the analysis is based on modeling the depth-dependent scattering length density (SLD), but here the signal arises from the fluorescence emitted by specific elements. The element-specific fluorescence spectrum allows the interfacial distribution to be determined for individual ion species, enabling a direct quantification of their enrichment or depletion at the liquid surface.

Using the laser pump - X-ray probe setup [40] at the LISA diffractometer [41] at P08, PETRA III, DESY [42] as shown in Fig. 1, we were able to collect X-ray reflectivity data up to a wave vector normal to the surface of $q_z = 0.8\,\text{Å}^{-1}$. *In situ* UV laser radiation with 258 nm was used to excite the halides electronically. This unique experimental setup enables us to directly track UV-induced changes in surface ion distribution, offering valuable insight into surface processes relevant to atmospheric chemistry. Within this study we focused on the equilibrium state in the absence of laser

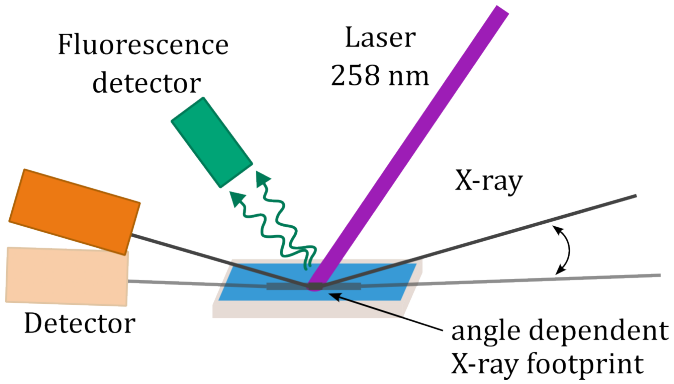

Figure 1: Schematic of the laser pump and X-ray reflectivity and X-ray fluorescence measurement setup for two incident angles and with the corresponding X-ray and laser footprint (not true-to-scale) at the LISA diffractometer [41, 40] at P08 [42], Petra III, DESY.

irradiation and on the average steady-state behavior during pulsed laser irradiation. The latter provides important preliminary data for future pump-probe studies of these interfaces with our setup.

2. Material and methods

2.1. Sample preparation

NaI (99.99%) was purchased from Sigma Aldrich. The salt was baked for >200 °C for more than 24 h to eliminate any possible organic contamination and moistures. 18 MΩ Milli-Q water (Elga Purelab Ultra Analytic, 18 MΩ cm^{-1}) was used to prepare the different salt concentrations shortly before the measurements. The error for all M concentrations is estimated to be ±0.2 M. All NaI solutions were stored at room temperature and in the dark to avoid production of triiodide.

2.2. X-ray reflectivity (XRR)

All X-ray reflectivity measurements were performed at the liquid diffractometer LISA [41] at P08, PETRA III, DESY [42]. The measurements were carried out at an energy of 18 keV with a bandwidth of $\Delta E/E = 1 \times 10^{-4}$. The beam size was trimmed to 70 µm vertical × 200 µm horizontal. Surface-normal wave vectors in the range of 0.018 Å^{-1} to 1 Å^{-1} were covered. A 195 × 40 mm PCTFE trough was used to hold the liquid samples. An area detector (Lambda 750k GaAs, pixel size 55 µm × 55 µm, XSpectrum GmbH) was positioned 1.098 m from the pivot point of the diffractometer where the sample is centered at.

For the extraction of XRR curves from the raw detector images, the region of interest (ROI) was set to 2.2 mm × 1.21 mm. This size was chosen to accommodate peak broadening upon laser irradiation while maintaining consistent ROI dimensions throughout the data set. Further details on data extraction are provided in Appendix A.1.

We used the Python package `refnx` version 0.1.47 [43] to analyze the X-ray reflectivity data using the Parratt algorithm [44]. A brief summary of the theoretical background relevant for XRR analysis is given in Appendix A.2. For a comprehensive introduction to the principles of X-ray reflectivity, see [45, 46]. The following model was fitted to the measured reflectivity curves to extract structural and interfacial properties:

No-layer model: This model describes air as a superphase with a fixed SLD of $0\,\text{Å}^{-2}$ and the salt solution as a subphase with a finite SLD representing the bulk. The free parameters - SLD, interface roughness, and a scaling factor — were fitted to analyze the bulk properties and surface structure.

Parameter uncertainties were estimated using a Markov Chain Monte Carlo approach (see Appendix A.3 for details). The fit was limited to $q_z < 0.6\,\text{Å}^{-1}$. At higher q_z, the decreasing q_{xy}-resolution (see Eq. A.3) leads to specular peak shape changes, as capillary waves scatter radiation away from the specular condition. Once these changes exceed the experimental uncertainty, this limits the applicability of the single roughness model (compare Eq. A.2) [47].

Following the FAIR principles, we supply not only the extracted XRR data but also the raw data including relevant metadata, the flatfield and pixel mask, and our Python script for the data extraction (see Sect. 9 for details).

2.3. X-ray fluorescence near total reflection (XRFNTR)

A XR100 FAST-SDD Amptek detector was used for the X-ray fluorescence measurements. The fluorescence signal was measured for X-ray incident angles between 0.016° to 0.13° probing a sample volume from 5 nm to 21 µm (see Supplementary Figure B.6). Calibration of the energy channels was done with a reference measurement on air. For this, the sample was moved out of the beam and the sample cell was filled with normal air atmosphere. As Ar is the only atom in air, that gives an observable X-ray fluorescence signal, its peak and the elastic peak can be identified and based on their position, the energy-channels conversion is calibrated. The signal intensity was normalised to the intensity of the elastic peak signal by fitting the Compton and elastic peaks with Gaussian functions. Assignment of the fluorescence peaks to the K- and L-shell emission lines was done by comparison with literature values [48] and is shown in Figure 3. The intensity of the fluorescence peaks is proportional to the

incoming beam intensity and depends on the angle of incidence because the incoming wave under grazing incidence interferes with the reflected wave at the interface. In this cross section, standing waves develop and the electromagnetic field is defined by the interference pattern, which dependents on the incident angle. Therefore, the angle dependent fluorescence signal allows the analysis of the depth-profile of layered structures. [35, 49, 37, 50] The intensity of a buried layer I_{L} inside the bulk at a distance z from the interface and with the thickness d can be calculated with [50]

$$I_{\mathrm{L}}(\alpha, z) = I_{\mathrm{n}}\,(1 - R(\alpha)) \cdot \frac{\alpha}{d} \cdot e^{-z/\Lambda(\alpha)} \cdot \left(1 - e^{-d/\Lambda(\alpha)}\right) \tag{1}$$

together with the Fresnel reflectivity $R(\alpha)$ and the penetration depth $\Lambda(\alpha)$

$$\begin{aligned} R(\alpha) &= \left|\frac{\alpha - \alpha\prime}{\alpha + \alpha\prime}\right|^2 \\ \Lambda &= \frac{\lambda}{2\sqrt{2}\pi \cdot \sqrt{\sqrt{(\alpha^2 - \alpha_c^2)^2 + 4\beta^2} - (\alpha^2 - \alpha_c^2)}} \end{aligned} \tag{2}$$

where λ is the wavelength of the incoming beam, α_{c} the critical angle and β the refractive index. For the analysis of the fluorescence signals Eq. 1 is fitted to the data and the SLD values is calculated from the derived critical angle α_{c}. All fluorescence measurements were done using the liquid cell described in [40] with a $40 \times 90\,\mathrm{mm}$ PCTFE trough. The cell was flushed with wet nitrogen gas to prevent evaporation of the liquid.

2.4. Laser specifications

We use pulsed UV laser radiation to excite the halides electronically. The Pharos femtosecond pulsed laser from Light Conversion available at P08, Petra III was operated at a repetition rate of 130.12 kHz and used as pump for the additional higher harmonic generator (Hiro module from Light Conversion) to generate the forth harmonics with a wavelength of 258 nm and pulse length of 251 fs. The setup is described in detail in [40]. With the external controllable Pockels cell of the laser unit the pulse energy was controlled and varied between 0.48 µJ and 6.66 µJ. During the XRR and XRFNTR measurements, the sample was continuously illuminated with the pulsed laser.

The gaussian laser spot profile was measured with the beam profiling camera beamage-4M from gentec-eo at the beginning of the beamtime. The laser spot size was determines to have diameters at full width at half-maximum (FWHM) of $(2.50 \pm 0.09) \times (2.36 \pm 0.13)$ mm. The elliptical shape originates from the oblique incidence of the laser beam at an angle of 60° relative to the sample surface plane. While the footprint of the laser remains constant, the footprint of the X-ray beam tracing the exited region of

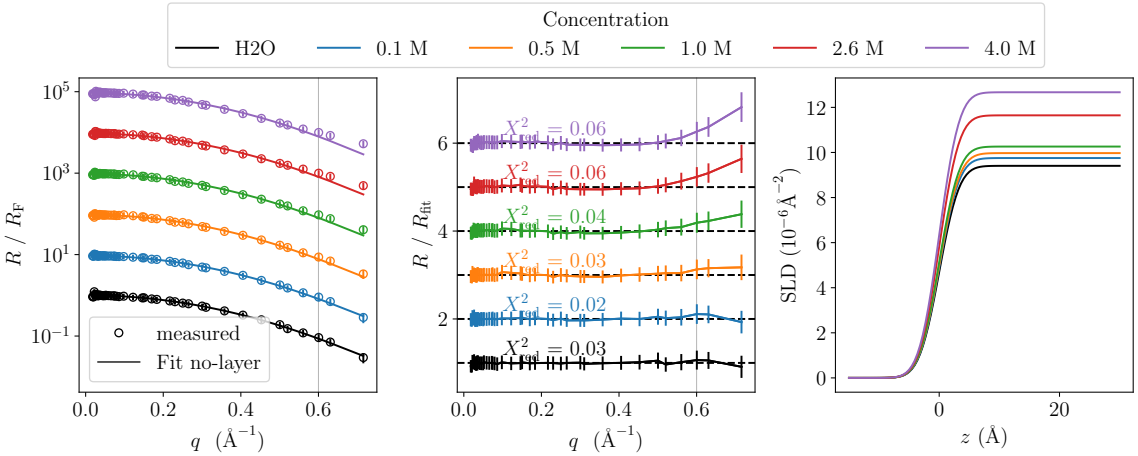

Figure 2: XRR of NaI solutions with concentrations stated in the upper legend. *Left:* Measured reflectivity curves normalized by the Fresnel reflectivity calculated for an ideal, perfectly smooth interface ($\sigma = 0\,\text{Å}$) and using the SLD of the corresponding best-fit result for each concentration. The curves are vertically offset by factors of 10 for clarity. Solid lines show the best-fit results using the no-layer model. The horizontal line indicates the maximum wave vector used in the fitting. *Middle:* Measured reflectivity curves divided by their respective best-fit curves from the no-layer model. The curves are shifted vertically by integers for clarity. *Right:* SLD profiles corresponding to the best-fit no-layer model for each concentration.

the sample depends on the wave vector q_z. At the lowest angle with $q = 0.018\,\text{Å}^{-1}$ (corresponds to an incident angle $\alpha \approx 0.06°$), the X-ray footprint is significantly larger with 70.9 mm. It decreases down to 2.13 mm for $q = 0.6\,\text{Å}^{-1}$ ($\alpha \approx 1.89°$). The point where both footprints are equal is at $q = 0.511\,\text{Å}^{-1}$.

3. Results

3.1. Near surface ion distribution

We first investigate the near-surface ion distribution of aqueous NaI solutions with concentrations ranging from 0.1 M to 4 M. To this end, we examine the XRR measurements presented in Figure 2. The best-fit results are summerized in Table 1.

The left panel of Figure 2 shows the measured reflectivity curves for different NaI concentrations, normalized by the Fresnel reflectivity for a flat surface. This normalization highlights deviations from ideal interfacial behavior. The measured curves do not exhibit any oscillatory features, known as Kiessig fringes, which arise from interference between reflections at different thin surface layers. The absence of such features

	XRR			XRFNTR					
Conc. (M)	SLD (10^{-6}Å^{-2})	Roughness (Å)	X^2_{red}	α_c (Å)	SLD (10^{-6}Å^{-2})	d (nm)	β (10^{-8})	X^2_{red}	expected bulk SLD (10^{-6}Å^{-2})
H_2O	9.41 ± 0.08	2.62 ± 0.06	0.03						9.41
0.10	9.75 ± 0.14	2.62 ± 0.06	0.02	0.0690 ± 0.0002	9.61 ± 0.03	460 ± 50	1.5 ± 0.2	0.000	9.47
0.50	9.97 ± 0.15	2.65 ± 0.06	0.03	0.0703 ± 0.0002	9.96 ± 0.05	390 ± 50	2.2 ± 0.3	0.001	9.70
1.00	10.26 ± 0.16	2.64 ± 0.06	0.04	0.0715 ± 0.0002	10.31 ± 0.06	430 ± 60	2.4 ± 0.3	0.005	9.98
2.60	11.65 ± 0.15	2.62 ± 0.06	0.05	0.0760 ± 0.0002	11.66 ± 0.04	360 ± 30	2.9 ± 0.2	0.001	10.96
4.00	12.67 ± 0.16	2.63 ± 0.06	0.06	0.0792 ± 0.0002	12.65 ± 0.06	290 ± 30	3.6 ± 0.3	0.003	11.79

Table 1: Summary of the best-fit parameters obtained from XRR and XFNTR measurements (without laser illumination) for NaI solutions at different concentrations. For XRR, the fitted parameters include the scattering length density (SLD) and surface roughness. For XFNTR, the yields the critical angle α_c, SLD, layer thickness d, and absorption parameter β. The final column lists the expected bulk SLD.

indicates that the NaI solutions do not form well-defined interfacial layers within the sensitivity of the measurement.

This observation is consistent with the no-layer model, which assumes a single, homogeneous liquid without additional surface layering. The corresponding best-fit curves are shown as solid lines in the left panel of Figure 2 and closely follow the measured reflectivity data across all concentrations. To better visualize any deviations, the middle panel shows the ratio of the measured reflectivity to the best-fit result. The agreement remains excellent, with reduced chi-squared values well below 0.1 (see also Table 1). No oscillations indicative of interference effects are observed here either. Only at wave vectors beyond $q_z \approx 0.6\,\text{Å}^{-1}$ do systematic deviations become apparent. These may result from the q_z-dependence of the resolution (Eq. A.3), which affects the effective roughness extracted from the reflectivity data (Eq. A.2). This supports the assumption that resolution effects can be neglected up to $q_z \approx 0.6\,\text{Å}^{-1}$. Beyond this range, the deviations become large enough to be significant, and the roughness may appear reduced — consistent with the flattening of the reflectivity curves at high q_z. Notably, the magnitude of these deviations increases with NaI concentration, which cannot be explained by resolution effects alone.

The right panel of Figure 2 shows the SLD profiles corresponding to the best-fit reflectivities. All profiles exhibit a comparable width at the air–liquid transition (around $z = 0$), indicating similar interfacial roughness for all concentrations (see also Table 1). For pure H_2O, the best-fit yields a roughness of 2.62 ± 0.06 Å, and the values obtained for the NaI solutions range from 2.62 ± 0.06 Å to 2.65 ± 0.06 Å. All values agree within their uncertainties, indicating that the interfacial roughness does not depend on the salt concentration.

As expected, the bulk SLD increases with increasing NaI concentration. The ex-

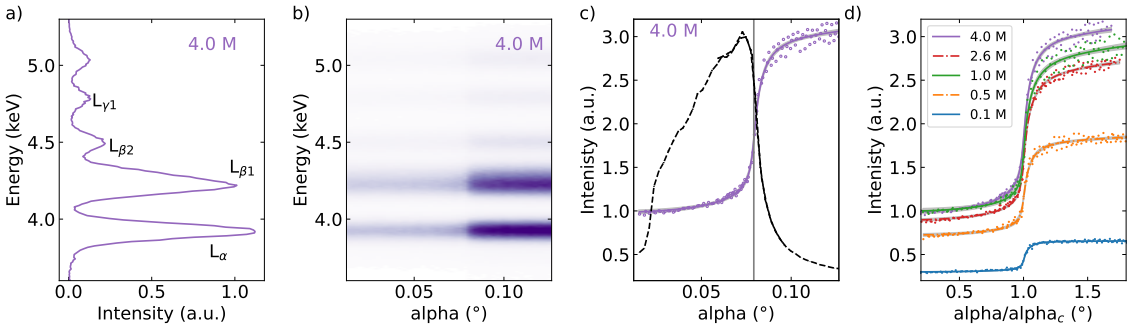

Figure 3: X-ray fluorescence near total reflection data taken from aqueous NaI solution with different concentrations without the laser. a) Fluorescence spectrum for the 4.0 M solution with the indication of the emission lines at an incident angle alpha of 0.066°. b) Colormap presenting the angle-depended spectra. c) Reflected intensity of the X-ray (black) and integrated intensity of the iodine L peaks for the 4.0 M NaI solution together with the fit of the fluorescence signal from a buried layer. The critical angle alpha$_c$ is marked as gray line. d) Integrated intensity of the iodine L_α peak and its fit for multiple concentrations against the incident angle alpha divided by the critical angle alpha$_c$ for each concentration. For the fits, the 95% confidence interval is shown in grey.

pected bulk SLDs for the NaI solutions were calculated for the given concentrations using the Neutron Activation and Scattering Calculator[2] and are listed in the last column of Table 1. Our best-fit result for pure H_2O, $9.41 \pm 0.08 \times 10^{-6}$ Å^{-2}, agrees well with the expected value. In contrast, for all NaI solutions, the fitted SLDs are consistently higher than the corresponding calculated bulk values (see Table 1).

While the XRR measurements provide valuable insights into the overall electron density profile and layering of the NaI solution, XRFNTR offers complementary, element-specific information by directly probing the spatial distribution of individual ions near the liquid–air interface [51]. This allows a more detailed assessment of the surface enrichment or depletion of specific ionic species. Consequently, in Figure 3d) we show the XRFNTR measurements of the NaI solutions with different concentrations.

In panel a) of Figure 3, we show exemplary the spectrum obtained for a NaI solution with a concentration of 4.0 M. Similar to the spectra obtained for the other concentrations, it shows distinct features with enhanced signals observed at 3.92 keV, 4.24 keV, 4.50 keV and 4.79 keV ± 0.01 keV corresponding to the L_α, $L_{\beta 1}$, $L_{\beta 2}$ and $L_{\gamma 1}$ iodine emission lines respectively. For comparison, the intensities of the L_α line at different incident angle α are compared for the NaI solutions with different concentra-

[2]https://www.ncnr.nist.gov/resources/activation/

tion in Figure 3, panel d), showing an increase of the signal intensity with increasing NaI concentration reflecting the higher ion density at the interface and in the bulk. In particular, the intensity rises significantly from 0.1 M to 0.5 M and further to 1 M, but shows only weak increase at higher concentrations of 2.6 M and 4.0 M. This effect is unlikely due to reaching the saturation limit of NaI in solution, as the concentrations used are well below the known solubility of NaI at room temperature.

XRFNTR measurements enable depth-resolved probing of the sample, as the penetration depth of the incident X-rays depends on the angle of incidence (see Figure B.6). This penetration depth corresponds to the 1/e decay length of the X-ray intensity within the sample. At higher incident angles, particularly in the bright region on the right-hand side of the spectrum, the measurements are sensitive to the bulk of the solution, with the X-rays penetrating up to 21 µm deep into the sample [52, 33]. The sharp increase in intensity observed around 0.069° corresponds to the critical angle for total external reflection. Below this angle, total reflection of the incident X-rays occurs resulting in a penetration of only a few nanometer into the sample, making the signal highly surface sensitive. The shape of the angle dependent intensity rise allows conclusions on the surface near structure. The typical shape of a flat and infinite thick substrate shows a step like increase in intensity at the critical angle and an approximately linear increase at angles larger than the critical angle. Meanwhile, any residuals or layers at the interface affect the shape and sharp peak-like or periodic oscillations in the intensity profile can be observed [37, 36, 50].

Analyzing the measured fluorescence signals shown in Figure 3d), a S-like shape of the intensity profile is observed and the profile was fitted using Eq. 1 for a layer directly at the interface ($z = 0$) and all fit values are listed in Tab. 1.

From the fit, the critical angle α_c and the thickness of the layer is derived directly. The critical angle α_c increases with increasing concentration and the calculated SLD values correspond well to the SLD values derived from the XRR measurements (see Fig. 5). The determined thicknesses of the layer d decrease from 460 ± 50 nm to 290 ± 30 nm with increasing concentration. These fitted layer thicknesses are about half of the maximum penetration depths Λ of about 1 µm and 0.4 µm for the 0.1 M and 4 M, respectively, concentrated aqueous NaI solutions. Therefore, this fitted thickness could origin from the dimension of the probed volume rather than an actual layer forming at the interface. Moreover, the simulated dimension of the ion enriched layer is on the Å length scale[11, 53] and the fitted layer thickness is by a factor 1000 larger.

3.2. Laser induced dynamics at the interface

In order to understand the effect of UV radiation on the surface structure of halide solutions, we have carried out XRR measurements under continuous *in situ* UV laser

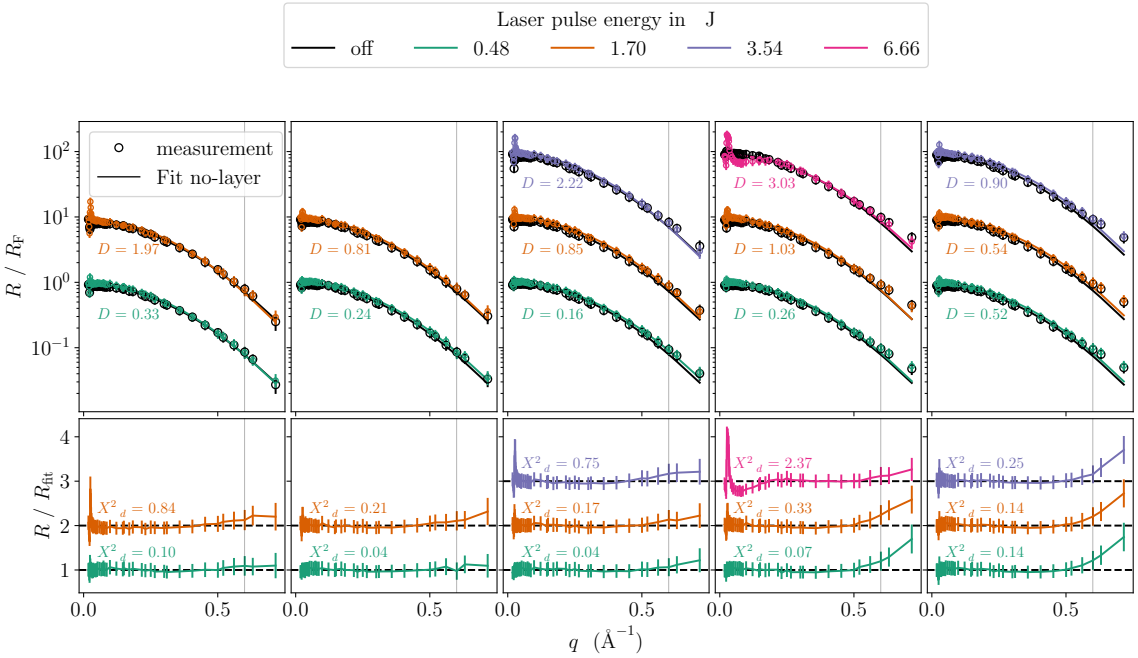

Figure 4: Overview of XRR measurements for different laser pulse energies, as indicated in the upper legend. The salt concentration increases from left to right, with each column labeled accordingly. *Upper row:* Measured reflectivity curves (circles) and no-layer best fits (solid lines) for different laser powers. The reflectivity curves measured with the UV-laser switched on are shifted vertically by factors of 100 for clarity. For each of the scaled curves, the measured reflectivity curve and the best fit for the measurement with the laser switched off are shown in black for direct comparison. *Lower row:* Ratios of measured reflectivity to the respective best-fit curves from the no-layer model, shown for each laser power. Curves are vertically offset by integer values for clarity. In all figure panels, the vertical dashed line marks the maximum wave vector of $0.6\,\text{Å}^{-1}$ included in the fitting.

illumination with different pulse energies. The resulting reflectivity curves are shown in Figure 4.

The upper row of Figure 4 shows the measured reflectivity curves for various NaI concentrations at increasing laser pulse energies. Deviations between the reflectivity curves recorded with the laser switched on and off are visible, particularly near the critical angle. To quantify these deviations, we introduce the metric

$$D = \langle (R_{\text{off}} - R_{\text{on}})^2 / (\delta R_{\text{off}} \delta R_{\text{on}}) \rangle, \tag{3}$$

that is the mean squared deviation from the reflectivities R_{off} and R_{on} in relation to the square error, which is calculated from the product of both measurement uncertainties

δR_{off} and δR_{on}. A value less than 1 indicates that the deviation is within the error bars on average, while a value greater than 1 suggests a significant deviation. For concentrations of 0.1 M, 1 M and 2.6 M, the metric exceeds 1 at higher laser energies, indicating that the observed differences cannot be explained by statistical uncertainty alone.

The most pronounced deviation occurs at 2.6 M for the highest laser pulse energy of 6.66 µJ. Here, a sharp peak near the critical angle is followed by a broader dip. This characteristic shape may indicate a distortion of the liquid surface, causing the reflected beam to originate from regions with slightly different surface inclinations. As a result, the reflectivity curve around the wave vector corresponding to the critical angle is effectively smeared out.

Despite these deviations, no oscillations such as Kiessig fringes are observed in any of the laser-on measurements. This, together with the good agreement between measured reflectivities and the no-layer model (see lower row of Figure 4), suggests that no well-defined interfacial layer forms even under UV illumination. The reduced chi-squared values remain below 0.84 in all cases, except for the most extreme condition (2.6 M, 6.66 µJ), where a value of 2.37 indicates a significant mismatch.

As in the laser-off measurements, deviations between fit and data increase beyond $q_z \approx 0.6\,\text{Å}^{-1}$, with the effect becoming more pronounced at higher concentrations.

Figure 5 summarizes the best-fit results for the SLD (top) and interfacial roughness (bottom) obtained from the XRR measurements at different laser pulse energies using the no-layer model.

For pure water, the SLD remains unaffected by laser illumination across the entire range of pulse energies. In contrast, for the NaI solutions, the SLD increases with laser pulse energy. This effect becomes significant above 1.7 µJ. A notable exception occurs at 2.6,M and 6.66 µJ, where the fitted SLD appears to agree with the laser-off value. However, this agreement should be interpreted with caution. The high reduced chi-squared value of 2.37 indicates that our model fails to adequately describe the measured data in this case. The uncertainty estimate provided by the MCMC sampling reflects the parameter distribution under the assumption that the model is valid. It does not account for model inadequacy.

The extracted interfacial roughness shows no systematic variation with laser illumination and remains constant within the errorbars across all concentrations and laser conditions. This is particularly noteworthy in light of the distortions observed in the reflectivity curves at high laser energies, which might result from surface deformation. If such deformation were present, one would expect an increase in the apparent roughness due to contributions from a broader distribution of surface inclinations.

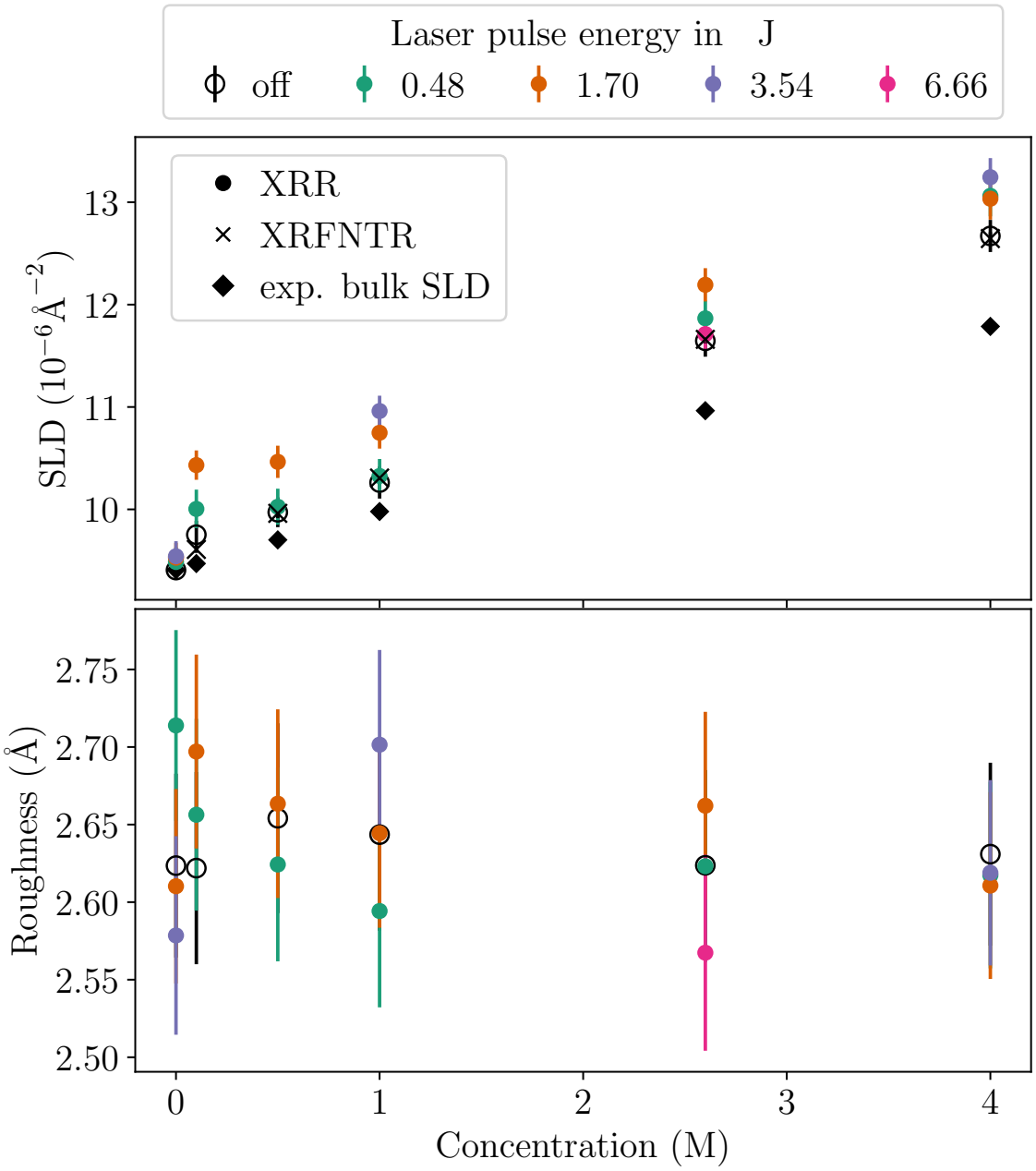

Figure 5: Summary of SLD (top) and interfacial roughness (bottom) as a function of NaI concentration from XRR and XFNTR measurements. The values shown represent the best-fit results obtained using the no-layer model. XRR data are shown for different laser pulse energies, including the laser-off condition, while XFNTR results were obtained without laser illumination. The expected bulk SLD values are shown as a reference.

4. Discussion

4.1. Near surface ion distribution

We begin our discussion of the interfacial structure by analyzing the scattering length density obtained from both XRR and XRFNTR measurements. The SLD values derived from both techniques are in very good agreement (compare Figure 5 and Table 1). For pure water, the SLD obtained from XRR is $9.41 \pm 0.08 \times 10^{-6}$ Å^{-2}, which matches the expected bulk value of 9.41×10^{-6} Å^{-2}.

In contrast, for all investigated NaI solutions, the measured SLD values are higher than expected based on bulk composition. A plausible explanation is the enrichment of ions at the interface. Theoretical studies have suggested that larger and more polarizable anions like I^- are expected to accumulate at the surface, enhancing the local electron density. Jungwirth and Tobias [11] reported molecular dynamics simulations of a 1.2 M NaI solution showing a pronounced interfacial structuring: I^- ions were enriched by a factor of 2.9 in a narrow layer near the interface, while slightly depleted just below that. In the same sub-surface region, an enrichment of Na^+ ions by a factor of $\sim$2 was observed.

Although we do not observe a well-defined layering in our XRR data, our measurements are particularly sensitive to the SLD of the interface. Even a thin surface layer with elevated ion concentrations could therefore result in a significantly higher interfacial SLD than expected from the bulk. This is consistent with our findings.

Fitting the XRR measurements, we obtain the total surface roughness $\sigma = \sqrt{\sigma_0^2 + \sigma_c^2}$, which consists of the intrinsic roughness σ_0 and the capillary wave roughness σ_c (Eq. A.2). The total roughness for different laser powers is plotted against the concentration of the aqueous NaI solution at the bottom of Figure 5. For pure water, we obtain a roughness of $\sigma = 2.62 \pm 0.06$ Å. With a capillary wave roughness of $\sigma_c = 2.59$ Å calculated from Eq. A.2, the intrinsic roughness results to $\sigma_0 = 0.40 \pm 0.16$ Å, which aligns with previous measurements of the intrinsic roughness of water [54].

With increasing NaI concentration, the total roughness remains constant within the error bars for the reflectivities measured with the laser off (black circles). The surface tension is expected to increase from 72.8 mN m^{-1} for pure water [55] to about 77 mN m^{-1} for an NaI solution at a concentration of 4 M [56]. Following Eq. A.2, this would imply a decrease in the capillary wave roughness by $\Delta\sigma_c = 0.08$ Å, resulting in $\sigma_c = 2.51$ Å. Given the total roughness of 2.62 ± 0.06 Å, this suggests a larger intrinsic roughness of $\sigma_0 = 0.75 \pm 0.11$ Å for the 4 M NaI solution compared to pure water.

4.2. Laser induced dynamics at the interface

A novel aspect of our study is the impact of UV irradiation on ion distribution at the liquid-air interface. To assess the potential influence of the 258 nm laser irradiation on

the interfacial properties of the NaI solutions, we consider several possible mechanisms: (1) laser-induced deformation of the interface, (2) local heating, (3) the influence of the laser's electric field, and (4) excitation or ionization. Additionally, we discuss implications of the spatial mismatch between the footprints of the laser and the X-ray probe beam.

Surface deformation. Laser excitation can lead to a deformation of the liquid surface through various mechanisms, including thermal expansion, evaporation, ablation, photon pressure, and local changes in surface tension. Warias et al. [40] reported the formation of a dip at the liquid surface under UV laser irradiation for both water and NaI solutions. In our experiments, this deformation manifests as a broadening of the specular peak, visible in the detector images as well as in the reflectivity curves. Despite this observable dip, we do not detect any significant change in SLD or interfacial roughness for pure water.

Temperature increase. UV laser irradiation can locally heat the surface, potentially increasing thermal capillary waves and roughness. However, we do not observe a significant change in roughness upon laser excitation. One possible explanation is a compensation between competing effects: on the one hand, increased temperature promotes surface roughening; on the other hand, increased surface enrichment of ions could raise the surface tension, suppressing thermal fluctuations. The balance of these effects may result in an unchanged effective roughness.

Electric field effects. The electric field of the laser pulse could exert a ponderomotive force on ions during the pulse, potentially displacing them from the laser-irradiated region. This effect would result in a decrease in interfacial SLD, which is not observed. Hence, if present, the ponderomotive effect does not dominate the interfacial ion distribution under our experimental conditions.

Ionization. The laser, with a wavelength of 258 nm (corresponding to 4.8 eV), provides sufficient photon energy to remove electrons from I^- ions (electron affinity of iodine is 3.06 eV). Additionally, water molecules (ionization energy 12.6 eV) could undergo multiphoton ionization under sufficiently intense laser excitation. The resulting free electrons have a greater X-ray scattering length than bound electrons, which could contribute to the observed increase in SLD upon laser excitation.

Mismatch of laser and X-ray footprint. A significant consideration is the spatial mismatch between the laser and X-ray footprints. While the size of the laser footprint is 2.5 mm, the X-ray footprint varies with incident angle, ranging from 70.9 mm at low q_z to 2.13 mm at the maximum considered wave vector (0.6 $Å^{-1}$). The footprints match

only at $q_z \approx 0.511$ Å^{-1}. Therefore, most of the X-ray signal integrates over both laser-illuminated and unperturbed regions. This implies that the laser-induced effects on the interfacial structure must be locally more pronounced than the average effect observed in the reflectivity signal.

5. Conclusion

In this study, we investigated the ion distribution at the liquid-air interface of aqueous NaI solutions using complementary X-ray reflectivity (XRR) and X-ray fluorescence near total reflection (XRFNTR) techniques. Our results build a basis for understanding the behavior of ions at interfaces and their potential impacts on fundamental atmospheric and surface chemistry.

Our measurements reveal that, across the considered range of concentrations 0.1 M to 4 M at room temperature, no well-defined layering forms at the liquid–air interface. Instead, the interface can be accurately described by a homogeneous no-layer model.

The complementary XRR and XRFNTR measurements provide consistent results for the scattering length density (SLD) of NaI solutions. The SLD of the NaI solutions increases linearly with concentration, indicating a rise in electron density at the interface and in the bulk as more NaI is dissolved. The determined SLD values the expected bulk values for all NaI solutions, indicating an enrichment of ions. This observation aligns with theoretical predictions and molecular dynamics simulations suggesting enhanced surface concentrations of polarizable anions.

A novel aspect of our work was the exploration of the effect of UV laser irradiation on the ion distribution and surface roughness. Upon UV laser illumination, we observe deviations in the reflectivity curves, particularly at higher pulse energies. The SLD increases, however, no evidence for the formation of a distinct surface layer under irradiation is found. The increase in interfacial SLD may point to photoinduced ionization processes. Despite these changes, the interfacial roughness remains largely unaffected by either salt concentration or laser excitation.

In conclusion, our study provides valuable insights into the behavior of ions at the liquid-air interface under UV irradiation. The observed consistency between complementary measurement techniques, as well as the alignment of our results with theoretical expectations, enhances our understanding of surface properties of ion-containing liquids. Yet, more sophisticated measurements are required to fully elucidate the effects of laser excitation, particularly to determine the precise role of ion enrichment and surface roughness modifications under UV irradiation.

6. Acknowledgements

We acknowledge DESY (Hamburg, Germany), a member of the Helmholtz Association HGF, for the provision of experimental facilities. This research was carried out at PETRA III beamline P08 via proposal II-20210020. We would like to thank René Kirchhof for assistance at P08 and Milena Lippman for chemistry lab support.

7. Funding sources

We acknowledge funding from Bundesministerium fuer Bildung und Forschung, ErUM-Pro (grant No. BMBF05K19FK2 and BMBF05K22FK3) for the LISA instrument and laser setup. We further acknowledge finacial support from the Center for Molecular Water Science (CMWS). This publication was written in the context of the work of the consortium DAPHNE4NFDI in association with the German National Research Data Infrastructure (NFDI) e.V. NFDI is financed by the Federal Republic of Germany and the 16 federal states and the consortium is funded by the Deutsche Forschungsgemeinschaft (DFG, German Research Foundation) - project number 460248799. The authors would like to thank for the funding and support. Furthermore, thanks go to all institutions and actors who are committed to the association and its goals.

8. Declaration of generative AI and AI-assisted technologies in the writing process

During the preparation of this work, the authors used ChatGPT to improve phrasings and the clarity of the text, and DeepL to translate parts of the text and ensure accurate translation. After using these tools, the authors reviewed and edited the content as needed and take full responsibility for the content of the published article.

9. Data Availability

In accordance with the FAIR principles, raw data, including metadata, extracted data, fit results, as well as extraction and analysis scripts, are available at: [Link to be provided later].

References

[1] J. H. Hu, Q. Shi, P. Davidovits, D. R. Worsnop, M. S. Zahniser, C. E. Kolb, Reactive uptake of cl2(g) and br2(g) by aqueous surfaces as a function of br- and

i- ion concentration: The effect of chemical reaction at the interface, The Journal of Physical Chemistry 99 (21) (1995) 8768–8776. doi:10.1021/j100021a050.

[2] H. Herrmann, Z. Majdik, B. Ervens, D. Weise, Halogen production from aqueous tropospheric particles, Chemosphere 52 (2) (2003) 485–502. doi:10.1016/S0045-6535(03)00202-9.
URL https://www.sciencedirect.com/science/article/pii/S0045653503002029

[3] C. A. Cuevas, R. P. Fernandez, D. E. Kinnison, Q. Li, J.-F. Lamarque, T. Trabelsi, J. S. Francisco, S. Solomon, A. Saiz-Lopez, The influence of iodine on the antarctic stratospheric ozone hole, Proceedings of the National Academy of Sciences 119 (7) (2022) e2110864119. doi:10.1073/pnas.2110864119.

[4] E. M. Knipping, M. J. Lakin, K. L. Foster, P. Jungwirth, D. J. Tobias, R. B. Gerber, D. Dabdub, B. J. Finlayson-Pitts, Experiments and simulations of ion-enhanced interfacial chemistry on aqueous nacl aerosols, Science 288 (5464) (2000) 301–306. doi:10.1126/science.288.5464.301.

[5] L. Magi, F. Schweitzer, C. Pallares, S. Cherif, P. Mirabel, C. George, Investigation of the uptake rate of ozone and methyl hydroperoxide by water surfaces, The Journal of Physical Chemistry A 101 (27) (1997) 4943–4949. doi:10.1021/jp970646m.

[6] V. S. J. Craig, B. W. Ninham, R. M. Pashley, Effect of electrolytes on bubble coalescence, Nature 364 (6435) (1993) 317–319. doi:10.1038/364317a0.
URL https://www.nature.com/articles/364317a0

[7] V. S. J. Craig, B. W. Ninham, R. M. Pashley, Effect of electrolytes on bubble coalescence, Nature 364 (6435) (1993) 317–319. doi:10.1038/364317a0.
URL https://www.nature.com/articles/364317a0

[8] P. K. Weissenborn, R. J. Pugh, Surface tension and bubble coalescence phenomena of aqueous solutions of electrolytes, Langmuir 11 (5) (1995) 1422–1426. doi:10.1021/la00005a002.

[9] S. Marčelja, Short-range forces in surface and bubble interaction, Current Opinion in Colloid & Interface Science 9 (1-2) (2004) 165–167. doi:10.1016/j.cocis.2004.05.024.
URL https://www.sciencedirect.com/science/article/pii/S1359029404000524

[10] V. S. Craig, Bubble coalescence and specific-ion effects, Current Opinion in Colloid & Interface Science 9 (1-2) (2004) 178–184. doi:10.1016/j.cocis.2004.06.002. URL https://www.sciencedirect.com/science/article/pii/S1359029404000627

[11] P. Jungwirth, D. J. Tobias, Ions at the air/water interface, The Journal of Physical Chemistry B 106 (25) (2002) 6361–6373. doi:10.1021/jp020242g.

[12] M. H. Cheng, K. M. Callahan, A. M. Margarella, D. J. Tobias, J. C. Hemminger, H. Bluhm, M. J. Krisch, Ambient pressure x-ray photoelectron spectroscopy and molecular dynamics simulation studies of liquid/vapor interfaces of aqueous nacl, rbcl, and rbbr solutions, The Journal of Physical Chemistry C 116 (7) (2012) 4545–4555. doi:10.1021/jp205500h.

[13] X. Sun, C. D. Wick, L. X. Dang, Computational studies of aqueous interfaces of srcl(2) salt solutions, The journal of physical chemistry. B 113 (42) (2009) 13993–13997. doi:10.1021/jp9079525.

[14] Y. Wang, S. Sinha, P. R. Desai, H. Jing, S. Das, Ion at air-water interface enhances capillary wave fluctuations: Energetics of ion adsorption, Journal of the American Chemical Society 140 (40) (2018) 12853–12861. doi:10.1021/jacs.8b06205.

[15] Y. Levin, A. P. dos Santos, A. Diehl, Ions at the air-water interface: an end to a hundred-year-old mystery?, Physical review letters 103 (25) (2009) 257802. doi:10.1103/PhysRevLett.103.257802.

[16] E. A. Raymond, G. L. Richmond, Probing the molecular structure and bonding of the surface of aqueous salt solutions, The Journal of Physical Chemistry B 108 (16) (2004) 5051–5059. doi:10.1021/jp037725k.

[17] D. Liu, G. Ma, L. M. Levering, H. C. Allen, Vibrational spectroscopy of aqueous sodium halide solutions and air−liquid interfaces: Observation of increased interfacial depth, The Journal of Physical Chemistry B 108 (7) (2004) 2252–2260. doi:10.1021/jp036169r.

[18] C. Tian, S. J. Byrnes, H.-L. Han, Y. R. Shen, Surface propensities of atmospherically relevant ions in salt solutions revealed by phase-sensitive sum frequency vibrational spectroscopy, The Journal of Physical Chemistry Letters 2 (15) (2011) 1946–1949. doi:10.1021/jz200791c.

[19] L. Piatkowski, Z. Zhang, E. H. G. Backus, H. J. Bakker, M. Bonn, Extreme surface propensity of halide ions in water, Nature Communications 5 (1) (2014) 4083. doi:10.1038/ncomms5083.
URL https://www.nature.com/articles/ncomms5083

[20] S. Ghosal, J. C. Hemminger, H. Bluhm, B. S. Mun, E. L. D. Hebenstreit, G. Ketteler, D. F. Ogletree, F. G. Requejo, M. Salmeron, Electron spectroscopy of aqueous solution interfaces reveals surface enhancement of halides, Science 307 (5709) (2005) 563–566. doi:10.1126/science.1106525.

[21] E. Sloutskin, J. Baumert, B. M. Ocko, I. Kuzmenko, A. Checco, L. Tamam, Ofer, E., Gog, T., O. Gang, M. Deutsch, The surface structure of concentrated aqueous salt solutions, Journal of Chemical Physics 126 (054704) (2007).

[22] P. Jungwirth, D. J. Tobias, Molecular structure of salt solutions: A new view of the interface with implications for heterogeneous atmospheric chemistry, The Journal of Physical Chemistry B 105 (43) (2001) 10468–10472. doi:10.1021/jp012750g.

[23] C. E. Williamson, K. C. Rose, Environmental science. when uv meets fresh water, Science 329 (5992) (2010) 637–639. doi:10.1126/science.1191192.

[24] P. J. Neale, C. E. Williamson, A. T. Banaszak, D.-P. Häder, S. Hylander, R. Ossola, K. C. Rose, S.-Å. Wängberg, R. Zepp, The response of aquatic ecosystems to the interactive effects of stratospheric ozone depletion, uv radiation, and climate change, Photochemical & Photobiological Sciences 22 (5) (2023) 1093–1127. doi:10.1007/s43630-023-00370-z.
URL https://link.springer.com/article/10.1007/s43630-023-00370-z

[25] L. Vanhaelewyn, D. van der Straeten, B. de Coninck, F. Vandenbussche, Ultraviolet radiation from a plant perspective: The plant-microorganism context, Frontiers in plant science 11 (2020) 597642. doi:10.3389/fpls.2020.597642.

[26] T. W. Marin, I. Janik, D. M. Bartels, Ultraviolet charge-transfer-to-solvent spectroscopy of halide and hydroxide ions in subcritical and supercritical water, Physical Chemistry Chemical Physics 21 (44) (2019) 24419–24428. doi:10.1039/C9CP03805A.

[27] D. Bhattacharyya, H. Mizuno, A. M. Rizzuto, Y. Zhang, R. J. Saykally, S. E. Bradforth, New insights into the charge-transfer-to-solvent spectrum of aqueous iodide: Surface versus bulk, The Journal of Physical Chemistry Letters 11 (5) (2020) 1656–1661. doi:10.1021/acs.jpclett.9b03857.

[28] J. Lan, M. Chergui, A. Pasquarello, Dynamics of the charge transfer to solvent process in aqueous iodide, Nature Communications 15 (1) (2024) 2544. doi:10.1038/s41467-024-46772-0.
URL https://www.nature.com/articles/s41467-024-46772-0

[29] M. C. Sauer, R. A. Crowell, I. A. Shkrob, Electron photodetachment from aqueous anions. 1. quantum yields for generation of hydrated electron by 193 and 248 nm laser photoexcitation of miscellaneous inorganic anions, The Journal of Physical Chemistry A 108 (25) (2004) 5490–5502. doi:10.1021/jp049722t.

[30] N. K. Bersenkowitsch, M. Ončák, J. Heller, C. van der Linde, M. K. Beyer, Photodissociation of sodium iodide clusters doped with small hydrocarbons, Chemistry (Weinheim an der Bergstrasse, Germany) 24 (47) (2018) 12433–12443. doi:10.1002/chem.201803017.
URL https://pmc.ncbi.nlm.nih.gov/articles/PMC6120481/

[31] A. M. Prophet, K. Polley, G. J. van Berkel, D. T. Limmer, K. R. Wilson, Iodide oxidation by ozone at the surface of aqueous microdroplets, Chemical Science 15 (2) (2024) 736–756. doi:10.1039/D3SC04254E.
URL https://pubs.rsc.org/en/content/articlehtml/2024/sc/d3sc04254e

[32] P. S. Pershan, M. Schlossman, Liquid surfaces and interfaces: synchrotron x-ray methods, Cambridge University Press, 2012.

[33] J. Als-Nielsen, K. Kjær, X-ray reflectivity and diffraction studies of liquid surfaces and surfactant monolayers, in: Phase Transitions in Soft Condensed Matter, NATO ASI Series, Springer US, Boston, MA, 1990, pp. 113–138. doi:10.1007/978-1-4613-0551-4{\textunderscore}11.
URL https://link.springer.com/chapter/10.1007/978-1-4613-0551-4_11

[34] D. K. de Boer, Influence of the roughness profile on the specular reflectivity of x rays and neutrons, Physical review. B, Condensed matter 49 (9) (1994) 5817–5820. doi:10.1103/PhysRevB.49.5817.

[35] A. Prange, Total reflection x-ray spectrometry: method and applications, Spectrochimica Acta Part B: Atomic Spectroscopy 44 (5) (1989) 437–452. doi:10.1016/0584-8547(89)80049-7.
URL https://www.sciencedirect.com/science/article/pii/0584854789800497

[36] R. Klockenkamper, J. Knoth, A. Prange, H. Schwenke, Total-reflection x-ray fluorescence, Analytical chemistry 64 (23) (1992) 1115A–1123A. doi:10.1021/ac00047a001.

[37] H. Schwenke, R. Gutschke, J. Knoth, M. Kock, Treatment of roughness and concentration gradients in total reflection x-ray fluorescence analysis of surfaces, Applied physics 54 (5) (1992) 460–465. doi:10.1007/BF00324172.
URL https://link.springer.com/article/10.1007/BF00324172

[38] B. M. Murphy, S. Festersen, O. M. Magnussen, The atomic scale structure of liquid metal–electrolyte interfaces, Nanoscale 8 (2016) 13859–13866. doi:10.1039/C6NR01571A.
URL http://dx.doi.org/10.1039/C6NR01571A

[39] G. Luo, W. Bu, M. Mihaylov, I. Kuzmenko, M. L. Schlossman, L. Soderholm, X-ray reflectivity reveals a nonmonotonic ion-density profile perpendicular to the surface of ercl 3 aqueous solutions, The Journal of Physical Chemistry C 117 (37) (2013) 19082–19090. doi:10.1021/jp4067247.

[40] J. E. Warias, L. Petersdorf, S. C. Hövelmann, R. P. Giri, C. Lemke, S. Festersen, M. Greve, P. Mandin, D. LeBideau, F. Bertram, O. M. Magnussen, B. M. Murphy, The laser pump x-ray probe system at lisa p08 petra iii, Journal of synchrotron radiation 31 (Pt 4) (2024) 779–790. doi:10.1107/S1600577524003400.

[41] B. M. Murphy, M. Greve, B. Runge, C. T. Koops, A. Elsen, J. Stettner, O. H. Seeck, O. M. Magnussen, A novel x-ray diffractometer for studies of liquid-liquid interfaces, Journal of synchrotron radiation 21 (Pt 1) (2014) 45–56. doi:10.1107/S1600577513026192.

[42] O. H. Seeck, C. Deiter, K. Pflaum, F. Bertam, A. Beerlink, H. Franz, J. Horbach, H. Schulte-Schrepping, B. M. Murphy, M. Greve, O. Magnussen, The high-resolution diffraction beamline p08 at petra iii, Journal of synchrotron radiation 19 (Pt 1) (2012) 30–38. doi:10.1107/S0909049511047236.

[43] A. R. J. Nelson, S. W. Prescott, *refnx*: neutron and X-ray reflectometry analysis in Python, Journal of Applied Crystallography 52 (1) (2019) 193–200. doi:10.1107/S1600576718017296.
URL https://doi.org/10.1107/S1600576718017296

[44] L. G. Parratt, Surface studies of solids by total reflection of x-rays, Phys. Rev. 95 (1954) 359–369. doi:10.1103/PhysRev.95.359.
URL https://link.aps.org/doi/10.1103/PhysRev.95.359

[45] J. Als-Nielsen, Des McMorrow, Elements of modern X-ray physics, 2nd Edition, Wiley, Hoboken, 2011. doi:10.1002/9781119998365.

[46] J. Daillant, A. Gibaud, X-ray and neutron reflectivity: Principles and applications, 2nd Edition, Vol. 770 of Lecture notes in physics, Springer, Berlin, 2009.
URL https://ebookcentral.proquest.com/lib/kxp/detail.action?docID=3063762

[47] P. S. Pershan, X-ray scattering from liquid surfaces: effect of resolution, The journal of physical chemistry. B 113 (12) (2009) 3639–3646. doi:10.1021/jp806113n.

[48] A. Thompson, D. Attwood, E. Gullikson, M. Howells, K.-J. Kim, J. Kirz, J. Kortright, I. Lindau, Y. Liu, P. Pianetta, Robinson, Arthur, Scofield, James, J. Underwood, G. Williams, H. Winick, X-ray Data Booklet, 3rd Edition, Center for X-ray Optics and Advanced Light Source, Lawrence Berkeley National Laboratory University of California Berkeley, CA 94720, 2009.

[49] D. de Boer, W. W. van den Hoogenhof, Total reflection x-ray fluorescence of single and multiple thin-layer samples, Spectrochimica Acta Part B: Atomic Spectroscopy 46 (10) (1991) 1323–1331. doi:10.1016/0584-8547(91)80181-2.
URL https://www.sciencedirect.com/science/article/pii/0584854791801812

[50] R. Klockenkämper, A. von Bohlen, Total-reflection X-ray fluorescence analysis and related methods, second edition Edition, Wiley, Hoboken New Jersey, 2015.

[51] J. M. Bloch, M. Sansone, F. Rondelez, D. G. Peiffer, P. Pincus, M. W. Kim, P. M. Eisenberger, Concentration profile of a dissolved polymer near the air-liquid interface: X-ray fluorescence study, Phys. Rev. Lett. 54 (1985) 1039–1042. doi:10.1103/PhysRevLett.54.1039.
URL https://link.aps.org/doi/10.1103/PhysRevLett.54.1039

[52] H. Dosch, Critical Phenomena at Surfaces and Interfaces: Evanescent X-Ray and Neutron Scattering, Vol. v. 126 of Springer Tracts in Modern Physics Ser, Springer Berlin / Heidelberg, Berlin, Heidelberg, 2006.

[53] P. B. Petersen, R. J. Saykally, On the nature of ions at the liquid water surface, Annual review of physical chemistry 57 (2006) 333–364. doi:10.1146/annurev.physchem.57.032905.104609.

[54] C. Shen, H. Zhang, B. M. Ocko, Reconstructing the reflectivity of liquid surfaces from grazing incidence X-ray off-specular scattering data, Journal of Applied Crystallography 57 (3) (2024) 714–727. doi:10.1107/S1600576724002887.
URL https://doi.org/10.1107/S1600576724002887

[55] N. B. Vargaftik, B. N. Volkov, L. D. Voljak, International Tables of the Surface Tension of Water, Journal of Physical and Chemical Reference Data 12 (3) (1983) 817–820. arXiv:https://pubs.aip.org/aip/jpr/article-pdf/12/3/817/11881808/817_1_online.pdf, doi:10.1063/1.555688.
URL https://doi.org/10.1063/1.555688

[56] Y. Uematsu, Electrification of water interface, Journal of Physics: Condensed Matter 33 (42) (2021) 423001. doi:10.1088/1361-648X/ac15d5.
URL https://dx.doi.org/10.1088/1361-648X/ac15d5

[57] T. Wadewitz, J. Winkelmann, Density functional theory: X-ray reflectivity studies of pure fluid liquid/vapour interfaces, Physical Chemistry Chemical Physics 1 (14) (1999) 3335–3343. doi:10.1039/a902914a.

[58] A. Braslau, P. S. Pershan, G. Swislow, B. M. Ocko, J. Als-Nielsen, Capillary waves on the surface of simple liquids measured by x-ray reflectivity, Physical review. A, General physics 38 (5) (1988) 2457–2470. doi:10.1103/PhysRevA.38.2457.

[59] P. Pershan, Effects of thermal roughness on x-ray studies of liquid surfaces, Colloids and Surfaces A: Physicochemical and Engineering Aspects 171 (1) (2000) 149–157. doi:https://doi.org/10.1016/S0927-7757(99)00557-9.
URL https://www.sciencedirect.com/science/article/pii/S0927775799005579

[60] D. K. Schwartz, M. L. Schlossman, E. H. Kawamoto, G. J. Kellogg, P. S. Pershan, B. M. Ocko, Thermal diffuse x-ray-scattering studies of the water-vapor interface, Phys. Rev. A 41 (1990) 5687–5690. doi:10.1103/PhysRevA.41.5687.
URL https://link.aps.org/doi/10.1103/PhysRevA.41.5687

[61] J. Goodman, J. Weare, Ensemble samplers with affine invariance, Communications in Applied Mathematics and Computational Science 5 (1) (2010) 65–80. doi:10.2140/camcos.2010.5.65.

[62] D. Foreman-Mackey, D. W. Hogg, D. Lang, J. Goodman, emcee : The mcmc hammer, Publications of the Astronomical Society of the Pacific 125 (925) (2013) 306–312. doi:10.1086/670067.

Appendix A. XRR mesaurements

Appendix A.1. Data extraction

The extraction of XRR curves from the raw detector images begins with flatfield correction and masking of defective detector pixels. A region of interest (ROI) is then selected and centered at the specular peak, covering the reflected intensity with dimensions of 2.2 mm × 1.21 mm. This ROI size is chosen to account for peak broadening upon laser irradiation while maintaining consistency throughout the dataset. The ROI center is automatically determined by summing and smoothing all detector images, then identifying the peak position along each axis in the resulting intensity profiles. The surface reflection intensity is calculated from the total intensity in the specular ROI subtracted by the background that is the average of the total intensities in the two adjacent off-specular ROIs. The signal is normalized to the signal from the ion chamber measuring upstream of the sample. Statistical uncertainty for each reflectivity point is estimated from the background signals, with an additional relative uncertainty of 10 % to account for ion chamber fluctuations.

To capture the wide dynamic range of the reflectivity signal, which spans several orders of magnitude depending on the wave vector, an absorber wheel with varying thicknesses and corresponding attenuation factors is placed in the beam path before the X-rays reach the sample. Consequently, scans recorded with different absorber thicknesses must be scaled accordingly. The scaling factors are determined by fitting parts of XRR curves measured for pure water using different absorber thicknesses to the Fresnel reflectivity. An uncertainty of 5 % in these scaling factors is also taken into account in the reflectivity uncertainty.

Due to the selected slit size and distances, the footprint of the X-ray beam at all measured angles remains smaller than the trough surface area at all measured angles, ensuring that no footprint correction is necessary for the reflectivity measurements.

Appendix A.2. Theoretical background on XRR

The central quantity in X-ray reflectivity analysis is the scattering length density (SLD), which is directly proportional to the material's electron density. At grazing incidence, total external reflection occurs when the angle of refraction inside the sample α' equals zero, defining the critical angle α_c that depends on the electron density. The corresponding critical wave vector q_c is related to the SLD by:

$$q_c = \sqrt{16\pi \mathrm{SLD}}. \tag{A.1}$$

X-ray reflectivity is also sensitive to thermally excited surface fluctuations, known as capillary waves, which lead to a reduction of the reflected intensity. This so-called

capillary roughness can be estimated from the following equation [57]:

$$\sigma_c^2 = \frac{k_\mathrm{B}T}{2\pi\gamma} \ln\left(\frac{q_\mathrm{max}}{\delta q_\mathrm{xy}}\right), \tag{A.2}$$

where k_B is the Boltzmann constant, T is the temperature, γ is the surface tension, δq_xy is the in-plane resolution, and q_max is the wave vector cut-off. The maximum wave vector cut-off q_max reflects the shortest surface fluctuations that can meaningfully contribute to the capillary roughness. It is limited by molecular dimensions and defined as $q_\mathrm{max} = \pi/a$, where a is the molecular size. The in-plane resolution [58, 59, 60]

$$\delta q_{xy} \approx 2\delta q_y = q_z \frac{l_v}{4L} \tag{A.3}$$

depends mainly on the resolution of the reflectometry measurement given by the vertical size of the detector area used for the collection of the reflectivity data, which is $l_v = 2.2\,\mathrm{mm}$, and the detector distance $L = 1.098\,\mathrm{m}$.

Appendix A.3. MCMC fitting procedure

To estimate posterior distributions of the fit parameters in the reflectivity models, we employed a Markov Chain Monte Carlo (MCMC) approach implemented in the Python package `refnx` (version 0.1.47) [43]. Sampling was carried out using the affine-invariant ensemble sampler proposed by Goodman and Weare [61], as implemented in `emcee` [62].

The parameter space was explored using 200 walkers, each representing an independent Markov chain. Initial positions of the walkers were randomly distributed within the parameter space. The ensemble was first evolved for 1000 steps to allow for burn-in, during which the chains converge toward the target posterior distribution. These initial steps were discarded. Subsequently, 2000 additional samples per walker were collected to build the posterior distributions.

Convergence was monitored by visual inspection of the walkers' temporal evolution. The best-fit parameter values were taken as the medians of the posterior distributions, and the uncertainties were estimated as half the interval between the 15th and 85th percentiles.

Appendix B. Additional Figures

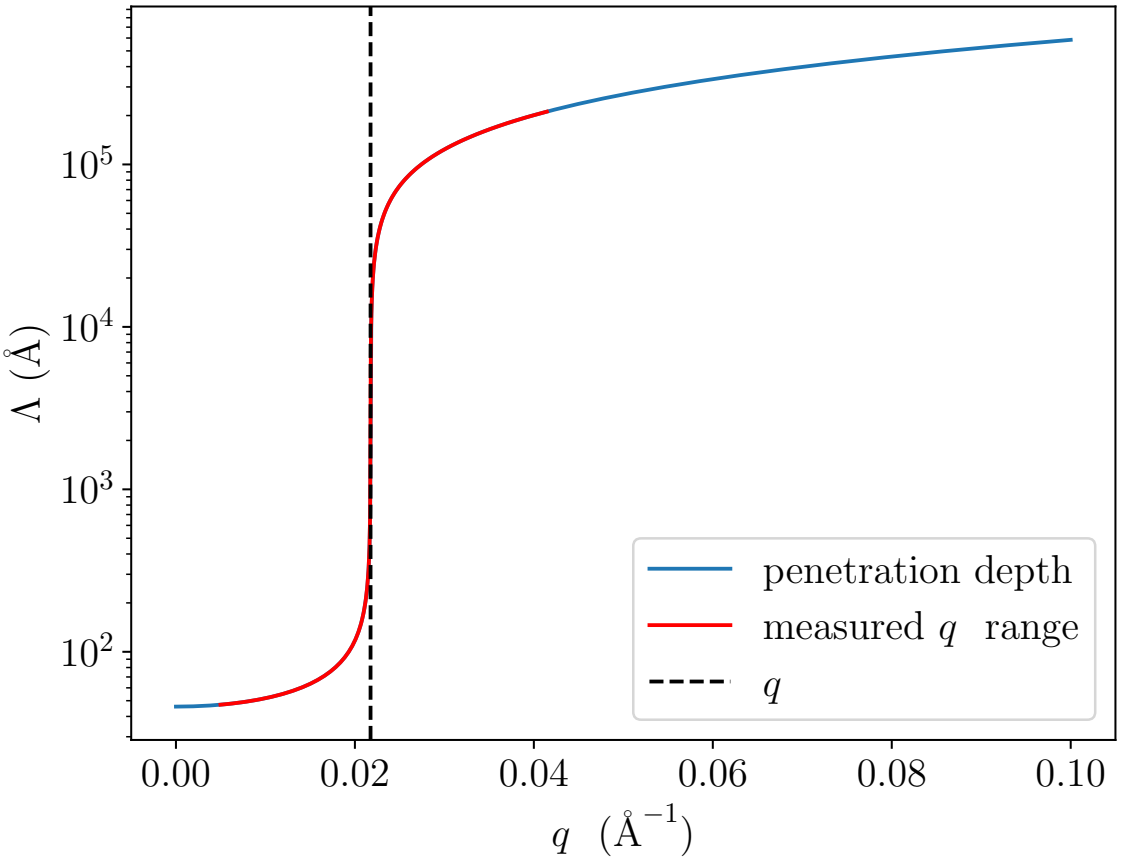

Figure B.6: Penetration depth Λ of the X-ray beam as a function of the angle of incidence, plotted against the corresponding wave vector q_z. The penetration depth corresponds to the 1/e decay length of the X-ray intensity within the sample. The vertical dashed line marks the critical angle q_c for H_2O.

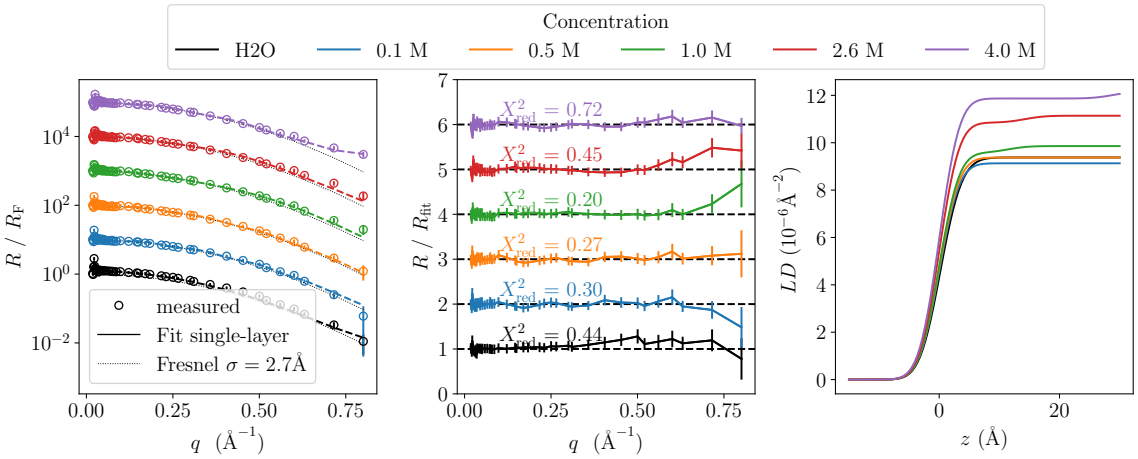

Figure B.7: Same as 2 but with the best-fit results for the single-layer model.

7.2.2 Laser Pump - X-ray fluorescence near total reflection at aqueous NaI surfaces

In addition to the XRFNTR data without laser irradiation included in the manuscript [MSH 2], data with laser radiation was taken during the same beamtime. The spectra were collected under continuous laser irradiation with varying laser power analogous to the XRR data with laser irradiation described in [MSH 2]. During the data collection time of 25 to 30 s, over 3 million laser pulses arrived at the sample and the accumulated effect was investigated. The XRFNTR data from 0.1, 0.5, 1, 2.6 and 4 M NaI solutions with and without laser irradiation are shown in Fig. 7.3. The laser power was varied between 0.48, 1.70, 3.54 and 6.66 ± 0.04 µJ. All fluorescence spectra show the same peaks belonging to the iodide L_α, $L_{\beta,1}$, $L_{\beta,2}$, and $L_{\gamma,1}$ peaks. The peaks were fitted as described in Sec. 4.6.4 and [PSH 2]. The angle dependent intensity of

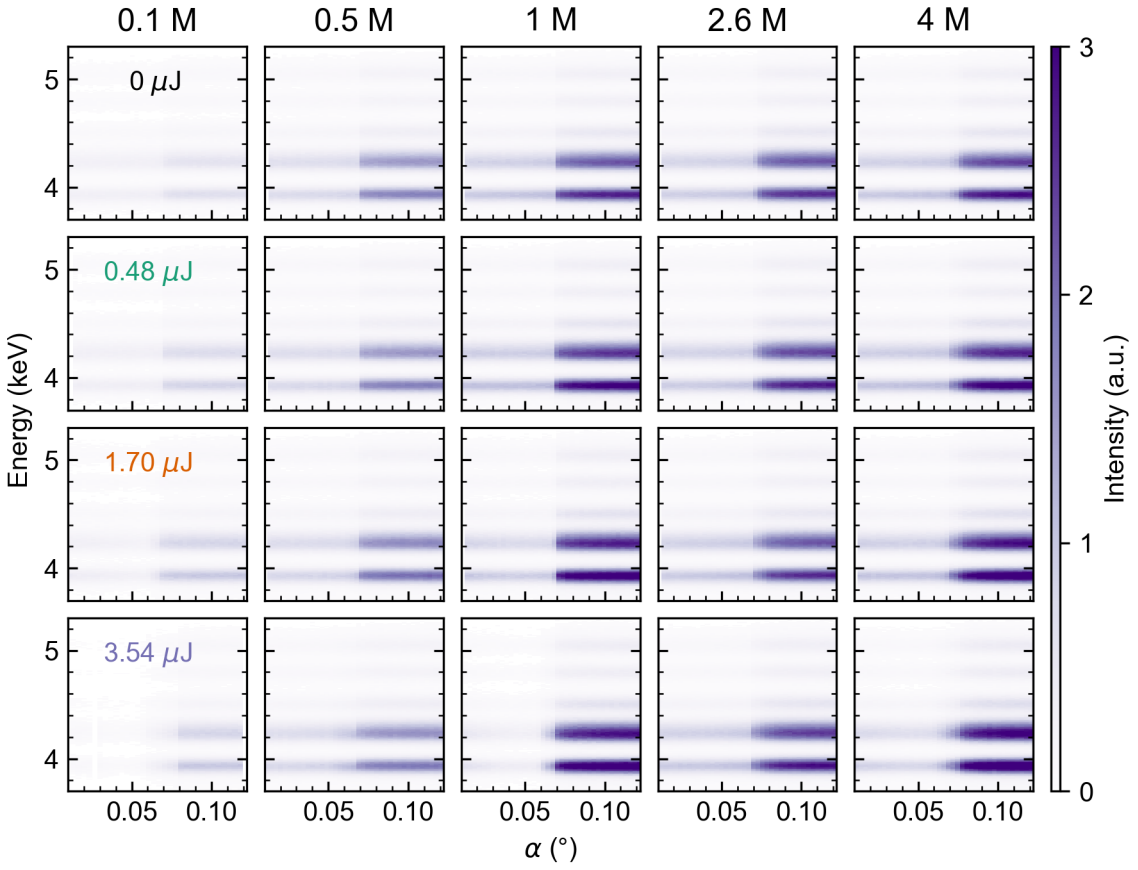

Figure 7.3: Fluorescence spectra taken at varying incident angle α from NaI solutions with a concentration of 0.1, 0.5, 1, 2.6 and 4 M without (row 1) and with (rows 2-4) laser irradiation. The spectra show the L_α, $L_{\beta,1}$, $L_{\beta,2}$, and $L_{\gamma,1}$ peaks.

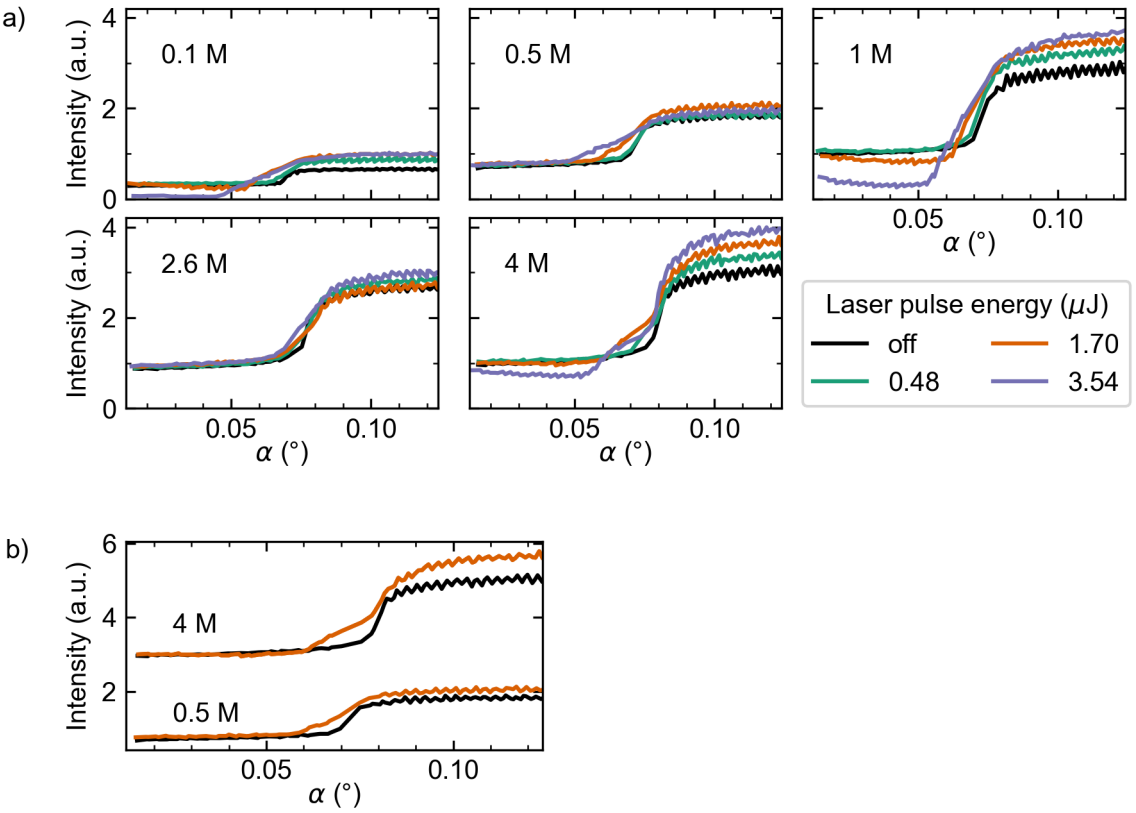

Figure 7.4: a) Intensity profile of the L_α peak in dependence of the incident angle α with (coloured) and without (black) laser irradiation for the 0.1, 0.5, 1, 2.6 and 4 M NaI solutions. b) Selection of the intensity profiles of the 0.5 M and 4 M solution without laser (black) and with laser irradiation with a laser pulse energy of 1.70 µJ (orange).

the L_α peak is shown in Fig. 7.4a for the different solutions and laser settings. The laser off profiles are the same as presented in the preprint [MSH 2]. First thing to notice is that the shape of intensity profiles change upon laser irradiation and the intensity increase around the critical angle looks less steep for the measurements with laser illumination. In addition, for the 4 M NaI solution a bump around the critical angle is observed. In Fig. 7.4b the intensity curve for the 0.5 M and 4 M NaI solution without and with laser for the same laser pulse energy are compared to highlight the flattening at low concentrations and the bump at high concentration. While the laser off profiles follow the expected S-like intensity increase for a bulk solution, the laser on profiles deviate significantly from this bulk profile. This deviation could be caused by multiple effects. On one hand, it could hint to a formation of a distinct layer at the interface. Depending on the thickness and electron density of this potential layer,

a sharp intensity increase and a shift in the position of the critical angle could be observed (see Fig. 2.11 in Sec. 2.3.5). On the other hand, the flattening could result from a roughening of the surface.

For rough surfaces of solid samples, a broadening of the step like profile is observed [161, 164], which looks similar to the observed broadening ffrom the studied liquid surface. However, unlike solid surfaces, the roughness of the water surface does mainly depend on the capillary roughness (see Sec. 2.1.2). Therefore, a roughening of the surface could only be related to a macroscopic geometric deformation of the surface, such as the creation of standing waves. From previous studies, we know that the laser pulses can induce a geometrical deformation of the surface profile. This geometric effect can be observed by a shift or a broadening of the reflected specular beam on the detector upon laser irradiation. By small movements of the last mirror reflecting the laser beam onto the surface, the relative position of the laser beam to the X-ray beam can be altered and the profile of the surface alternation can be detected. For laser irradiation on water based liquid surfaces, a dip with a diameter of few mm and depth of few µm is formed by the laser. A detailed discussion and calculation of this surface deformation is given in [183]. Reference and control measurements on water and salt solutions with alternating laser powers, laser spot positions and at different wavevectors showed that the contribution of surface deformation to the observed effects can be neglected compared to the laser induced excitation [183]. Yet, during the XRFNTR measurements low laser powers were chosen to reduce the surface deformation and broadening of the specular beam and the overlap of the laser and X-ray spot was carefully adjusted.

Nevertheless, measuring at very shallow incident angles, the X-ray is most sensitive to any change in surface topology and the X-ray footprint on the sample is large compared to the laser spot size. The XRFNTR measurements are performed with incident angles between 0.016 to 0.13° which results in a very elongated X-ray footprint. The XRFNTR data shown in Fig. 7.3 and Fig. 7.4 were collected with an X-ray beam height of 100 µm. This results in a footprint of about (71 ± 5) mm at the lowest X-ray incident angle. Compared to the FWHM of the laser beam size with (2.50 ± 0.20) mm, the X-ray spot is roughly 28 times larger than the laser spot. Therefore, laser excited and non-excited regions of the surface are probed with the X-ray simultaneously, which complicates clear identification of laser induced effect. Considering the collected fluorescence signals to be the sum of the non and laser irradiated regions, the laser irradiated region contributes to a 5 % fraction of the total intensity (neglecting the angle dependency of the X-ray footprint). If the small bump in intensity profile from the 4 M NaI solution belongs to the laser irradiated region, the low intensity could be due to the low percentage. However, the intensity

difference between the bump and the intensity at a high angle is roughly a factor 1.5 and not 20. Moreover, the shape of the bump is not unambiguous. It could be a sharp peak increase belonging to a layer inside the solution or an S-like shape profile, suggesting a solution without layer but with a lower electron density (see Fig. 2.11 for comparison). Unfortunately, the collected data is not sufficient to draw distinct conclusions. Further studies beyond this thesis are necessary to identify the origin of the observed laser induced effects. One option to overcome the challenge of the footprint mismatch, is to utilise a µm focused X-ray beam with a beam height of only 13 µm in future measurements and works.

8
Conclusion

This work was motivated by the plurality of chemical and physical processes taking place at liquid interfaces and the main goal was to understand three specific light-induced interactions in more detail: two at the water-air interface and one in bulk water. Two of the three interactions of interest are light-induced morphological changes in lipid membranes containing photoswitchable glycolipids at the water-air interface and in bulk water. The results from these two studies, compiled in the publication [PSH 1], the manuscripts [MSH 1] and [MSH 3] and sections in this work, improve the fundamental understanding of the influence synthetic photoswitchable lipids have on the structure of lipid membranes and their potential to induce structural changes which find applications in studies on controlling protein and bacteria activity at membranes, drug delivery systems and membrane fusion. In addition to the biological systems, the presence of salt ions at the water-air interface and how laser irradiation in the UV range interacts with the ions and influences the surface properties were investigated. An increase or decrease of ions at the interface directly impacts chemical processes at liquid interfaces and is important to explain chemical reactions in the field of atmospherical chemistry. The results, obtained in this work and presented in the manuscript [MSH 2] and within in this work, help to describe the presence of ions without and during irradiation with UV light.

To understand the light-induced interactions and to characterise the structural properties of the interfaces a variety of X-ray scattering techniques were utilised. The morphologies of the lipid aggregates in the bulk solution were determined with small angle X-ray scattering (SAXS). These structures were related to the lipid phases after performing differential scanning calorimetry (DSC) measurements to determine the phase transition temperatures. Meanwhile, the phases of the lipid monolayers were characterised with Langmuir isotherms and further investigated with X-ray reflectivity (XRR), neutron reflectivity (NR) and grazing incidence diffraction (GID). The XRR and NR measurements gave access to the layer thickness and electron density profile in direction of the surface normal and the interface

roughness. Additional information on the tilt angle and molecule-molecule distance of the lipids in the Langmuir monolayer was received with GID. For the aqueous salt solutions, the electron density and roughness were determined with XRR and complemented with X-ray fluorescence near total reflection (XRFNTR) measurement. Combined, XRR and XRFNTR are powerful techniques to identify layers forming at the surface and to determine the chemical composition at the interface. During the X-ray scattering measurements, the samples were irradiated with UV or visible light to induce structural changes. The biological membranes were illuminated with UV and visible light emitted from LEDs. Whereas, for the studies on the aqueous salt solutions, the solutions were irradiated with a laser. Utilising fs laser pulses to excite the sample allows studying dynamics on time scales of fs to µs. However, these laser pump - X-ray probe measurements are challenging and require especially designed and optimised instruments such as the Liquid Interface Scattering Apparatus (LISA) at P08, PETRA III.

During this thesis, the laser pump - X-ray probe setup at LISA was extended and modified to broaden the fields of applications for the laser pump experiments as published in [PSH 2]. On one hand, a beam profile shaper was incorporated into the laser beam path to transform the Gaussian shaped beam to a flat top beam with a homogeneous intensity distribution over the whole beam profile. A flat top shaped beam is especially advantageous for measurements on heat sensitive samples as the irradiated area is heated up evenly and the high laser fluency at the center of the Gaussian shaped beam is reduced, which reduces the risk of exceeding the damage threshold of the sample. In addition to these developments on the laser beam path, the accessible time delays between the laser and X-ray pulses were extended to cover the previously unavailable time range between few µs and s. By including an additional delay generator and gating the Pockels cells inside the fs laser, the time delays can be varied seamlessly and efficiently. This enhances the user experience and enables measurements on diverse samples with short (ps to ns) and long (µs to ms) relaxations times or to determine the relaxation times during one beamtime without alterations of the measurement setup.

This laser setup at the LISA instrument was used to study the ion distribution at the surface of aqueous NaI solutions with concentrations between 0.1 to 4 M. The ion distribution was investigated with XRR and XRFNTR. Assigning the peaks in the fluorescence signal to the emission lines of the iodide ions proved their presence at the surface. Moreover, the absence of a fluorescence signal originating from the sodium ions supports the theoretical expected attraction of the iodide ions to the surface

and repulsion of the sodium ions from the interface. Though no distinct layering of the iodide ions at the surface was observed at 21 °C for either of the studied concentrations, an increase of the electron density compared to the expected density for a bulk solution was observed. By combining XRR and XRFNTR measurements with laser irradiation at a wavelength of 258 nm, the influence of UV light on the local ion distribution of the NaI solutions was studied. The XRR investigations showed an increase of the electron density with increasing laser fluency while the surface roughness was constant within the measurement uncertainty. A possible explanation for the increase of electron density is the attraction of ions to the surface and formation of a higher concentrated region. While the XRR results show a clear structural effect, the XRFNTR results with laser irradiation are inconclusive. The XRFNTR data displays a laser driven difference in the surface by a deformation of the intensity profile of the fluorescence signal. This deformation could result from a formation of a layer with another concentration and the subsequent superposition of the fluorescence signals from the layer and the bulk. Combining the XRR and XRFNTR methods allowed to confidently conclusion: firstly, under laser radiation iodide ions are still present at the surface while sodium ions are absent as for the non-illuminated solution and secondly, the laser has a not yet clarified effect on the local iodide ion distribution.

The work also focused on light-induced structural changes in lipids membranes and the possible application of photoswitchable glycolipids to control protein or bacteria attachment at lipid monolayers. The presented studies on Langmuir monolayers composed by a lipid ratio of 9:1 of DPPC and one of the azobenzene mimetics AZOL-C16, AZGL-C16 or AZLL-C16 showed for all three systems repeatable and reversible changes in the surface pressure, vertical and in-plane structure of the lipids. All three mimetics possess a tail group consisting of two saturated acyl chains and differ in the type of carbohydrate attached to the head group. For reference the mimetic AZOL-C16 with a non-glycosylated hydroxyl group was investigated in addition to the β-D-glucopyranosyl (glucose) and β-D-lactosyl (lactose) moieties attached to the mimetics AZGL-C16 and AZLL-C16, respectively. In the Langmuir isotherm studies, the additional phase transitions LC'_{trans} and LC'_{cis} were found for the *trans* and *cis* state for all azobenzene mimetics and defined a range of area per molecules at which surface pressure and structural changes can be induced by isomerisation of the azobenzene mimetics. Upon illumination and switching of the azobenzene mimetics, an increase of few $\mathrm{mN\,m^{-1}}$ in the surface pressure was observed. Time-resolved surface pressure measurements revealed the same linear dependency between the relative surface pressure change and the time needed to reach the corresponding surface pressures for all three azobenzene mimetics containing

monolayers independent of the carbohydrate head group.

In addition to studying the surface pressure change, XRR and GID measurements were performed to quantify the change in layer thickness, tilt angle of the tail group and molecule packing. Switching the azobenzene mimetics with their ratio of 10 % in the monolayer to their *cis* state induced a closer packing of all molecules. This closer packing was visible in the increase of the tail layer thickness and decrease of the tilt angle of the tail groups. In addition to the changes in the tail group, a significant rearrangement in the head group ordering was found. In the *trans* state, the GID results showed a head group ordering which disappeared for the monolayers with AZOL-C16 and AZGL-C16 upon switching to the *cis* state. Moreover, the tilting of the head group and subsequently reorientation of the head group was revealed by XRR and NR studies on AZGL-C16 containing monolayers. This makes the mimetic AZGL-C16 a promising candidate for designing model systems to light-control bacteria activity at the lipid monolayer.

In an initial study, lyotropic liquid crystals containing DPPC and the azobenzene mimetic AZOL-C16 (no sugar group) were investigated to identify and characterise light-induced structural changes of the crystal morphology. The SAXS results of the aggregates with a ratio up to 20 % of the mimetic AZOL-C16 revealed light and temperature-induced mesophase transitions. The temperature-induced transition was found in aggregates with the mimetics AZOL-C16 in the *trans* state upon heating from 25 °C to 37 °C and showed a transition from the lamellar to the bicontinuous cubic $Pn3m$ phase. This transition could be assigned to the phase transition from the gel phase to the liquid crystalline phase with DSC measurements. Meanwhile, for aggregates with the *cis* isomer of the mimetic AZOL-C16 the $Pn3m$ mesophase was identified for both phases, the gel and liquid crystalline phase, and thus no temperature induced mesophase transition was found. Focusing on the gel phase of the lipid aggregates and illuminating them to switch the mimetics AZOL-C16 between its *trans* and *cis* isomer, a reproducible and reversible mesophase transition from the lamellar phase in the *trans* state to the $Pn3m$ phase in the *cis* state was observed.

A subsequent time-resolve SAXS study investigated the kinetics of the mesophase transitions and identified the mesophases for various model systems comprised of one of seven azobenzene mimetics or seven reference mimetics in combination with DPPC or DLPC with ratios varying from 0 to 100 %. The obtained overview of mesophases for the 47 lyotropic liquid crystals composed by the variety of lipid compositions revealed that a photo-induced mesophase transition was observed for combinations with the mimetics AZOL-C12 and AZOL-C16, both without a sugar group attached

to the head group. In addition to the mesophase transition, a difference in the repeating distances was found for few aggregates upon photoswitching between the *trans* and *cis* isomers. To investigate the mesophase transition induced in the aggregates containing the mimetic AZOL-C12, time-resolved SAXS measurements were performed and revealed that the first structural change was observed after 30 s of continuous illumination and the mesophase transition was finalised after 120 s.

In summary, Langmuir isotherm, DSC, XRR, GID and XRFNTR were successfully utilised to investigate and determine light-induced structural changes in lipid monolayers, lyotropic liquid crystals and at aqueous salt solution interfaces. Especially, the advantages of combining complementary methods such as XRR and XRFNTR in the presented study on aqueous NaI solutions and XRR and GID for the lipid monolayers showed how beneficial diverse measurement methods are to identify the structures perpendicular and parallel to the surface.

Three aspects of interactions at liquid interfaces were investigated in this thesis and the observed structural changes hold high potential for continuing investigations succeeding this work. On one hand, the experiments on the laser-induced effects on aqueous ions solutions can be extended to samples containing other halides and time-resolved experiments utilising the laser pump - X-ray probe setup at LISA, P08, Petra III, can be conducted to study dynamics at the interface on time scales from ps to ms. On other hand, the investigations on the lipid membranes in this work identified promising candidates of the photoswitchable glycolipids for designing model systems for drug delivery systems or controlling bacteria or protein activity. A perspective for further experiments is to perform *in situ* studies on Langmuir monolayers with added bacteria or proteins in the water to monitor the bacteria activity at the monolayer interface. In addition, future studies can concentrate on incorporating drugs into the lyotropic liquid crystals and to measure the release of the drugs upon photoswitching.

Bibliography

[1] P. H. Gleick. *Water in crisis: A guide to the world's fresh water resources.* Oxford University Press, New York, 1993. ISBN 0195076273.

[2] K. Munk, C. Abröll, T. Kurth, T. Langer, and R. Nethe-Jaenchen. *Taschenlehrbuch Biologie: Biochemie - Zellbiologie.* Taschenlehrbuch Biologie. Thieme, Stuttgart, 1. auflage edition, 2008. ISBN 9783131519917.

[3] Z. Cournia, T. W. Allen, I. Andricioaei, B. Antonny, D. Baum, G. Brannigan, N.-V. Buchete, J. T. Deckman, L. Delemotte, C. Del Val, R. Friedman, P. Gkeka, H.-C. Hege, J. Hénin, M. A. Kasimova, A. Kolocouris, M. L. Klein, S. Khalid, M. J. Lemieux, N. Lindow, M. Roy, J. Selent, M. Tarek, F. Tofoleanu, S. Vanni, S. Urban, D. J. Wales, J. C. Smith, and A.-N. Bondar. Membrane protein structure, function, and dynamics: a perspective from experiments and theory. *The Journal of Membrane Biology*, 248(4):611–640, 2015. doi: 10.1007/s00232-015-9802-0.

[4] G. W. Jones and R. E. Isaacson. Proteinaceous bacterial adhesins and their receptors. *Critical Reviews in Microbiology*, 10(3):229–260, 1983. doi: 10.3109/10408418209113564.

[5] K. A. Karlsson. Microbial recognition of target-cell glycoconjugates. *Current opinion in structural biology*, 5(5):622–635, 1995. doi: 10.1016/0959-440X(95)80054-9.

[6] O. Ces and X. Mulet. Physical coupling between lipids and proteins: a paradigm for cellular control. *Signal Transduction*, 6(2):112–132, 2006. doi: 10.1002/sita.200500079.

[7] J. A. Op den Kamp. Lipid asymmetry in membranes. *Annual Review of Biochemistry*, 48(1979):47–71, 1979. doi: 10.1146/annurev.bi.48.070179.000403.

[8] R. Blumenthal, M. J. Clague, S. R. Durell, and R. M. Epand. Membrane fusion. *Chemical Reviews*, 103(1):53–69, 2003. doi: 10.1021/cr000036.

[9] A. Iglič, A. Garcia-Sáez, and M. Rappolt, editors. *Advances in Biomembranes and Lipid Self-Assembly.* Academic Press, 2017. ISBN 2451-9634.

[10] P. L. Yeagle. *The Structure of Biological Membranes: 2nd Edition.* CRC Press, 2004. ISBN 9780429120640.

[11] G. van Meer, D. R. Voelker, and G. W. Feigenson. Membrane lipids: where they are and how they behave. *Nature Reviews. Molecular Cell Biology*, 9(2): 112–124, 2008. doi: 10.1038/nrm2330.

[12] E. G. Kelley, P. D. Butler, R. Ashkar, R. Bradbury, and M. Nagao. Scaling relationships for the elastic moduli and viscosity of mixed lipid membranes. *Proceedings of the National Academy of Sciences*, 117(38):23365–23373, 2020. doi: 10.1073/pnas.2008789117.

[13] J. J. Myher, A. Kuksis, and S. Pind. Molecular species of glycerophospholipids and sphingomyelins of human erythrocytes: improved method of analysis. *Lipids*, 24(5):396–407, 1989. doi: 10.1007/BF02535147.

[14] T. El-Bacha and A. G. Torres. Phospholipids: Physiology. In Benjamin Caballero, Paul M. Finglas, and Fidel Toldrá, editors, *Encyclopedia of Food and Health*, pages 352–359. Academic Press, Oxford, 2016. ISBN 978-0-12-384953-3.

[15] J. M. López-Pinto, M. L. González-Rodríguez, and A. M. Rabasco. Effect of cholesterol and ethanol on dermal delivery from dppc liposomes. *International Journal of Pharmaceutics*, 298(1):1–12, 2005. doi: 10.1016/j.ijpharm.2005.02.021.

[16] Rob Phillips, Tristan Ursell, Paul Wiggins, and Pierre Sens. Emerging roles for lipids in shaping membrane-protein function. *Nature*, 459(7245):379–385, 2009. doi: 10.1038/nature08147.

[17] A. Ivankin, I. Kuzmenko, and D. Gidalevitz. Cholesterol-phospholipid interactions: new insights from surface X-ray scattering data. *Physical Review Letters*, 104(10):108101, 2010. doi: 10.1103/PhysRevLett.104.108101.

[18] M. Manna, T. Róg, and I. Vattulainen. The challenges of understanding glycolipid functions: An open outlook based on molecular simulations. *Biochimica et Biophysica Acta*, 1841(8):1130–1145, 2014. doi: 10.1016/j.bbalip.2013.12.016.

[19] B. Nepal and K. J. Stine. Monolayers of carbohydrate-containing lipids at the water- air interface. In Radwa Ali Mehanna, editor, *Cell Culture*. IntechOpen, 2019. ISBN 978-1-78984-866-3.

[20] N. Sharon and H. Lis. Lectins as cell recognition molecules. *Science*, 246(4927): 227–234, 1989. doi: 10.1126/science.2552581.

[21] K. Bock, K.-A. Karlsson, N. Strömberg, and S. Teneberg. Interaction of viruses, bacteria and bacterial toxins with host cell surface glycolipids. aspects on receptor identification and dissection of binding epitopes. In *The Molecular Immunology of Complex Carbohydrates*, pages 153–186. Springer, Boston, MA, 1988. ISBN 978-1-4613-1663-3. doi: 10.1007/978-1-4613-1663-3_7.

[22] J. P. Renou, J. B. Giziewicz, I. C. Smith, and H. C. Jarrell. Glycolipid membrane surface structure: orientation, conformation, and motion of a disaccharide headgroup. *Biochemistry*, 28(4):1804–1814, 1989. doi: 10.1021/bi00430a057.

[23] J. Volarić, W. Szymanski, N. A. Simeth, and B. L. Feringa. Molecular photoswitches in aqueous environments. *Chemical Society Reviews*, 50(22):12377–12449, 2021. doi: 10.1039/d0cs00547a.

[24] G. Despras, V. Poonthiyil, and T. K. Lindhorst. *Photochromic Carbohydrate Conjugates*. Molecular Photoswitches. Wiley, 2022. ISBN 9783527351046.

[25] L. M. Friedrich and T. K. Lindhorst. Orthogonal photoswitching of heterobivalent azobenzene glycoclusters: the effect of glycoligand orientation in bacterial adhesion. *Beilstein Journal of Organic Chemistry*, 21(1):736–748, 2025. doi: 10.3762/bjoc.21.57.

[26] G. A. Cross. Glycolipid anchoring of plasma membrane proteins. *Annual Review of Cell Biology*, 6(1):1–39, 1990. doi: 10.1146/annurev.cb.06.110190.000245.

[27] S. V. Evans and C. R. MacKenzie. Characterization of protein-glycolipid recognition at the membrane bilayer. *Journal of Molecular Recognition*, 12 (3):155–168, 1999. doi: 10.1002/(SICI)1099-1352(199905/06)12:3<155::AID-JMR456>3.0.CO;2-S.

[28] H. C. Jarrell, A. J. Wand, J. B. Giziewicz, and I. C. Smith. The dependence of glyceroglycolipid orientation and dynamics on head-group structure. *Biochimica et Biophysica Acta*, 897(1):69–82, 1987. doi: 10.1016/0005-2736(87)90316-6.

[29] K. G. Yager and C. J. Barrett. Novel photo-switching using azobenzene functional materials. *Journal of Photochemistry and Photobiology A: Chemistry*, 182(3):250–261, 2006. doi: 10.1016/j.jphotochem.2006.04.021.

[30] M.-M. Russew and S. Hecht. Photoswitches: from molecules to materials. *Advanced materials (Deerfield Beach, Fla.)*, 22(31):3348–3360, 2010. doi: 10.1002/adma.200904102.

[31] Andrew A. Beharry and G. Andrew Woolley. Azobenzene photoswitches for biomolecules. *Chemical Society Reviews*, 40(8):4422–4437, 2011. doi: 10.1039/c1cs15023e.

[32] Z. L. Pianowski, editor. *Molecular Photoswitches*. Wiley, 2022. ISBN 9783527351046. doi: 10.1002/9783527827626.

[33] G. S. Hartley. The cis-form of azobenzene. *Nature*, 140(3537):281, 1937. doi: 10.1038/140281a0.

[34] H. M. D. Bandara and S. C. Burdette. Photoisomerization in different classes of azobenzene. *Chemical Society Reviews*, 41(5):1809–1825, 2012. doi: 10.1039/c1cs15179g.

[35] E. H. G. Backus, J. M. Kuiper, J. B. F. N. Engberts, B. Poolman, and M. Bonn. Reversible optical control of monolayers on water through photoswitchable lipids. *The Journal of Physical Chemistry B*, 115(10):2294–2302, 2011. doi: 10.1021/jp1113619.

[36] N. Basílio and L. García-Río. Photoswitchable vesicles. *Current Opinion in Colloid & Interface Science*, 32:29–38, 2017. doi: 10.1016/j.cocis.2017.09.004.

[37] J. E. Warias, F. Reise, S. C. Hövelmann, R. P. Giri, M. Röhrl, J. Kuhn, M. Jacobsen, K. Chatterjee, T. Arnold, C. Shen, S. Festersen, A. Sartori, P. Jordt, O. M. Magnussen, T. K. Lindhorst, and B. M. Murphy. Photoinduced bidirectional switching in lipid membranes containing azobenzene glycolipids. *Scientific reports*, 13(1):11480, 2023. doi: 10.1038/s41598-023-38336-x.

[38] P. Urban, S. D. Pritzl, M. F. Ober, C. F. Dirscherl, C. Pernpeintner, D. B. Konrad, J. A. Frank, D. Trauner, B. Nickel, and T. Lohmueller. A lipid photoswitch controls fluidity in supported bilayer membranes. *Langmuir*, 36 (10):2629–2634, 2020. doi: 10.1021/acs.langmuir.9b02942.

[39] D. D. Lasic. The mechanism of vesicle formation. *Biochemical Journal*, 256(1): 1–11, 1988. doi: 10.1042/bj2560001.

[40] P. Walde and S. Ichikawa. Lipid vesicles and other polymolecular aggregates—from basic studies of polar lipids to innovative applications: 81 p. *Applied Sciences*, 11(21):10345, 2021. doi: 10.3390/app112110345.

[41] C. V. Kulkarni. Lipid crystallization: from self-assembly to hierarchical and biological ordering. *Nanoscale*, 4(19):5779–5791, 2012. doi: 10.1039/c2nr31465g.

[42] H. T. McMahon and E. Boucrot. Membrane curvature at a glance. *Journal of Cell Science*, 128(6):1065–1070, 2015. doi: 10.1242/jcs.114454.

[43] J. F. Nagle and S. Tristram-Nagle. Structure of lipid bilayers. *Biochimica et Biophysica Acta*, 1469(3):159–195, 2000. doi: 10.1016/S0304-4157(00)00016-2.

[44] J. Jouhet. Importance of the hexagonal lipid phase in biological membrane organization. *Frontiers in Plant Science*, 4:494, 2013. doi: 10.3389/fpls.2013.00494.

[45] J. D. Nickels, S. Chatterjee, C. B. Stanley, S. Qian, X. Cheng, D. A. A. Myles, R. F. Standaert, J. G. Elkins, and J. Katsaras. The in vivo structure of biological membranes and evidence for lipid domains. *PLOS Biology*, 15(5): e2002214, 2017. doi: 10.1371/journal.pbio.2002214.

[46] V. Luzzati. Biological significance of lipid polymorphism: the cubic phases. *Current opinion in structural biology*, 7(5):661–668, 1997. doi: 10.1016/S0959-440X(97)80075-9.

[47] Z. A. Almsherqi, T. Landh, S. D. Kohlwein, and Y. Deng. Chapter 6 cubic membranes: The missing dimension of cell membrane organization. In *Inter-*

national Review of Cell and Molecular Biology, volume 274, pages 275–342. Academic Press, 2009. ISBN 1937-6448. doi: 10.1016/S1937-6448(08)02006-6.

[48] S.-J. Marrink and D. P. Tieleman. Molecular dynamics simulation of spontaneous membrane fusion during a cubic-hexagonal phase transition. *Biophysical Journal*, 83(5):2386–2392, 2002. doi: 10.1016/S0006-3495(02)75252-1.

[49] W. Wickner and R. Schekman. Membrane fusion. *Nature Structural & Molecular Biology*, 15(7):658–664, 2008. doi: 10.1038/nsmb.1451.

[50] L. P. Cavalcanti, O. Konovalov, and I. L. Torriani. Lipid model membranes for drug interaction study. *European Biophysics Journal*, 35(5):431–438, 2006. doi: 10.1007/s00249-006-0050-1.

[51] R. Hirlekar, S. Jain, M. Patel, H. Garse, and V. Kadam. Hexosomes: a novel drug delivery system. *Current Drug Delivery*, 7(1):28–35, 2010. doi: 10.2174/156720110790396526.

[52] A. Zabara and R. Mezzenga. Controlling molecular transport and sustained drug release in lipid-based liquid crystalline mesophases. *Journal of Controlled Release*, 188:31–43, 2014. doi: 10.1016/j.jconrel.2014.05.052.

[53] E. Di Cola, I. Grillo, and S. Ristori. Small angle X-ray and neutron scattering: Powerful tools for studying the structure of drug-loaded liposomes. *Pharmaceutics*, 8(2), 2016. doi: 10.3390/pharmaceutics8020010.

[54] J. C. Shah, Y. Sadhale, and D. M. Chilukuri. Cubic phase gels as drug delivery systems. *Advanced Drug Delivery Reviews*, 47(2-3):229–250, 2001. doi: 10.1016/S0169-409X(01)00108-9.

[55] O. Albrecht, H. Gruler, and E. Sackmann. Polymorphism of phospholipid monolayers. *Journal de Physique*, 39(3):301–313, 1978. doi: 10.1051/jphys:01978003903030100.

[56] L. Kalvodova, N. Kahya, P. Schwille, R. Ehehalt, P. Verkade, D. Drechsel, and K. Simons. Lipids as modulators of proteolytic activity of bace: involvement of cholesterol, glycosphingolipids, and anionic phospholipids in vitro. *The Journal of biological chemistry*, 280(44):36815–36823, 2005. doi: 10.1074/jbc.M504484200.

[57] B. W. Muir, G. Zhen, P. Gunatillake, and P. G. Hartley. Salt induced lamellar to bicontinuous cubic phase transitions in cationic nanoparticles. *The Journal of Physical Chemistry. B*, 116(11):3551–3556, 2012. doi: 10.1021/jp300239g.

[58] I. R. Ribeiro, M. F. Immich, D. Lundberg, F. Poletto, and W. Loh. Physiological neutral ph drives a gradual lamellar-to-reverse cubic-to-reverse hexagonal phase transition in phytantriol-based nanoparticles. *Colloids and surfaces. B, Biointerfaces*, 177:204–210, 2019. doi: 10.1016/j.colsurfb.2019.01.055.

[59] D. Wang, R. Dong, P. Long, and J. Hao. Photo-induced phase transition from multilamellar vesicles to wormlike micelles. *Soft Matter*, 7(22):10713, 2011. doi: 10.1039/C1SM05949A.

[60] W. D. Harkins and H. M. McLaughlin. The structure of films of water on salt solutions i. surface tension and adsorption for aqueous solutions of sodium chloride. *Journal of the American Chemical Society*, 47(8):2083–2089, 1925. doi: 10.1021/ja01685a002.

[61] D. Meranda and W. F. Furter. Elevation of the boiling point of water by salts at saturation: data and correlation. *Journal of Chemical and Engineering Data*, 22(3):315–317, 1977. doi: 10.1021/je60074a023.

[62] M. Boström, W. Kunz, and B. W. Ninham. Hofmeister effects in surface tension of aqueous electrolyte solution. *Langmuir*, 21(6):2619–2623, 2005. doi: 10.1021/la047437v.

[63] E. Sloutskin, B. M. Ocko, L. Tamam, I. Kuzmenko, T. Gog, and M. Deutsch. Surface layering in ionic liquids: an X-ray reflectivity study. *Journal of the American Chemical Society*, 127(21):7796–7804, 2005. doi: 10.1021/ja0509679.

[64] Poul B. Petersen, Justin C. Johnson, Kelly P. Knutsen, and Richard J. Saykally. Direct experimental validation of the jones–ray effect. *Chemical Physics Letters*, 397(1-3):46–50, 2004. doi: 10.1016/j.cplett.2004.08.048.

[65] M. A. Wilson and A. Pohorille. Interaction of monovalent ions with the water liquid-vapor interface: a molecular dynamics study. *The Journal of Chemical Physics*, 95(8):6005–6013, 1991. doi: 10.1063/1.461592.

[66] P. Jungwirth and D. J. Tobias. Molecular structure of salt solutions: A new view of the interface with implications for heterogeneous atmospheric chemistry. *The Journal of Physical Chemistry B*, 105(43):10468–10472, 2001. doi: 10.1021/jp012750g.

[67] P. B. Petersen and R. J. Saykally. On the nature of ions at the liquid water surface. *Annual Review of Physical Chemistry*, 57(Volume 57, 2006):333–364, 2006. doi: 10.1146/annurev.physchem.57.032905.104609.

[68] D. J. Tobias, A. C. Stern, M. D. Baer, Y. Levin, and C. J. Mundy. Simulation and theory of ions at atmospherically relevant aqueous liquid-air interfaces. *Annual Review of Physical Chemistry*, 64:339–359, 2013. doi: 10.1146/annurev-physchem-040412-110049.

[69] J. A. Kloepfer, V. H. Vilchiz, V. A. Lenchenkov, and S. E. Bradforth. Femtosecond dynamics of photodetachment of the iodide anion in solution: resonant excitation into the charge-transfer-to-solvent state. *Chemical Physics Letters*, 298(1-3):120–128, 1998. doi: 10.1016/S0009-2614(98)01210-X.

[70] J. A. Kloepfer, V. H. Vilchiz, V. A. Lenchenkov, A. C. Germaine, and S. E. Bradforth. The ejection distribution of solvated electrons generated by the one-photon photodetachment of aqueous i− and two-photon ionization of the solvent. *The Journal of Chemical Physics*, 113(15):6288–6307, 2000. doi: 10.1063/1.1309011.

[71] M. C. Sauer, R. A. Crowell, and I. A. Shkrob. Electron photodetachment from aqueous anions. 1. quantum yields for generation of hydrated electron by 193 and 248 nm laser photoexcitation of miscellaneous inorganic anions. *The Journal of Physical Chemistry A*, 108(25):5490–5502, 2004. doi: 10.1021/jp049722t.

[72] V. H. Vilchiz, X. Chen, J. A. Kloepfer, and S. E. Bradforth. Solvent effects on geminate recombination dynamics after photodetachment. *Radiation Physics and Chemistry*, 72(2-3):159–167, 2005. doi: 10.1016/j.radphyschem.2004.06.013.

[73] F. Messina, O. Bräm, A. Cannizzo, and M. Chergui. Real-time observation of the charge transfer to solvent dynamics. *Nature Communications*, 4(1):2119, 2013. doi: 10.1038/ncomms3119.

[74] B. M. Murphy, M. Greve, B. Runge, C. T. Koops, A. Elsen, J. Stettner, O. H. Seeck, and O. M. Magnussen. A novel X-ray diffractometer for studies of liquid-liquid interfaces. *Journal of Synchrotron Radiation*, 21(Pt 1):45–56, 2014. doi: 10.1107/S1600577513026192.

[75] O. H. Seeck, C. Deiter, K. Pflaum, F. Bertam, A. Beerlink, H. Franz, J. Horbach, H. Schulte-Schrepping, Bridget M. Murphy, M. Greve, and O. Magnussen. The high-resolution diffraction beamline P08 at PETRA III. *Journal of Synchrotron Radiation*, 19(Pt 1):30–38, 2012. doi: 10.1107/S0909049511047236.

[76] A. W. Adamson and A. P. Gast. *Physical Chemistry of Surfaces*. Wiley, New York, 6th ed. edition, 1997. ISBN 0471148733.

[77] Phuong Nguyen-Tri, Trong-On Do, and Tuan Anh Nguyen. *Smart nanocontainers*. Micro & nano technologies series. Elsevier, Amsterdam Netherlands, 2020. ISBN 9780128167700.

[78] W. R. Fawcett. *Liquids, solutions, and interfaces: From classical macroscopic descriptions to modern microscopic details*. Oxford University Press, Oxford and New York, 2004. ISBN 9780195094329.

[79] P. S. Pershan and M. Schlossman. *Liquid Surfaces and Interfaces: Synchrotron X-ray Methods*. Cambridge University Press (CUP), Cambridge, 2012. ISBN 9781139045872.

[80] A. Braslau, M. Deutsch, P. S. Pershan, A. H. Weiss, J. Als-Nielsen, and J. Bohr. Surface roughness of water measured by X-ray refelctivity. *Physical Review Letters*, 54(2):114–117, 1985. doi: 10.1103/PhysRevLett.54.114.

[81] A. Braslau, P. S. Pershan, G. Swislow, B. M. Ocko, and J. Als-Nielsen. Capillary waves on the surface of simple liquids measured by X-ray reflectivity. *Physical Review. A, General physics*, 38(5):2457–2470, 1988. doi: 10.1103/PhysRevA.38.2457.

[82] P. S. Pershan. Structure of surfaces and interfaces as studied using synchrotron radiation. liquid surfaces. *Faraday Discussions of the Chemical Society*, 89:231, 1990. doi: 10.1039/dc9908900231.

[83] T. Wadewitz and J. Winkelmann. Density functional theory: X-ray reflectivity studies of pure fluid liquid/vapour interfaces. *Physical Chemistry Chemical Physics*, 1(14):3335–3343, 1999. doi: 10.1039/a902914a.

[84] M. J. Regan, P. S. Pershan, O. M. Magnussen, B. M. Ocko, M. Deutsch, and Le Berman. Capillary-wave roughening of surface-induced layering in liquid gallium. *Physical Review. B, Condensed Matter*, 54(14):9730–9733, 1996. doi: 10.1103/physrevb.54.9730.

[85] A. M. Willis and J. B. Freund. Thermal capillary waves relaxing on atomically thin liquid films. *Physics of Fluids*, 22(2):022002, 2010. doi: 10.1063/1.3326077.

[86] B. Runge, S. Festersen, C. T. Koops, A. Elsen, M. Deutsch, B. M. Ocko, O. H. Seeck, B. M. Murphy, and O. M. Magnussen. Temperature- and potential-dependent structure of the mercury-electrolyte interface. *Physical Review B*, 93(16), 2016. doi: 10.1103/PhysRevB.93.165408.

[87] Y. Zhang, J. E. Sprittles, and D. A. Lockerby. Thermal capillary wave growth and surface roughening of nanoscale liquid films. *Journal of Fluid Mechanics*, 915, 2021. doi: 10.1017/jfm.2021.164.

[88] D. M. Mitrinović, A. M. Tikhonov, Ming Li, Zhengqing Huang, and M. L. Schlossman. Noncapillary wave structure water alkane interface. *Physical Review Letters*, 85(3):582–585, 2000.

[89] A. Datta, S. Kundu, M. K. Sanyal, J. Daillant, D. Luzet, C. Blot, and B. Struth. Dramatic enhancement of capillary wave fluctuations of a decorated water surface. *Physical Review. E, Statistical, nonlinear, and soft matter physics*, 71 (4 Pt 1):041604, 2005. doi: 10.1103/PhysRevE.71.041604.

[90] B. M. Ocko, X. Z. Wu, E. B. Sirota, S. K. Sinha, and M. Deutsch. X-ray reflectivity study of thermal capillary waves on liquid surfaces. *Physical Review Letters*, 72(2):242–245, 1994. doi: 10.1103/PhysRevLett.72.242.

[91] C. Wagner. Die oberflächenspannung verdünnter elektrolytlösungen. *Chemisches Zentralblatt*, 25:474, 1924.

[92] G. Jones and W. A. Ray. The surface tension of solutions. *Journal of the American Chemical Society*, 57(5):957–958, 1935. doi: 10.1021/ja01308a506.

[93] E. M. Knipping, M. J. Lakin, K. L. Foster, P. Jungwirth, D. J. Tobias, R. B. Gerber, D. Dabdub, and B. J. Finlayson-Pitts. Experiments and simulations of ion-enhanced interfacial chemistry on aqueous nacl aerosols. *Science*, 288 (5464):301–306, 2000. doi: 10.1126/science.288.5464.301.

[94] A. Laskin, Daniel J. Gaspar, W. Wang, Sherri W. Hunt, J. P. Cowin, S. D. Colson, and B. J. Finlayson-Pitts. Reactions at interfaces as a source of sulfate formation in sea-salt particles. *Science*, 301(5631):340–344, 2003. doi: 10.1126/science.1085374.

[95] P. Jungwirth and D. J. Tobias. Ions at the air/water interface. *The Journal of Physical Chemistry B*, 106(25):6361–6373, 2002. doi: 10.1021/jp020242g.

[96] L. X. Dang. Computational study of ion binding to the liquid interface of water. *The Journal of Physical Chemistry B*, 106(40):10388–10394, 2002. doi: 10.1021/jp021871t.

[97] M. Mucha, T. Frigato, L. M. Levering, H. C. Allen, D. J. Tobias, L. X. Dang, and P. Jungwirth. Unified molecular picture of the surfaces of aqueous acid, base, and salt solutions. *The Journal of Physical Chemistry B*, 109(16): 7617–7623, 2005. doi: 10.1021/jp0445730.

[98] P. Jungwirth and D. J. Tobias. Specific ion effects at the air/water interface. *Chemical Reviews*, 106(4):1259–1281, 2006. doi: 10.1021/cr0403741.

[99] X. Sun, C. D. Wick, and L. X. Dang. Computational studies of aqueous interfaces of SrCl(2) salt solutions. *The journal of physical chemistry. B*, 113 (42):13993–13997, 2009. doi: 10.1021/jp9079525.

[100] E. Sloutskin, J. Baumert, B. M. Ocko, I. Kuzmenko, A. Checco, L. Tamam, E. Ofer, T. Gog, O. Gang, and M. Deutsch. The surface structure of concentrated aqueous salt solutions. *The Journal of Chemical Physics*, 126(5):054704, 2007. doi: 10.1063/1.2431361.

[101] J.E. Escalante-Martinez, L.J. Morales-Mendoza, C. Calderon-Ramon, L.D. Romero Juarez, and J. Martinez-Castillo. Fractional derivatives modeling dielectric properties of biological tissue. pages 1–3, 2018. doi: 10.1109/INTERCON.2018.8526460.

[102] A. D. Bangham, M. W. Hill, and N. G. A. Miller. Preparation and use of liposomes as models of biological membranes. In *Methods in Membrane Biology*, pages 1–68. Springer, Boston, MA, 1974. ISBN 978-1-4615-7422-4. doi: 10.1007/978-1-4615-7422-4_1.

[103] Li, Q., editor. *Liquid Crystals Beyond Displays*. John Wiley & Sons, Ltd, 2012. ISBN 9781118078617.

[104] Aleš Iglič, Michael Rappolt, and Patricia Losada Perez. *Advances in bio-*

membranes and lipid self-assembly. Advances in biomembranes and lipid self-assembly. Academic Press, London, United Kingdom, 2024.

[105] A. Blume. Lipids at the air–water interface. *ChemTexts*, 4(1), 2018. doi: 10.1007/s40828-018-0058-z.

[106] V. M. Kaganer, H. Möhwald, and P. Dutta. Structure and phase transitions in langmuir monolayers. *Reviews of Modern Physics*, 71(3):779–819, 1999. doi: 10.1103/RevModPhys.71.779.

[107] E. Fahy, D. Cotter, M. Sud, and S. Subramaniam. Lipid classification, structures and tools. *Biochimica et Biophysica Acta*, 1811(11):637–647, 2011. doi: 10.1016/j.bbalip.2011.06.009.

[108] G. Cevc. How membrane chain-melting phase-transition temperature is affected by the lipid chain asymmetry and degree of unsaturation: an effective chain-length model. *Biochemistry*, 30(29):7186–7193, 1991. doi: 10.1021/bi00243a021.

[109] A. Blume. A comparative study of the phase transitions of phospholipid bilayers and monolayers. *Biochimica et Biophysica Acta*, 557(1):32–44, 1979. doi: 10.1016/0005-2736(79)90087-7.

[110] L. Wilhelmy. Ueber die abhängigkeit der capillaritäts–constanten des alkohols von substanz und gestalt des benetzten festen körpers. *Annalen der Physik*, 195(6):177–217, 1863. doi: 10.1002/andp.18631950602.

[111] K. Y. C. Lee. Collapse mechanisms of langmuir monolayers. *Annual Review of Physical Chemistry*, 59:771–791, 2008. doi: 10.1146/annurev.physchem.58.032806.104619.

[112] Z. Cai and S. A. Rice. Langmuir monolayers: structures and phase transitions. *Faraday Discussions of the Chemical Society*, 89:211, 1990. doi: 10.1039/DC9908900211.

[113] P. Dynarowicz-Łątka and K. Kita. Molecular interaction in mixed monolayers at the air/water interface. *Advances in Colloid and Interface Science*, 79(1): 1–17, 1999. doi: 10.1016/S0001-8686(98)00064-5.

[114] D. Vollhardt. Brewster angle microscopy: A preferential method for mesoscopic characterization of monolayers at the air/water interface. *Current Opinion in Colloid & Interface Science*, 19(3):183–197, 2014. doi: 10.1016/j.cocis.2014.02.001.

[115] K. Jacobson and D. Papahadjopoulos. Phase transitions and phase separations in phospholipid membranes induced by changes in temperature, ph, and concentration of bivalent cations. *Biochemistry*, 14(1):152–161, 1975. doi: 10.1021/bi00672a026.

[116] Charles Tanford. *The hydrophobic effect: formation of micelles and biological membranes*. New York, Wiley, 1973. ISBN 0471844608.

[117] J. N. Israelachvili, D. J. Mitchell, and B. W. Ninham. Theory of self-assembly of hydrocarbon amphiphiles into micelles and bilayers. *Journal of the Chemical Society, Faraday Transactions 2: Molecular and Chemical Physics*, 72(0):1525, 1976. doi: 10.1039/F29767201525.

[118] T. Kaasgaard, C. Leidy, J. H. Crowe, O. G. Mouritsen, and K. Jørgensen. Temperature-controlled structure and kinetics of ripple phases in one- and two-component supported lipid bilayers. *Biophysical Journal*, 85(1):350–360, 2003. doi: 10.1016/S0006-3495(03)74479-8.

[119] D. V. Soloviov, Yu E. Gorshkova, O. I. Ivankov, A. N. Zhigunov, L. A. Bulavin, V. I. Gordeliy, and A. I. Kuklin. Ripple phase behavior in mixtures of dppc/popc lipids: SAXS and sans studies. *Journal of Physics: Conference Series*, 351: 012010, 2012. doi: 10.1088/1742-6596/351/1/012010.

[120] W. Rawicz, K. C. Olbrich, T. McIntosh, D. Needham, and E. Evans. Effect of chain length and unsaturation on elasticity of lipid bilayers. *Biophysical Journal*, 79(1):328–339, 2000. doi: 10.1016/S0006-3495(00)76295-3.

[121] M Peikert, X. Chen, L. Chi, G. Brezesinski, S. Janich, E.-U. Würthwein, and H. J. Schäfer. Phase behavior and molecular packing of octadecyl phenols and their methyl ethers at the air/water interface. *Langmuir*, 30(20):5780–5789, 2014. doi: 10.1021/la404340h.

[122] G. M. M. El Maghraby, A. C. Williams, and B. W. Barry. Interactions of surfactants (edge activators) and skin penetration enhancers with liposomes. *International Journal of Pharmaceutics*, 276(1-2):143–161, 2004. doi: 10.1016/j.ijpharm.2004.02.024.

[123] S. Mabrey and J. M. Sturtevant. Investigation of phase transitions of lipids and lipid mixtures by sensitivity differential scanning calorimetry. *Proceedings of the National Academy of Sciences*, 73(11):3862–3866, 1976. doi: 10.1073/pnas.73.11.3862.

[124] R. N. McElhaney. The use of differential scanning calorimetry and differential thermal analysis in studies of model and biological membranes. *Chemistry and Physics of Lipids*, 30(2-3):229–259, 1982. doi: 10.1016/0009-3084(82)90053-6.

[125] R. L. Biltonen and D. Lichtenberg. The use of differential scanning calorimetry as a tool to characterize liposome preparations. *Chemistry and Physics of Lipids*, 64(1-3):129–142, 1993. doi: 10.1016/0009-3084(93)90062-8.

[126] M. H. Chiu and E. J. Prenner. Differential scanning calorimetry: An invaluable tool for a detailed thermodynamic characterization of macromolecules and their interactions. *Journal of Pharmacy & Bioallied Sciences*, 3(1):39–59, 2011. doi: 10.4103/0975-7406.76463.

[127] J. Penfold and R. K. Thomas. The application of the specular reflection of neutrons to the study of surfaces and interfaces. *Journal of Physics: Condensed Matter*, 2(6):1369–1412, 1990. doi: 10.1088/0953-8984/2/6/001.

[128] J. Daillant and A. Gibaud. *X-ray and neutron reflectivity: Principles and applications*, volume 770 of *Lecture Notes in Physics*. Springer, Berlin, 2nd ed. edition, 2009. ISBN 978-3-540-88587-0.

[129] J. J. Skrzypek and F. Rustichelli. *Innovative Technological Materials*. Springer Berlin Heidelberg, Berlin, Heidelberg, 2010. ISBN 978-3-642-12058-9. doi: 10.1007/978-3-642-12059-6.

[130] J. Als-Nielsen and D. McMorrow. *Elements of modern X-ray physics*. Wiley, Hoboken, 2nd ed. edition, 2011. ISBN 9780470973950.

[131] P. Lindner and J. Oberdisse, editors. *Neutrons, X-rays, and Light: Scattering Methods Applied to Soft Condensed Matter*. Elsevier, Chantilly, 2nd ed. edition, 2025. ISBN 9780443291173.

[132] O. H. Seeck and B. M. Murphy, editors. *X-ray diffraction: Modern experimental techniques*. Pan Stanford Publishing, Singapore, 2015. ISBN 9789814303590.

[133] J. Als-Nielsen, D. Jacquemain, K. Kjaer, F. Leveiller, M. Lahav, and L. Leiserowitz. Principles and applications of grazing incidence X-ray and neutron scattering from ordered molecular monolayers at the air-water interface. *Physics Reports*, 246(5):251–313, 1994. doi: 10.1016/0370-1573(94)90046-9.

[134] P. S. Pershan. The effects of surface profile and interface correlations on X-ray reflectivity from fluid interfaces. *Journal of Physics: Condensed Matter*, 6 (23A):A37–A50, 1994. doi: 10.1088/0953-8984/6/23A/005.

[135] S. Dietrich and A. Haase. Scattering of X-rays and neutrons at interfaces. *Physics Reports*, 260(1-2):1–138, 1995. doi: 10.1016/0370-1573(95)00006-3.

[136] K. Stoev and K. Sakurai. Recent theoretical models in grazing incidence X-ray reflectometry. *Rigaku Journal*, 14:22–37, 1997.

[137] J. Als-Nielsen, F. Christensen, and P. S. Pershan. Smectic- a order at the surface of a nematic liquid crystal: Synchrotron X-ray diffraction. *Physical Review Letters*, 48(16):1107–1110, 1982. doi: 10.1103/PhysRevLett.48.1107.

[138] P. S. Pershan and J. Als-Nielsen. X-ray reflectivity from the surface of a liquid crystal: Surface structure and absolute value of critical fluctuations. *Physical Review Letters*, 52(9):759–762, 1984. doi: 10.1103/PhysRevLett.52.759.

[139] P. S. Pershan. Liquid surface order: X-ray reflectivity. *Physica A: Statistical Mechanics and its Applications*, 231(1-3):111–116, 1996. doi: 10.1016/0378-4371(95)00456-4.

[140] L. Nevot and P. Croce. Characterization of surfaces by grazing X-ray reflection:

Application to the study of the polishing of various silicate glasses. *Physical Review Applied*, 15:761–779, 1980.

[141] H. Dosch. *Critical Phenomena at Surfaces and Interfaces: Evanescent X-ray and Neutron Scattering*. Springer Berlin / Heidelberg, Berlin, Heidelberg, 2006. ISBN 9783540384564.

[142] D. K. Schwartz, M. L. Schlossman, E. H. Kawamoto, G. J. Kellogg, P. S. Pershan, and B. M. Ocko. Thermal diffuse X-ray-scattering studies of the water-vapor interface. *Physical Review. A, Atomic, Molecular, and Optical Physics*, 41(10):5687–5690, 1990. doi: 10.1103/physreva.41.5687.

[143] D. Vaknin, W. Bu, J. Sung, Y. Jeon, and D. Kim. Thermally excited capillary waves at vapor/liquid interfaces of water-alcohol mixtures. *Journal of Physics: Condensed Matter*, 21(11):115105, 2009. doi: 10.1088/0953-8984/21/11/115105.

[144] L. G. Parratt. Surface studies of solids by total reflection of X-rays. *Physical Review*, 95(2):359–369, 1954. doi: 10.1103/PhysRev.95.359.

[145] J. H. Hubbell, Wm. J. Veigele, E. A. Briggs, R. T. Brown, D. T. Cromer, and R. J. Howerton. Atomic form factors, incoherent scattering functions, and photon scattering cross sections. *Journal of Physical and Chemical Reference Data*, 4(3):471–538, 1975. doi: 10.1063/1.555523.

[146] V. F. Sears. Neutron scattering lengths and cross sections. *Neutron News*, 3 (3):26–37, 1992.

[147] B. L. Henke, E. M. Gullikson, and J. C. Davis. X-ray Interactions: Photoabsorption, Scattering, Transmission, and Reflection at E = 50-30,000 eV, Z = 1-92. *Atomic Data and Nuclear Data Tables*, 54(2):181–342, 1993. doi: 10.1006/adnd.1993.1013.

[148] G. I. King and S. H. White. Determining bilayer hydrocarbon thickness from neutron diffraction measurements using strip-function models. *Biophysical Journal*, 49(5):1047–1054, 1986. doi: 10.1016/S0006-3495(86)83733-X.

[149] A. V. Garmay, K. V. Oskolok, O. V. Monogarova, and N. V. Alov. Total reflection X-ray fluorescence analysis of highly mineralized water samples using relative intensities and scattered radiation. *Spectrochimica Acta Part B: Atomic Spectroscopy*, 152:74–83, 2019. doi: 10.1016/j.sab.2018.12.011.

[150] K. Kjaer, J. Als-Nielsen, C. A. Helm, L. Laxhuber, and H. Möhwald. Ordering in lipid monolayers studied by synchrotron X-ray diffraction and fluorescence microscopy. *Physical Review Letters*, 58(21):2224–2227, 1987. doi: 10.1103/PhysRevLett.58.2224.

[151] K. Kjaer. Some simple ideas on X-ray reflection and grazing-incidence diffraction from thin surfactant films. *Physica B: Condensed Matter*, 198(1-3): 100–109, 1994. doi: 10.1016/0921-4526(94)90137-6.

[152] G. Brezesinski, M. Thoma, B. Struth, and H. Möhwald. Structural changes of monolayers at the air/water interface contacted with n -alkanes. *The Journal of Physical Chemistry*, 100(8):3126–3130, 1996. doi: 10.1021/jp952117t.

[153] J. Majewski, T. L. Kuhl, J. Y. Wong, and G. S. Smith. X-ray and neutron surface scattering for studying lipid/polymer assemblies at the air-liquid and solid-liquid interfaces. *Journal of Biotechnology*, 74(3):207–231, 2000. doi: 10.1016/s1389-0352(00)00011-8.

[154] V. M. Kaganer, I. R. Peterson, R. M. Kenn, M. C. Shih, M. Durbin, and P. Dutta. Tilted phases of fatty acid monolayers. *The Journal of Chemical Physics*, 102(23):9412–9422, 1995. doi: 10.1063/1.468809.

[155] C. Stefaniu, V. M. Latza, O. Gutowski, P. Fontaine, G. Brezesinski, and E. Schneck. Headgroup-ordered monolayers of uncharged glycolipids exhibit selective interactions with ions. *The Journal of Physical Chemistry Letters*, 10 (8):1684–1690, 2019. doi: 10.1021/acs.jpclett.8b03865.

[156] C. J. Gommes, S. Jaksch, and H. Frielinghaus. Small-angle scattering for beginners. *Journal of Applied Crystallography*, 54(Pt 6):1832–1843, 2021. doi: 10.1107/S1600576721010293.

[157] P. V. Konarev, A. Yu Gruzinov, H. D. T. Mertens, and D. I. Svergun. Restoring structural parameters of lipid mixtures from small-angle X-ray scattering data. *Journal of Applied Crystallography*, 54(Pt 1):169–179, 2021. doi: 10.1107/S1600576720015368.

[158] A. Guinier and G. Fournet. *Small-angle Scattering of X-rays*. John Wiley & Sons, Ltd, New York, 1955.

[159] G. Porod. Die röntgenkleinwinkelstreuung von dichtgepackten kolloiden systemen. *Colloid and Polymer Science*, 124(2):83–114, 1951. doi: 10.1007/BF01512792.

[160] D.K.G. de Boer and W. W. van den Hoogenhof. Total reflection X-ray fluorescence of single and multiple thin-layer samples. *Spectrochimica Acta Part B: Atomic Spectroscopy*, 46(10):1323–1331, 1991. doi: 10.1016/0584-8547(91)80181-2.

[161] R. Klockenkamper, J. Knoth, A. Prange, and H. Schwenke. Total-reflection X-ray fluorescence. *Analytical chemistry*, 64(23):1115A–1123A, 1992. doi: 10.1021/ac00047a001.

[162] R. Klockenkämper and A. von Bohlen. *Total-reflection X-ray fluorescence analysis and related methods*. Wiley, Hoboken New Jersey, second edition edition, 2015. ISBN 9781118460276.

[163] A. Prange. Total reflection X-ray spectrometry: method and applications.

Spectrochimica Acta Part B: Atomic Spectroscopy, 44(5):437–452, 1989. doi: 10.1016/0584-8547(89)80049-7.

[164] H. Schwenke, R. Gutschke, J. Knoth, and M. Kock. Treatment of roughness and concentration gradients in total reflection X-ray fluorescence analysis of surfaces. *Applied Physics*, 54(5):460–465, 1992. doi: 10.1007/BF00324172.

[165] M. Eichhorn. *Laserphysik*. Springer Berlin Heidelberg, Berlin, Heidelberg, 2013. ISBN 978-3-642-32647-9.

[166] J. J. Degnan. The waveguide laser: A review. *Applied Physics B*, 11(1):1–33, 1976. doi: 10.1007/BF00895012.

[167] B. Eicher, F. A. Heberle, D. Marquardt, G. N. Rechberger, J. Katsaras, and G. Pabst. Joint small-angle X-ray and neutron scattering data analysis of asymmetric lipid vesicles. *Journal of Applied Crystallography*, 50(Pt 2):419–429, 2017. doi: 10.1107/S1600576717000656.

[168] D. E. Spence, P. N. Kean, and W. Sibbett. 60-fsec pulse generation from a self-mode-locked ti:sapphire laser. *Optics Letters*, 16(1):42–44, 1991. doi: 10.1364/OL.16.000042.

[169] H. Sun, J. Li, M. Liu, D. Yang, and F. Li. A review of effects of femtosecond laser parameters on metal surface properties. *Coatings*, 12(10):1596, 2022. doi: 10.3390/coatings12101596.

[170] X. Wang, H. Yu, P. Li, Y. Zhang, Y. Wen, Y. Qiu, Z. Liu, Y. Li, and L. Liu. Femtosecond laser-based processing methods and their applications in optical device manufacturing: A review. *Optics & Laser Technology*, 135:106687, 2021. doi: 10.1016/j.optlastec.2020.106687.

[171] D. Sands. Pulsed laser heating and melting. In *Heat Transfer - Engineering Applications*. InTech, 2011. ISBN 978-953-307-361-3.

[172] E. Rabinowitch. Electron transfer spectra and their photochemical effects. *Reviews of Modern Physics*, 14(2-3):112–131, 1942. doi: 10.1103/RevModPhys.14.112.

[173] M J. Blandamer and M. F. Fox. Theory and applications of charge-transfer-to-solvent spectra. *Chemical Reviews*, 70(1):59–93, 1970. doi: 10.1021/cr60263a002.

[174] G. Markovich, S. Pollack, R. Giniger, and O. Cheshnovsky. Photoelectron spectroscopy of Cl−, Br−, and I− solvated in water clusters. *The Journal of Chemical Physics*, 101(11):9344–9353, 1994. doi: 10.1063/1.467965.

[175] X. Chen and S. E. Bradforth. The ultrafast dynamics of photodetachment. *Annual Review of Physical Chemistry*, 59(Volume 59, 2008):203–231, 2008. doi: 10.1146/annurev.physchem.58.032806.104702.

[176] H. Iglev, A. Trifonov, A. Thaller, I. Buchvarov, T. Fiebig, and A. Laubereau. Photoionization dynamics of an aqueous iodide solution: the temperature dependence. *Chemical Physics Letters*, 403(1-3):198–204, 2005. doi: 10.1016/j.cplett.2005.01.014.

[177] T. W. Marin, I. Janik, and D. M. Bartels. Ultraviolet charge-transfer-to-solvent spectroscopy of halide and hydroxide ions in subcritical and supercritical water. *Physical Chemistry Chemical Physics*, 21(44):24419–24428, 2019. doi: 10.1039/C9CP03805A.

[178] M. Sud, E. Fahy, D. Cotter, A. Brown, E. A. Dennis, C. K. Glass, A. H. Merrill, R. C. Murphy, C. R. H. Raetz, D. W. Russell, and S. Subramaniam. Lmsd: Lipid maps structure database. *Nucleic Acids Research*, 35:D527–32, 2007. doi: 10.1093/nar/gkl838.

[179] O. S. Andersen and R. E. Koeppe. Bilayer thickness and membrane protein function: an energetic perspective. *Annual Review of biophysics and biomolecular structure*, 36:107–130, 2007. doi: 10.1146/annurev.biophys.36.040306.132643.

[180] C. Tanford. Micelle shape and size. *The Journal of Physical Chemistry*, 76 (21):3020–3024, 1972. doi: 10.1021/j100665a018.

[181] C. A. Helm, H. Möhwald, K. Kjaer, and J. Als-Nielsen. Phospholipid monolayers between fluid and solid states. *Biophysical Journal*, 52(3):381–390, 1987. doi: 10.1016/S0006-3495(87)83226-5.

[182] F. Reise, J. E. Warias, K. Chatterjee, N. R. Krekiehn, O. Magnussen, B. M. Murphy, and T. K. Lindhorst. Photoswitchable glycolipid mimetics: Synthesis and photochromic properties of glycoazobenzene amphiphiles. *Chemistry A European Journal*, 24(66):17497–17505, 2018. doi: 10.1002/chem.201803112.

[183] J. E. Warias, L. Petersdorf, S. C. Hövelmann, R. P. Giri, C. Lemke, S. Festersen, M. Greve, P. Mandin, D. LeBideau, F. Bertram, O. M. Magnussen, and B. M. Murphy. The laser pump X-ray probe system at lisa p08 petra iii. *Journal of Synchrotron Radiation*, 31(Pt 4):779–790, 2024. doi: 10.1107/S1600577524003400.

[184] S. C. Hövelmann. Collection of python scripts for analysis of X-ray and neutron scattering data, Langmuir isotherms, differential scanning calorimetery data. 2025. URL `https://codebase.helmholtz.cloud/lisa/publications/2025-hoevelmann-dissertation`.

[185] S. C. Hövelmann and B. M. Murphy. SAXS and DSC data and scripts for publication: Photoinduced bidirectional mesophase transition in vesicles containing azobenzene amphiphiles. 2024. doi: 10.57892/100-49.

[186] M. D. Wilkinson, M. Dumontier, I. J. J. Aalbersberg, G. Appleton, M. Axton, A. Baak, N. Blomberg, J.-W. Boiten, L. B. Da Silva Santos, P. E. Bourne, J. Bouwman, A. J. Brookes, T. Clark, M. Crosas, I. Dillo, O. Dumon, S. Ed-

munds, C. T. Evelo, R. Finkers, A. Gonzalez-Beltran, A. J. G. Gray, P. Groth, C. Goble, J. S. Grethe, J. Heringa, P. A. C. 't Hoen, R. Hooft, T. Kuhn, R. Kok, J. Kok, S. J. Lusher, M. E. Martone, A. Mons, A. L. Packer, B. Persson, P. Rocca-Serra, M. Roos, R. van Schaik, S.-A. Sansone, E. Schultes, T. Sengstag, T. Slater, G. Strawn, M. A. Swertz, M. Thompson, J. van der Lei, E. van Mulligen, J. Velterop, A. Waagmeester, P. Wittenburg, K. Wolstencroft, J. Zhao, and B. Mons. The fair guiding principles for scientific data management and stewardship. *Scientific Data*, 3(1):160018, 2016. doi: 10.1038/sdata.2016.18.

[187] Wiebke Lohstroh, Frank Weber, Sebastian Busch, Heike Görzig, Bridget M. Murphy, Paola Coan, Hafiz Fahad, Markus Osterhoff, Yuliia Tymoshenko, Sebastian Paripsa, Astrid Schneidewind, and Christoph Herb. DAPHNE4NFDI - Draft recommendations on metadata capture and specifications. 2024. doi: 10.5281/ZENODO.12169109.

[188] A. Barty, C. Gutt, W. Lohstroh, B. M. Murphy, A. Schneidewind, J.-D. Grunwaldt, F. Schreiber, S. Busch, T. Unruh, M. Bussmann, H. Fangohr, H. Görzig, A. Houben, T. Kluge, I. Manke, D. Lützenkirchen-Hecht, T. R. Schneider, F. Weber, G. Bruno, O. Einsle, C. Felder, E. M. Herzig, U. Konrad, H. Marköter, K. Rossnagel, T. Sheppard, and D. Turchinovich. DAPHNE4NFDI - Consortium Proposal. 2023. doi: 10.5281/zenodo.8040605.

[189] J. E. Warias. *Aufbau und Test der Optical Pump – X-Ray Probe Option des „Liquide Interface Scattering Apparatus" an PETRA III*. Master's thesis, Kiel University, 2015.

[190] A. Thompson, D. Attwood, E. Gullikson, M. Howells, K.-J. Kim, J. Kirz, J. Kortright, I. Lindau, Y. Liu, P. Pianetta, A. Robinson, J. Scofield, J. Underwood, G. Williams, and H. Winick. *X-ray Data Booklet*. Center for X-ray Optics and Advanced Light Source, Lawrence Berkeley National Laboratory University of California Berkeley, CA 94720, 3rd edition, 2009.

[191] D. M. Smilgies, N. Boudet, B. Struth, and O. Konovalov. Troika II: a versatile beamline for the study of liquid and solid interfaces. *Journal of Synchrotron Radiation*, 12(Pt 3):329–339, 2005. doi: 10.1107/S0909049505000361.

[192] S. C. Hövelmann, L. Petersdorf, L. Pithan, S. I. Reinheimer, and K. Steinkirchner. Kinetics of photo-switching in lipid monolayers containing DPPC and azobenzene-glycolipids [Dataset]. *European Synchrotron Radiation Facility*, 2026. doi: 10.15151/ESRF-ES-1306470976.

[193] N. L. Yamada, N. Torikai, K. Mitamura, H. Sagehashi, S. Sato, H. Seto, T. Sugita, S. Goko, M. Furusaka, T. Oda, M. Hino, T. Fujiwara, H. Takahashi, and A. Takahara. Design and performance of horizontal-type neutron reflectometer

sofia at j-parc/mlf. *The European Physical Journal Plus*, 126(11):1–13, 2011. doi: 10.1140/epjp/i2011-11108-7.

[194] K. Mitamura, N. L. Yamada, H. Sagehashi, N. Torikai, H. Arita, M. Terada, M. Kobayashi, S. Sato, H. Seto, S. Goko, M. Furusaka, T. Oda, M. Hino, H. Jinnai, and A. Takahara. Novel neutron reflectometer sofia at j-parc/mlf for in-situ soft-interface characterization. *Polymer Journal*, 45(1):100–108, 2013. doi: 10.1038/pj.2012.156.

[195] A. R. J. Nelson and S. W. Prescott. refnx: neutron and X-ray reflectometry analysis in python. *Journal of Applied Crystallography*, 52(Pt 1):193–200, 2019. doi: 10.1107/S1600576718017296.

[196] M. Dargasz, J. Bolle, A. Faulstich, E. Schneider, M. Kowalski, C. Sternemann, J. Savelkouls, Bridget M. Murphy, and M. Paulus. X-ray scattering at beamline bl2 of delta: Studies of lysozyme-lysozyme interaction in heavy water and structure formation in 1-hexanol. *Journal of Physics: Conference Series*, 2380 (1):012031, 2022. doi: 10.1088/1742-6596/2380/1/012031.

[197] A. P. Hammersley, S. O. Svensson, A. Thompson, H. Graafsma, Å. Kvick, and J. P. Moy. Calibration and correction of distortions in two-dimensional detector systemsa). *Review of Scientific Instruments*, 66(3):2729–2733, 1995. doi: 10.1063/1.1145618.

[198] A. P. Hammersley, S. O. Svensson, M. Hanfland, A. N. Fitch, and D. Hausermann. Two-dimensional detector software: From real detector to idealised image or two-theta scan. *High Pressure Research*, 14(4-6):235–248, 1996. doi: 10.1080/08957959608201408.

[199] A. P. Hammersley. Fit2d: An introduction and overview', 1997.

[200] A. P. Hammersley. Fit2d : a multi-purpose data reduction, analysis and visualization program. *Journal of Applied Crystallography*, 49(2):646–652, 2016. doi: 10.1107/S1600576716000455.

[201] S. T. Hyde. Identification of lyotropic liquid crystalline mesophases. *Handbook of Applied Surface and Colloid Chemistry*, pages edited by Krister Holmberg, pp. 299–327, John Wiley & Sons, Ltd, 2001.

[202] K. Hansen. *Schaltverhalten von Azobenzene - Glycolipiden in Langmuir Monolagen*. Bachelor's thesis, Kiel University, 2020.

[203] S. I. Reinheimer. *Abhängigkeit des Schaltverhaltens der Azobenzen-Glycolipide von der polaren Gruppe der Phospholipide in Langmuir-Monolagen*. Bachelor's thesis, Kiel University, 2023.

[204] E. Dieball. *Untersuchungen an photoschaltbaren Vesikeln mittels Kleinwinkel-Röntgenstreuung*. Bachelor's thesis, Kiel University, 2022.

[205] K. Steinkirchner. *Langmuir-Isotherm Untersuchungen von Lichtsammelkomplex II in Phospholipidmonolagen*. Bachelor's thesis, Kiel University, 2023.

[206] G. F. Frahm. *VSFG-Spektroskopische Untersuchung photoschaltbarer gemischter Azobenzolglykolipid/DPPC-Monolagen*. Bachelor's thesis, Kiel University, 2022.

[207] Jule Kuhn. Untersuchung photoschaltbarer vesikel mittels kleinwinkelröntgenstreuung, 2024.

[208] A. M. March, A. Stickrath, G. Doumy, E. P. Kanter, B. Krässig, S. H. Southworth, K. Attenkofer, C. A. Kurtz, L. X. Chen, and L. Young. Development of high-repetition-rate laser pump/X-ray probe methodologies for synchrotron facilities. *Review of Scientific Instruments*, 82(7):073110, 2011. doi: 10.1063/1.3615245.

[209] H. Navirian, R. Shayduk, W. Leitenberger, J. Goldshteyn, P. Gaal, and M. Bargheer. Synchrotron-based ultrafast X-ray diffraction at high repetition rates. *Review of Scientific Instruments*, 83(6):063303, 2012. doi: 10.1063/1.4727872.

[210] H. Wang, C. Yu, X. Wei, Z. Gao, G. L. Xu, R. Da Sun, Z. Li, Y. Zhou, Q. J. Li, B. B. Zhang, J. Q. Xu, L. Wang, Y. Zhang, Y. Lei Tan, and Y. Tao. Development of picosecond time-resolved X-ray absorption spectroscopy by high-repetition-rate laser pump/X-ray probe at Beijing Synchrotron Radiation Facility. *Journal of Synchrotron Radiation*, 24(Pt 3):667–673, 2017. doi: 10.1107/S1600577517003277.

[211] M. Burian, B. Marmiroli, A. Radeticchio, C. Morello, D. Naumenko, G. Biasiol, and H. Amenitsch. Picosecond pump-probe X-ray scattering at the elettra SAXS beamline. *Journal of Synchrotron Radiation*, 27(Pt 1):51–59, 2020. doi: 10.1107/S1600577519015728.

[212] M. Wullf, A. Plech, L. Eybert, R. Randler, F. Schotte, and P. Anfinrud. The realization of sub-nanosecond pump and probe experiments at the ESRF. European Synchrotron Radiation Facility. *Faraday Discussions*, 122:13–26; discussion 79–88, 2003. doi: 10.1039/B202740M.

[213] D. Issenmann, S. Ibrahimkutty, R. Steininger, J. Göttlicher, T. Baumbach, N. Hiller, A-S Müller, and A. Plech. Ultrafast laser pump X-ray probe experiments by means of asynchronous sampling. *Journal of Physics: Conference Series*, 425(9):092007, 2013. doi: 10.1088/1742-6596/425/9/092007.

[214] H. Enquist, A. Jurgilaitis, A. Jarnac, Å. U. J. Bengtsson, M. Burza, F. Curbis, C. Disch, J. C. Ekström, M. Harb, L. Isaksson, M. Kotur, D. Kroon, F. Lindau, E. Mansten, J. Nygaard, A. I. H. Persson, T. van Pham, M. Rissi, S. Thorin, C. M. Tu, E. Wallén, X. Wang, S. Werin, and J. Larsson. Femtomax - an X-ray beamline for structural dynamics at the short-pulse facility

of max iv. *Journal of Synchrotron Radiation*, 25(Pt 2):570–579, 2018. doi: 10.1107/S1600577517017660.

[215] C. Laulhé, M. Cammarata, M. Servol, R. J. Dwayne Miller, M. Hada, and S. Ravy. Impact of laser on bismuth thin-films. *The European Physical Journal Special Topics*, 222(5):1277–1285, 2013. doi: 10.1140/epjst/e2013-01922-0.

[216] Y. Fukuyama, N. Yasuda, J. Kim, H. Murayama, T. Ohshima, Y. Tanaka, S. Kimura, H. Kamioka, Y. Moritomo, K. Toriumi, H. Tanaka, K. Kato, T. Ishikawa, and M. Takata. Ultra-high-precision time control system over any long time delay for laser pump and synchrotron X-ray probe experiment. *Review of Scientific Instruments*, 79(4):045107, 2008. doi: 10.1063/1.2906232.

[217] M. Reinhard, D. Skoien, J. A. Spies, A. T. Garcia-Esparza, B. D. Matson, J. Corbett, K. Tian, J. Safranek, E. Granados, M. Strader, K. J. Gaffney, R. Alonso-Mori, T. Kroll, and D. Sokaras. Solution phase high repetition rate laser pump X-ray probe picosecond hard X-ray spectroscopy at the stanford synchrotron radiation lightsource. *Structural Dynamics (Melville, N.Y.)*, 10 (5):054304, 2023. doi: 10.1063/4.0000207.

[218] International Organization for Standardization 2018 Optics and photonics. Optics and photonics — Lasers and laser-related equipment — Test methods for laser beam power (energy) density distribution (ISO 13694-3:2018), 2018.

Acronyms

CPP critical packing parameter

SLD scattering length density

AZ-R 4-Hydroxy-4'-propargyloxy azobenzene

AZGL-C12 (E)-[*p*-[(1,2-Didodecanoyloxycarbonyl)propyloxy]-*p*′-[(2-{2-[2-(1-ethoxy-4-methoxy-1,2,3-triazolyl)]ethoxy}ethyl)-β-D-glucopyranosyloxy]]azobenzene

AZGL-C16 (E)-[*p*-[(1,2-Dihexadecanoyloxycarbonyl)propyloxy]-*p*′-[(2-{2-[2-(1-ethoxy-4-methoxy-1,2,3-triazolyl)]ethoxy}ethyl)-β-D-glucopyranosyloxy]]azobenzene

AZGL-S-C16 1-*O*-(4-(4-(*S*-β-D-Glucopyranosyl)thiophenyldiazenyl)benzene)-2,3-di-*O*-hexadecanoyl-*rac*-glycero

AZLL-C12 (E)-[*p*-[(1,2-Didodecanoyloxycarbonyl)propyloxy]-*p*′-[(2-{2-[2-(1-ethoxy-4-methoxy-1,2,3-triazolyl)]ethoxy}ethyl)-β-D-galactopyranosyl-(1→4)β-D-glucopyranosyloxy]]azobenzene

AZLL-C16 (*E*)-[*p*-[(1,2-Dihexadecanoyloxycarbonyl)propyloxy]-*p*′-[(2-{2-[2-(1-ethoxy-4-methoxy-1,2,3-triazolyl)]ethoxy}ethyl)-β-D-galactopyranosyl-(1→4)β-D-glucopyranosyloxy]]azobenzene

AZOL-C12 (E)-[*p*-[(1,2-Didodecanoyloxycarbonyl)propyloxy]-*p*′-(2-{2-[2-(1-ethoxy-4-methoxy-1,2,3-triazolyl)]ethoxy}ethyl)]azobenzene

AZOL-C16 (E)-[*p*-[(1,2-Dihexadecanoyloxycarbonyl)propyloxy]-*p*′-(2-{2-[2-(1-ethoxy-4-methoxy-1,2,3-triazolyl)]ethoxy}ethyl)]azobenzene

CTTS charge-transfer-to-solvent

CW continuous wave

DELTA Dortmund Electron Accelerator

DESY Deutsches Elektronen-Synchrotron

DLPC 1,2-Dilauroyl-*sn*-glycero-3-phosphocholine

DOE diffractive optical element

DPPA 1,2-Dipalmitoyl-*sn*-glycero-3-phosphate

DPPC 1,2-Dipalmitoyl-*sn*-glycero-3-phosphocholine

DPPE 1,2-Dipalmitoyl-*sn*-glycero-3-phosphoethanolamine

DPPG 1,2-Dipalmitoyl-*sn*-glycero-3-phosphoglycerol

DSC differential scanning calorimetry

EMBL European Molecular Biology Laboratory

ESRF European Synchrotron Radiation Facility

FWHM full width half maximum

GID grazing incidence diffraction

GL-C12 1-{2-[2-(2-(β-D-Glucopyranosyloxy)ethoxy)ethoxy]ethyl]}-4-{[(1,2-didodecanoyloxycarbonyl)propyloxy]methoxy}-1,2,3-triazole

GL-C16 1-{2-[2-(2-(β-D-Glucopyranosyloxy)ethoxy)ethoxy]ethyl]}-4-{[(1,2-dihexadecanoyloxycarbonyl)propyloxy]methoxy}-1,2,3-triazole

HBr(aq) hydrobromic acid

HCl(aq) hydrochloric acid

HEREON Helmholtz-Zentrum Hereon

HI(aq) hydroiodic acid

IGSN International Generic Sample Number

J-PARC Japan Proton Accelerator Research Complex

LISA Liquid Interface Scattering Apparatus

LL-C12 1-{2-[2-(2-((β-D-Galactopyranosyl-(1→4)β-D-glucopyranosyloxy)ethoxy)ethoxy]ethyl]}-4-{[(1,2-didodecanoyloxycarbonyl)propyloxy]methoxy}-1,2,3-triazole

LL-C16 1-2-[2-(2-(β-D-Galactopyranosyl-(1→44)β-D-glucopyranosyloxy)ethoxy)ethoxy]ethyl]-4-[(1,2-dihexadecanoyloxycarbonyl)propyloxy]methoxy-1,2,3-triazole

MCMC Markov Chain Monte Carlo

MD molecular dynamics

MLV multilamellar vesicle

NaCl sodium chloride

NaI sodium iodide

NaOH (aq) sodium hydroxide

NMR nuclear magnetic resonance

NR neutron reflectivity

OL-C12 1-{2-[2-(2-Hydroxyethoxy)ethoxy]ethyl]}-4-{[(1,2-didodecanoyloxy-carbonyl)propyloxy]methoxy}-1,2,3-triazole

OL-C16 1-{2-[2-(2-Hydroxyethoxy)ethoxy]ethyl]}-4-{[(1,2-dihexadecanoyloxy-carbonyl)propyloxy]methoxy}-1,2,3-triazole

PP pulse picker

RA regenerative amplifier

RbBr rubidium bromide

RbOH (aq) rubidium hydroxide

ROI region of interest

SAXS small angle X-ray scattering

SFG sum frequency generation

SHG second-harmonic generation

ULV unilamellar vesicle

VSFG vibrational sum frequency generation

XRFNTR X-ray fluorescence near total reflection

XRR X-ray reflectivity

Eidesstadliche Erklärung

Hiermit erkläre ich, dass

1. die vorliegende Arbeit – abgesehen von der Beratung durch meine Betreuerin PD Dr. Bridget M. Murphy und den angegebenen Hilfsmitteln – nach Inhalt und Form die eigene Arbeit ist;

2. die Arbeit weder ganz noch zum Teil im Rahmen eines Prüfungsverfahrens vorgelegen hat oder vorliegt;

3. Teile der Arbeit im Fachmagazin *IUCrJ*, *Journal of Applied Crystallography* und *Journal of Physics: Conference Series* veröffentlicht worden sind;

4. die Arbeit unter Einhaltung der Regeln guter wissenschaftlicher Praxis der Deutschen Forschungsgemeinschaft entstanden ist;

5. mir kein akademischer Grad entzogen wurde.

Kiel, den

Svenja C. Hövelmann

Wissenschaftliche Beiträge / Eigenanteil

Im Laufe dieser Arbeit sind die folgenden Veröffentlichungen in Fachzeitschriften erfolgt. Zudem wurden die unten stehenden wissenschaftlichen mündliche Vorträge und Posterpräsentationen auf Konferenzen gehalten.
Der Eigenanteil bei den Veröffentlichungen wird in den folgenden sechs Abreitsbereichen mit jeweils einem Wert zwischen 0 (kein Arbeitsanteil) und 10 (vollständig) eingeschätzt:

- Experimentelles Konzept
- Planung/ Vorbereitung
- Messung
- Auswertung
- Texterstellung
- Korrektur und Finalisierung

Die Bewertung des Eigenanteils ist eine subjektive Einschätzung des erbrachten Arbeitsanteils nach bestem Wissen und Gewissen und spiegelt nicht zwangsläufig die Einschätzung der beteiligten Koautoren wider.

Veröffentlichungen in Fachzeitschriften und Manuskripte:

[**PSH 1**] Hövelmann, S. C., Dieball, E., Kuhn, J., Dargasz, M., Giri, R. P., Reise, F., Paulus, M., Lindhorst, T. K. & Murphy, B. M. (2024). Photoinduced bidirectional mesophase transition in vesicles containing azobenzene amphiphiles. *IUCrJ*, **11**, 4. DOI: 10.1107/S2052252524004032

Konzept	Planung	Messung	Auswertung	Manuskript	Korrektur
7/10	9/10	9/10	9/10	8/10	9/10

[**PSH 2**] Hövelmann, S. C., Warias, J. E., Petersdorf, L., Schmidt, D., Gaal, P., Giri, R. P., Hayen, N.m Jordt, P., Magnussen, O. M., Shen, C., Bertram, F. & Murphy, B. M. (2025). Extending the laser pump -X-ray probe system at LISA P08 PETRA III. *Journal of Physics: Conference Series (JPCS) 3010, in print.*

Konzept	Planung	Messung	Auswertung	Manuskript	Korrektur
6/10	7/10	7/10	8/10	8/10	8/10

[**MSH 1**] Hövelmann, S. C., Röhrl, M., Dieball, E., Dargasz, M., Kuhn, J., Giri, R. P., Reise, F., Soloviov, D., Blanchet, C. F., Paulus, M., Lindhorst, T. K. & Murphy, B. M. (2025). Kinetics of light induced mesophase transitions in azobenzene amphiphiles containing lyotropic crystals. *Manuscript submitted.*

Konzept	Planung	Messung	Auswertung	Manuskript	Korrektur
7/10	9/10	8/10	9/10	8/10	7/10

[**MSH 2**] Kobus, J., Hövelmann, S. C., Petersdorf, L., Jordt, P., Hayen, N., Shen, C., Bertram, F., Magnussen, O. M., Giri, R. P. & Murphy, B. M. Laser excitation at the liquid-air interface of aqueous NaI solutions. *Manuscript submitted.*

Konzept	Planung	Messung	Auswertung	Manuskript	Korrektur
6/10	5/10	8/10	5/10	5/10	4/10

[**MSH 3**] Hövelmann, S. C., Warias, J., Hansen, K., Kuhn, J., Sartori, A., Jordt, P., Giri, R. P., Reise, F., Arnold, T., Rennie A., Lindhorst, T. K. & Murphy, B. M. Light-induced reorientation of the sugar head group of photoswitchable glycolipids in phospholipid monolayers. *Manuscript.*

Konzept	Planung	Messung	Auswertung	Manuskript	Korrektur
6/10	8/10	8/10	9/10	7/10	-

Im Rahmen dieser Arbeit wurde an weiteren Publikationen mitgewirkt, die jedoch nicht als Grundlage dieser Dissertation dienen. Bei den ersten zwei Publikationen in der folgenden Liste, war der Anteil der Mitwirkung besonders groß. Die zusätzlichen Publikationen sind der Vollständigkeit halber chronologisch aufgeführt:

Warias, J. E., Reise, F., Hövelmann, S. C., Giri, R. P., Röhrl, M., Kuhn, J., Jacobsen, M., Kuntal C., Arnold, T., Shen, C., Festersen, S., Sartori, A., Jordt, P., Magnussen, O. M., Lindhorst, T. K. & Murphy, B. M. (2023). Photoinduced bidirectional switching in lipid membranes containing azobenzene glycolipids. *Scientific reports*, **13**, 11480.

Konzept	Planung	Messung	Auswertung	Manuskript	Korrektur
0/10	0/10	4/10	3/10	1/10	3/10

Warias, J. E., Petersdorf, L., Hövelmann, S. C., Giri, R. P., Lemke, C., Festersen, S., Greve, M., Mandin, P., LeBideau, D., Bertram, F., Magnussen, O. M. & Murphy, B. M. (2024). The laser pump X-ray probe system at LISA P08 PETRA III. *Journal of Synchrotron Radiation*, **31**, 4.

Konzept	Planung	Messung	Auswertung	Manuskript	Korrektur
0/10	0/10	4/10	3/10	3/10	4/10

Sartori, A., Giri, R. P., Fujii, H., Hövelmann, S. C., Warias, J. E., Jordt, P., Shen, C., Murphy, B. M. & Magnussen O., M. (2022). Role of chemisorbing species in growth at liquid metal-electrolyte interfaces revealed by in situ X-ray scattering. *Nature communications*, **13**, 5421.

Konzept	Planung	Messung	Auswertung	Manuskript	Korrektur
0/10	0/10	1/10	0/10	0/10	1/10

Striker, N. N., Lokteva, I., Dartsch, M., Dallari, F., Goy, C., Westermeier, F., Markmann, V., Hövelmann, S. C., Grübel, G. & Lehmkühler, F. (2023). Dynamics and Time Scales of Higher-Order Correlations in Supercooled Colloidal Systems.

Journal of Physical Chemistry Letters, **14**, 20.

Konzept	Planung	Messung	Auswertung	Manuskript	Korrektur
0/10	0/10	1/10	0/10	1/10	1/10

Hayen, N., Jordt, P., Hövelmann, S. C., Petersdorf, L., Mewes, M., Thormählen L., Meyners, D., Sun, N. X., Sternemann, C., Paulus, M., Lützenkirchen-Hecht & D., Murphy, B. M. (2024). In Situ X-Ray Absorption Studies on Local Structure of Annealed Metallic Glasses FeGaB and FeCoSiB. *Physica Status Solidi A*, **2400607**.

Konzept	Planung	Messung	Auswertung	Manuskript	Korrektur
0/10	0/10	1/10	0/10	1/10	1/10

Amelung, L., Barty, A., Murphy, B. M., Grunwaldt, J.-D., Hövelmann, S. C., Leonau, A., Paripsa, S., Schneidewind, A., Busch, S., Gutt, C., Lohstroh, W., Schreiber, F., Unruh & Unruh, T. (2025). DAPHNE4NFDI - Improving Research data management at Synchrotron Facilities. *Journal of Physics: Conference Series (JPCS) 3010, in print.*

Konzept	Planung	Messung	Auswertung	Manuskript	Korrektur
1/10	2/10	NA	NA	3/10	2/10

Bauer, R. P. C., Gierke, A., Goy, C., Pudell, J.-E., Jo, W., Valerio, J., Adriano, L„ Möller, J., Wrigley, J., Boesenberg, U., Rodriguez-Fernandez, A., Shayduk, R., Youssef3, M., Striker, N. N., Giesselmann, N. C., Hövelmann, S. C., Roseker, W., Ayyer, K., Paulus, M., Sternemann, C., Grisenti, R. E., Madsen, A., Schulz, J. & Lehmkühler, F. (2025). Femtosecond pulse pair distribution functions at MID at the European XFEL. *Journal of Physics: Conference Series (JPCS) 3010, in print.*

Konzept	Planung	Messung	Auswertung	Manuskript	Korrektur
0/10	0/10	1/10	0/10	1/10	1/10

Striker, N. N., Krywka, C., Goy, C., Hövelmann, S. C., Giesselmann, N. C., Schulz,

F., Lokteva, I., Westermeier, F., Caupin, F., Paulus, M. & Lehmkühler, F. (2025). Phase behavior of silica-PNIPAm nanogels under high hydrostatic pressure. *J. Appl. Cryst.*, **58**, 3.

Konzept	Planung	Messung	Auswertung	Manuskript	Korrektur
0/10	0/10	1/10	0/10	1/10	1/10

Mündliche Vorträge auf wissenschaftlichen Konferenzen:

Fast and ultrafast dynamics of liquid surfaces, *NanoMat Science Day*, Hamburg, Deutschland, 2021.

X-ray reflectivity investigations of dynamics at water and salt solutions, *CMWS Early Science Day*, online, 2021.

X-ray pump-probe studies on the ion distribution at the water-vapour interface, *DESY Photon Science Users' Meeting, Satellite Meeting*, online, 2022.

Dynamics at water surfaces studies with X-rays, *CMWS Early Science Project*, online, 2022.

Influence of saccharides on photo-induced structural changes in lipid membranes studied with X-ray diffraction, *SNI*, Berlin, Deutschland, 2022.

Photoswitchable azobenzene-glycoconjugates induce bidirectional switching in phospholipid monolayers and vesicles, *GEM congress*, Autrans, Frankreich, 2023.

X-ray studies of bidirectional switching in phospholipid membranes containing photoswitchable glycolipids, *DPG-Frühjahrstagung der Sektion Kondensierte Materie*, Dresden, Deutschland, 2023.

Photoinduced bidirectional switching in phospholipid membranes, *IUCr*, Melbourne, Australien, 2023.

Static and dynamic X-ray studies on photoswitchable lipid self-assemblies, *SXNS*, Grenoble, Frankreich, 2024.

The Pump-Probe Laser Setup at P08, DESY, *Small angle scattering (SAS)*, Taipeh, Taiwan, 2024.

X-ray scattering studies of light induced dynamics at liquid interfaces and biological membranes, *CMWS Days*, Hamburg, Deutschland, 2025.

Posterpräsentationen auf wissenschaftlichen Konferenzen:

Dynamics of photoswitchable lipid monolayers, *DESY Photon Science Users' Meeting*, online, 2021.

X-ray studies of photo-induced structural changes in lipid monolayers, *DPG-Frühjahrstagung BP-CPP-DY-SOE*, online, 2021.

X-ray studies on dynamics of photoswitchable lipid membranes, *Heraeus Seminar Nanoscale Physics of Electrochemical and Biological Media*, online, 2021.

X-ray studies of the influence of saccharides on photo-induced structural changes in lipid membranes, *SXNS*, online, 2022.

Influence of saccharides on structural changes in lipid membranes induced by photoswitchable glycolipids, *DESY Photon Science Users' Meeting*, online, 2022.

X-ray studies on light induced structural changes in phospholipid monolayers and vesicles, *RAC Summer School*, Varberg, Schweden, 2022.

Photo-induced structural changes in phospholipid monolayers and vesicles containing azobenzene-glycoconjugate, *DESY Photon Science Users' Meeting*, Hamburg, Deutschland, 2023.

Light-induced bidirectional structural changes in phospholipid monolayers at the water-air interface, *CMWS Water Days*, Hamburg, Deutschland, 2023.

Static and dynamic X-ray studies on photoswitchable lipid self-assemblies, *DESY Photon Science Users' Meeting*, Hamburg, Deutschland, 2024.

Neural Network based reflectometry analysis of liquid-gas interfaces, *Machine learning conference*, Garching bei München, Deutschland, 2024.

X-ray scattering studies of optical induced dynamics on liquid-vapour interfaces, *Condensed matter physics and chemistry*, Hamburg, Deutschland, 2024.

FAIR data pipeline of the DAPHNE4NFDI liquid XRR use case at P08, *SRI*, Ham-

burg, Deutschland, 2024.

Photoinduced mesophase transitions in vesicles containing azobenzene amphiphiles, *Small angle scattering (SAS)*, Taipeh, Taiwan, 2024.

A FAIR study of light-induced phase transitions in lipid membranes, *DESY Photon Science Users' Meeting*, Hamburg, Deutschland, 2025.

Betreute Arbeiten

Im Rahmen dieser Arbeit wurden die folgenden wissenschaftlichen Arbeiten bearbeitet und betreut:

Karin Hansen, *Schaltverhalten von Azobenzene - Glycolipiden in Langmuir Monolagen*, *Bachelorarbeit*, 2020

Lukas Petersdorf, *Time Resolved Pump-Probe Studies on Aqueous Salt Solutions via X-ray Reflectivity*, *Masterarbeit*, 2022

Ella Dieball, *Untersuchungen an Photoschaltbaren Vesikeln mittels Kleinwinkelröntgenstreuung*, *Bachelorarbeit*, 2022

Sonja I. Reinheimer, *Abhängigkeit des Schaltverhaltens der Azobenzen-Glycolipide von der Polaren Gruppe der Phospholipide in Langmuir-Monolagen*, *Bachelorarbeit*, 2023

Luca Hutzfeldt, *Phasenübergangstemperaturen von Gemischten Phospholipid und Azobenzen-Lipid Vesikeln*, *Bachelorarbeit*, 2023

Danksagung

Während der letzten Jahre habe ich von vielen verschiedenen Personen wertvolle fachliche, technische und persönliche Unterstützung erhalten. Ohne ihre Hilfe wäre diese Arbeit in ihrer jetzigen Form nicht möglich gewesen. Dafür möchte ich meinen herzlichen Dank aussprechen.

Ein besonderer Dank gilt meiner Betreuerin Bridget Murphy, die mir ermöglicht hat diese Arbeit zu schreiben und viele Erfahrungen in dieser Zeit zu sammeln. Zudem stand sie mir mit fachlichem und persönlichem Rat stehts zur Seite.

Des Weiteren danke ich Thisbe K. Lindhorst für ihre Zusammenarbeit und Unterstützung meiner Forschung insbesondere durch das Bereitstellen von Lipidproben. Ein Dank geht auch an Michael Röhrl, der mich durch die Probenherstellung, fachliche Diskussionen und das Begleiten zu Messzeiten unterstützt hat.

Ich bedanke mich bei Olaf Magnussen für die herzliche Aufnahme in seiner Arbeitsgruppe und die fachlichen Diskussionen. Auch möchte ich Fabian Schröfel, Timo Fuchs, Reihaneh Amirbeigiarab, Talina Rusch, Jan Ole Fehrs, Jonas Bunge, Lasse Kattwinkel, Finn Schröter, Carl Scharf, Knud Schröter, Jochim Stettner, Victor de Manuel González und allen weiteren aktuellen und ehemaligen Mitgliedern der Arbeitsgruppe für die freundliche Gruppenatmosphäre danken.

Ein Danke geht auch an Gerhard Grübel für die Aufnahme in seiner Arbeitsgruppe am DESY sowie Felix Lehmkühler, Claudia Goy, Robert Bauer, Wojciech Roseker, Fransceso Dallari, Irina Lokteva, Leonard Müller, Nele Striker, Alexander Gierke, Niels Giesselmann, Michael Walther, Randeer Gautam und allen weiteren aktuellen oder ehemaligen Mitgliedern der Arbeitsgruppe, die ich kennen lernen durfte, für ihr herzliches Willkommen und die angenehme Gruppenatmosphäre.

Claudia Läufer, Linda Sommer und Donatella Rosetti danke ich für die freundliche Hilfe insbesondere bei bürokratischen Belangen und Formalitäten. Zudem danke ich Matthias Greve und Karsten Tarhouni für ihre technische Unterstützung ohne die viele Messaufbauten nicht entstanden wären.

Ich danke insbesondere Jonas Warias, dass er sein Wissen am Anfang meiner Promotion mit mir geteilt hat und stehts für fachliche Fragen und Diskussionen zur Verfügung stand. Mein besonderer Dank gilt auch Lukas Petersdorf, mit dem ich im Büro viele anregende fachliche Gespräche und Diskussionen führen konnte.

Die im Rahmen dieser Arbeit durchgeführten Messungen wären ohne die Unterstützung zahlreicher Personen nicht möglich gewesen. Zum einen danke ich allen aktuellen und ehemaligen Mitgliedern des LISA-Teams: Nicolas Hayen, Philipp Jordt, Julia, Kobus, Rajendra Prassas Giri, Prashant Hitaischi, Ali Ashtiani, Andrea Sartori, Jule Kuhn, Karin Hansen, Sonja Reinheimer, Katharina Steinkirchner, Mathis Mewes, Luca Hutzfeldt, Carlotta Mager, Ella Dieball und Otto Lippmann. Zum anderen gilt mein Dank Michelle Dargasz, Thomas Arnold und Adrian Rennie für ihre Hilfe während der Messzeiten sowie für die wertvollen Diskussionen zur Datenauswertung. Außerdem danke ich den Beamline-Wissenschaftlern Florian Bertram, Chen Shen, Clement E. Blanchet, Dmytro Soloviov, Michael Paulus, Maciej Jankowski und Norifumi Yamada für ihre tatkräftige Unterstützung während der Messungen.

Zum Schluss möchte ich mich bei Allen bedanken, die mich insbesondere in den arbeitsreichen Wochen unterstützt haben. Ganz besonders bedanke ich mich bei Tobias Klann, Sonja Sapora, Jana Kähler, Karin Hansen, meiner gesamten Familie und allen Freunden für ihre unermüdliche Unterstützung und Freundschaft.

Appendix

A.1 Calculation of the intensity distribution along the laser beam profiles

The intensity profile of the Gaussian shaped laser spot can be described as a 2-dimensional function in the x and y direction

$$f(x,y) = I_0 \cdot \exp\left(-\left(\frac{x^2}{2\sigma_x^2} + \frac{y^2}{2\sigma_y^2}\right)\right) \tag{A.1}$$

with the maximum fluence I_0 at the center and the width σ_x and σ_y along the two axes. The integrated volume $V = 2\pi \cdot I_0 \cdot \sigma_x \cdot \sigma_y$ corresponds to the total intensity of the laser beam with $(14.4 \pm 0.1)\,\mathrm{W}$. The width σ_x and σ_y were determined by fitting a Gaussian curve to the measured profile as shown in Fig. 7.2 to $(1.58 \pm 0.01)\,\mathrm{mm}$ and $(1.35 \pm 0.01)\,\mathrm{mm}$, respectively. Thus, the maximum fluence is $I_0 = (1.07 \pm 0.03)\,\mathrm{W\,mm^{-2}}$.

Similarly, the fluence can be calculated for the flat top shaped laser beam. The area for the flat top shaped beam is approximated as rectangular. As the power is evenly distributed over the spot area, the total power of $(13.4 \pm 0.1)\,\mathrm{W}$ is divided by the area of the laser beam $A = (5.65 \pm 0.01)\,\mathrm{mm} \cdot (2.44 \pm 0.01)\,\mathrm{mm}$. This results in the maximum fluence of $I_0 = (0.97 \pm 0.01)\,\mathrm{W\,mm^{-2}}$.

A.2 Permissions for reprint

IUCr Journals

permissions

Reuse permissions

If you wish to quote short passages or to reprint any figures or tables from IUCr Journals in a scientific publication, prior permission is not required, subject to the following conditions:

- Reproduction is intended in a journal, book, thesis or similar publication.
- The original article in which the material appeared is cited.
- Where possible the wording "Reproduced with permission of the International Union of Crystallography" should be included. In electronic form, this acknowledgement must be visible at the same time as the reused materials, and must be linked to the original article using its DOI.

copyright and licencing policy

Authorship of a scientific article is associated with certain intellectual property rights, protected within the framework of copyright laws. Under the most widespread international agreement, the Berne Convention, copyright in an article automatically belongs to the creator or creators of the article, except for works performed `for hire', in which case the employer or funding body may own the copyright in the work. Whether authors publish their article behind a paywall or as an open-access article, the IUCr does not require authors to transfer copyright. Instead, we offer authors the option to agree either a licence to publish or a CC-BY open-access licence.

Author rights prior to acceptance

Although authors retain full rights over their article prior to its acceptance for publication, there is a normal standard of good behaviour to safeguard the journal's investment of resources in peer review, and the confidentiality of the submitted article while it is in an unfinished form. Therefore, provided the authors acknowledge that the article has been submitted for publication in an IUCr journal, they may:

- share print or electronic copies of the article with colleagues;
- post an electronic version of the article on their personal website, their employer's website/repository and on free public servers (including preprint servers) in their subject area.

Author rights after acceptance

Licence to publish

Provided that a full bibliographic reference to the article as published in an IUCr journal is made, **authors** of such articles may, without needing to seek permission from the IUCr:

- Share print or electronic copies of the article with colleagues.
- Use all or part of the article and abstract, without revision or modification, in theses and/or dissertations, in personal compilations or other publications of their own work (and may receive a royalty or other payment for such work).
- Use the article within their employer's institution or company for educational or research purposes, including use in course packs.
- Post a copy of the author accepted manuscript on their own personal website, on their employer's website/repository and on not-for-profit repositories in their subject area. The site must give full attribution to the article and must provide a permanent link from the posting to the final published article on the IUCr website. A CC-BY licence may be applied to the author accepted manuscript, as required by some funders.
- Post an authorised electronic reprint of the article on their own personal website, on their employer's website/repository and on not-for-profit repositories in their subject area. The site must give full attribution to the article and must provide a permanent link from the posting to the final published article on the IUCr website.

IOP

Conference Series: copyright and permissions

The content in IOP Publishing's Conference Series journals are all published on a gold open access basis.

All of our conference series articles are currently published under a CC BY licence. For further information on what the CC BY licence allows, please refer to this page.

Licence terms and conditions

By submitting the paper to the conference organizer, you, as copyright owner and author/representative of all the authors, grant a worldwide perpetual royalty free exclusive licence to IOP Publishing Limited (IOP) to use the copyright in the paper for the full term of copyright in all ways otherwise restricted by copyright, including, but not limited to, the right to reproduce, distribute and communicate the article to the public under the terms of the Creative Commons Attribution (CC BY) licence (creativecommons.org/licenses/by/4.0 or any newer version of the licence) and to make any other use which IOP may choose world-wide, by all means, media and formats, whether known or unknown at the date of submission, to the conference organizer.

This licence does not transfer the copyright in the paper as submitted which therefore remains with the authors or their employer, as appropriate. Authors may not offer the paper to another publisher unless the article is withdrawn by the author(s) or rejected by IOP.

Once published, the paper may be reused in accordance with the terms of the applicable Creative Commons Attribution (CC BY) licence, including appropriate citation information (for electronic use best efforts must be made to include a link to the online abstract of the paper on IOPscience), a link to the Creative Commons Attribution (CC BY) licence, and indicating if any changes have been made to the original paper.

The IOP Proceedings Licence Notice

The IOP Proceedings Licence Notice should be displayed as:

'Published under licence in *Journal Title* by IOP Publishing Ltd.
 Content from this work may be used under the terms of the Creative Commons Attribution 4.0 International licence. Any further distribution of this work must maintain attribution to the author(s) and the title of the work, journal citation and DOI.'

Where *Journal Title* is one of:

- *Journal of Physics: Conference Series*
- *IOP Conference Series: Materials Science and Engineering*
- *IOP Conference Series: Earth and Environmental Science*